

# L-H transition studies on spherical tokamaks

Lena Howlett

Doctor of Philosophy

University of York

Physics, Engineering and Technology

January 2024

# Abstract

While the higher fusion power achieved in high confinement (H-)mode make it a desirable regime for tokamak devices, the transition from low confinement (L-)mode to H-mode is a complex, multi-faceted process whose dynamics are still not fully understood. It would not be possible to explore the entire physics of the L-H transition in a single project, but a selection of aspects have been studied and presented here for the spherical tokamaks MAST and MAST-U. Spherical tokamaks are known to differ from conventional tokamaks in a number of physics areas, including the L-H transition, but our understanding is limited by a comparative lack of experimental data. A comprehensive study of the density dependence of the H-mode power threshold  $P_{LH}$  on MAST is presented, showing for the first time the presence of the low-density branch and describing different types of boundary behaviours and intermediate confinement states. As expected for spherical tokamaks, the commonly used empirical scaling laws significantly underestimate  $P_{LH}$ . The low-density branch is further explored in a comprehensive study of the L-H transition values of the ion and electron heat flux in the edge. Here the effects of fast ion losses on the NBI heating efficiency are demonstrated, and a strong density dependence of the absorbed NBI power is found, independent of the actual injected power. The presence of the low-density branch of  $P_{LH}$  is not explained by the heating effects however, and appears to originate in the rate of change of stored energy instead. As the improved confinement in H-mode is characterised by a suppression in turbulence, the turbulence data in the form of 2D density fluctuations measured by beam emission spectroscopy (BES) is explored for selected L-H transition shots, with a cross-correlation time delay estimation (CCTDE) technique used to calculate poloidal and radial velocities from BES data. Finally, a set of experiments performed on MAST-U to explore the power threshold in conventional and Super-X divertor configurations is described and preliminary results are presented.

# Contents

<b>Abstract</b>	<b>2</b>
<b>List of Tables</b>	<b>6</b>
<b>List of Figures</b>	<b>7</b>
<b>Acknowledgements</b>	<b>11</b>
<b>Declaration</b>	<b>12</b>
<b>1 Introduction</b>	<b>13</b>
1.1 Introduction to fusion . . . . .	13
1.1.1 Fusion for energy . . . . .	15
1.2 Tokamaks . . . . .	17
1.2.1 Spherical tokamaks . . . . .	21
1.3 Turbulence . . . . .	23
1.4 Confinement regimes . . . . .	25
1.5 L-H transition . . . . .	28
1.5.1 Power threshold . . . . .	29
1.6 Outline of thesis . . . . .	30
<b>2 Tools used in this thesis</b>	<b>32</b>
2.1 Tokamaks used in this project . . . . .	32
2.1.1 Mega-Amp Spherical Tokamak (MAST) . . . . .	33
2.1.2 Upgrade to MAST-U . . . . .	35
2.2 Diagnostics most relevant to this project . . . . .	35
2.2.1 Deuterium Balmer $\alpha$ emission ( $D_\alpha$ ) . . . . .	36

<i>CONTENTS</i>	4
2.2.2 CO <sub>2</sub> interferometer . . . . .	37
2.2.3 Multi-channel bolometer system . . . . .	38
2.2.4 Thomson scattering (TS) . . . . .	39
2.2.5 Charge-exchange recombination spectroscopy (CXRS) . . . . .	40
2.2.6 Fission chamber . . . . .	42
2.2.7 Mirnov coils . . . . .	44
2.2.8 Beam emission spectroscopy . . . . .	45
2.3 Established codes used for this project . . . . .	47
2.3.1 EFIT: equilibrium reconstruction . . . . .	47
2.3.2 TRANSP: transport code with NBI module (NUBEAM) . . . . .	49
2.4 Dataset from L-H transition experiment on MAST used in Chapters 3 and 4	50
2.4.1 Favourable and unfavourable configurations . . . . .	51
<b>3 Power threshold studies</b>	<b>54</b>
3.1 Overview . . . . .	54
3.2 Motivation . . . . .	54
3.3 Net power calculations . . . . .	55
3.4 Plasma behaviour categorisation . . . . .	60
3.4.1 $D_\alpha$ analysis . . . . .	63
3.4.2 Point selection . . . . .	70
3.5 Density dependence of $P_{LH}$ on MAST . . . . .	72
3.5.1 Fit to data . . . . .	73
3.5.2 Comparison with scaling laws . . . . .	75
3.5.3 Alternative $P_{\text{net}}$ definitions . . . . .	78
3.5.4 Impact of H-mode control through $\delta r_{\text{sep}}$ . . . . .	81
3.5.5 Impact of transition time selection . . . . .	81
3.6 Comparison with $n_{e,\text{min}}$ scaling . . . . .	82
3.6.1 Re-evaluating $n_{e,\text{min}}$ scaling . . . . .	84
3.6.2 Modifying $n_{e,\text{min}}$ scaling with adjusted $P_{LH}$ . . . . .	86
3.7 Summary . . . . .	89
3.7.1 Absorbed beam power calculations by TRANSP . . . . .	92

<i>CONTENTS</i>	5
<b>4 Heat flux studies</b>	<b>93</b>
4.1 Motivation . . . . .	93
4.2 Method: Interpretative simulations with TRANSP . . . . .	94
4.2.1 Energy balance in a tokamak . . . . .	95
4.2.2 Setting up TRANSP runs with OMFITprofiles . . . . .	97
4.2.3 Matching neutron rates with anomalous diffusivity . . . . .	100
4.3 Results . . . . .	105
4.3.1 Beam heating efficiency . . . . .	107
4.3.2 Consequences for the $P_{LH}$ curve . . . . .	115
4.3.3 Comparison with results from other devices . . . . .	117
<b>5 Turbulence studies</b>	<b>120</b>
5.1 Motivation, background and previous work . . . . .	120
5.2 BES data analysis . . . . .	124
5.2.1 Requirements to obtain useful data . . . . .	125
5.2.2 Extracting fluctuation data . . . . .	126
5.2.3 Mode powers, phase velocities, etc . . . . .	130
5.2.4 Velocimetry . . . . .	145
5.2.5 Wavenumber-frequency spectra . . . . .	156
5.2.6 Further steps to energy transfer . . . . .	161
<b>6 Conclusion and further work</b>	<b>163</b>
6.1 Conclusion of MAST work . . . . .	164
6.2 MAST-U experiments . . . . .	166
6.3 MAST, MAST-U and potential extrapolation to STEP . . . . .	169
<b>A Derivation of energy balance</b>	<b>175</b>
A.1 Particle balance . . . . .	176
A.2 Momentum balance . . . . .	177
A.3 Energy balance . . . . .	178
<b>B TRANSP neutron deficit - Cecconello 2019</b>	<b>183</b>
<b>List of References</b>	<b>185</b>

# List of Tables

2.1	Typical parameters for MAST and MAST-U . . . . .	34
3.1	Different net power, NBI and ohmic power variables used in this thesis. . . . .	58
3.2	Parameter changes between ITPA MAST data and data used in this project . . . . .	76
6.1	Parameters for the different MAST and MAST-U data used in this project . . . . .	172
6.2	Parameters for example STEP design concept and possible $P_{LH}$ values . . . . .	174

# List of Figures

1.1	Binding energy per nucleon . . . . .	14
1.2	Diagram showing tokamak geometry and schematic to illustrate flux surfaces and divertors. . . . .	18
1.3	Conventional vs spherical tokamak. . . . .	22
1.4	Turbulence suppression through zonal flows . . . . .	25
1.5	Temperature, density and radial electric field profiles for L- and H-mode . . .	26
1.6	Density and $D_\alpha$ traces during an L-H transition . . . . .	27
1.7	Martin $P_{LH}$ scaling and its performance for spherical tokamaks. . . . .	30
2.1	Divertor configurations that can be studied with MAST-U. . . . .	34
2.2	The laser path(s) of the interferometer system on MAST-U . . . . .	38
2.3	Poloidal and tangential views of the bolometer system on MAST . . . . .	39
2.4	CXRS: the desmearing correction applied to $T_i$ data measured from the South NBI . . . . .	41
2.5	Location of the Mirnov coils with respect to a typical plasma separatrix . . .	44
2.6	BES array view on MAST. . . . .	45
2.7	Schematic workflow of an interpretive TRANSP simulation. . . . .	49
2.8	Density peaking for all Thomson scattering data points in the dataset. . . . .	51
2.9	Change of $\delta r_{\text{sep}}$ as H-mode control technique. . . . .	53
3.1	Time traces of $P_{\text{loss}}$ components for an example shot . . . . .	57
3.2	Example $\bar{n}_e$ and $D_\alpha$ traces for behaviour categories. . . . .	61
3.3	Determining frequencies present in $D_\alpha$ signals for I-phases. . . . .	64
3.4	Determining frequencies present in $D_\alpha$ signals for H-modes and dithery peri- ods. . . . .	65

3.5	Comparison of methods to find frequencies in $D_\alpha$ signal, and of frequencies found in upper and midplane $D_\alpha$ . . . . .	67
3.6	Representation of skewness and kurtosis . . . . .	69
3.7	Results of the $D_\alpha$ analysis for frequency, skewness and kurtosis of behaviour categories. . . . .	71
3.8	$P_{\text{loss}}$ vs $\bar{n}_e$ results with scaling laws. . . . .	74
3.9	$P_{\text{loss}}$ vs $\bar{n}_e$ with ITPA data points. . . . .	77
3.10	$P_{\text{net}}$ vs $\bar{n}_e$ for TRANSP and EFIT ohmic power. . . . .	79
3.11	Impact of $P_{\text{rad}}$ on $P_{\text{net}}$ . . . . .	80
3.12	Impact of $\delta r_{\text{sep}}$ control technique on $P_{LH}$ . . . . .	82
3.13	$P_{\text{loss}}$ vs $\bar{n}_e$ comparison of different transition time choices. . . . .	83
3.14	Plot showing all the $n_{e,\text{min}}$ scaling [1] results for different derivation options. . . . .	88
4.1	Toroidal velocity estimated by the South beam CXRS diagnostic and its dependence on density and power variables. . . . .	95
4.2	Anomalous diffusivity and its effect on neutron rate calculated by TRANSP . . . . .	102
4.3	Neutron rate match and anomalous diffusivity comparisons for the initial faulty PID controller, the corrected PID controller version and the results of further manual improvements to the anomalous diffusivity. . . . .	103
4.4	Electron and ion heat flux density dependence on MAST compared with $P_{\text{loss}}$ . . . . .	105
4.5	Density dependence of beam power losses . . . . .	107
4.6	Effect of neutral density outside of LCFS on TRANSP beam loss components . . . . .	108
4.7	Mirnov signals for low- and high-density example shots, as a proxy for fast ion losses . . . . .	109
4.8	Mirnov signals for example shot, showing evolution of MHD instabilities . . . . .	111
4.9	TAEs and chirping TAEs . . . . .	113
4.10	fishbones and LLM . . . . .	113
4.11	Example of a locked mode . . . . .	116
4.12	Density dependence $P_{\text{loss,th}}$ corrected for fast ion losses . . . . .	117
4.13	Results plots from a reference paper: Ryter et al. 2014 Nucl. Fusion 54 . . . . .	118
5.1	Kinetic energy transfer and other turbulence parameters . . . . .	122
5.2	Nonlinear kinetic energy transfer on C-Mod . . . . .	123

5.3	The arrangement of the BES array channel labels on MAST . . . . .	125
5.4	Effect of strong MHD modes on Mirnov and BES data. . . . .	127
5.5	Example of density fluctuations measured by BES array for a double null MAST shot . . . . .	128
5.6	NBI power and raw BES signal variation and frequency spectra . . . . .	129
5.7	Mirnov and BES data (including spectrograms) with density and $D_\alpha$ for sam- ple shot 29378 . . . . .	131
5.8	TAE burst and ELM-precursor summary plots of Mirnov and BES spectrograms	132
5.9	Fitting the BES fluctuation spectrum during a TAE burst and an ELM- precursor to estimate the mode frequencies . . . . .	134
5.10	Coherence and phase between all channels and reference channel 5 during a TAE burst, along with example plots of the coherence analysis for this time slice between the reference channel and channel 20 . . . . .	135
5.11	Average phases calculated for minimum coherence levels of 0.5 and 0.75 for TAE burst and ELM-precursor plotted as contour plots of the BES array with the LCFS . . . . .	137
5.12	Coherence and phase between all channels and reference channel 4 during an ELM-precursor, along with example plots of the coherence analysis for this time slice between the reference channel and channel 11 . . . . .	138
5.13	For the ELM-precursor and reference channel 4, plots of the mode frequency (calculated with multiple methods), mode power, phase (from several sources) and phase gradient are plotted for each row as a function of $\rho_{\text{eff},N}$ . . . . .	140
5.14	For the TAE burst and reference channel 5, plots of the mode frequency (calculated with multiple methods), mode power, phase (from several sources) and phase gradient are plotted for each row as a function of $\rho_{\text{eff},N}$ . . . . .	142
5.15	Average phases and mode power for TAE burst and ELM-precursor as contour plots of the BES array with the LCFS . . . . .	143
5.16	Phase velocity calculations for ELM-precursor . . . . .	144
5.17	CCTDE velocimetry method using a $250\mu\text{s}$ correlation window for the poloidal velocity in a SOL channel of a LSN shot during L-mode . . . . .	146
5.18	CCTDE velocimetry method using a $250\mu\text{s}$ correlation window for the radial velocity in a SOL channel of a LSN shot during L-mode . . . . .	148

5.19	Tilted filament structure moving poloidally . . . . .	150
5.20	Poloidal and radial velocity correlation . . . . .	152
5.21	Effect of poloidal displacement of channels on radial velocity . . . . .	153
5.22	Poloidal velocity results for an edge and a SOL channel . . . . .	154
5.23	Poloidal and radial velocity in an edge channel of a LSN shot, showing the strongly fluctuating $v_r$ during L-mode . . . . .	155
5.24	Applying the velocimetry method to Mirnov coil data . . . . .	157
5.25	Conditional $k - f$ spectra at different radial locations from [2] . . . . .	158
5.26	$k - f$ spectra for MAST L-mode BES data from three radial locations: original version and normalised conditional spectra . . . . .	159
5.27	$k - f$ spectra for increasing radius showing changing structures . . . . .	160
5.28	$k - f$ spectra for MAST L-mode BES data with strong MHD mode . . . . .	161
6.1	First results from a power threshold study on MAST-U comparison Super-X and conventional configurations . . . . .	168
6.2	$P_{\text{loss}}$ and $P_{\text{loss,th}}$ vs $\bar{n}_e$ for 2011-13 MAST data with fits, along with 2001-03 MAST ITPA data and $P_{LH}$ scalings . . . . .	170
6.3	Comparison of MAST and MAST-U L-H transition $P_{\text{loss}}(\bar{n}_e)$ data . . . . .	171
B.1	Neutron rate match and anomalous diffusivity comparisons for neutron rate matches with and without the inclusion of the ‘‘Cecconello factor’’ (though note that this was based on false assumptions). . . . .	185

# Acknowledgments

First, I would like to thank my supervisors, István and Simon, who have been incredible throughout my PhD in their mentoring, advice, engaging physics discussions and general support. This project would not have been possible without their help and their support was invaluable in strengthening my skills and confidence. I would also like to thank my parents, who have been very supportive throughout my entire education and enabling me to pursue a PhD, even while we were living in different countries from another for almost half of my life. The friends I have made during my Masters, during my PhD and at Culham have also been incredibly helpful, with other students being a comforting source of advice and understanding, and especially those who have experienced the stresses of a PhD being incredibly kind in supporting me through mine. I would like to thank everyone at Culham, at the University and the wider research community who have helped me with various specific or more vague problems, either directly or through fruitful discussions. I would also like to thank those who have been there for me in my personal life at various stages leading up to the end of this journey, I will forever be grateful for all your help.

# Declaration

This thesis has not previously been accepted for any degree and is not being concurrently submitted in candidature for any degree other than Doctor of Philosophy of the University of York. This thesis is the result of my own investigations, except where otherwise stated. All other sources are acknowledged by explicit references.

The present work was presented at the following conferences:

- L-H transition studies on MAST and MAST-U, *18th International Workshop on H-mode Physics and Transport Barriers*, Princeton, NJ, USA, Sep 2022 [INVITED]
- L-H transitions and intermediate behaviours on MAST and MAST-U, *European Physical Society 48th Conference on Plasma Physics*, Virtual, Jun 2022
- Turbulence in confinement transitions on MAST, *25th Joint EU-US Transport Task Force Meeting*, Virtual, Sep 2021
- Turbulence in confinement transitions on MAST, *European Physical Society 47th Conference on Plasma Physics*, Virtual, Jun 2021

And led to the publication of the following article and conference proceedings:

- L. Howlett *et al.*, L-H transition studies on MAST: power threshold and heat flux analysis, *Nuclear Fusion*, 63(5):052001, 2023
- L. Howlett *et al.*, L-H transitions and intermediate behaviours on MAST and MAST-U, EPS Conference Proceedings 48, 2022 *post-submission*
- L. Howlett *et al.*, Turbulence in L-H transitions on MAST, EPS Conference Proceedings 47, 2021 *published*

Material presented in Chapters 3 and 4 is (heavily) based on the publication in Nuclear Fusion [3], with additional work included.

# Chapter 1

## Introduction

### 1.1 Introduction to fusion

The mass of an atomic nucleus is always less than the combined masses of the constituent nucleons, with the difference known as the mass defect. The energy equivalent to this mass through Einstein's equation

$$E = mc^2$$

is called the binding energy  $E_B$ , which can be experimentally or theoretically determined for each isotope. The binding energy per nucleon  $E_B/A$  represents the average energy required to remove one nucleon from the nucleus, and values in MeV are plotted against mass number  $A$  for selected isotopes in Figure 1.1. A higher binding energy corresponds to a more stable nucleus, and processes moving a nucleus from a region of lower  $E_B/A$  to a region of higher  $E_B/A$  release energy, while processes moving in the opposite direction consume energy. The most stable isotopes are clustered around iron  $^{56}\text{Fe}$  with  $Z = 26$ . For isotopes lighter than this, energy is released through nuclear fusion processes, in which nuclei are merged to form elements of higher atomic charge  $Z$ . Isotopes with greater mass than  $^{56}\text{Fe}$  would require more energy to fuse than the process releases, and they move to more stable configurations through fission instead. Nuclear fusion is the process which generates the vast energies released from stars, which begin their lives by fusing hydrogen ( $Z = 1$ ) and continue moving to higher  $Z$  throughout their lifetime, with the most massive ones creating elements up to iron ( $Z = 26$ ) and nickel ( $Z = 28$ ). For elements with  $Z \gg 26$ , the fusion process requires more energy

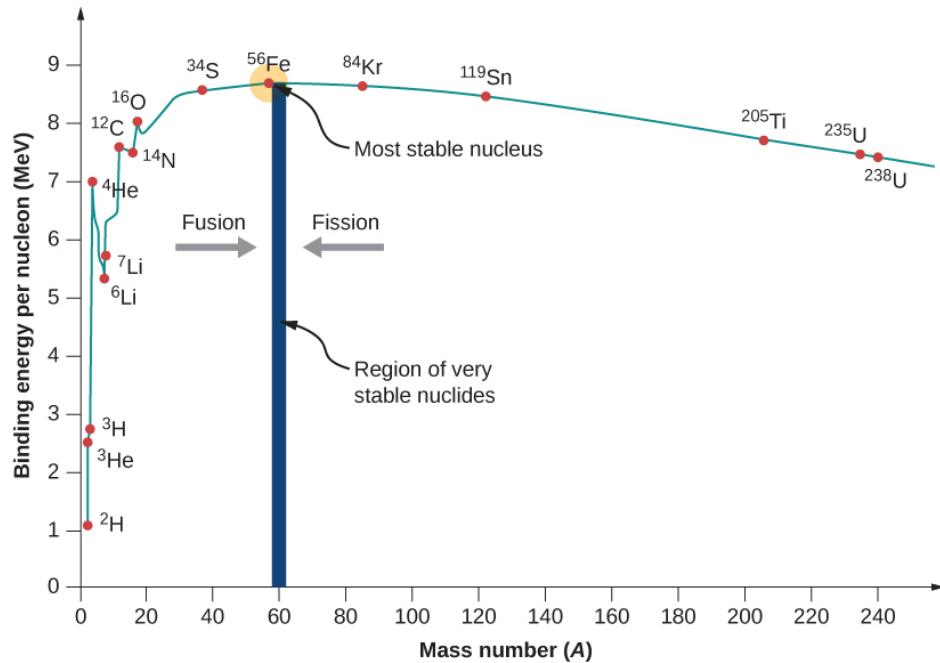


Figure 1.1: Binding energy per nucleon as a function of mass number for selected isotopes. Elements below iron ( $^{56}\text{Fe}$ ) will release energy through fusion, while elements above it will release energy through fission. Note the local peak for  $^4\text{He}$ . [4]

than it releases, so these are largely produced in supernovae instead.

Since nuclei are always positively charged, they are normally prevented from approaching each other at distances close enough to fuse. For fusion to occur, the nuclei must therefore have sufficient energy to overcome this Coulomb potential, resulting in extreme conditions. Because of this high energy requirement, the conditions under which fusion occurs are extreme, resulting in the matter being in the form of a plasma, with most or all of the electrons stripped away from the nuclei and the positive ions and negative electrons forming a quasi-neutral (positive and negative charges very nearly balance) ionised gas which responds to electromagnetic forces. In stellar cores, the high energies are obtained through high temperatures (several million K in the core) and due to their immense masses, the gravitational pressures in stars are extreme (hundreds of billions of atmospheres or larger). These conditions do not naturally occur on Earth, and sustaining optimal fusion conditions for long enough to generate a net energy output is a challenging task which the fusion community has been working on for decades.

### 1.1.1 Fusion for energy

The large release of energy per reaction and the potential for abundant fuels and comparatively safe products have made fusion an attractive prospect for future power plants. Attempts to harness controlled nuclear fusion on Earth for human energy use have been ongoing since the 1940s. While immense progress has been made in the fusion community, the conditions in a fusion reactor have revealed many new physics phenomena which are still only partially understood. As a result, the initial goal of producing more fusion power than is required to heat the fuel and run the machine has yet to be realised. A number of research devices of different designs have been built and provide a rich database of physics and engineering knowledge which will ultimately allow the construction and operation of an economic fusion power plant to provide near limitless, comparatively safe and clean energy with low carbon emissions. Fusion in stars involves many different reactions, but for controlled fusion for human energy use a few reactions are most promising. Fusing the lightest elements releases the largest amount of energy per nucleon, and low- $Z$  ions are less susceptible to large radiative losses through bremsstrahlung, so most terrestrial fusion efforts focus on fusing hydrogen isotopes. The most favourable reaction is generally considered to be the fusion of deuterium ( $A = 2$ ) and tritium ( $A = 3$ ),



as it has the highest fusion cross-section in the relevant temperature range as well as the largest energy release per reaction. As about 0.017% of hydrogen in all water molecules is in the form of the stable deuterium isotope, deuterium for fusion can be harvested in abundance from seawater. Tritium however is radioactive with a short half-life of 12.5 years so must be produced through other nuclear processes. For current limited research use, tritium produced in some fission reactors is enough supply, but for future reactors tritium will need to be bred on site, likely through lithium blankets on the reactor which capture the moderated fusion neutrons to produce tritium and helium [5]. Most current fusion experiments, including those involved in this project, use pure deuterium plasmas instead, which fuse in two reactions with

$\sim 50 - 50$  probability,



where the tritium produced in the first reaction will then likely undergo the DT reaction in Equation 1.1.

The fusion power density in a plasma is [6]

$$p_{\text{fus}} = \frac{1}{4}n^2\langle\sigma v\rangle\epsilon \quad (1.4)$$

where  $n$  is the plasma (i.e. electron) number density in  $\text{m}^{-3}$ ,  $\epsilon$  is the energy released in a fusion reaction (e.g. 17.6MeV for D-T), and  $\langle\sigma v\rangle$  is the reactivity for a particular fusion reaction (such as D-T or D-D). The reactivity contains the reaction cross-section  $\sigma$  and the particle velocity  $v$ . For the favourable and achievable temperature range of 10-20keV, the reactivity for D-T can be approximated by [6]

$$\langle\sigma v\rangle = 1.1 \times 10^{-24}T^2\text{m}^3\text{s}^{-1} \quad (1.5)$$

with  $T$  in keV. To show the dependence of fusion power on plasma pressure, the fusion power can be estimated [6] from the power density of Equation 1.4 with a simplified geometry of a torus with a circular poloidal cross-section of minor radius  $a$  centred around major radius  $R_0$ ,

$$P_{\text{fus}} = \pi^2 R_0 \epsilon \int_0^a n^2 \langle\sigma v\rangle r dr \quad (1.6)$$

which together with the expression for  $\langle\sigma v\rangle$  from Equation 1.5 demonstrates the dependence of fusion power on plasma pressure  $p$ ,

$$P_{\text{fus}} \propto n^2 T^2 \quad , \text{ i.e. } P_{\text{fus}} \propto p^2, \quad (1.7)$$

giving some indication of what conditions will be favourable for fusion power output, which will be expanded on in Section 1.4.

Since fusion conditions such as the temperature are so extreme, all current fusion projects

have to supply external heating power to obtain the plasma at these conditions. The aim for future power stations is that the plasma will be able to maintain fusion conditions mainly through self-heating, achieved with improved confinement and alpha particle heating. Once a plasma can sustain fusion conditions without external heating, it is said to have ignited. An important parameter is therefore the ignition condition, the Lawson criterion

$$n\tau_E > \frac{12T}{\langle\sigma v\rangle\epsilon_\alpha} \quad (1.8)$$

which describes the condition in terms of the density  $n$ , energy confinement time  $\tau_E$ , temperature  $T$ , reactivity  $\langle\sigma v\rangle$  and alpha particle energy  $\epsilon_\alpha$ . Together with the expression for reactivity in Equation 1.5, the Lawson criterion for DT fusion can be rewritten as the fusion triple product [6]

$$nT\tau_E \geq 3 \times 10^{21} \text{m}^{-3} \text{keV s}. \quad (1.9)$$

This form of the ignition criterion is used in magnetic confinement fusion (MCF), one of the two main approaches for controlled fusion. The two approaches highlight the important parameter dependencies, with MCF favouring a long confinement time at relatively low densities, and the other being inertial confinement fusion (ICF), where the density is extremely high and no attempt is made to increase the confinement time beyond simple inertia. For this report, only magnetic confinement fusion is considered. The principle of MCF lies in the fact that the plasma consists of charged particles, which can therefore be directed and confined using magnetic fields.

## 1.2 Tokamaks

A charged particle of mass  $m_j$  and charge  $q_j$  moving in a magnetic field  $\mathbf{B}$  at velocity  $\mathbf{v}_j$  experiences the Lorentz force,

$$m_j \frac{d\mathbf{v}_j}{dt} = q_j(\mathbf{E} + \mathbf{v}_j \times \mathbf{B}) \quad (1.10)$$

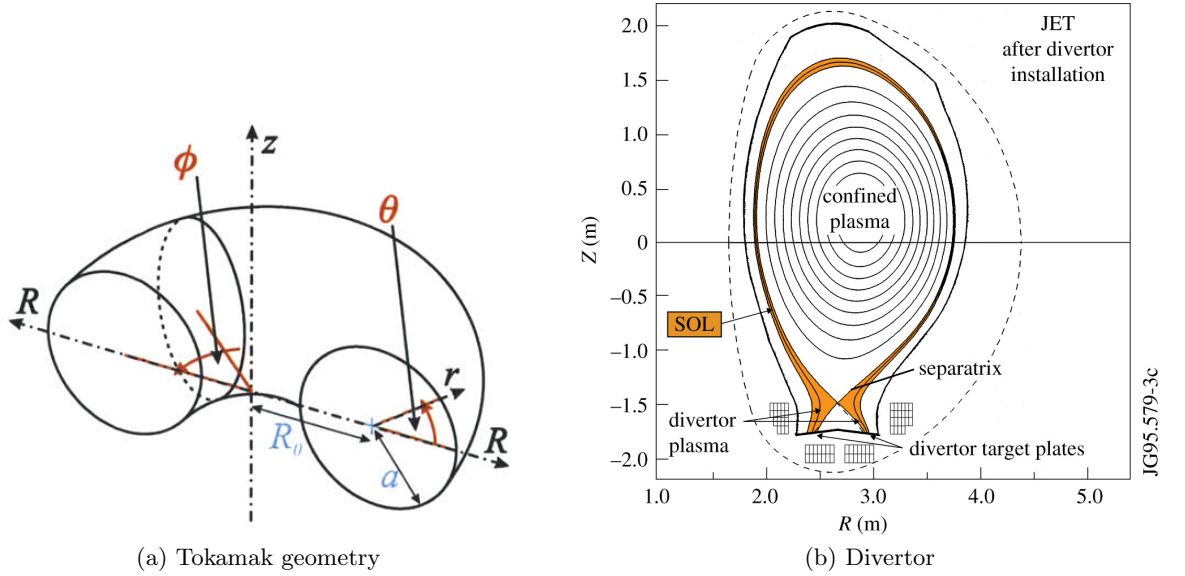


Figure 1.2: (a) Schematic of a tokamak geometry, showing the angle and radius parameters. [2] (b) Schematic of JET illustrating concepts of divertors, separatrix and SOL. [7]

which causes the particle to gyrate around magnetic field lines in Larmor orbits. The frequency of gyration is given by the cyclotron frequency

$$\omega_c = \frac{|q_j|B}{m_j} \quad (1.11)$$

and the size of the orbit is described by the Larmor radius

$$\rho_L = \frac{v_\perp}{\omega_c} = \frac{m_j v_\perp}{|q_j|B}. \quad (1.12)$$

Charged particles in a magnetic field are thus able to freely move parallel to field lines while their cross-field transport is limited. Since the Lawson criterion for tokamaks (at densities  $\geq 10^{20} \text{ m}^{-3}$ ) requires confinement times of the order of seconds, the magnetic field of a tokamak must be optimised to avoid confinement losses as much as possible. In a simple description, the tokamak concept begins by confining the plasma in a cylinder with magnetic field coils placed around it. End losses are avoided by bending the plasma tube into a torus. The shape enclosing the plasma can then be described by the major radius  $R_0$ , which is the distance between the symmetry axis and the magnetic axis, the minor radius  $a$ , which is the distance between the magnetic axis and the edge of the plasma, a toroidal angle  $\phi$  going around the symmetry axis and a poloidal angle  $\theta$  going around the magnetic axis, illustrated

in Figure 1.2a.

This toroidal magnetic field is not sufficient to confine the plasma though, as drifts will quickly lead to large particle losses. The point or line about which the particle gyrates is known as the guiding centre, and particle drifts cause the guiding centre to drift away from the field line. The strength of the toroidal magnetic field is not constant inside the coils but is rather inversely proportional to the major radius, i.e.  $1/R$ , leading to a high-field side (HFS) on the inboard and a low-field side (LFS) on the outboard sections of the torus. This spatial dependence of the magnetic field causes a charge-dependent  $\nabla\mathbf{B}$  drift in the vertical direction, separating electrons and ions, which in turn forms a vertical electric field and causes an  $\mathbf{E} \times \mathbf{B}$  drift outwards, leading to loss of confinement. The  $\mathbf{E} \times \mathbf{B}$  drift does not depend on charge and therefore causes both electrons and ions to drift outwards.

To prevent this outward drift, a second magnetic field component is required. This poloidal magnetic field  $B_p = B_\theta$  combines with the toroidal magnetic field  $B_T = B_\phi$  to form a helical field around the torus. As the particles move along this helical field, their  $\nabla\mathbf{B}$  drift averages out to zero, and the outward  $\mathbf{E} \times \mathbf{B}$  drift is inhibited. In a tokamak, the poloidal field component is generated by driving a current  $I_p$  through the plasma in the toroidal direction. In current devices, this current is induced by changing the magnetic flux through the centre of the plasma, commonly achieved by ramping a current through a solenoid in the centre of the torus. The interaction between the solenoid and the plasma is similar to the action of a transformer. Inductive current drive sets an upper limit on the duration of each plasma discharge (or shot), so for future devices non-inductive current drive methods are being investigated.

The inductively-driven plasma current  $I_p$  travelling through the plasma energises the particles and causes electron-ion collisions, which create a resistance  $\eta$ , commonly described with the Spitzer resistivity [8]  $\eta_{\text{Sp}} = \frac{4\sqrt{2}\pi}{3} \frac{Ze^{[2]}m_e^{1/2}\ln\Lambda}{(4\pi\epsilon_0)^2(k_B T_e)^{3/2}}$  where  $Z$  is the ionisation of the nuclei,  $e$  is the electron charge,  $m_e$  is the electron mass,  $\ln\Lambda$  is the Coulomb logarithm,  $\epsilon_0$  is the electric permittivity of free space,  $k_B$  is the Boltzmann constant and  $T_e$  is the electron temperature. This resistance acts to heat the plasma through a process known as ohmic heating, but since the resistance decreases as the temperature increases,  $\eta \propto T^{-3/2}$ , ohmic heating becomes less effective at higher temperatures. To reach desired plasma temperatures, auxiliary heating methods are therefore required.

The helical twist of the magnetic field requires the use of a further parameter to describe

the configuration, the safety factor  $q$ ,

$$q = \frac{1}{2\pi} \oint \frac{B_\phi}{RB_\theta} ds = \frac{m}{n}. \quad (1.13)$$

It is defined as the number of times a field line wraps around toroidally ( $n$ ) for each poloidal revolution ( $m$ ) and describes how tightly wound the field lines are. The magnetic configuration allows for a description of the plasma in terms of flux surfaces, which are surfaces of constant toroidal magnetic flux  $\psi = \int q\delta\psi$  and constant pressure  $p$  connected through the twisting field lines. The plasma can move freely along a flux surface, so only closed flux surfaces which do not intersect solid structures confine the plasma, while those which do intersect are called open flux surfaces. The boundary between regions of open and closed flux surfaces is called the last closed flux surface (LCFS) or separatrix, as shown in Figure 1.2b. Plasma quantities which are constant on a flux surface, such as pressure or heat flux, are known as flux quantities, and profiles of these can be presented along a spatial dimension of normalised toroidal magnetic flux  $\psi_N$  or normalised effective radius  $\rho_{\text{eff},N}$  which are defined as  $\psi_N = \psi/\psi_{\text{max}}$  and  $\rho_{\text{eff},N} = \sqrt{\psi_N}$  respectively, and have a range of 0 in the core to 1 at the LCFS. Most modern tokamak designs include one or two divertors, located at the top and/or bottom of the device, where the open field lines intersect with specially designed plates to withstand the large heat fluxes, shown as divertor target plates in Figure 1.2b. These divertors therefore act as exhausts for the tokamak, allowing for the expulsion of the helium ash which is created during fusion reactions and will lead to reduced performance if not flushed out. The divertor plates are also the points at which the plasma will deposit the large amount of energy that necessarily escapes confinement. Use of divertors allows for the separation of the confined core plasma and diverted plasma, by creating a magnetic field configuration with points of zero poloidal field on the LCFS called X-points. Separating the divertor plates from the main chamber allows for use of high melting point materials such as tungsten without absorbing too many high-Z impurities into the core plasma, which would otherwise lead to enhanced radiative losses. The thin region of open field lines wrapping around the torus which intersect with the divertor plates is called the scrape-off-layer (SOL), and is marked in orange in Figure 1.2b.

Tokamaks have a number of sources of instabilities, many related to the magnetic field geometry. One of the factors that can influence the plasma stability are the relative directions

of the toroidal magnetic field curvature and the pressure gradient. The curvature  $\kappa$  points towards the centre of the perceived circle, so in a tokamak the direction of curvature is always towards the symmetry axis ( $R = 0$ ). The pressure is highest in the plasma core, so the direction of the pressure gradient goes from the LCFS to the core. This results in the curvature and pressure gradient pointing in the same direction on the outboard side (large  $R$ ) and in opposite directions on the inboard side (small  $R$ ). On the outboard side,  $\kappa \cdot \nabla p > 0$ , so instabilities (known as interchange instabilities) are allowed to grow, while on the inboard side  $\kappa \cdot \nabla p < 0$  and these instabilities are suppressed. The two sides are thus known as the bad curvature region and good curvature region respectively. Many tokamak instabilities, known as ballooning modes, have maximum amplitudes on the bad curvature side.

Describing or modelling a tokamak plasma with individual particles is unfeasible due to number of calculations that would need to be performed for each time step. The collective effects displayed by a plasma however enable descriptions in terms of kinetic or fluid approximations. One of the simplest descriptions is magnetohydrodynamics (MHD), which assumes the plasma to be one single fluid where the mass is carried by ions and the current carried by electrons. One of the more complex descriptions which can still handle a tokamak-sized plasma is gyrokinetics, which averages kinetic equations over the gyromotion, so that the movement of the guiding centre is calculated instead. The stability of a plasma can be analysed through any of these descriptions, though for many tokamak-relevant instabilities MHD theory is sufficient. While MHD theory is not sufficient to describe some common other instabilities, MHD instabilities tend to be more severe in their reaction and more easily driven unstable, so they are of particular concern for tokamak operation. As will become clearer in Chapters 4 and 5, they can strongly influence both fast ion (i.e. neutral beam heating particle) losses and the quality or availability of turbulence data in relevant turbulence diagnostics such as beam emission spectroscopy (more in Chapter 2). MHD instabilities can be highly problematic for tokamak operation, and their avoidance is an important operating goal.

### 1.2.1 Spherical tokamaks

As research reactors, every tokamak currently existing is unique, but different major design choices can be identified which allow the description of sub-categories of tokamaks. One

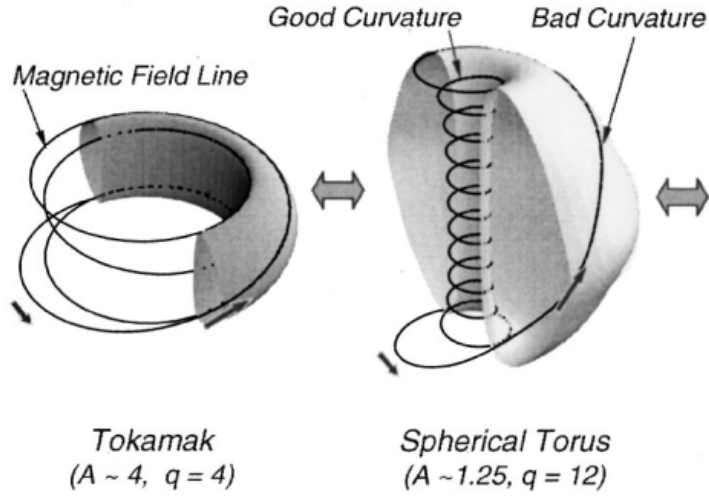


Figure 1.3: The magnetic configurations of conventional (left) and spherical tokamaks (right), showing an example path of a plasma particle. In the more compact and elongated ST, the particles spend more time in the good curvature region. [9]

such category is the concept of a spherical tokamak, of which MAST and MAST-U, the tokamaks used in this project, represent important examples. Spherical tokamaks have a more compact shape compared to conventional ones, with a thinner inner column and taller plasma shape. A simple way to differentiate between the two concepts quantitatively is the aspect ratio, the ratio between the major and minor radius  $R_0/a$ , which ranges from 1.1–1.8 in a spherical tokamak to 2.5–3.5 in a conventional tokamak. Spherical tokamaks generate the toroidal magnetic field through a current-carrying rod placed in the centre of the torus, with a smaller space occupied by toroidal field coils surrounding the plasma. This allows, for a smaller, elongated (taller) torus, with a low aspect ratio. Spherical tokamaks are smaller than conventional tokamaks operating at similar plasma pressures, reducing the material costs and time for construction, and improved shaping capabilities (which can be used to enable the particles to spend more time in the ‘good’ curvature region) allow for operation at high plasma beta [10], where

$$\beta = \frac{p}{B^2/(2\mu_0)}, \quad (1.14)$$

is the ratio of the thermal energy of a plasma to its magnetic energy, so that for the same plasma pressure  $p$  lower magnetic fields  $B$  and therefore coil currents are required. For conventional tokamaks,  $\beta$  has an upper limit before the plasma becomes unstable to bal-

looning modes [11], and it is usually below 10% with most conventional tokamaks operating with  $\beta \approx 1\%$ . For spherical tokamaks, access to high- $\beta$  scenarios is improved through high safety factor  $q$  values at the plasma edge, enabling the plasma particles to spend more time in the ‘good’ curvature region by the centre column, with improved confinement and reduced growth of MHD instabilities (see Figure 1.3). The pre-cursor to MAST, the spherical tokamak START (Small Tight Aspect Ratio Tokamak) regularly achieved a  $\beta \geq 30\%$  [12].

For this thesis, data from the spherical tokamak MAST and some experimental results from the upgrade MAST-U are utilised and presented. These STs, along with relevant diagnostics and the dataset used, are presented in Chapter 2.

### 1.3 Turbulence

While the magnetic field configuration of a tokamak was designed to confine the particles to move along the field lines on Larmor orbits, a finite amount of cross-field transport which degrades this confinement was always expected. In the simplest picture, collisions between particles can cause their guiding centre to move outwards across field lines. This type of transport is called classical transport, and while it occurs it is not sufficient to describe the level of transport found experimentally.

Taking the magnetic geometry of a tokamak into account leads to a description of neoclassical transport. As the particles move on their helical orbits from the outboard low-field side to the inboard high-field side, the magnetic mirror effect can reduce and even reverse their parallel velocity, leading to a trapping of the particles to orbits on the low-field side. Due to a gradient in the magnetic field, the particles experience a  $\mathbf{B} \times \nabla \mathbf{B}$  drift, giving these ‘banana’ orbits a characteristic width. The banana width is typically an order of magnitude larger than the Larmor radius, leading to a greater rate of cross-field transport than in the classical case.

Even neoclassical theory does not predict the rate of transport actually observed in tokamaks. Since this additional transport was not theoretically predicted, it was named ‘anomalous transport’. Anomalous transport, which accounts for the vast majority of cross-field transport, is now widely accepted to be caused by turbulence.

Turbulence is a state of nonlinear, apparently random fluctuations of plasma parameters including density, temperature, velocity or electrostatic potential. The electrostatic or

electromagnetic fluctuations are strongly time-dependent, sensitive to initial conditions and cover a large range of size- and timescales. The vast majority of cross-field transport is due to turbulent, radially outward motion caused by these fluctuations, which therefore leads to significant confinement degradation. Turbulence is characterised by a nonlinearly saturated state of linear microinstabilities [13], which commonly are instabilities with wavelengths comparable to the ion Larmor radius, though electron scale turbulence is also present, particularly in spherical tokamaks. They cannot be described with a simple magneto-hydrodynamic (MHD) model, but rather require more complex models with separate treatment of electrons and ions, such as gyro-fluid, gyro-kinetic, or even full kinetic models. To first order, some of these modes are electrostatic and are driven by gradients in temperature and/or density. These gradients are very steep in the edge region, where magnetic confinement results in a drop in temperature from  $\sim 1\text{keV}$  to effectively zero, and a drop in density from the core values of order  $10^{20}\text{m}^{-3}$  to effectively vacuum. The instabilities driven by these gradients excite turbulent transport which acts to reduce these gradients by particle and heat transport outwards, degrading confinement. Some examples of these instabilities are ion temperature gradient (ITG) and electron temperature gradient (ETG) modes, driven by temperature gradients, and TEM (trapped electron modes), which are driven by trapped particles.

Turbulence is difficult to model, and any predictive theory is required to be based on statistical properties of the parameter fields. While the core turbulence can be modelled as fluctuations on a background with simplified approximations, simulating the edge region with its steep gradients and proportionally larger fluctuations would ideally require a full, multi-dimensional kinetic treatment producing a distribution function  $f(t, \vec{r}, \vec{v})$ , something which is computationally prohibitively expensive. Full kinetic simulations are incredibly difficult to scale to full-size tokamaks, so gyrokinetic simulations, which average over the particles' gyromotion to remove one velocity dimension and thus reduce the model equations to six dimensions, have been used to approximate turbulence even in the edge region [14] and during complex plasma state evolutions such as L-H transitions [15] (more on this in the following sections).

Since turbulence leads to confinement degradation, and current experimental results are still far below the required level of confinement, mechanisms that suppress this turbulence are desirable and important to understand. One way the small-scale turbulent eddies can be modified is through large-scale sheared flow, such as zonal flows.

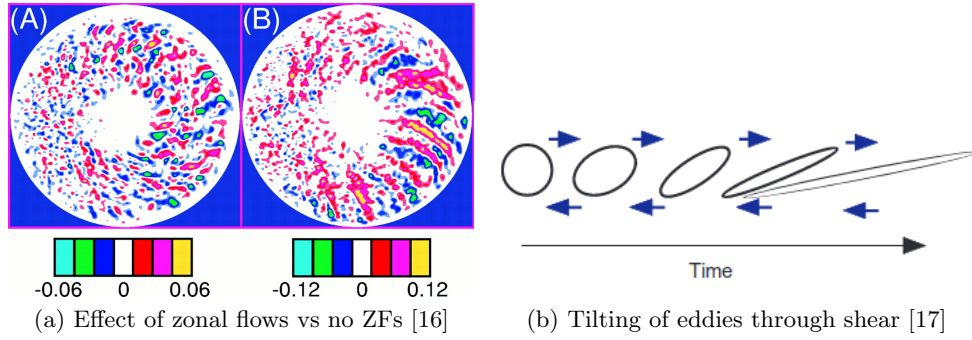


Figure 1.4: Zonal flow importance to turbulence suppression, (a) showing poloidal contour plots for fluctuation potential of a simulation allowing zonal flows (A) and suppressing them (B), and (b) showing the tilting effect shear flows can have on the eddies.

Zonal flows are poloidally and toroidally symmetric ( $n = m = 0$ ) electric field perturbations, which appear in the plasma as radially sheared  $\mathbf{E} \times \mathbf{B}$  flows. These laminar flows act to tilt the turbulent eddies and elongate them (see Figure 1.4b), and are even able to break up large eddies associated with extended modes [16]. Interestingly, the process that drives these zonal flows is turbulence itself, resulting in a predator-prey situation with zonal flows receiving energy transfer from drift-wave turbulence which reduces the intensity of this turbulence [18] (see Figure 1.4a). This leads to a description of zonal flows as a self-organisation process. A closely related mode is the geodesic acoustic mode (GAM) [19], which exhibits similar behaviour, properties and drive processes, but can be identified by poloidal mode number  $m = 1$  and its finite frequency branch ( $\sim 10 - 20\text{kHz}$ ) in contrast to the quasi-zero-frequency zonal flow.

Zonal flows and the factors that lead to turbulence suppression are highly relevant turbulence phenomena for confinement regime transitions, and thus for this project.

## 1.4 Confinement regimes

As processes such as the cross-field transport caused by turbulence can significantly influence the quality of confinement in tokamak plasmas, different operating regimes characterised by their level of confinement exist in these devices. Since turbulence is the leading cause of confinement degradation, the different confinement regimes can be described in part by their states of turbulence. The default confinement regime for diverted tokamak plasmas is known as the low confinement mode (L-mode), though it naturally received its name only after the discovery of the high confinement mode (H-mode). The L-mode is a strongly

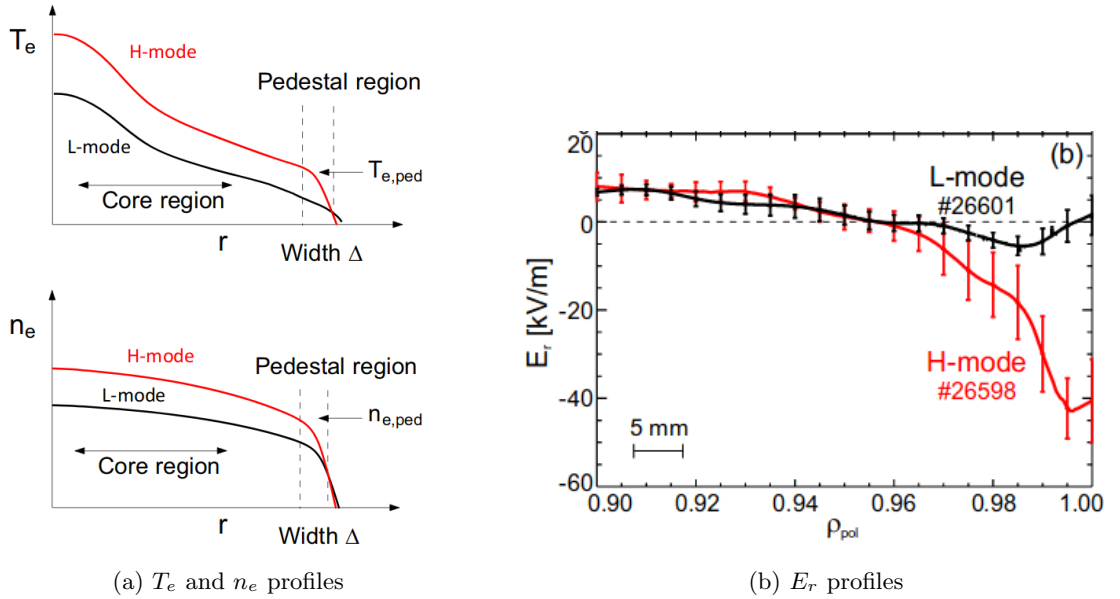


Figure 1.5: (a) Temperature and density profiles for L- and H-mode plasmas, showing the steep gradients in the pedestal region for H-modes. (b) Radial electric field profiles for L- and H-modes, showing the H-mode  $E_r$  well close to the separatrix [23].

turbulent regime, with the relatively large amount of cross-field transport leading to a lower confinement quality. The H-mode in turn is characterised by a suppression of turbulence in the edge, where the formation of an edge transport barrier [20] prevents cross-field particle and energy transport and thus improves confinement and fusion performance. The steep edge pressure gradients in H-mode allow for higher core plasma pressures, and the square dependence of fusion power on pressure (seen in Equation 1.7) makes this a desirable regime for ITER [21], DEMO and power plant operation.

The existence of different confinement states was discovered with the first observations of the H-mode in 1982 on the ASDEX tokamak in Germany [22]. As ohmic heating efficiency decreases with increasing temperature, to achieve the required temperatures for the Lawson criterion (Equation 1.9), it proved necessary to heat the plasma through auxiliary means such as resonance heating or neutral beam injection. The initial response of the plasma was disappointing, as the confinement time appeared to decrease with increasing auxiliary heating power, now recognised as a feature of the L-mode [20], but the ASDEX team found that once the heating power crossed a threshold value, the plasma confinement suddenly improved significantly as the plasma transitioned into a new confinement regime, H-mode [22].

In H-mode, the edge transport barrier slows the particle and energy transport out of the

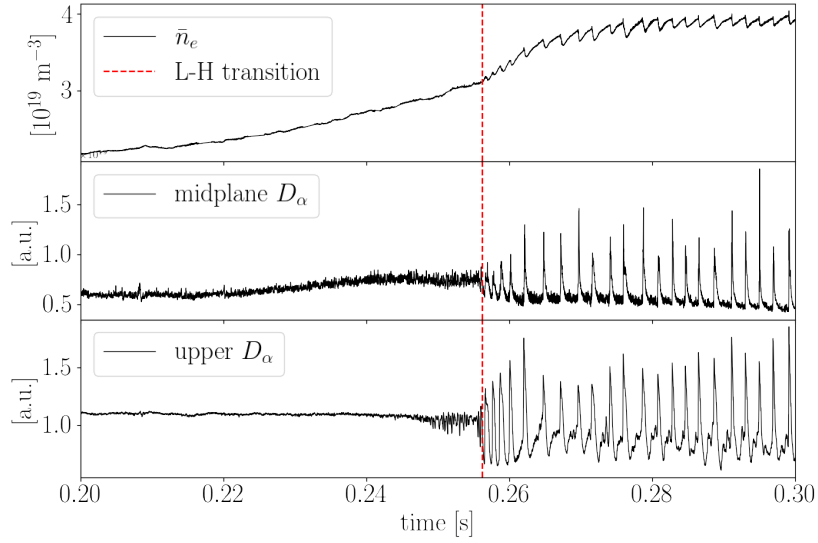


Figure 1.6: The line integrated density  $\bar{n}_e$  and the midplane and upper  $D_\alpha$  emission traces for a MAST shot that transitioned from L- to H-mode, with the transition time marked in dashed red.

edge plasma. Steep edge gradients in density, temperature and pressure define a pedestal region, while the bulk profiles are similar to those in L-mode, but shifted higher to sit on top of this pedestal, as shown in Figure 1.5a. The density, temperature and pressure profiles in the core region are "stiff", as microinstabilities such as ITG modes tend to limit gradients there, which together with the edge pedestal that develops during the L-H transition leads to the improvement (or increase) of core pressure seen in H-mode.  $D_\alpha$  emission occurs when the plasma interacts with neutrals and is primarily located in the edge, so the reduction in interactions with neutrals due to the change in confinement quality associated with the transition to H-mode results in a sharp drop in the  $D_\alpha$  signal. The drop in  $D_\alpha$  and concurrent rise in density are defining markers for the identification of an L-H transition, as seen in Figure 1.6. As can be seen in Figure 1.5b, a well in the radial electric field is also observed [24], corresponding to a sheared  $\mathbf{E} \times \mathbf{B}$  flow which is dominated by the ion pressure gradient [25]. The edge transport barrier results in a steady increase in temperature and density throughout the H-mode, which either periodically relax through violent edge localised modes (ELMs) [26], visible as large spikes in  $D_\alpha$  (see Figure 1.6), or move the plasma into a density region with higher threshold power (more in Section 1.5.1), causing a H-L back-transition.

How an H-mode sustains itself is fairly well understood, thought to be a cycle of pressure gradients, localised radial electric fields leading to shear suppression, which reduces turbulence and transport, leading back to the pressure gradients. The transition into H-mode

requires further study though, and a working predictive model still requires information on the trigger mechanism and the plasma evolution leading up the transition.

## 1.5 L-H transition

Many often connected phenomena before and during the transition from L- to H-mode have been observed and subsequently physically explained. While the exact trigger and order of importance of these multiple effects has not yet been definitively solved, several effects are currently thought to play an important role. During the L-H transition, an edge transport barrier forms just inside the last closed flux surface, and the improved particle and energy confinement leads to a buildup of pressure in the core and a pedestal region with steep gradients in the edge. It is universally accepted that the improved confinement in H-mode is due to a reduction in anomalous cross-field transport, i.e. turbulence. The fact that turbulence is suppressed by interaction with sheared  $E \times B$  flows and that a lot of the important micro-physics effects are occurring in the plasma edge, just inside the separatrix, is also widely accepted. The sheared mean flows form a predator-prey relationship with the turbulence, until a critical kinetic energy transfer from turbulence to the mean (zonal) flows suppresses the turbulence and the plasma transitions to a new confinement state, H-mode [27]. The shear flow can be triggered by different mechanisms, such as a self-generation by turbulent stresses or generation through neoclassical effects [16]. One observation common throughout different devices is the existence of a well in the radial electric field  $E_r$  profile, just inside the separatrix which grows more negative at the transition [25, 28]. It is thought that the strong  $E_r$  shear induced by the  $\nabla E_r$  in the edge could produce the necessary sheared  $E \times B$  flow for turbulence suppression. Neoclassical theory suggests that the gradient of the ion temperature plays a significant role in the  $E_r$  profile, and studies on several devices (e.g. ASDEX Upgrade [1] and C-Mod [29]) have found link between the ion heat flux  $q_i$  at the edge and the L-H transition. Outside of an ideal density range with a minimum power requirement to achieve an L-H transition (the power threshold described in the next section), transitioning to H-mode becomes more difficult for both increasing and decreasing density (called high-density and low-density branches). L-H transition theory as described by Malkov et al. [30] suggests that the low-density branch might be caused by a decrease in both the collisional electron-to-ion energy transfer and the heating fraction which is coupled

to the ions, two processes which are known to strengthen the edge electric field shear, so a reduction in these processes would make a transition less likely.

### 1.5.1 Power threshold

For a tokamak plasma to transition into H-mode, the net power  $P_{\text{net}}$  must cross a minimum value  $P_{\text{net}} \geq P_{LH}$ , defined as the threshold power  $P_{LH}$ .  $P_{LH}$  reveals the necessary amount of external heating power for H-mode operation which must be included in the design of future fusion reactors or power plants. The threshold power has been experimentally found to have many complicated dependencies on physics and engineering parameters such as plasma-facing wall material [31], plasma current  $I_p$  [32], toroidal magnetic field  $B_T$  [33], electron density  $n_e$ , shaping parameters [34,35] (including divertor configuration parameters, X-point height, elongation, etc), edge neutral density [36], main species isotope [37], plasma rotation [38,39] and many more. While progress has been made to improve our understanding of the physical processes governing the L-H transition, there are so far no models which can predict  $P_{LH}$  for new devices or operating scenarios. This task instead relies on the use of empirical scaling laws, which are based on large experimental databases of L-H transitions from a number of tokamaks. The currently most widely used scaling law (also known as the ITER scaling) was derived by Martin et al. [40] in 2008,

$$P_{LH} = 0.0488 n_{e20}^{0.717} B_T^{0.803} S^{0.941}, \quad (1.15)$$

which provides an estimate for  $P_{LH}$  in MW and includes scalings of the density ( $n_{e20}$  in units of  $10^{20} \text{m}^{-3}$ ), toroidal magnetic field  $B_T$  in units of  $T$  and plasma surface area  $S$  in units of  $\text{m}^2$ . As can be seen, most of the experimentally shown parameter dependencies are not represented, while those that are included are only valid for limited scenarios or ranges, and many more are potentially still unknown or not quantified. The density dependence of  $P_{LH}$  has been experimentally revealed to possess a characteristic non-monotonic U-shape (e.g. on JET [32], C-Mod [33], ASDEX Upgrade [41,42], or HL-2A [43]), with a minimum  $P_{LH}$  achieved at a particular density  $n_{e,\text{min}}$ , a moderate rise in  $P_{LH}$  for densities greater than this value and an increased heating power requirement to achieve a transition at densities lower than this value. This U-shape then varies with other parameters such as the magnetic field [34,44]. Scaling laws like Equation 1.15 attempt to fit only the high-density branch of

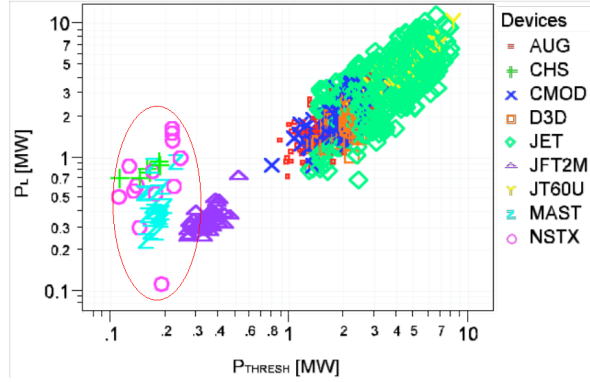


Figure 1.7: The performance of the Martin scaling for plasma shots of various devices.  $P_{LH}$  ( $P_{\text{THRESH}}$  in the figure) as calculated by the scaling is reasonably close to  $P_{\text{loss}}$  ( $P_L$  in the figure) at the L-H transition for most conventional tokamak shots, while STs (circled in red) consistently have higher  $P_{\text{loss}}|_{t=t_{LH}}$  than the prediction. Reproduced from [40]

$P_{LH}$  and the low-density branch is not captured.

For some cases, especially those where the conditions are close to those of the majority of the shots included in the database, the scaling laws give reasonable estimates for  $P_{LH}$ , but for other cases the estimates can be very poor. One such case is presented by spherical tokamaks. Figure 1.7 shows the loss power  $P_L$  ( $\equiv P_{\text{loss}}$ ) for a number of L-H transitions in plasma shots from multiple devices against the calculated  $P_{\text{THRESH}}$  ( $\equiv P_{LH}$ ) using the Martin scaling. The conventional tokamaks mostly lie on the  $P_{\text{loss}} = P_{LH}$  line with some deviations, but the spherical tokamaks MAST and NSTX, as well as the stellarator CHS, circled in red, lie consistently above this line, i.e. the scaling appears to under-predict the actual  $P_{LH}$  values. There are much fewer ST devices and discharges than conventional ones, and a scaling based on an ST database has not yet been attempted.

## 1.6 Outline of thesis

This thesis describes work done improving our understanding of the L-H transition on spherical tokamaks. Chapter 1 introduced the concept of fusion as an energy source, the geometry and associated parameters of tokamaks and the concept of spherical tokamaks (STs). It further introduced plasma turbulence as the main source of confinement degradation, the concept of confinement regimes such as L- and H-mode, the transition between them as well as the required L-H power threshold. Chapter 2 introduces MAST and MAST-U, the specific STs used in this project, as well as selected diagnostics and codes which are relevant to

this project. The data set used for the power threshold and heat flux analyses discussed in Chapters 3 and 4 is also presented. Chapter 3 presents power threshold studies of the MAST data. The details of the net power calculation method are described. The plasma behaviour of the discharges studied was categorised into different types of confinement states, and analysis of the  $D_\alpha$  emission signals for the different categories is presented. The results of the power threshold analysis are shown, along with comparisons to existing scaling laws and experimental fits to the data. Chapter 4 presents a study of the ion and electron heat flux in the plasma edge, with the motivation based on results from other devices and the method using TRANSP described. The results are presented along with a discussion of possible conclusions and reasons behind them. Chapter 5 presents the turbulence analysis performed on selected MAST data, including the motivation and aim of calculating the energy transfer, and the different types of data analysis performed on the beam emission spectroscopy data including calculations of mode powers, phase velocities and the comprehensive CCTDE velocimetry analysis. Higher order spectra such as the wavenumber-frequency spectra and further steps required to obtain estimates of the energy transfer are also discussed. Chapter 6 presents the conclusions of the work on MAST data from the previous chapters and summarises the future work suggested for these studies. It also presents a summary of the experiments performed on MAST-U, starting with the experimental aims and motivations for studying divertor effects, continuing with the timeline and experience of the experiments along with the challenges faced, and concluding with the results of a preliminary analysis and an outlook on how the experiments will progress in future campaigns.

## Chapter 2

# Tools used in this thesis

The analysis of existing data and collection of new data that underlies this thesis required the use of tokamak devices, diagnostic instruments on these devices and large-scale established plasma codes. Chapters 3-5 involve the analysis of legacy data from the spherical tokamak MAST, and the planning and execution of experiments on the new tokamak MAST-U(pgrade) is described in Chapter 6. The two tokamaks are introduced in this Chapter, along with relevant diagnostics and codes used in the different studies presented in this thesis. The MAST dataset from a previous L-H transition experiment which was used for the power threshold and heat flux studies of Chapters 3 and 4 is also presented here.

### 2.1 Tokamaks used in this project

Both tokamaks in this project are continuations from the first full-sized spherical tokamak START (Small Tight Aspect Ratio Tokamak) which was operational between 1990 and 1998 and located in the Culham Centre for Fusion Energy. When START was retired in 1998, it was succeeded by MAST (Mega-Amp Spherical Tokamak) which ran from 1999 to 2013, and then after a longer period of reconstruction and improvements, the newest tokamak on the Culham site, MAST-Upgrade, began its campaigns in 2020. All tokamaks mentioned here are or were the UK's national fusion experiments of the time and located at the main site of the United Kingdom Atomic Energy Authority (UKAEA). The next generation of the national spherical tokamak experiment will be STEP (Spherical Tokamak for Energy Production), a much larger power plant concept (DEMO-class) whose design phase began in 2019 and which is expected to have completed construction in the 2040s. One of the earliest

fusion devices, the ZETA (Zero Energy Thermonuclear Assembly) pinch confinement device, began operation at Harwell campus in 1957 as the largest and most powerful fusion device at the time [45], but other devices of similar concepts managed to achieve better results with much lower capital investments, the device suffered from insufficient diagnostic capabilities, and the pinch concept revealed fundamental flaws, so the upgrade plans were scrapped and a former Royal Navy airbase was purchased to house development of new ideas. Construction on site began in the early 60's and it was officially opened in 1965 as the dedicated plasma and fusion research facility of UKAEA, Culham Laboratory (now Culham Science Centre). After Culham was opened as the dedicated site, fusion research had largely relocated there, with it remaining the main site for (public sector) fusion devices in the UK, until the decision (after a bidding and decision process between several suitable sites) to build STEP at the site of a former coal power plant in Nottinghamshire. [46]

### 2.1.1 Mega-Amp Spherical Tokamak (MAST)

The Mega-Amp Spherical Tokamak MAST [47–49] was a medium-sized spherical tokamak with an aspect ratio of  $R_0/a = 0.85\text{m}/0.65\text{m} \sim 1.3$ , graphite walls, and auxiliary heating provided by neutral beam injection (NBI). During its operational time, it was the UK's official fusion experiment as well as one of two leading spherical tokamak experiments in the world (the other being NSTX at PPPL (Princeton) in the US). MAST was a highly diagnosed device and ran campaigns from 1999 to 2013, resulting in a wealth of data that is still being analysed. As a second generation ST it was designed to study highly elongated plasmas with low aspect ratio and low collisionality, with a plasma current and poloidal cross-section comparable to medium-sized conventional tokamaks such as DIII-D [50] and ASDEX-Upgrade [51].

The external heating system consisted of two neutral beams [52], South (SS) and South-west (SW), with their toroidal locations shown in the later figure for the beam emission spectroscopy diagnostic schematic, Figure 2.6. Both beams inject co-current (i.e. in the direction of the plasma current), on-axis (at  $Z = 0$ ), and with a beam energy of 75keV. The maximum beam powers were typically 3.5MW, with 2MW from SS and 1.5MW from SW. As its name suggests, it was capable of plasma currents of 1MA (with maximum 1.3MA achieved), with typical plasmas operated at 0.45-0.75MA. The pulse length was limited to 1s due to the central solenoid flux swing, and typical pulse lengths were 0.5-0.7s. Some of

Parameter	MAST	MAST-U [current]	MAST-U [planned]
First wall material	C (graphite)	C (graphite)	C (graphite)
Major radius $R_0$ [m]	0.85	0.85	0.85
Minor radius $a$ [m]	0.65	0.65	0.65
Pulse length [s]	0.7	1.0	5.0
Maximum plasma current [MA]	1.3	1.0	2.0
Maximum toroidal magnetic field [T]	0.52	0.65	0.8
Maximum NBI heating [MW]	3.8	3.5	5
Maximum elongation $\kappa$	2.6	2.5	2.5

Table 2.1: Typical plasma and engineering parameters for MAST and MAST-U.

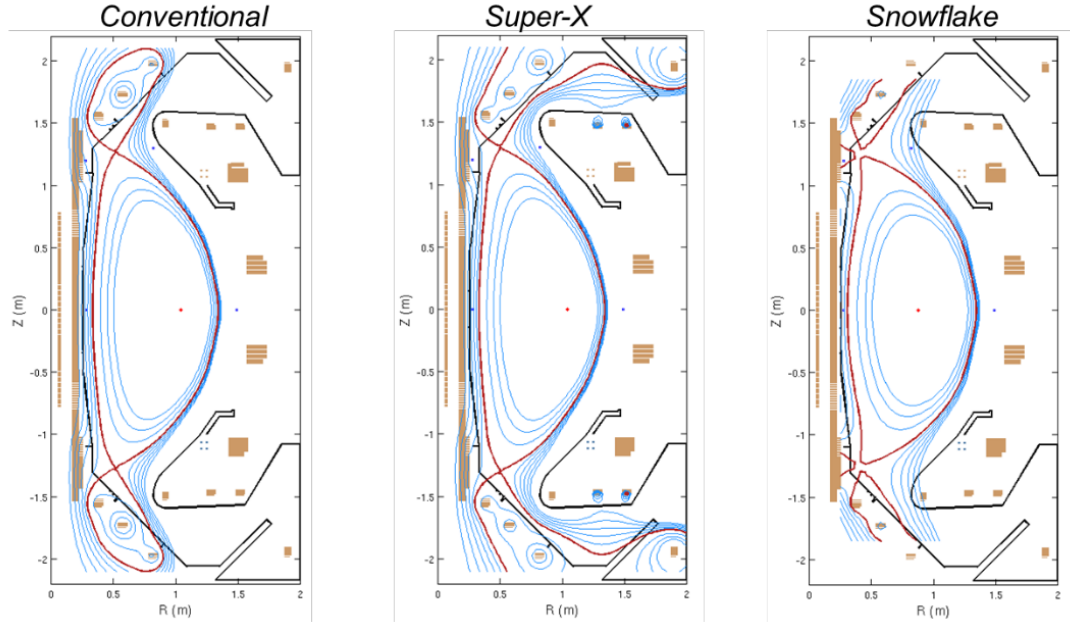


Figure 2.1: Cross-section of MAST-U vessel, with plasma-facing components in black, magnetic coils in orange, flux surfaces in blue and the last closed flux surface in red. The conventional divertor configuration (left) is similar to MAST, while the Super-X and Snowflake are new configurations which can be studied on MAST-U. [53]

the important device and plasma parameters for MAST are summarised in Table 2.1, along with current and planned parameters for the upgraded version, MAST-U.

### 2.1.2 Upgrade to MAST-U

After MAST completed its scheduled campaigns in 2013, the device was upgraded to the new ST MAST-Upgrade with experiments beginning in 2020. MAST-U was designed with enhanced divertor capabilities, allowing the study of advanced divertor configurations such as Super-X and Snowflake (see Figure 2.1), which aim to improve power handling for future devices as the divertor heat loads are expected to be significantly reduced. As seen in Table 2.1, MAST-U has retained many features of MAST, such as the vessel size and graphite first wall material, but upgrades were made to improve performance of certain shot parameters and to allow studies in exciting new physics areas including for fast ions and exhaust physics. The new solenoid doubles the inductive flux, allowing for a maximum plasma current of 2MA [54] as well as an increased pulse length (2s for maximum  $I_p$  and  $B_T$ , 5s for  $I_p = 1MA$ ). The maximum toroidal field has been increased by 50% to 0.8T. The installation of 17 new poloidal field coils allow the implementation of flexible divertor configurations and separate study of aspects of the magnetic geometry, such as flux expansion and connection length [53, 55]. The new closed divertor chambers fitted with cryopumps (available in later campaigns) will allow access to lower collisionality regimes to test pedestal physics and ELM control for ITER [53]. Compared with a conventional divertor, the Super-X divertor is expected to be strongly detached at similar plasma conditions [56]. Like MAST, MAST-U receives external heating from two neutral beams (initially at similar total power, but with the eventual upgrade anticipating up to 5MW total power), but one of the beams (SW) has been moved off-axis ( $Z = 65\text{cm}$ ), facilitating better current profile control and fast ion physics studies, as the combination of on- and off-axis beams allow for a range of fast ion profiles from centrally peaked to hollow [55]. The fast ion distribution and  $q$  profile can be tailored to avoid MHD instabilities [54].

## 2.2 Diagnostics most relevant to this project

Like all research tokamaks, MAST (and MAST-U) host a comprehensive suite of diagnostics, which are scientific instruments designed to measure or deduce certain physical properties of the plasma. Diagnostics can be active, i.e. requiring something (e.g. probes, gas, particle or photon beams) to be inserted into the plasma and therefore perturbing it to varying degrees, or passive, i.e. measuring the plasma as is and not perturbing it. Diagnostics

are based on different physical mechanisms or principles in the plasma and are focused on measuring selected aspects of one or multiple plasma (i.e. fuel ions (usually hydrogen isotopes) and free electrons) or impurity species (originating from deliberate introductions through e.g. seeding or diagnostics, leaks/impure vacuum, and nuclei or molecules “freed” from the vessel components through processes such as sputtering). There are a large number of plasma diagnostics in operation around the world, with many being slight variations on common techniques, e.g. often the diagnostic setup is unique to a particular tokamak but based on a common principle and thus variations of it are found across multiple tokamaks. Both MAST and MAST-U employ a subset of possible diagnostic techniques, with the limited space and to a lesser degree funding forcing the tokamak leaders and teams to make choices on which diagnostics to include. STs with their smaller scale often have a greater space limitation than conventional devices. Nevertheless MAST was still a very well diagnosed device, and only a small subset of its diagnostics are introduced here, namely those which are most relevant for the different sets of analysis performed for this project. As the MAST-U study comprised only a small part of the thesis, the main focus here is on diagnostics for MAST with notable changes in the MAST-U setup highlighted.

### 2.2.1 Deuterium Balmer $\alpha$ emission ( $D_\alpha$ )

The  $D_\alpha$  diagnostic is one of the most fundamental tokamak diagnostics, describing the photon emission from the interactions of the plasma with neutrals. Since neutrals are mostly found in the SOL and edge, with the deuterium in the core generally fully ionised, the emission is highly localised to this region as well (though it is collected from the entire plasma in the line of sight). The  $D_\alpha$  signal can reveal information about the confinement state and quality of the plasma, as an improved confinement (such as in the transition to H-mode) leads to a reduction in the interaction with neutrals and therefore a sharp drop in the  $D_\alpha$  emission. It involves collecting the photon emission from the plasma in one of several different view regions (such as midplane, top divertor or bottom divertor) which is then fed into a corresponding photo-multiplier tube (PMT) and digitiser such that a 1D signal is recorded (i.e. a time history of the signal amplitude). As a spectroscopic system, this diagnostic collects and filters emissions of a particular wavelength or frequency (line emission). The plasma consists of the hydrogenic isotope deuterium, and the signal usually focused on, including throughout this project, is the first in the Balmer series,  $D_\alpha$ .  $D_\alpha$  emission occurs when the electron in

a deuterium atom transitions from energy level  $3 \rightarrow 2$ , emitting a photon of a well-defined wavelength  $\lambda_{D_\alpha}$ . The wavelength  $\lambda_{D_\alpha}$  for  $D_\alpha$  emission can be calculated from the Rydberg formula,

$$\frac{1}{\lambda} = \mu R_\infty \left( \frac{1}{n_f^2} - \frac{1}{n_i^2} \right) \quad (2.1)$$

where  $R_\infty = \frac{m_e e^4}{8 \epsilon_0^2 h^3 c} = 1.097373 \times 10^7 \text{m}^{-1}$  is the Rydberg constant (with the electron mass  $m_e$ , electron charge  $e$ , permittivity of free space  $\epsilon_0$ , Planck constant  $h$  and speed of light  $c$ ),  $\mu m_e = \frac{m_{\text{nucl.}} m_e}{m_{\text{nucl.}} + m_e}$  is the reduced mass of the electron (with  $m_e$  on the LHS taken from  $R_\infty$ ) and the nucleus, and  $n_i$  and  $n_f$  are the initial and final energy levels of the excited electron during the emission process. For deuterium, the reduced mass is calculated with the deuteron mass as  $m_{\text{nucl.}}$  such that  $\mu = 0.9997276$ . The Balmer series describes transitions to the final energy level  $n_f = 2$ , and the Balmer  $\alpha$  emission comes from the transition from initial energy level  $n_i = 3$ . The wavelength can thus be calculated as  $\lambda_{D_\alpha} = 656.291 \text{nm}$ . Since the deuterium in the core is fully ionised and the Balmer series emission lines are dark, the signal collected is localised in the plasma edge where neutral deuterium atoms can be found. The  $D_\alpha$  signal has a high time resolution and is useful in determining the evolution of the state of the plasma, as events or behaviours such as L-H and H-L transitions, ELMs, I-phases and occasionally fishbones are visible in the signal. The  $D_\alpha$  signal of the upper divertor view especially is used extensively in Chapter 3, including a section describing the study of the  $D_\alpha$  signal for a categorisation of different L-H boundary behaviours. Throughout this thesis, the signal is used to illustrate types of L- or H-modes and the time points as well as time histories of L-H transitions.

### 2.2.2 CO<sub>2</sub> interferometer

A high resolution time history of the line averaged electron density can be obtained from the interferometer system on MAST. The system comprises two interferometers, a CO<sub>2</sub> interferometer which operates at  $10.6 \mu\text{m}$  and is sensitive to both the electron density and to vibrations, and a HeNe interferometer which operates at  $633 \text{nm}$  and is only sensitive to vibrations. Subtracting the HeNe signal from the CO<sub>2</sub> signal returns the electron density integrated along the line of sight. The line of sight passes twice through the vessel, close to the centre column, and is therefore  $\sim 8 \times a$  where  $a$  is the minor radius. The line integrated

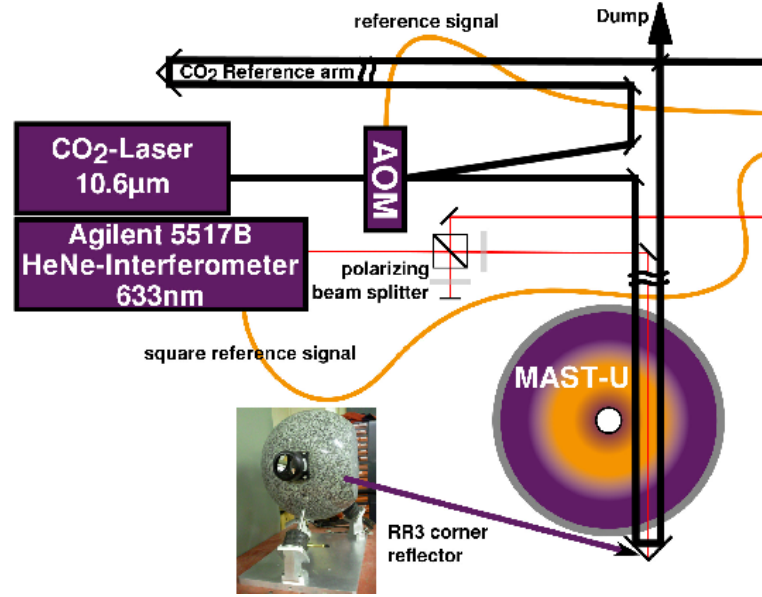


Figure 2.2: A schematic of the paths of the two interferometer laser (the FPGA-based system on the right hand side has been cut off). The path of the CO<sub>2</sub> laser has been marked in bold black, and the path through the plasma can be seen to be approximately equal to  $\sim 8 \times a$ . [adapted from [57]]

electron density can therefore be converted to the line averaged density by dividing through the length of the line of sight. A schematic of the interferometer system on MAST-U (very similar to MAST) is shown in Figure 2.2. The line averaged electron density is used in combination with the  $D_\alpha$  signal to identify the L-H transition and can give information on e.g. the size of ELMs and the impact of plasma behaviours, modes or instabilities on density.

### 2.2.3 Multi-channel bolometer system

A bolometer is a device which can measure radiation through the use of an absorptive element which has a temperature-dependent electrical resistance. On MAST, the bolometer system has gold foil sensors which are sensitive to total radiation from the near-UV to the soft X-ray spectrum and neutral particle energy flux. The sensor element is heated by the incident power, and the total incident energy is inferred from the temperature rise of the element, corrected for losses due to cooling. The system consists of eight four-channel cameras, i.e. 32 channels, which are combined to form a poloidal (vertical) array with 16 channels and two tangential arrays, one viewing co-NBI with 12 channels and the other viewing counter-NBI with four channels. The poloidal and tangential views of the bolometer system are shown in Figure 2.3. Data from the poloidal views of the bolometer system is used for a small section

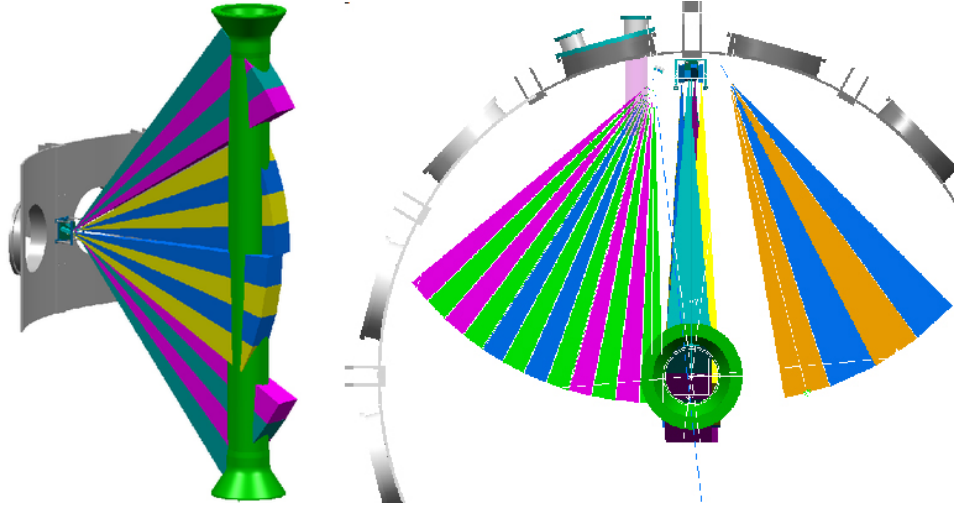


Figure 2.3: The bolometer system on MAST consisted of 32 channels in the poloidal array (left image) and two tangential arrays, one viewing co-NBI with 12 channels and the other viewing counter-NBI with four channels (right image).

of Chapter 3, where the power crossing the separatrix  $P_{\text{sep}} = P_{\text{loss}} - P_{\text{rad}}$  is compared with the loss power  $P_{\text{loss}}$ , and the radiated power  $P_{\text{rad}}$  is supplied by the bolometer system as an integral over the poloidal views.

#### 2.2.4 Thomson scattering (TS)

Thomson scattering (TS) is the scattering of electromagnetic radiation by free electrons, an important process in plasma physics. It can be contrasted with Rayleigh scattering (by bound electrons) and Raman scattering (by molecules). Both Thomson and Rayleigh scattering processes are elastic, so the scattered photon will have the same wavelength as the incident photon, while Raman scattering is inelastic and the resulting scattered photon's wavelength will vary. In plasmas with a low ionisation degree, TS is often significantly weaker than the other two processes, but for fusion plasmas this is less of a concern. In the TS diagnostic used in plasma physics to measure profiles of electron density and temperature, the incoming photon is generated with a laser pointing into the plasma, making it an active optical diagnostic, and due to the small cross-section of the scattering process a high power laser is usually required. The electric field of the incoming laser photon accelerates free electrons in the plasma, causing them to emit radiation in the form of a scattered photon of the same frequency which is then collected by the diagnostic's collection optics. Collection optics for a TS system usually involve a triple-grating spectrometer to reduce stray light and

a mask blocking the central wavelength to filter out Rayleigh scattering. The TS spectrum is then fitted from the rest of the data. The intensity of the scattered light can give us the plasma electron density as the total number of scattered photons is directly proportional to the electron density, while the spectral distribution of the scattered light reveals information on the electron temperature through the thermal velocity distribution. At low temperatures, the spectrum of the scattered radiation is approximately centred around the laser wavelength and the temperature scales with the square of the spectral width  $T_e \propto \Delta\lambda_s^2$ , with an increased spectral width corresponding to a higher electron temperature, while relativistic effects at high temperatures cause the spectrum to be blue-shifted to lower wavelengths. The TS system on MAST [58] consisted of eight 1.6J Nd:YAG infrared ( $\lambda_L = 1.064\mu\text{m}$ ) lasers, each with a repetition rate of 30Hz, which are combined in equispaced operation to provide measurements with a sampling rate of 240Hz. The laser pulses are 6ns long and in standard operation are fired approximately every 4ms throughout the shot, or in a “burst” mode operation every  $5\mu\text{s}$  at selected intervals to allow for detailed (i.e. high time resolution) study of the evolution of profiles e.g. during an ELM. The Nd:YAG lasers are viewed by the collection optics of a “core” system with 130 spatial points [59] and an edge system [60] with 16 spatial points at  $R = 1.2 - 1.5\text{m}$ . The number of spatial points is determined by the number of polychromators and independent fibre bundles. At the time of the experiments on MAST which are analysed in this thesis, both TS systems had a spatial resolution of  $< 10.5\text{mm}$  [58, 60]. Before then, at the time of the design of the edge system, the core system had only 19 spatial points covering the entire plasma, so the new system’s increased resolution was necessary to capture profile features at the pedestal [60]. With the update of the core system in 2010 [59], the entire profile including the pedestal region is well diagnosed by the core system, and the edge system is not used for this project. The TS diagnostic forms a vital part of the TRANSP setup process in the heat flux studies of Chapter 4, and  $n_e$  and  $T_e$  profiles for different plasma states were investigated during the behaviour categorisations in Chapter 3.

### 2.2.5 Charge-exchange recombination spectroscopy (CXRS)

Charge exchange recombination spectroscopy (CXRS) analyses the light emitted by impurity ions when they undergo a charge exchange reaction. During this reaction, a fully stripped impurity ion receives an electron from a neutral particle, such as those provided by a neutral

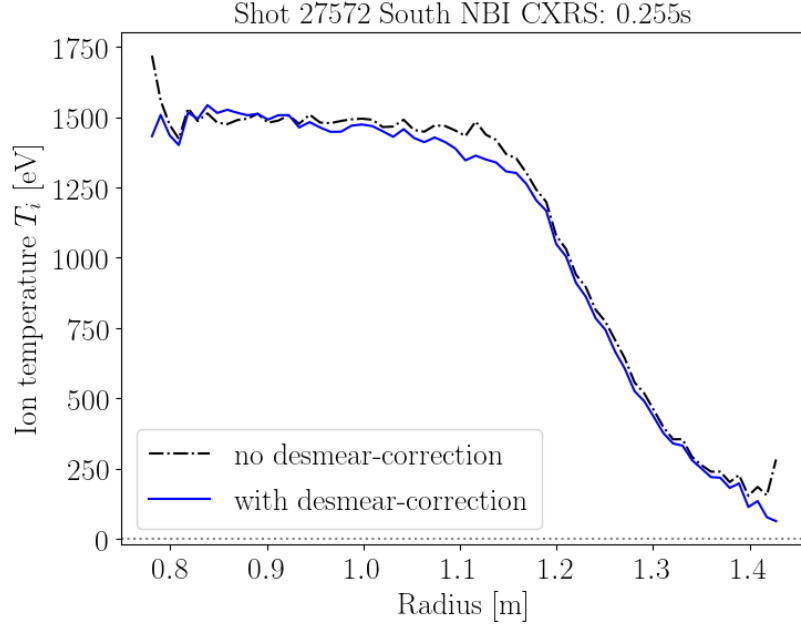


Figure 2.4: CXRS data in the edge, such as the ion temperature  $T_i$  measured from the South NBI, need to have desmearing corrections applied in order to be able to resolve down to lower temperatures.

heating beam. The impurity ion receives this electron in an excited state so it will return to the ground state, losing its excess energy through line emission. Since the neutral beams are the only source of neutrals in the plasma core the measurement is highly localised.

The width of the emission line is caused by Doppler broadening, making it a measure of the thermal velocity distribution and hence of the local ion temperature. The Doppler shift of the emission line with respect to its rest wavelength gives the velocity in the direction of the line of sight. Taking into account the geometry of the CXRS system this velocity component can be transformed into a toroidal plasma rotation. Information about impurities which can not otherwise be measured is also provided by CXRS, with the intensity of the emission line being proportional to the density of the impurity ions. The vast majority of impurities (especially in a carbon device like MAST) are low- $Z$  and thus present mostly as fully stripped ions, which do not emit line radiation by themselves and would therefore provide no spectroscopic information without the charge exchange excitation from CXRS.

Due to the graphite PFCs on the walls and in the divertor, the dominant impurity species on MAST is carbon, so the CXRS system [61] is set up to measure the  $N = 8 \rightarrow 7$  transition of CVI ( $C^{+5}$ ) with wavelength  $\lambda = 529.05\text{nm}$ . The source of neutrals is provided by the neutral beams. The MAST system has 64 toroidal channels on each beam with a spatial

resolution of  $\sim 1\text{cm}$ , while on MAST-U due to necessary restructuring of diagnostics only the South (SS) beam and background views remain. The spectrometer has a 5ms time resolution and a wavelength resolution of  $0.4\text{\AA}$  per CCD camera pixel. The measurable temperature range is 50eV-5keV and velocity range is -50km/s to +500km/s. The carbon ion temperature  $T_i$  and toroidal velocity  $v_{\text{tor}}$  are routinely analysed for every shot, but the impurity density requires expert analysis with help of modelling, calibration, ADAS coefficients and cross diagnostic consistency checks, and may therefore be more infrequently provided. Some plasma scenarios can create conditions which make the production and analysis of CXRS data challenging, such as strong carbon emission at the edge, low carbon density in the core or rapid beam attenuation. The system is set up to measure ion quantities in the core and the data can rapidly deteriorate towards the edge, with the separatrix and SOL usually not captured at all. One way of improving the quality of CXRS data is through correcting the CCD signal to account for frame transfer smearing before the spectra are fitted. This had at the time of the MAST experiments which are used in this thesis not been performed automatically, so the current responsible officer (RO) for the CXRS diagnostic (Chris Beckley, PhD) helped improve the signal by applying the desmearing corrections for use of the  $T_i$  profiles in TRANSP. Figure 2.4 shows the difference in the acquired  $T_i$  profiles before (dot-dashed black) and after (blue) performing this correction. Note especially the improvements in the core and edge of the plasma.

For this project, CXRS data is used primarily in the heat flux studies of Chapter 4, including as a major component in the set up of TRANSP runs to calculate heat flux and heating efficiency components, with ion temperature profiles (along with electron temperature and density profiles from TS) fitted for each simulation time step.

### 2.2.6 Fission chamber

Fission chambers in a tokamak measure the neutron flux of a plasma, which is essentially a measure of the rate of fusion reactions, due to the fact that both D-D and D-T reactions produce one neutron each.

MAST and MAST-U use pure deuterium ( $A = 2$ ) as fuel, so the initial fusion reactions will be D-D reactions. D-D fusion has two possible reactions which occur at approximately equal probability (Eq. 1.2). The added tritium ( $A = 3$ ) in the fuel will almost exclusively fuse with deuterium in a D-T reaction due to its high fusion cross-section, (Equation 1.1)

while the addition of He-3 can result in either  ${}^3_2\text{He}-{}^3_2\text{He}$  or  $\text{D}-{}^3_2\text{He}$  reactions, both being aneutronic,



We can therefore see that (in a perfect situation) each D-D fusion reaction will produce exactly one neutron, however since it is not guaranteed that each tritium ion will react, this is more of an approximation.

Due to their neutral charge and small interaction cross-section with materials neutrons can be difficult to detect. Fission chamber neutron diagnostics generate a detectable electrical signal from the neutron's kinetic energy transfer during collisions with a detection medium [62]. The fission chambers used on MAST and MAST-U are made up of uranium oxide coated electrodes sealed in aluminium containers with an argon-nitrogen gas mix [63]. Neutrons incident on the uranium-coated electrodes cause a fission reaction to occur, and the high energy fission products ionise the Ar-N fill gas which is then drawn to the electrodes, registering as a current pulse that is measured by the data acquisition system [63]. As both neutrons and gamma rays can cause fission reactions to occur, the fission chambers are shielded with lead to protect from gamma rays. Since the fission cross-section of the uranium coating is higher for neutrons at thermal energies than the 2.45MeV of fusion neutrons, the shielding of the chamber includes a polyethylene layer to thermalise incoming neutrons [63]. Fission chambers measure a time-resolved neutron flux  $Y_n$  which can be assumed to be isotropic if the diagnostic is located at a far enough distance away from the neutron source, which is the case for MAST and MAST-U. MAST had one fission chamber [64], whereas MAST-U has two fission chambers which are located at different toroidal and radial locations, and the results of the first campaigns have shown that the isotropic approximation is valid. The total neutron yield  $Y_n$  on MAST typically ranged between  $10^{13}$  and  $2 \times 10^{14}\text{s}^{-1}$ . The fission chamber(s) can be helpful to diagnose H-modes due to the expected increase in neutron rate, and are especially useful for the transport code TRANSP (introduced in the next section), as the measured neutron rate is compared with the neutron rate calculated by TRANSP, which occurs during the run-time of TRANSP adjusting free parameters to improve the match or with the results of the run to make a statement on the

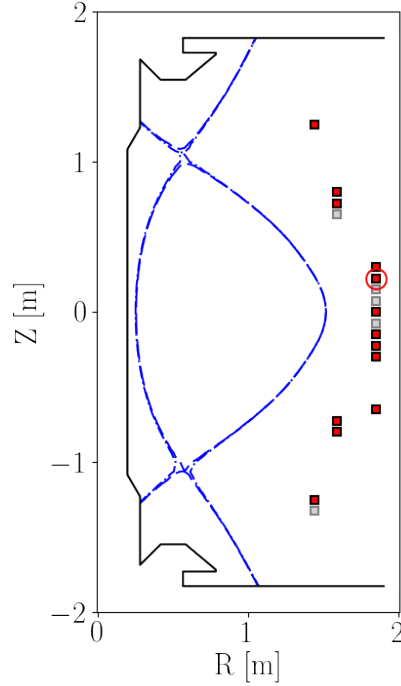


Figure 2.5: The location of the outboard vertical Mirnov coils at a toroidal angle of  $270^\circ$  on MAST (squares), with the coils that contain usable data shown in red and those that had no usable data for the shots in this project shown in grey. The sample Mirnov coil chosen to visualise data in the following chapters is circled in red. The two separatrices for a representative double null shot are plotted in blue.

quality of the TRANSP data. This process and therefore the data from the fission chamber is especially important for the heat flux studies of Chapter 4.

### 2.2.7 Mirnov coils

Mirnov coils are one of a number of magnetics diagnostics available on MAST. There are multiple Mirnov coil arrays at different locations around and inside the vessel, with the outboard vertical array mainly used in this project. The Mirnov oscillations measured with these coils are amplitude perturbations of the vertical and radial components of the magnetic field in a plasma and are often simply called magnetic oscillations. They can reveal important information on plasma instabilities in a tokamak since these create local fluctuations in the current, inducing a varying magnetic flux density which is picked up by the coils as described in Faraday's law of induction. The outboard vertical Mirnov coil array consists of 19 coils situated at a toroidal angle of  $270^\circ$ , placed around the outboard side of the plasma at major radius between 1.44m and 1.85m and heights of 0.0m to 1.325m above and below the

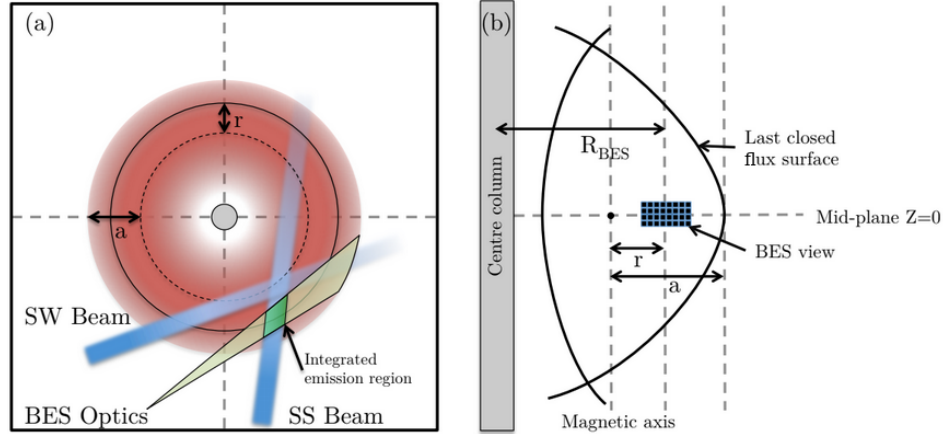


Figure 2.6: (a) View of MAST from above, showing the location of the two neutral beams and the BES view. (b) Poloidal cross-section of a MAST plasma, with the view location of the BES array. [65]

midplane (shown in Figure 2.5), as well as two additional coils at the midplane ( $R = 1.85\text{m}$ ,  $z = 0.0\text{m}$ ) but at toroidal angles of  $150^\circ$  and  $330^\circ$ . The full array of coils was used during the turbulence studies in Chapter 5 when the velocimetry routine was applied to Mirnov coil data to compare with the results from the BES data, whereas data from a representative coil was used in the heat flux studies of Chapter 4 to verify conclusions about fast ion losses from TRANSP results, and in Chapter 5 to visualise Mirnov data as a representation of MHD activity.

### 2.2.8 Beam emission spectroscopy

One of the most common ways of measuring turbulence in experiments is through the spatial and temporal localisation of small-scale density fluctuations. To capture the complex turbulence dynamics, these diagnostics must be able to image across different length- and time-scales. Some common optical turbulence diagnostics include gas puff imaging (GPI), beam emission spectroscopy (BES) and Doppler backscattering (DBS), with only the latter two available on MAST and MAST-U. The main diagnostic used during this project in the turbulence studies of MAST data (Chapter 5) is the 2D spatially resolved BES system.

Beam emission spectroscopy (BES) is an optical turbulence diagnostic which utilises either a dedicated diagnostic beam or (as on MAST and MAST-U) one of the neutral heating beams to extract a 2D spatially localised image of density fluctuations [66]. The neutral

particles injected into the plasma collide with the plasma particles and become excited. Since the neutral particles enter the plasma with significant energy, the emission generated by excitation and de-excitation processes will be a Doppler shifted  $D_\alpha$  emission line. This allows the detector to distinguish the BES data from the background  $D_\alpha$  emission, and spatially localised measurements of the intensity variations can be obtained. The variations in light intensity can be related to local density fluctuations, and an array of detectors ( $4 \times 8$  for MAST,  $8 \times 8$  for MAST-U) allows for a 2D image of plasma turbulence.

The MAST NBI beam energy of 75keV results in Doppler shifts of 2-3nm from the characteristic  $D_\alpha$  line at 656.3nm, with the splitting of spectral lines caused by the motional Stark fields. The motional Stark effect occurs when fast neutral beam particles move across the magnetic field in the plasma, experiencing a Lorentz electric field in their rest frame which causes wavelength splitting of the Balmer line and polarisation of the emission with respect to the Lorentz electric field. [67] The position of the heating beam and the viewing location of the BES system are shown in Figure 2.6. The line of sight is oriented such that it points along the magnetic field where it intersects the beam, as the fluctuations are elongated in the direction of the field and spatial localisation of the measurement is thus optimised [68]. To achieve a high signal-to-noise ratio, avalanche photodiodes (APDs) are used for the BES detectors.

The sampling frequency of the BES data is 2MHz, allowing for a good temporal resolution, but the spatial resolution is somewhat limited. The pixel size limits the spatial resolution to approximately 2cm per pixel [68], and further effects due to high energies of the beam particles result in spatial non-localities, as their velocities of around  $10^6\text{ms}^{-1}$  combined with the  $D_\alpha$  relaxation time of around  $10^{-8}\text{s}$  allow the particles to travel distances of order cm before relaxing. Nevertheless, large-scale turbulent structures over the majority of the beam width (10-20cm) should be resolvable [69].

The line of sight of the detector can be adjusted to measure data from (major) radial locations of 0.706m to 1.6m, allowing studies of turbulence from the inner region across the core to outside the LCFS. On MAST, one detector array allows for imaging of a  $16\text{cm} \times 8\text{cm}$  area of the plasma centred at a particular radial location on the midplane, so the stacked arrays featured in the BES upgrade on MAST-U will be able to image a  $16\text{cm} \times 16\text{cm}$  area, covering a significant portion of the plasma.

## 2.3 Established codes used for this project

Along with data from diagnostics such as those introduced above, output from established plasma codes was used in analysis, interpretation and presentation of data. The two main codes of interest are the equilibrium code EFIT and the transport code TRANSP, which are both introduced in this section. TRANSP especially played a significant part in this thesis, with the heat flux study of Chapter 4 based almost entirely on results from interpretive TRANSP runs of the shots of an L-H transition experiment.

### 2.3.1 EFIT: equilibrium reconstruction

EFIT [70] is an equilibrium solver which utilises measurements from diagnostics such as Motional Stark Effect (MSE) [67, 71], external magnetic probes and poloidal flux loops to solve the force-balance-derived Grad-Shafranov equilibrium equation (and constrain the solutions) in cylindrical coordinates

$$r \frac{\partial}{\partial r} \left( \frac{1}{r} \frac{\partial \psi}{\partial r} \right) + \frac{\partial^2 \psi}{\partial z^2} = -\mu_0 r^2 \frac{dp(\psi)}{d\psi} - F \frac{dF(\psi)}{d\psi} \quad (2.4)$$

which contains three unknown quantities: the poloidal flux function  $\psi$  (poloidal magnetic flux enclosed in the equi-pressure (or magnetic flux) surface per radian), the pressure  $p(\psi)$  and the poloidal current function  $F(\psi) \equiv rB_\phi$  (total poloidal current enclosed in the equi-pressure (or magnetic flux) surface per radian). The G-S equation is a non-linear, second order partial differential equation, and in order to obtain the physical locations of the flux surfaces  $\psi(r, z)$  for the complex shapes of a tokamak plasma, it must be solved numerically.

Optimising the solution with the available constraints, EFIT can then provide useful information on the plasma geometry, stored energy and current profiles. Throughout the project (and this thesis), the equilibrium provided by EFIT is used for the visualisation of flux surfaces in the plasma, including the last closed flux surface (LCFS) or separatrix, and various plasma geometry-related quantities and variables. For the turbulence studies of Chapter 5, the EFIT-provided flux surfaces  $\psi(r, z)$  are used in a quantitative manner in the velocimetry calculations to provide accurate poloidal and radial velocities through mapping the BES APD channels to their equivalent positions on the flux surfaces and measuring either along (for  $v_\theta$ ) or perpendicular to (for  $v_r$ ) the flux surface associated with a particular channel. Further details on the use of the equilibrium reconstructions in BES data analysis

are discussed in Chapter 5. For the power threshold studies of Chapter 3, the plasma geometry information calculated by EFIT includes estimates of elongations and triangularities, and the midplane radial distance between the separatrices associated with each of the two X-points,  $\delta r_{\text{sep}}$ . This last quantity is used to determine the plasma geometry's location on the single null (SN) - double null (DN) scale, and for this particular dataset used in the project the change in  $\delta r_{\text{sep}}(t)$  represents one of the plasma control techniques used in these experiments. More about this control technique and the significance of  $\delta r_{\text{sep}}$  is discussed in Section 2.4. In Chapter 3, some EFIT outputs can be used as the components of the net power  $P_{\text{net}}$ , as EFIT calculates both the ohmic heating power  $P_{\text{ohm}}$  and the stored energy in the plasma  $W$ . The ohmic power calculated by EFIT showed some unphysical behaviour (e.g. negative values), so TRANSP (see next section) was used to determine  $P_{\text{ohm}}$  instead. As the settings for default EFIT runs were unsuitable for the requirements of calculating the rate of change of stored energy  $dW/dt$ , new dedicated equilibrium reconstructions with a higher time resolution (0.2ms instead of the default 5ms) were performed. More details on the use of EFIT in the power threshold analysis are contained in Chapter 3. For the heat flux studies of Chapter 4, dedicated equilibrium reconstructions using EFIT are performed for each new TRANSP run, during the setup process in OMFIT. The equilibrium produced by EFIT is further used to localise the two-dimensional TRANSP output quantities explored during this analysis, including the ion and electron heat fluxes, to points along the normalised effective radius  $\rho_{\text{eff},N}$  or normalised toroidal magnetic flux  $\psi_N$ , which are defined in Chapter 1. This is possible since these quantities are flux quantities, i.e. constant on a flux surface. For the MAST-U experiments of Chapter 6, the automatic post-shot EFIT runs were useful on experiment days as they provided data quickly so could be used in between shots to determine what happened in the previous shot and what to change or improve for the next shot. EFIT could show whether a particular shot was vertically unstable or grew too large in outer radius, as well as when these issues occurred, so that they could be correlated with shot design choices like beam start times, the time history of the height of the magnetic axis, radial feedback control or changes in coil currents. As discussed here, EFIT is extremely versatile and was used throughout the project.

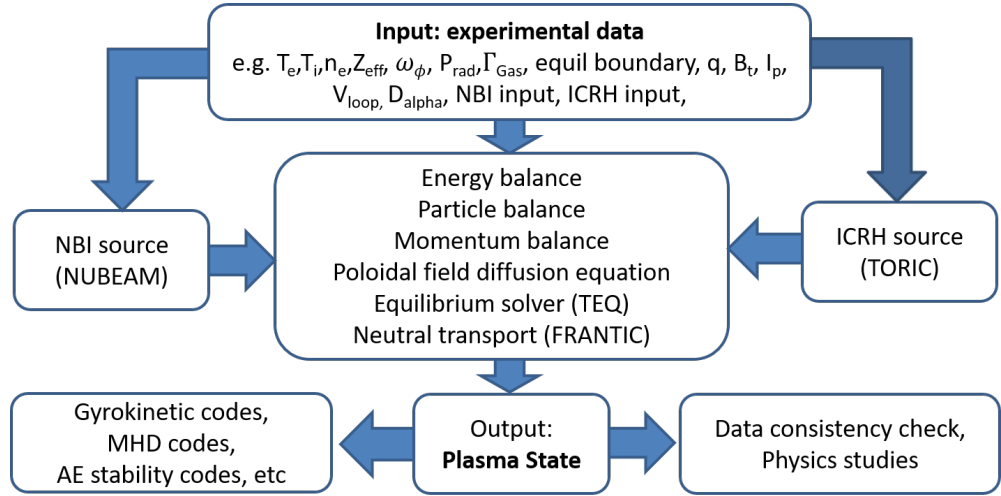


Figure 2.7: Generalised schematic workflow of an interpretive TRANSP simulation. [72]

### 2.3.2 TRANSP: transport code with NBI module (NUBEAM)

TRANSP [73] is a whole plasma model transport code developed and maintained by PPPL which solves plasma fluid transport and poloidal field diffusion equations, with separate numerical models for heating, momentum, particle and current sources (such as NUBEAM [74] for NBI heating). While the code can be run in a predictive (where the evolution of profiles is predicted by models) or interpretive (where temperature and density profiles are provided from experimental measurements and the transport coefficients, which are not otherwise measurable, are inferred) mode, all simulations in this project were run in an interpretive mode as they were used to analyse experimental data. The generalised schematic workflow of an interpretive TRANSP simulation is shown in Figure 2.7. The time dependent flux surface geometry can be constructed in TRANSP or input from EFIT solutions, and experimental data from many sources, including profiles from Motional Stark Effect (MSE), Thomson Scattering (TS) and Charge-exchange (CXRS) diagnostics are utilised to constrain the solutions to the transport equations. TRANSP can provide information on the power balance, including heating terms and heat flux profiles. Running a less-involved version of TRANSP without dedicated EFIT runs and profile fitting for each timestep was sufficient for the power threshold analysis of Chapter 3, but as the heat flux analysis of Chapter 4 required the use of both time- and space-resolved outputs, a more comprehensive version of TRANSP had to be employed. More information on TRANSP is therefore contained in Chapter 4, such as the steps involved in setting up the more involved TRANSP runs as

well as information on the equations solved by TRANSP (including a full derivation of these equations in Appendix A).

## 2.4 Dataset from L-H transition experiment on MAST used in Chapters 3 and 4

As low-aspect ratio (spherical) tokamaks are much less common, most of the results from multi-device studies such as commonly used scaling laws like that from Martin et al. [40] are based largely on conventional tokamak data and often don't describe ST behaviour very well. While there have been L-H transition studies performed on MAST (introduced in Section 2.1), especially early in its operation phase [75], no comprehensive  $P_{LH}$  study had been published at the time of the start of this project. An experimental proposal to study, among other things, the density dependence of  $P_{LH}$  had performed its allocated shots in 2011-2013, but due to the experimental leader's time constraints the data hadn't yet been analysed or the results published. Analysing this data to produce the first comprehensive  $P_{LH}(n_e)$  curve for MAST, and spherical tokamaks in general, formed part of this PhD project. The dataset was used for Chapter 3 and Chapter 4, i.e. for the power threshold analysis and the heat flux studies. Attempts were made to use this dataset for a turbulence study as well, but the BES data was unfortunately not suitable (more detail on this in Chapter 5).

The experiment was performed on a number of days between 2011 and 2013, resulting in 66 usable shots with shot numbers between 27035 and 28330. The shots included in the analysis have plasma currents of  $I_p = 740 \pm 20\text{kA}$  and toroidal magnetic fields of  $B_T = 0.55 \pm 0.07\text{T}$ , are in double null configurations with  $\delta r_{\text{sep}} = 0.0 \pm 1.5\text{mm}$  for the time periods analysed, have elongations of  $\kappa = 1.78 \pm 0.05$ , and upper and lower triangularities of  $\delta_u = 0.47 \pm 0.01$  and  $\delta_l = 0.48 \pm 0.01$ . For the main purpose of the experiment, the NBI heating power and the plasma density were varied, while keeping the rest of the plasma as consistent from shot-to-shot as possible. Not counting further density increases during H-mode, the density was varied between  $0.15n_G$  and  $0.63n_G$ , where the Greenwald density  $n_G = I_p/(\pi a^2)$  (units of  $10^{20} \text{ m}^{-3}$ , MA and m) describes an operational limit for the density in tokamaks [76]. As can be seen in Figure 2.8, the density peaking, i.e. the ratio between core density and line averaged density  $n_e(0)/\bar{n}_e$ , generally decreases with increasing line averaged density from 1.8 to about 1.2 in the presence of a partial or full transport barrier (i.e. for H-modes and

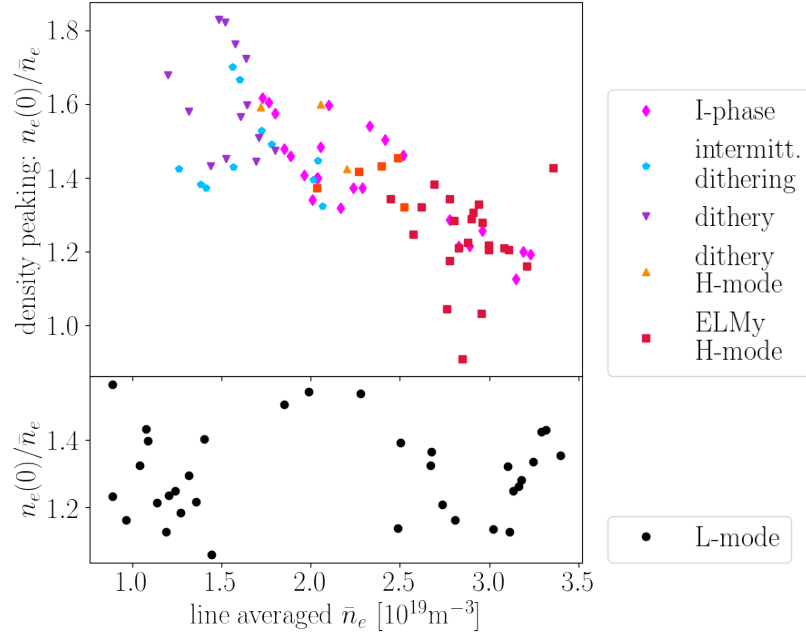


Figure 2.8: Density peaking  $n_e(0)/\bar{n}_e$  as a function of line averaged density  $\bar{n}_e$  for all time-points in the dataset which have Thomson scattering data. The top panel shows the values for transitions to H-mode and intermediate categories (more on the categorisation in Chapter 3) while the bottom panel shows the L-mode points.

intermediate categories) and is  $1.3 \pm 0.1$  in L-mode, independent of line averaged density.

As a control technique for H-mode entry based on favourable and unfavourable configurations in a tokamak was used in this set of plasma shots, the reasoning behind and effect of the control technique are introduced in the following section.

### 2.4.1 Favourable and unfavourable configurations

Conventional tokamaks most commonly operate in single null (SN) configuration, i.e. with one dominant X-point, while spherical tokamaks often operate in double null (DN) with two X-points, but are also capable of operating in SN. Either configuration will technically have two X-points and a separatrix associated with each, but in a SN case the second X-point will be very weak (note that weak here means that the point of zero poloidal field lies far away from the main separatrix marking the transition from confined to unconfined plasma, and therefore less of the exhaust is channelled through this X-point) and the second (outer) separatrix will be far removed from the main separatrix, so the plasma essentially behaves as if there is only one X-point. For DN, both X-points are strong enough that both divertors will share the power exhaust. In a perfect connected double null (CDN) configuration, the

divertors share the exhaust equally, and the two separatrices will lie on top of each other, so that the midplane radial distance between them  $\delta r_{\text{sep}} \rightarrow 0$ , fulfilling the condition of  $\delta r_{\text{sep}} \ll \rho_{L,i}$ , i.e the midplane radial distance between the two separatrices is much less than the size of the ion Larmor radius. If one of the two X-points is stronger, such that its divertor will deal with a higher proportion of the exhaust, the configuration is known as disconnected double null (DDN). A plasma can generally be understood to be in DDN if  $|\delta r_{\text{sep}}|$  is greater than the ion Larmor radius ( $\sim 6\text{mm}$  on MAST) [77]. The separatrix associated with the dominant X-point will always lie inside the less dominant separatrix, and  $\delta r_{\text{sep}}$  is calculated as  $\delta r_{\text{sep}} = r_{\text{sep,low}} - r_{\text{sep,up}}$ , so that a positive  $\delta r_{\text{sep}}$  corresponds to a dominant upper X-point and a negative  $\delta r_{\text{sep}}$  to a dominant lower X-point. SN configurations can also be associated with an upper X-point (USN) or a lower X-point (LSN).

In SN plasmas, it was found on several devices that switching the configuration from LSN to USN while keeping the direction of the plasma current and other plasma conditions unchanged significantly increased the power threshold  $P_{LH}$  [78]. The same effect can be seen if the dominant divertor is not changed but instead the plasma current  $I_p$  or toroidal magnetic field  $B_T$  direction is reversed [27]. This configuration is called “unfavourable”, due to the increased difficulty in accessing H-mode, while the reverse is termed “favourable”. From our current understanding, the two configurations are defined by the direction of the  $\mathbf{B} \times \nabla \mathbf{B}$  drift with respect to the dominant X-point, with the drift pointing towards the X-point in the favourable and away from it in the unfavourable configuration.

For DN plasmas, this can be utilised to prevent or delay H-mode entry by keeping the plasma in a DDN configuration with the  $\mathbf{B} \times \nabla \mathbf{B}$  drift pointing away from the dominant X-point while H-mode is undesirable (with respect to the experiment aims) and shifting it towards CDN when H-mode is acceptable. This H-mode entry control technique was utilised on MAST [79], and an example shot is detailed in Figure 2.9. The plot on the left shows the  $\delta r_{\text{sep}}$  trace as the plasma is shifted from DDN to CDN at around 0.25s, which prompted an L-H transition as seen from the  $\bar{n}_e$  and  $D_\alpha$  traces. The separatrices associated with each X-point are shown for two time points, one in the DDN phase and one in the CDN phase. The separatrices for the CDN are very close together and the X-points are almost equally weighted, while for the DDN the dominant upper X-point is noticeable and the distance between the two separatrices is much greater.

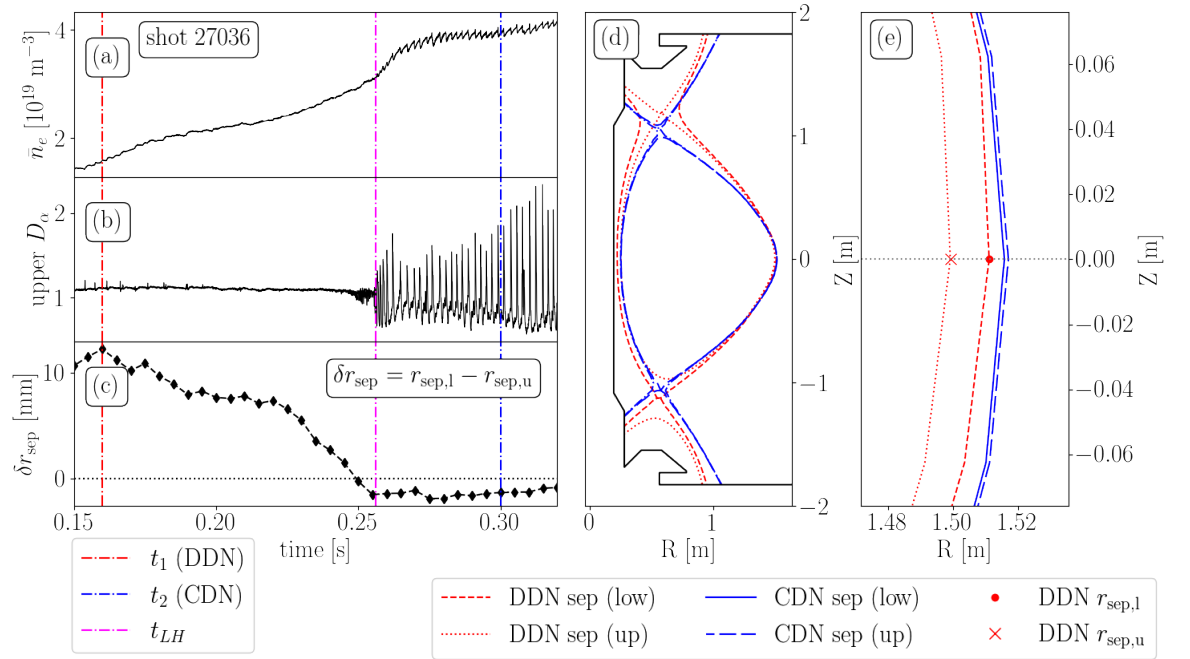


Figure 2.9: (a) Line averaged density  $\bar{n}_e$ , (b) upper  $D_\alpha$  and (c)  $\delta r_{\text{sep}}$  traces for a shot which transitioned from L- to H-mode shortly after the configuration was changed from a disconnected double null (DDN) to a connected double null (CDN). The separatrices for two time points, one during DDN phase ( $t_1 = 0.16\text{s}$ , red dashed) and one during CDN ( $t_2 = 0.3\text{s}$ , blue) are shown in (d) and (e). The  $\delta r_{\text{sep}}$  variable corresponds to the midplane distance between the two separatrices associated with each X-point, with  $\delta r_{\text{sep}} = r_{\text{sep},l} - r_{\text{sep},u}$ , and the larger value for DDN can be seen in the zoomed in plot (e).

## Chapter 3

# Power threshold studies

### 3.1 Overview

This Chapter includes an analysis of different transition behaviours (including I-phases and dithery H-modes), based especially on the types of fluctuations in the  $D_\alpha$  signal, and a detailed calculation of the net power  $P_{\text{net}}$  for the transition times of each shot included in a database from an L-H transition experiment performed on MAST. The methods of both the net power determination and the descriptions of the transition behaviours are detailed, with an analysis of the  $D_\alpha$  signal for each behaviour category and a comparison of the results for different definitions of  $P_{\text{net}}$ . The results for both are shown and the fit to the  $P_{\text{net}}(\bar{n}_e)$  data is compared with typical scaling laws for  $P_{LH}$ . The impact of various choices (such as the transition time selection and the TRANSP variables for the NBI power) are explored. Finally, a scaling for  $n_{e,\text{min}}$  by Ryter *et al.* [1] is re-evaluated and modified to apply to MAST data, and the significant discrepancies are explored. Much of this chapter and parts of Chapter 4 have been published in an article in a special edition of Nuclear Fusion for the H-mode workshop 2022 [3].

### 3.2 Motivation

As was mentioned in Chapter 1, the power threshold  $P_{LH}$ , i.e. the net power required for a tokamak plasma to transition into the improved (particle and energy) confinement H-mode regime, is an important quantity to know for present-day experimental and future reactor-relevant operation. As L-H transition models are not yet able to predict  $P_{LH}$ , the

fusion community relies on empirical scaling laws and experience with specific tokamaks to estimate  $P_{LH}$  for different operating scenarios. Knowing  $P_{LH}$  and how it responds to different parameter changes is important for experimental studies, whether the aim is to avoid H-mode or to obtain it, and for the design of future devices, to answer questions such as whether there will be enough auxiliary power available for H-mode operation or whether there will be a sufficiently large parameter space to explore alternative confinement regimes.

### 3.3 Net power calculations

Determining  $P_{LH}$  requires the calculation of the net power  $P_{\text{net}}$ , which is determined from the balance of input and output powers. The input powers are the ohmic heating power  $P_{\text{ohm}}$  and the auxiliary heating power  $P_{\text{aux}}$ , and their sum is then corrected for the rate of change of stored energy  $W$  in the plasma, i.e.  $dW/dt$ . This version of the net power is called loss power  $P_{\text{loss}}$ , and is commonly used in most power threshold studies. If the net power is then additionally corrected for the power lost by radiation from the core  $P_{\text{rad}}$ , the result is defined as  $P_{\text{sep}}$ , i.e. the power (due to plasma) crossing the separatrix.

$$P_{\text{loss}} = P_{\text{ohm}} + P_{\text{aux}} - \frac{dW}{dt} \quad (3.1)$$

$$P_{\text{sep}} = P_{\text{ohm}} + P_{\text{aux}} - \frac{dW}{dt} - P_{\text{rad}} = P_{\text{loss}} - P_{\text{rad}}. \quad (3.2)$$

While physics explanations of the transition suggest that  $P_{\text{sep}}$  is more relevant, most power threshold studies as well as the scaling laws [40,80] take the net power as  $P_{\text{loss}}$ , as the radiated power is generally smaller than the other components and can be difficult to determine precisely.  $P_{\text{rad}}$  has a majority contribution from Bremsstrahlung losses, and as these scale with  $Z^2$ ,  $P_{\text{rad}}$  is usually only significant in the presence of large amounts of high- $Z$  impurities, such as on ASDEX Upgrade which has a tungsten ( $Z = 74$ ) first wall. MAST and MAST-U both have carbon ( $Z = 6$ ) walls, so radiative losses are less significant. As part of the power threshold study described in this chapter, the core radiated power for MAST ( $P_{\text{rad}}$  estimated from bolometry data) was also investigated and the results for  $P_{\text{sep}}$  are presented alongside  $P_{\text{loss}}$  in Section 3.5.3.2, but as  $P_{\text{rad}}$  was not found to be of qualitative significance (since it showed no significant dependence on density or transition type) this thesis primarily focuses on results using  $P_{\text{loss}}$ .

For the  $P_{\text{loss}}$  calculations, both the equilibrium code EFIT [70] and the transport code

TRANSP [73] were utilised (see Chapter 2 for a description of both).

As was mentioned in Chapter 1, the resistance generated by the plasma current  $I_p$  heats the plasma through a process known as ohmic or Joule heating with power  $P_{\text{ohm}} = \int_V \eta j^2 dV$ , where  $\eta$  is the resistivity and  $j$  the current density. In a tokamak, the ohmic power can be determined from quantities measured by different magnetic coils placed around the plasma, with the simplified product of the plasma current and the loop voltage  $P_{\text{ohm}} \approx I_p V_{\text{loop}}$  approximating a more complex expression of  $P_{\text{ohm}} = I_p (V_{\text{loop}} - 2\pi d\psi_{\text{sep}}/dt) - dW_B/dt$ , where  $\psi_{\text{sep}}$  is the poloidal flux at the boundary and  $W_B$  the magnetic energy. Both EFIT and TRANSP calculate estimates of the ohmic power which are returned as outputs, and either of the two estimates can be used in the  $P_{\text{loss}}$  calculation. The  $P_{\text{ohm}}^{\text{EF}}$  estimate by EFIT has a tendency to gradually decrease during the flat top phase, which occasionally results in negative (i.e. unphysical)  $P_{\text{ohm}}$  values. This motivated the initial decision to perform TRANSP runs on this dataset to obtain an alternative  $P_{\text{ohm}}^{\text{TR}}$  estimate. The ohmic power calculation relies on settings in the TRANSP code which can be adjusted during set-up to avoid negative  $P_{\text{ohm}}$  values, such as enabling current evolution and utilising the Sauter resistivity and bootstrap models. Even with several iterations of diagnosing run issues and improving settings, for some of the shots in this dataset no successful TRANSP runs were obtained, mostly due to either missing data for essential diagnostics such as TS or CXRS or the fast ion density growing larger than the plasma density, which occurred in some shots even with the inclusion of an anomalous diffusivity (more on this in Chapter 4). To enable the production of  $P_{\text{net}}(\bar{n}_e)$  plots with the entire dataset and to check for differences in the results, two methods for the  $P_{\text{net}}$  calculations were performed, named  $P_{\text{loss}}^{\text{TR}}$  or  $P_{\text{loss}}^{\text{EF}}$  after their source for the  $P_{\text{ohm}}$  calculation. Except for one plot comparing the results when using  $P_{\text{ohm}}^{\text{EF}}$  in Section 3.5.3.1, the TRANSP method is used throughout this thesis, and  $P_{\text{loss}}$  will generally refer to  $P_{\text{loss}}^{\text{TR}}$ .

For both MAST and MAST-U the auxiliary heating is provided exclusively by neutral beam injection, so that  $P_{\text{aux}} = P_{\text{NBI}}$ . For the NBI power  $P_{\text{NBI}}$ , there can be significant discrepancies between the injected power and the power absorbed by the plasma, especially in low-density scenarios, where reduced attenuation of the beam by the plasma can lead to shine-through losses [52]. Instead of the injected power  $P_{\text{inj}}^{\text{NBI}}$ , the captured beam power estimated by TRANSP  $P_{\text{cap}}^{\text{NBI}}$  corrected for shine-through losses is used. In addition to the shine-through losses, fast ion losses such as charge-exchange and orbit losses can further

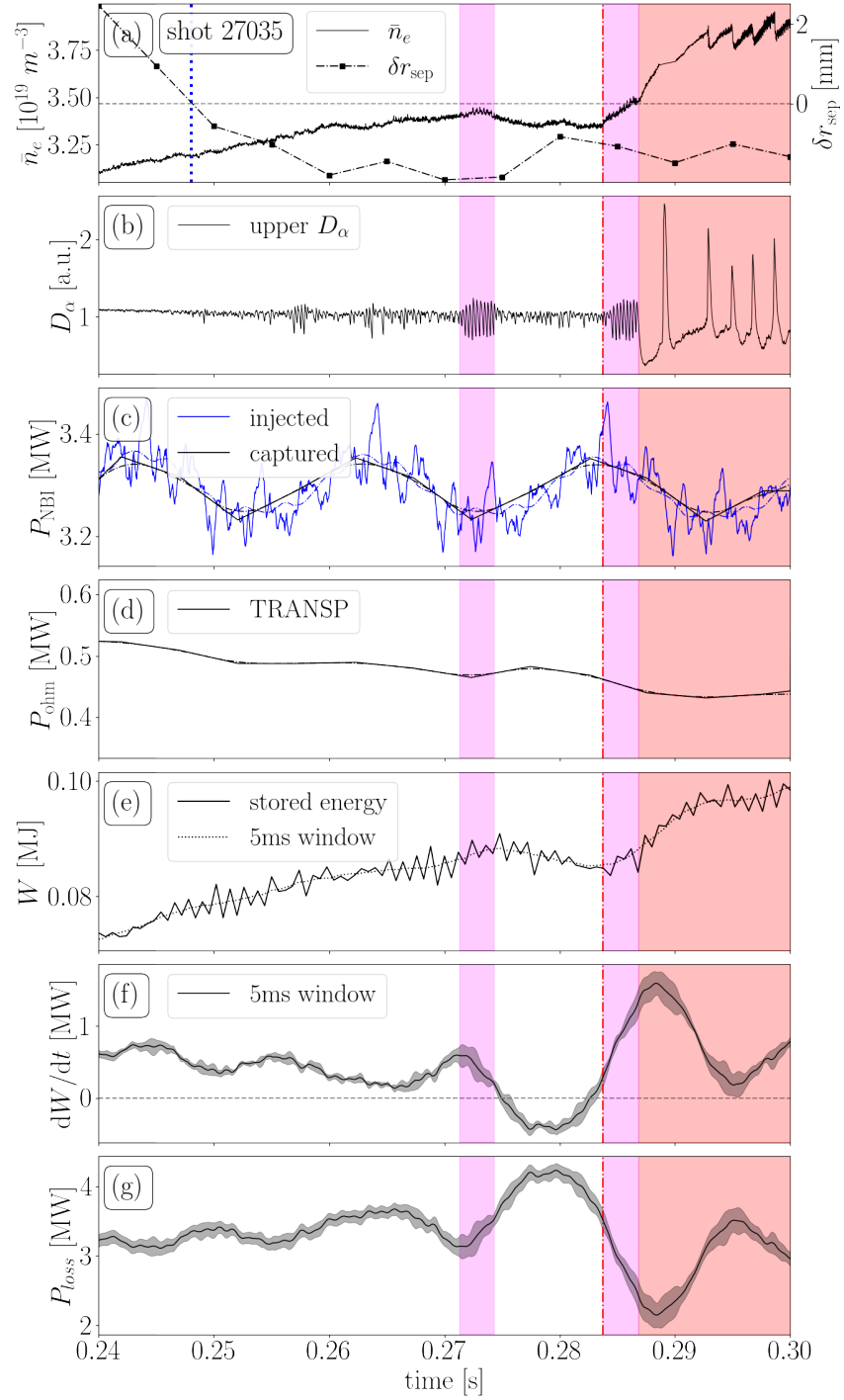


Figure 3.1: For an example H-mode shot, traces of (a) line averaged density  $\bar{n}_e$  (left axis) and  $\delta r_{\text{sep}}$  (right axis), (b) deuterium Balmer  $\alpha$  ( $D_\alpha$ ), (c) injected and captured  $P_{\text{NBI}}$ , (d)  $P_{\text{ohm}}$  as calculated by TRANSP, (e) the stored energy from EFIT with a 5ms smoothing window applied, (f) the rate of change of stored energy with an uncertainty range based on smoothing window sizes of 2-8ms, (g)  $P_{\text{loss}} = P_{\text{loss}}^{\text{TR}} = P_{\text{cap}}^{\text{NBI}} + P_{\text{ohm}}^{\text{TR}} - dW/dt$  results. The blue dotted line in (a) marks the start of the constant  $\delta r_{\text{sep}}$  period, which for this shot occurred 35ms before the transition (red dot-dashed line). The plasma behaviour categories described in Chapter 3.4 are shown here as shaded regions, with I-phases shown in fuchsia and an ELMy H-mode in red.

	<b>Description</b>
$P_{\text{net}}$	net power, general term
$P_{\text{loss}}$	loss power, used in power threshold studies. Here $P_{\text{NBI}} = P_{\text{cap}}^{\text{NBI}}$ is used. $P_{\text{loss}} = P_{\text{ohm}} + P_{\text{NBI}} - dW/dt$
$P_{\text{loss,th}}$	loss power corrected for fast ion losses, i.e. $P_{\text{NBI}} = P_{\text{heat}}^{\text{NBI}}$ is used.
$P_{\text{sep}}$	power crossing the separatrix $P_{\text{sep}} = P_{\text{ohm}} + P_{\text{NBI}} - dW/dt - P_{\text{rad}}$
$P_{\text{NBI}}$	NBI power, general term
$P_{\text{inj}}^{\text{NBI}}$	injected NBI power
$P_{\text{cap}}^{\text{NBI}}$	captured NBI power, the injected power with shine-through losses subtracted.
$P_{\text{heat}}^{\text{NBI}}$	total beam heating of the plasma (corrected for shine-through and fast ion losses)
$P_{\text{ohm}}$	ohmic power, general term
$P_{\text{ohm}}^{\text{EF}}$	ohmic power calculated by EFIT
$P_{\text{ohm}}^{\text{TR}}$	ohmic power calculated by TRANSP (used throughout unless otherwise specified)

Table 3.1: Different net power, NBI and ohmic power variables used in this thesis.

decrease the absorbed  $P_{\text{NBI}}$ . In this work,  $P_{\text{loss}}$  refers to cases with  $P_{\text{NBI}} = P_{\text{cap}}^{\text{NBI}}$  corrected for shine-through losses, while for  $P_{\text{loss,th}}$ ,  $P_{\text{NBI}} = P_{\text{heat}}^{\text{NBI}}$  is additionally corrected for further fast ion losses.

$$P_{\text{loss}} = P_{\text{ohm}}^{\text{TR}} + P_{\text{cap}}^{\text{NBI}} - \frac{dW}{dt} \quad (3.3)$$

$$P_{\text{loss,th}} = P_{\text{ohm}}^{\text{TR}} + P_{\text{heat}}^{\text{NBI}} - \frac{dW}{dt} \quad (3.4)$$

Determining the magnitude of further beam power losses due to fast ion effects (i.e. fast ion losses) requires more involved TRANSP simulations. These were performed on a limited set of plasma shots for the heat flux analysis in Chapter 4. The power threshold study was then repeated for  $P_{\text{loss,th}}$ . For this chapter, which includes the entire data set, the power threshold study was performed for  $P_{\text{loss}}$ . An overview of the different net power and NBI power variables used in this thesis are shown in Table 3.1. The beam modulation (seen in Figure 3.1c) can provide an estimate for the uncertainty on  $P_{\text{NBI}}$ .

The rate of change of stored energy can be a challenging term to calculate, as it requires the calculation of the gradient of a discrete, noisy time series with limited resolution. Both

EFIT and TRANSP return estimates of  $W$ . The default EFIT runs performed for each MAST shot have a time resolution of 5ms, which on L-H transition timescales is not high enough to capture relevant processes. For the  $dW/dt$  calculations, new equilibrium reconstructions using EFIT at a time resolution of 0.2ms were performed. To obtain reasonable estimates of  $dW/dt$ , the  $W$  time series must be interpolated and smoothed so as to avoid sharp spikes in the gradient. As the size of the smoothing window will influence the result of the gradient calculation, different sizes were compared. Smoothing window sizes greater than 10ms were found to suppress or even reverse the trends of the time history of  $dW/dt$ , but window sizes between 2ms and 8ms appeared to return similar general trends, with different levels of noise suppression. A window size of 5ms was chosen for the calculation to optimise noise filtering and signal feature preservation, with the range of values from window sizes between 2ms and 8ms incorporated into an uncertainty on  $dW/dt$ .

For the  $P_{\text{net}}$  results, all terms are interpolated onto a common time base and additionally time-averaged over 5ms, and the uncertainties are combined to return an uncertainty on  $P_{\text{net}}$ .

Figure 3.1 shows a selection of important traces for the identification of the L-H transition time  $t_{LH}$  and the net power calculation. The line averaged density  $\bar{n}_e$  and the upper divertor  $D_\alpha$  traces in (a) and (b) are used to identify  $t_{LH}$  and specific plasma behaviour categories (see following section), where for this example shot the red dashed line shows  $t_{LH}$  as the start of the I-phase immediately preceding the ELMy H-mode phase. On the right axis in (a) the  $\delta r_{\text{sep}}$  trace is plotted, used to identify the time delay between reaching a stable connected double null configuration and the transition. The injected NBI power and the estimate for captured NBI power by TRANSP are plotted in (c) and the ohmic power estimate from TRANSP is plotted in (d). This is one of the highest-density shots in the data set, so the shine-through losses are low and the captured NBI power in (c) is close to the injected power. The stored energy  $W$  estimate from EFIT is plotted in (e) along with an average of  $W$  smoothed over a 5ms window. The rate of change of stored energy  $dW/dt$  is shown in (f), with the solid line calculated from  $W$  smoothed over 5ms, while the range of values for smoothing window sizes between 2ms and 8ms are shown as the shaded region. In both the  $W$  and  $dW/dt$  traces, (e) and (f), it can be seen that the rise associated with H-mode entry begins with the pre-H I-phase, a feature further discussed in the following sections. The final panel (g) shows the result for  $P_{\text{loss}} = P_{\text{loss}}^{\text{TR}} = P_{\text{cap}}^{\text{NBI}} + P_{\text{ohm}}^{\text{TR}} - dW/dt$  along with a combined uncertainty range.

As the auxiliary heating on MAST is provided solely through neutral beam injection, and it was not possible to provide a smooth ramp-up in power throughout a plasma discharge, the experiment focused on density ramping (through fuelling) combined with the disconnected double null configuration technique described in Section 2.4.1 to explore the parameter space for L-H transitions. The  $P_{\text{NBI}}$  traces are therefore mostly constant (apart from e.g. the beam modulation) throughout the current flat top phase and the transitions.

### 3.4 Plasma behaviour categorisation

For L-H transition studies, it is necessary to be able to identify the plasma's confinement state as well as times of transitions between states, but in practice this can be difficult. Plasmas close to the H-mode boundary or of low density can exhibit more complex behaviours that are not immediately categorised as either an L-mode or an H-mode, making the identification of L-H transition times challenging. We know from numerous studies that L- and H-mode are not the only confinement states that can be found in a tokamak plasma, though the other states are usually found in a narrower range of conditions and some have only been seen on a few devices. In addition to alternative confinement states, there are also phenomena related to the L-H transition itself such as limit-cycle oscillations or other possible H-mode pre-cursors, and finally there are multiple sub-types of H-mode, mostly related to the frequency and character of ELMs. These can all appear differently in the parameter traces used to identify L-H transitions, so a careful treatment is necessary for an accurate  $P_{LH}$  study. Based on their signatures in relevant traces, a number of distinct though potentially related behaviour categories were identified. These intermediate categories as well as the sub-classification of H-modes are introduced and described in the following section, after a general overview of how L-H transitions are usually identified.

The behaviour categories and the inter-category transition times can be identified as a first step from visual inspection of the  $D_\alpha$  and line averaged density  $\bar{n}_e$  traces. The transition from L- to H-mode is visible as a drop in  $D_\alpha$  signal coinciding with a steep rise in  $\bar{n}_e$ . The main source of  $D_\alpha$  emission is the interaction of the plasma with neutrals, usually localised in the SOL and edge, and the change in particle confinement quality associated with the transition to H-mode leads to a reduction in the interaction with neutrals and thus is seen in the sharp drop in  $D_\alpha$  emission. The increased particle confinement during H-mode also

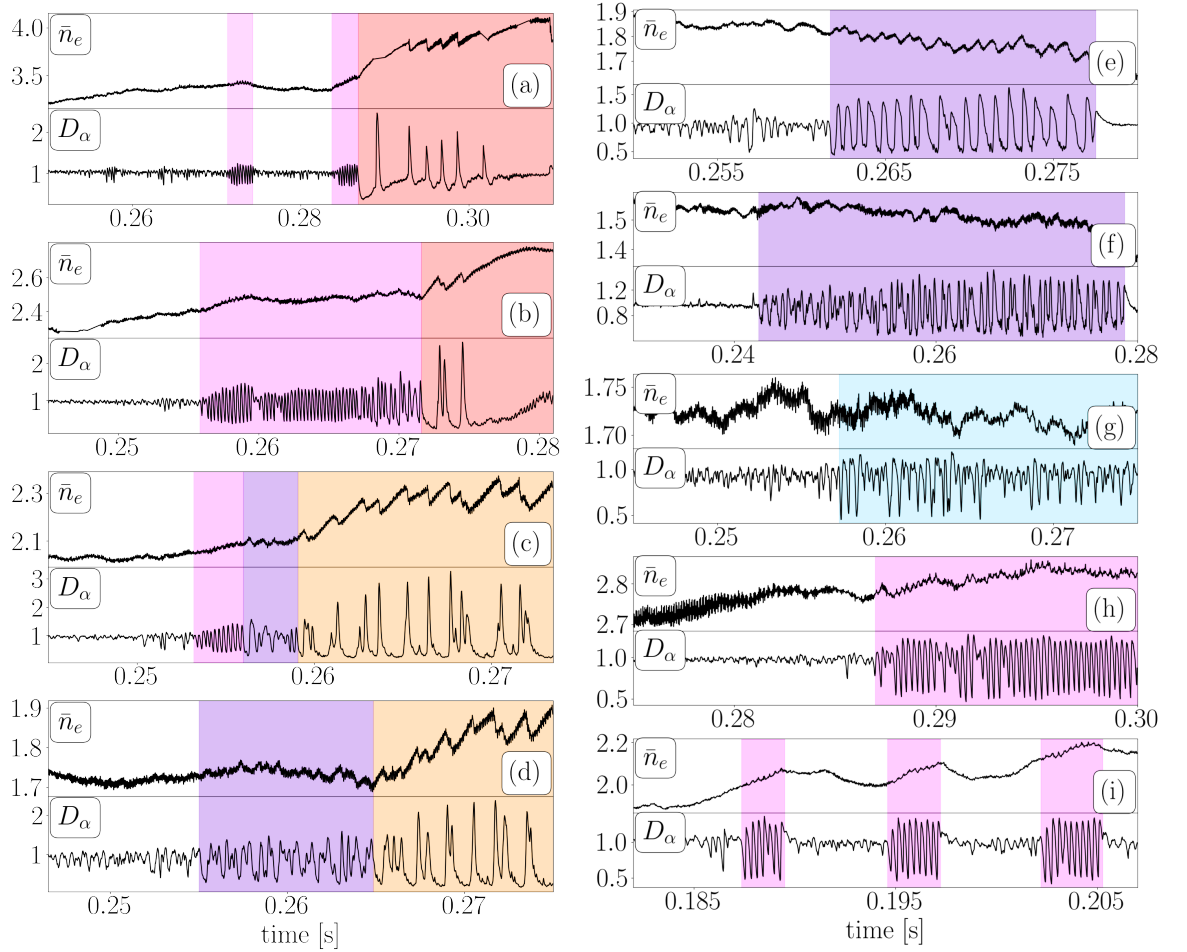


Figure 3.2: Example  $\bar{n}_e$  and  $D_\alpha$  traces for behaviour categories: (a) ELMy H-mode with intermittent preceding I-phases, (b) H-mode with long continuous preceding I-phase which displays the peak-skipping evolution towards the end, (c) and (d) dithery H-modes, (e) and (f) show dithery periods that did not reach H-mode confinement levels, (g) shows intermittent dithering, while (h) shows a long continuous I-phase and (i) intermittent short I-phases. I-phases are coloured in fuchsia, dithery periods in purple, intermittent dithering in light blue, dithery H-modes in orange and conventional H-modes in red.

results in an accumulation of density in the core, explaining the rise in  $\bar{n}_e$  visible after the transition. H-modes are also characterised by a reduction in fluctuations visible in turbulence diagnostics and the formation of a density and temperature pedestal in the profiles measured by the Thomson scattering diagnostic. H-modes are usually unstable due to the steep edge gradients, accumulate large amounts of fuel and impurity particles, and will often expel these accumulations in edge localised modes (ELMs) [81].  $D_\alpha$  emission can be collected from different plasma locations, and distinguishing features can be more or less visible in these different signals. The two signals that this work focused on were collected at the tangential midplane (midplane  $D_\alpha$ ) and the upper divertor or outer strike point (upper  $D_\alpha$ ). For the majority of this chapter, the upper  $D_\alpha$  is used for presentation and analysis, as it was less noisy and more easily enabled the identification of intermediate categories.

The intermediate categories are seen both during transition from L- to H-mode and at net powers close to  $P_{LH}$ . Discussions around some of these phenomena with respect to their identities and their relation to each other and to L- and H-mode are ongoing, with no consensus reached yet between different devices and research groups, so a standardised nomenclature is not available. For this thesis, the chosen categories have been named to be internally consistent with some input taken from previous work. Figure 3.2 shows examples for the  $D_\alpha$  and  $\bar{n}_e$  traces of the different categories defined below.

- **I-phases:** distinctive regular 3-4kHz oscillations in  $D_\alpha$  (sine-like in upper  $D_\alpha$  and miniature ELM-like in midplane  $D_\alpha$ ). Also seen in the vertical velocity of the plasma  $v_z$ . Found at  $\bar{n}_e \sim 1.6 - 3.2 \times 10^{19} \text{ m}^{-3}$ . Examples shown in Figure 3.2h-i.
- **pre-H I-phases:** I-phase preceding an H-mode. In some cases, the I-phase oscillations will evolve by skipping peaks, decreasing in frequency and growing in amplitude until the H-mode period begins, as seen in Figure 3.2b. The pre-H I-phase length is usually 2-3ms ( $\sim 0.1\tau_E$ ), but can be up to 10-30ms ( $\sim \tau_E$ ) for lower densities  $\bar{n}_e \sim 2.0 - 2.5 \times 10^{19} \text{ m}^{-3}$ . Examples shown in Figure 3.2a-c.
- **H-modes:** (a general description of H-modes is included in the preceding text, so the specifics of the H-modes in this data set are described here:) most H-modes in this study are type-III ELMy, with ELM frequency  $f_{ELM} \sim 500 - 600\text{Hz}$ , consistent with expected values for the studied densities on MAST [82]. The transition either occurs directly from L-mode or through one or more pre-H I-phase periods. Transitions occurred at

$\bar{n}_e \sim 2.0 - 3.3 \times 10^{19} \text{ m}^{-3}$ . Examples shown in Figure 3.2a-b.

- **dithery H-modes:** low-density H-modes with irregular ELMs, including double- or triple-ELMs. Each ELM filament expels a larger fraction of the density (than for the more conventional higher density H-modes described in the previous category) and the H-modes are more difficult to sustain. Found at  $\bar{n}_e \sim 1.7 - 2.2 \times 10^{19} \text{ m}^{-3}$ . Examples are shown in Figure 3.2c-d.
- **dithery periods:** clearly defined periods of irregular fluctuations in  $D_\alpha$  but confinement below H-mode levels. Occur at low plasma density,  $\bar{n}_e \sim 1.2 - 1.8 \times 10^{19} \text{ m}^{-3}$ . Examples shown in Figure 3.2d-f.
- **intermittent dithering:** noisy or L-mode-like dithery periods without clearly defined start and end points. Occur at similar densities to **dithery periods** but lower powers. Example shown in Figure 3.2g.
- **L-mode:** default state of the plasma, assigned based on exclusion of other categories. Low-density L-modes often contain irregular fluctuations in  $D_\alpha$  while high-density L-modes are generally “quiet”.

It is likely that the dithery periods and I-phases are not entirely distinct phenomena but rather aspects of the same mechanism, such as limit-cycle-oscillations (LCOs). The label “dithery” is used here to highlight the irregular nature of the fluctuations in those categories, especially contrasted with the strong regularity of I-phase fluctuations. The plasma states assigned to the label “intermittent dithering” could simply be noisier L-modes.

### 3.4.1 $D_\alpha$ analysis

From visual inspection of the  $D_\alpha$  signals, the differences between the behaviour categories can clearly be qualitatively defined, as can be seen in Figure 3.2. To solidify the categorisations and expand the identification of behaviour categories from just qualitative, visual inspection of signal traces to a quantifiable difference in the signals between the categories, especially the intermediate categories (dithery and I-phases), the  $D_\alpha$  signals were analysed further.

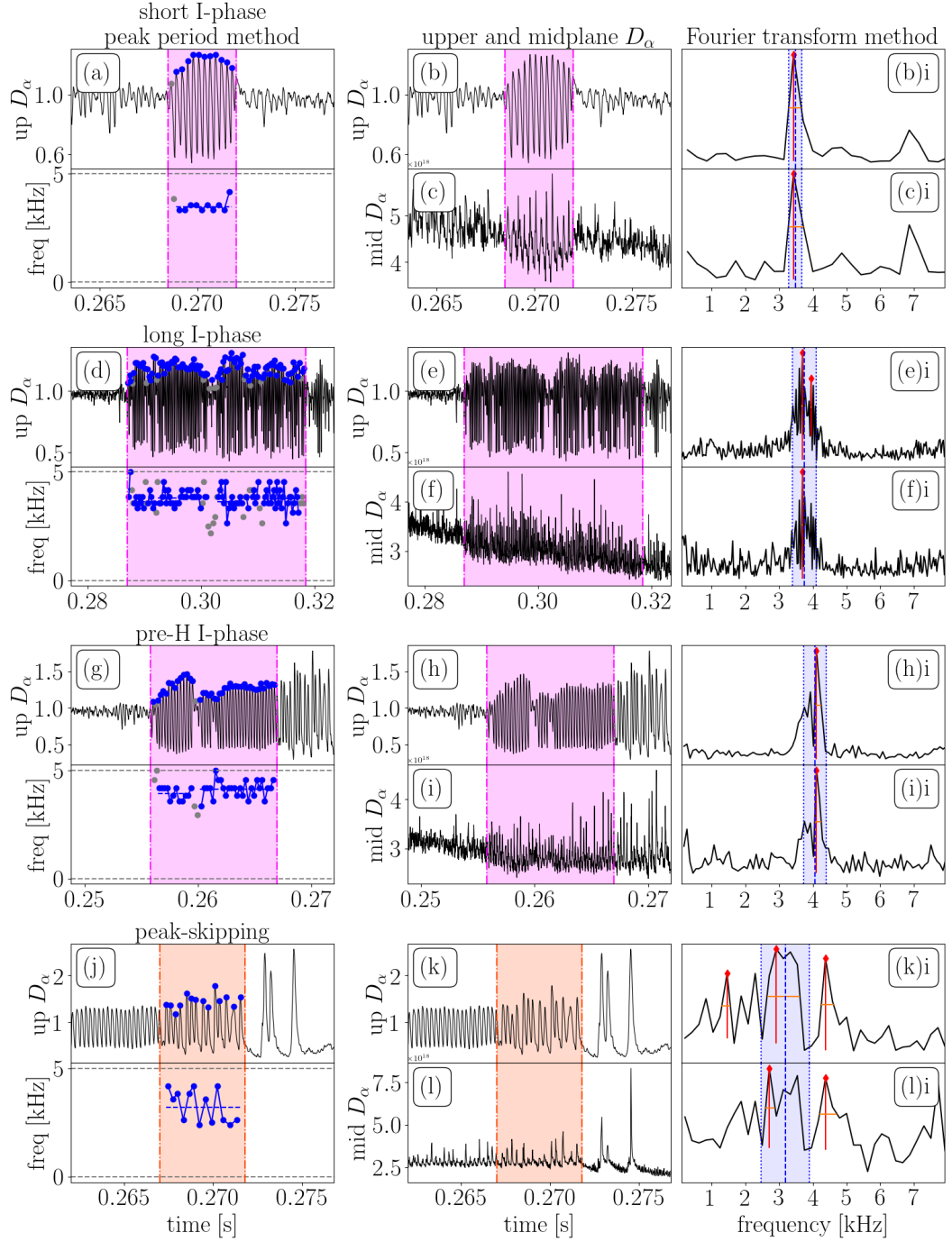


Figure 3.3: Example plots for the two methods of determining frequencies present in  $D_\alpha$  signals for a short I-phase ((a)-(c)i), a long I-phase ((d)-(f)i), a pre-H I-phase ((g)-(i)i) and subsequent peak-skipping behaviour ((j)-(l)i). The first method, which involves averaging over the time delay between peaks in the signal, is shown in the first column. The second column compares the time signals of upper and midplane  $D_\alpha$  and the third column shows the second method for both signals, which involves taking the Fourier transform and identifying the peaks in the frequency spectrum. The blue lines and shaded region in the spectra show the frequencies and standard deviation found in the first method, based on the accepted peaks shown in blue in the first column, while the spectral peaks are shown in red.

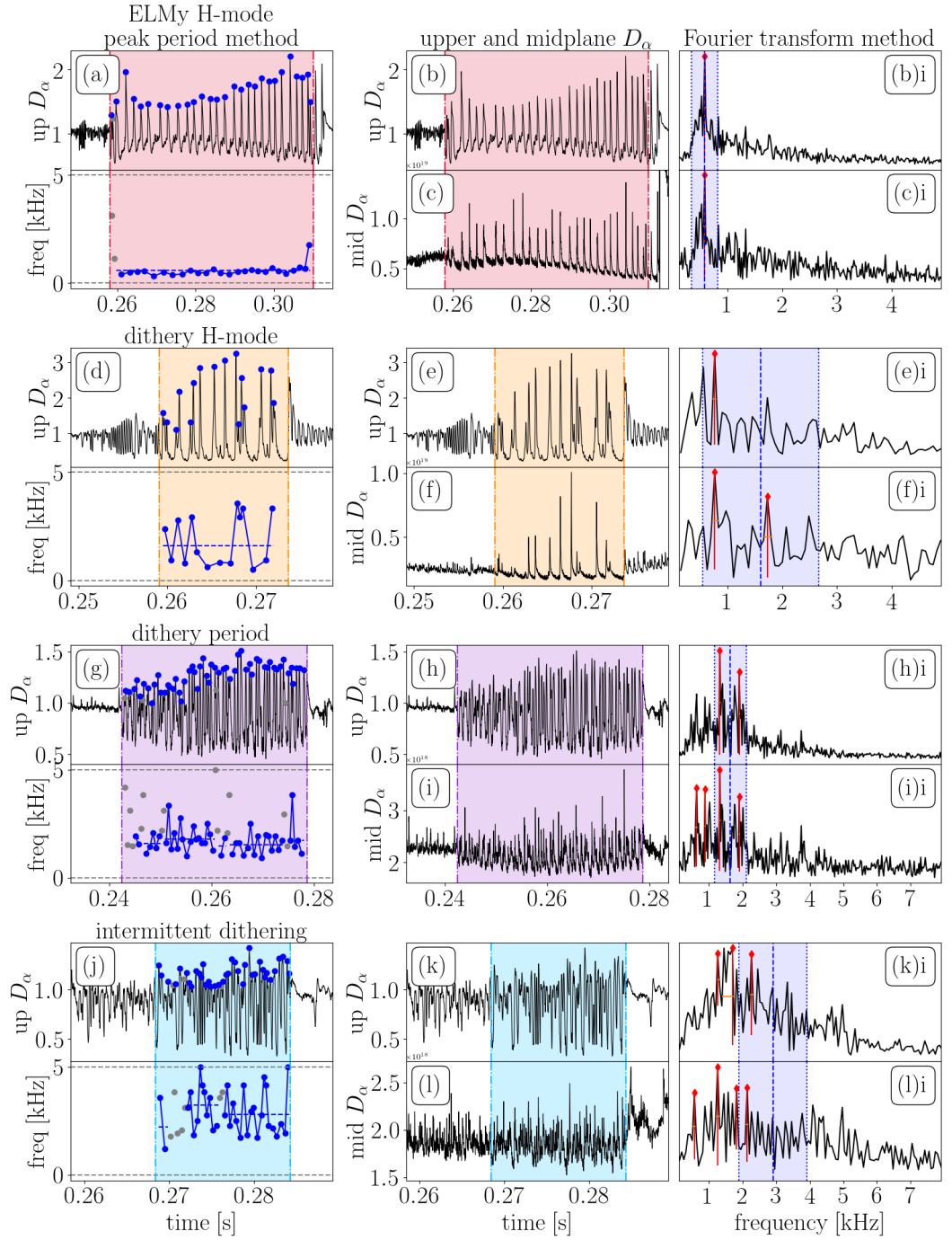


Figure 3.4: Example plots for the two methods of determining frequencies present in  $D_\alpha$  signals for an ELMy H-mode ((a)-(c)i), a dithery H-mode ((d)-(f)i), a dithery period ((g)-(i)i) and intermittent dithery ((j)-(l)i). The first method, which involves averaging over the time delay between peaks in the signal, is shown in the first column. The second column compares the time signals of upper and midplane  $D_\alpha$  and the third column shows the second method for both signals, which involves taking the Fourier transform and identifying the peaks in the frequency spectrum. The blue lines and shaded region in the spectra show the frequencies and standard deviation found in the first method, based on the accepted peaks shown in blue in the first column, while the spectral peaks are shown in red.

### 3.4.1.1 Fluctuation frequency

One of the most obvious differences between the categories can be seen in the frequency of the  $D_\alpha$  fluctuations. I-phases have the highest frequency oscillation, dithery periods have very irregular fluctuations, while the ELMs present in H-modes have the highest amplitude and lowest frequency. The frequencies of  $D_\alpha$  fluctuations can be found either by considering the period between individual peaks directly in the  $D_\alpha$  signal or by identifying the peaks in the frequency spectrum of the  $D_\alpha$  signal. Example plots for how the two methods determine frequencies for different categories are shown in Figures 3.3 and 3.4. For both methods, the time trace of the  $D_\alpha$  signal is first divided into time periods relevant to the particular categories. For the first method (shown in the first column in Figures 3.3 and 3.4), the intensity peaks in the time period are identified and the time delay between them is measured. First all peaks are identified (plotted in grey in Figures 3.3 and 3.4), then peaks are accepted based on the peak prominence (relative amplitude) (the prominent peaks are plotted in blue in the figures), and the time delay between peaks is measured if at least three consecutive peaks are accepted. The prominence of the peaks is then used in inverse form as weights to calculate a weighted average and standard deviation of the time delay. The fluctuation frequency corresponding to those peaks is then calculated from the inverse of the time delay. This method will generally give smaller uncertainties on time periods with a regular time delay, while those with very irregular fluctuations will have a large uncertainty. In the second method (shown in the second and third column in Figures 3.3 and 3.4 for both upper and midplane  $D_\alpha$ ), a Fourier Transform (FT) is computed for the same time periods, resulting in a frequency spectrum for each time period (third column). The peaks in the spectrum can then be identified, along with the full width half maximum (FWHM) as the width of each peak. Most I-phases and ELMy H-modes have one clear peak in the spectrum, but some cases, along with many of the dithery periods, have multiple peaks of similar heights. In those cases, a weighted average of the frequency peaks is calculated with the peak heights taken as weights, and an uncertainty is calculated by considering the frequency range of the peaks.

The frequencies computed by each method can be compared for the different categories, with the results shown in Figure 3.5a-d. The I-phase and ELMy H-mode frequencies generally agree quite well. The uncertainty on the I-phase frequencies is quite small for the first method, since the fluctuations are fairly regular, but can be larger for the second (FT) method

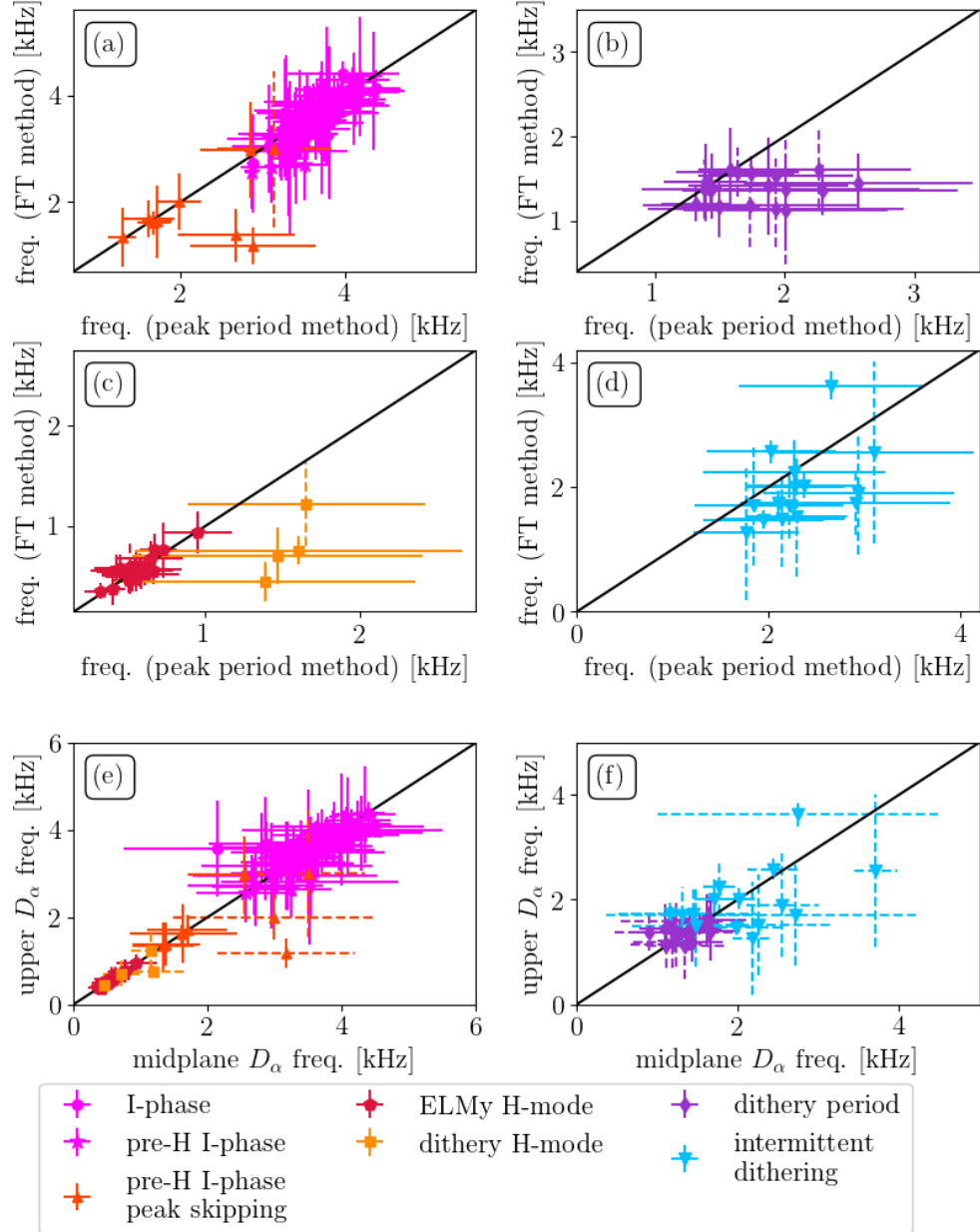


Figure 3.5: (a)-(d) Comparison of frequencies estimated for behaviour categories with two different methods, with the first method (averaging the period between the  $D_\alpha$  peaks) on the x-axis and the second method (identifying peaks in the frequency spectrum) on the y-axis. Dashed error bars signify averaging over multiple peaks in the spectrum. (e)-(f) Comparison of frequencies found in the spectra of tangential midplane  $D_\alpha$  (x-axis) and upper divertor  $D_\alpha$  (y-axis). Dashed error bars signify averaging over multiple peaks in the spectrum.

when the time periods are quite short and the frequency resolution therefore low, leading to a larger peak width, such as in Figure 3.3b)i. In Figure 3.3, the effect of the peak skipping behaviour present in some pre-H I-phases can be seen when comparing panels (g) and (j), or (h)i and (k)i, which show the initial and final stages of the pre-H I-phase for shot 27452. The initial stage of the I-phase has a clear 4kHz frequency in both methods, while the peak skipping stage can be seen in the lower average frequency with larger uncertainty and multiple peaks in the frequency spectrum. For the dithery H-modes, the first method computes larger frequencies than those for ELMy H-modes, with very large uncertainties, reflecting the irregular nature of those H-modes. In the second method by contrast, the dithery H-modes are mostly indistinguishable from ELMy H-modes in frequency and uncertainty. As can be seen in Figure 3.4, the spectra for dithery H-modes do differ from those of ELMy H-modes, with less power in the main frequency peak and additional higher frequencies present. The spectra suggest that the fundamental ELM frequency in the dithery H-modes agrees with the ELM frequency of ELMy H-modes, but the dithery nature with double or triple ELMs introduces additional higher frequencies. Dithery periods in the first method have a range of frequencies (1.3-2.7kHz) with large uncertainties, while in the second method they are confined to a smaller frequency range (1.1-1.7kHz) with slightly reduced uncertainties. Both dithery periods and to a larger extent intermittent dithering have spectra with multiple frequency peaks, leading to larger uncertainties in the second method. These are marked as dashed error bars in Figure 3.5.

While the upper  $D_\alpha$  signal is used throughout this work due to the lower noise level and clear I-phase oscillation features, the tangential midplane  $D_\alpha$  signal was also checked to verify that the results agree. As mentioned earlier in this chapter, the I-phase fluctuations have a different appearance in the two signals, sine-like in the upper  $D_\alpha$  and miniature ELM-like in the midplane  $D_\alpha$  (shown in Figure 3.3), but the frequency results are generally in good agreement with each other, as can be seen in Figure 3.5e-f.

#### 3.4.1.2 Skewness and kurtosis

In addition to the fluctuation frequency, the  $D_\alpha$  signals of the different categories can be described through their skewness and kurtosis. Skewness  $S$  and kurtosis  $K$  are the third and

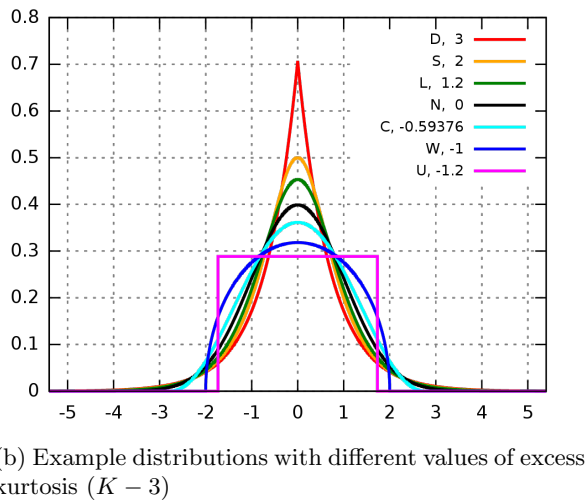
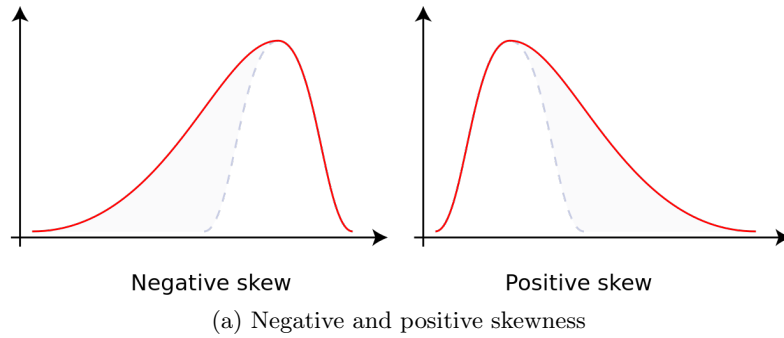


Figure 3.6: (a) Representations of distribution functions with negative and positive skewness  $S$ . (b) A few representative unimodal, symmetric distributions with a mean and skewness of zero, with parameters chosen to result in a variance of 1 for each case, are shown here for decreasing values of excess kurtosis ( $K - 3$ ). The numbers in the legend represent the values of excess kurtosis, while the letters in front represent the type of distribution (e.g. L for logistical, N for normal and U for uniform).

fourth standardised moments of the distribution function,

$$S = \frac{\langle (X - \mu)^3 \rangle}{\sigma^3} \quad (3.5)$$

$$K = \frac{\langle (X - \mu)^4 \rangle}{\sigma^4} \quad (3.6)$$

and describe its asymmetry and “tailedness” respectively. Figure 3.6 shows representations of skewness and (excess) kurtosis ( $K - 3$ ) for different cases.

ELMy H-mode periods have strong positive skewness and kurtosis, though both are reduced when the ELM frequency increases. I-phases are clustered close to zero skewness in the upper  $D_\alpha$  signal, reflecting their more symmetrical sine-like shape. The three categories of dithery behaviour are separated in skewness, with dithery H-modes at positive skewness values and the skewness growing more negative as the confinement decreases, with intermittent dithering at the lowest skewness values. While the categories are well separated in the  $f - S$  parameter space (Figure 3.7a), they are not easily distinguishable in kurtosis (Figure 3.7c). The categories can also be plotted in the  $S - K$  space (Figure 3.7b), where they can be fitted with a quadratic polynomial as  $K = 1.52S^2 - 0.24S + 1.75$ . Mathematically, any  $S - K$  relationship must be greater than  $K > S^2 + 1$ , with the minimum plotted in a dashed line. If the categories are not related, there is no a priori reason to expect a good fit in  $S - K$  since the values do not push against the minimum. Comparing the  $S - K$  relation of the data with selected Pearson distributions (Figure 3.7d) shows that they overwhelmingly lie in the parameter space of beta (I) distributions.

### 3.4.2 Point selection

To produce a  $P_{\text{loss}}(\bar{n}_e)$  plot, timepoints must be chosen to represent the categories and shots. For I-phases and dithery periods with clear transitions visible in  $D_\alpha$  data, the transition from L-mode to I-phase or L-mode to dithery period is chosen. Transitions from L-mode to intermittent dithering are generally more blurry, with the  $D_\alpha$  fluctuation level gradually rising, rather than a sharp change in features, so the timepoint selection is more uncertain. For L-mode points, no transition occurs, so the timepoint is chosen to reflect a fairly steady-state period, with no sudden changes in density or  $P_{\text{loss}}$  components, and only the time periods after the establishment of the connected double null configuration are considered. For H-modes, the transition time is chosen. This is simple for those shots which transitioned

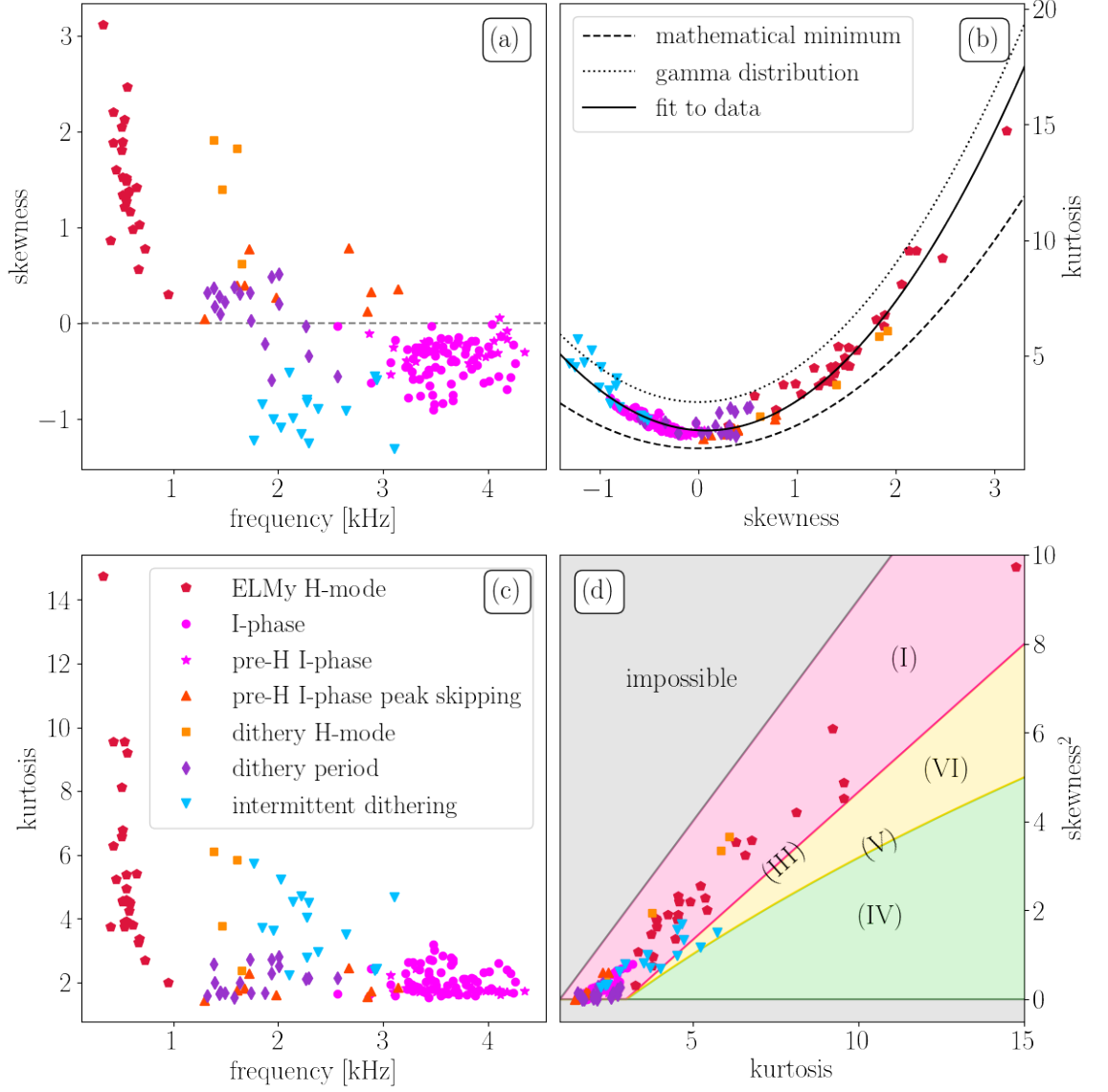


Figure 3.7: For the individual upper  $D_\alpha$  time periods of the categories, the fluctuation frequency  $f$ , skewness  $S$  and kurtosis  $K$  were determined. The panels show the (a)  $f - S$ , (b)  $S - K$ , (c)  $f - K$ , and (d)  $K - S^2$  relationships. Also plotted in panel (b) are the mathematical minimum of the S-K relationship (dashed) and that of a gamma distribution (dotted), as well as a quadratic least squares fit to the data points (solid line). Panel (d) shows the parameter spaces of selected Pearson distributions: (I: beta, III: gamma, VI: beta prime or F, V: inverse gamma). The categories are almost entirely located in the beta distribution space.

directly from L- to H-mode, but for those which transitioned through one or more pre-H I-phase periods the picture is slightly more complicated. For shots with an L→I→H transition, there are two potential transitions to consider, the L→I and the I→H transition (I in this case refers to the I-phase). In some cases, for example Figure 3.2b, there is a somewhat continuous transition from pre-H I-phase into H-mode through a period in which I-phase peaks in  $D_\alpha$  are skipped in regular intervals, reducing the frequency and increasing the amplitude to an intermediate stage between those of I-phases and ELMs. This feature highlights the connection between the I-phase and the subsequent H-mode period. This picture is consistent with studies of I-phases or LCOs on ASDEX Upgrade, which have shown that the I-phase contains many H-mode characteristics and proposed that the L- to I-phase transition is more relevant to L-H studies than the I-phase- to H-mode transition [83]. Another way in which the pre-H I-phase appears to signal the beginning of the H-mode transition is through the stored energy  $W$ . The rise in stored energy  $W$  due to the improved energy confinement is a feature of H-mode operation. As can be seen in Figure 3.1e,  $W$  begins increasing at the start of the pre-H I-phase, as the average confinement increases due to the intermittent periods of improved confinement.

For the results in this thesis, the transition time is taken as the L-mode→I-phase transition for H-modes with a preceding I-phase, and the L-mode→H-mode transition for those without an I-phase. Section 3.5.5 briefly presents the impact of using the I-phase→H-mode transition instead.

### 3.5 Density dependence of $P_{LH}$ on MAST

For each transition or equivalent L-mode point, the loss power  $P_{\text{loss}}$  is plotted against the line-averaged density  $\bar{n}_e$ , with the main results of this study shown in Figure 3.8.

The boundary separating the H-mode and L-mode regions reveals a similar non-monotonic U-shaped density dependence as seen on other devices (e.g. JET [32], C-Mod [33], ASDEX Upgrade [42], HL-2A [43]). H-modes are sparse in the density range below  $2.5 \times 10^{19} \text{m}^{-3}$ , but the minimum of the  $P_{LH}$  curve,  $n_{e,\text{min}}$ , appears to lie in the region of  $2 - 2.5 \times 10^{19} \text{m}^{-3}$  with a minimum  $P_{LH}$  of around 2MW. H-modes above  $2.5 \times 10^{19} \text{m}^{-3}$  are ELMy, with no or short pre-H I-phases, while H-modes below this density have longer pre-H I-phases or are dithery. I-phases with no subsequent H-mode are found at the  $P_{LH}$  boundary in a wide

range for  $\bar{n}_e > 1.6 \times 10^{19} \text{m}^{-3}$ . Dithery periods are located on the low-density branch, in a narrower density range of  $1.2 \times 10^{19} \text{m}^{-3} < \bar{n}_e < 2 \times 10^{19} \text{m}^{-3}$  but a wider  $P_{\text{loss}}$  range, reflecting the steep increase or gradient in the low-density branch. Due to the lack of low-density H-modes, the dithery periods were utilised to define the  $P_{LH}$  boundary in the low-density branch. Intermittent dithery is found at lower powers than the clear dithery periods, presumably further away from  $P_{LH}$ . L-modes are ubiquitous both at very low densities and at higher densities and lower powers, but it is harder to achieve lasting L-modes around  $n_{e,\text{min}}$ , especially without considering purely ohmically heated shots.

### 3.5.1 Fit to data

The H-mode control technique of keeping  $\delta r_{\text{sep}}$  high initially, along with the limited ability to scan the NBI power, results in a large scatter in H-mode points on the  $P_{\text{loss}}(\bar{n}_e)$  plot, as  $P_{\text{loss}}|_{t=t_{LH}} \geq P_{LH}$  rather than  $= P_{LH}$ . More details of how this impacts the results is described in Section 3.5.4, but for the purpose of the high-density branch fit to find an equation for  $P_{LH}$ , only points close to the boundary between the L-mode and H-mode data points were considered, so those H-modes with  $P_{\text{loss}}$  much greater than values for transitions at similar densities were excluded. The data in the high density branch ( $\bar{n}_e > 2.4 \times 10^{19} \text{m}^{-3}$ ) close to the  $P_{LH}$  boundary was fit with two free parameters, as  $P_{LH} = \alpha \times \bar{n}_{e20}^\gamma$ , with  $\alpha$  containing all other parameter dependencies aside from the density, which were kept consistent between discharges. Using the Python function *scipy.optimize.curve\_fit*, i.e. non-linear least squares to fit the function above to the  $\bar{n}_e$  and  $P_{\text{loss}}$  values of the included data points, the equation for the line of best fit (shown in Figure 3.8) with a one standard deviation error on the two parameters  $\alpha$  and  $\gamma$  was found to be

$$P_{LH} = (11.35 \pm 2.30) \times \bar{n}_{e20}^{(1.19 \pm 0.16)} \quad (3.7)$$

with the goodness of fit represented by  $R^2 = 0.66$ . The low density branch plotted in Figure 3.8 is assumed to take the form of  $P_{LH} \sim 1/(\beta(\bar{n}_{e20} - \delta))$  with a range of values for  $\beta$  and  $\delta$  shown in the shaded area. The estimated  $P_{LH}$  line should represent the boundary between H-mode-accessible and -inaccessible regions, so for the high-density branch both H-mode and L-mode points close to the boundary were included in the fit estimation. For the low-density branch fit, as the boundary region is more diffuse and there is no generally

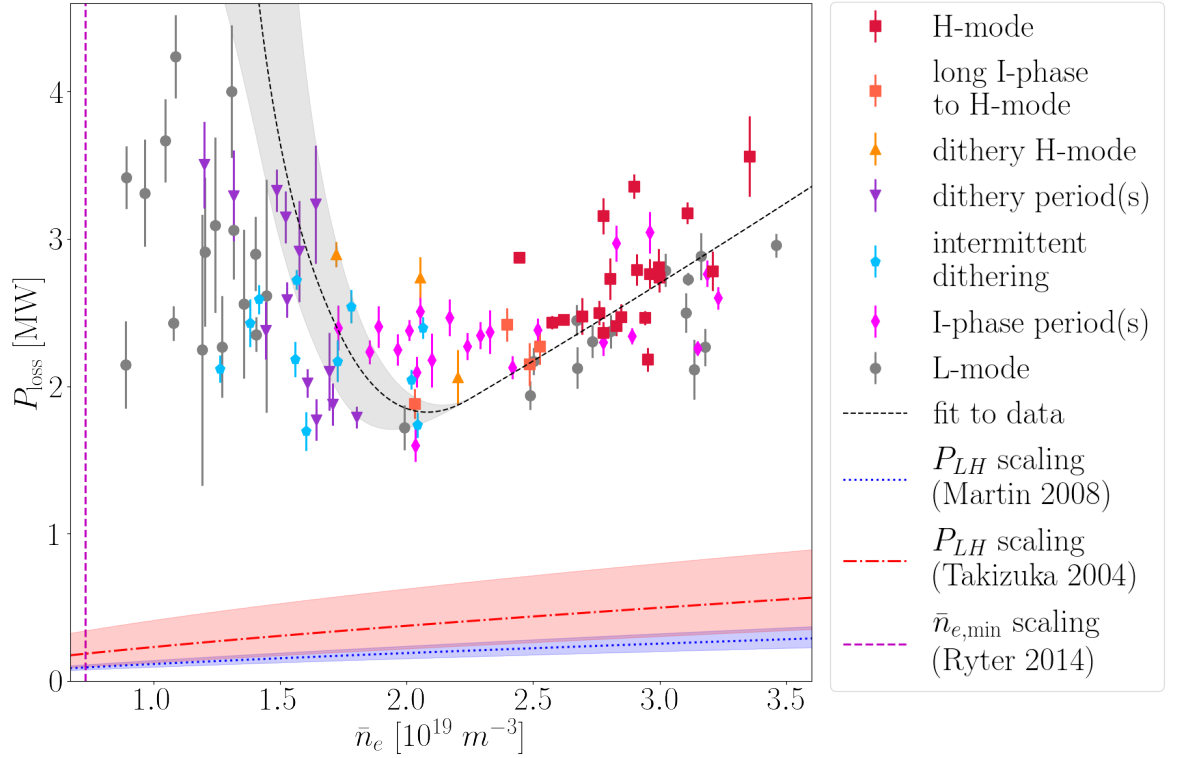


Figure 3.8:  $P_{\text{loss}}$  ( $P_{\text{loss}}^{\text{TR}}$ , using  $P_{\text{ohm}}^{\text{TR}}$  and  $P_{\text{cap}}^{\text{NBI}}$ ) with the  $P_{LH}$  ITER scaling from Martin et al. and the low-aspect ratio modified version from Takizuka et al. The uncertainty range on the scalings include the uncertainty from the scaling law itself and the range in the included parameters for the shots studied here. The black dashed line is the fit performed for the data set. The magenta vertical line shows the projected  $\bar{n}_{e,\text{min}}$  from the scaling in Section 3.6. For H-mode points with a pre-H I-phase, the transition time is taken at the start of the last I-phase immediately preceding the H-mode period, while for those without a pre-H I-phase the points are chosen at the transition from L- to H-mode. For dithery periods and I-phases, the times are taken at the transition from L-mode to each respective regime, while L-mode points are taken at times where the plasma is in a relatively steady state and comparable to the points of the other categories.

expected expression for the relationship, the fit expression and uncertainty range were estimated by trialling different combinations of a range of values for  $\beta$  and  $\delta$ . The low-density branch of the fit line shown in Figure 3.8 is estimated as  $P_{LH} \sim 1/(6.0(\bar{n}_{e20} - 0.1))$  with the uncertainty region shown for  $5.0 \leq \beta \leq 10.0$  and  $0.08 \leq \delta \leq 0.12$ .

### 3.5.2 Comparison with scaling laws

Several empirical scaling laws for  $P_{LH}$  have been derived from large multi-machine databases, including the widely used ITER scaling from Martin et al. [40] (Equation 1.15). This scaling is not well suited to spherical tokamaks such as MAST and NSTX, though some attempts have been made to adjust it accordingly, for example by Takizuka et al. [80]

$$P_{LH}^T = 0.072 |B|_{out}^{0.7} \bar{n}_{e20}^{0.7} S^{0.9} \left( \frac{Z_{eff}}{2} \right)^{0.7} \frac{0.1A}{1 - \left( \frac{2}{1+A} \right)^{0.5}} \quad (3.8)$$

where  $B_T$  has been replaced by the absolute  $B$  at the outer midplane of the separatrix,

$$|B|_{out} = \left( \left( \frac{B_T \times A}{A+1} \right)^2 + \left( \frac{\mu_0 I_p}{2\pi a} \times (1 + A^{-1}) \right)^2 \right)^{0.5} \quad (3.9)$$

taking into account the aspect ratio  $A$ , plasma current  $I_p$  and minor radius  $a$ . Correction factors for the effective charge  $Z_{eff}$  and aspect ratio, with a factor proportional to the fraction of untrapped particles, have also been added.

Using the values for the MAST dataset of this project (listed in Table 3.2) for the parameters in Equations 1.15 and 3.8, both scaling laws were compared with the data, and as can be seen in Figure 3.8, the observed  $P_{LH}$  is at least an order of magnitude higher than that predicted by either scaling law. To directly compare with the fit of Equation 3.7, the scaling laws for the parameters of this MAST study can be written as  $P_{LH}^M = 0.601 \times \bar{n}_{e20}^{0.717}$  and  $P_{LH}^T = 1.156 \times \bar{n}_{e20}^{0.7}$ . The density dependence of the fit (Equation 3.7) has a 66% higher exponent than the scaling laws. The large discrepancy between the data and the scaling laws is mostly due to the leading factor (which includes other parameter dependencies). From the dataset analysed in this work, it is impossible to pinpoint where the discrepancy comes from, therefore further studies of other parameters and their effects on  $P_{LH}$ , as well as comparison with other spherical tokamaks are needed to illuminate the issue further. As STs usually operate in double null configuration, and the conventional tokamak database for

Parameter	MAST [ITPA]	MAST [this project]
Dates of data collection	2001 – 2003	2011 – 2013
First wall material	Stainless steel	C (graphite)
Divertor design	Ribbed	Fan-shaped tiles (MID)
Major radius $R_0$ [m]	0.74 – 0.89	0.85
Minor radius $a$ [m]	0.48 – 0.62	0.65
Aspect ratio $A$	1.4 – 1.6	1.3
Plasma current $I_p$ [MA]	0.5 – 0.65	0.72 – 0.76
Toroidal magnetic field $B_T$ [T]	0.42 – 0.63	0.5 – 0.6
Elongation $\kappa$	1.64 – 2.02	1.73 – 1.83
Triangularity $\delta$	0.27 – 0.5	0.46 – 0.49

Table 3.2: Some of the differences between the MAST dataset used in the Takizuka scaling (ITPA) and that used in this project.

scaling laws is based on single null geometries, the difference in  $P_{LH}$  could also be due to the configuration, rather than inherent differences in STs themselves.

The limited understanding of how divertors and configurations affect  $P_{LH}$  especially for STs clearly demonstrates the need for more studies in this field. Additionally, as some heating methods primarily heat one channel or species (e.g. electrons for ECRH), and the ion heat flux is thought to be a critical L-H transition parameter (e.g. [1]), the heating method will likely result in further differences in the L-H transition behaviour. Some of the effects of different heating methods on L-H transitions are discussed in Chapter 4.

### 3.5.2.1 Comparison with MAST data from ITPA database

The Takizuka scaling was developed to improve the  $P_{LH}$  prediction for STs and included sample data sets from both MAST and NSTX, which were then found to fit the new scaling law much better. Some key differences between the MAST data used by Takizuka and the data set analysed in this project are listed in Table 3.2 and could account for the discrepancy in the performance of the Takizuka scaling. The data set used by Takizuka (from now on referred to as the ITPA dataset, as it was used by the H-mode working group of the International Tokamak Physics Activity (ITPA) in the development of the scaling laws) consists of 14 L-H transitions from 2001, one from 2002, and five from 2003. MAST underwent several

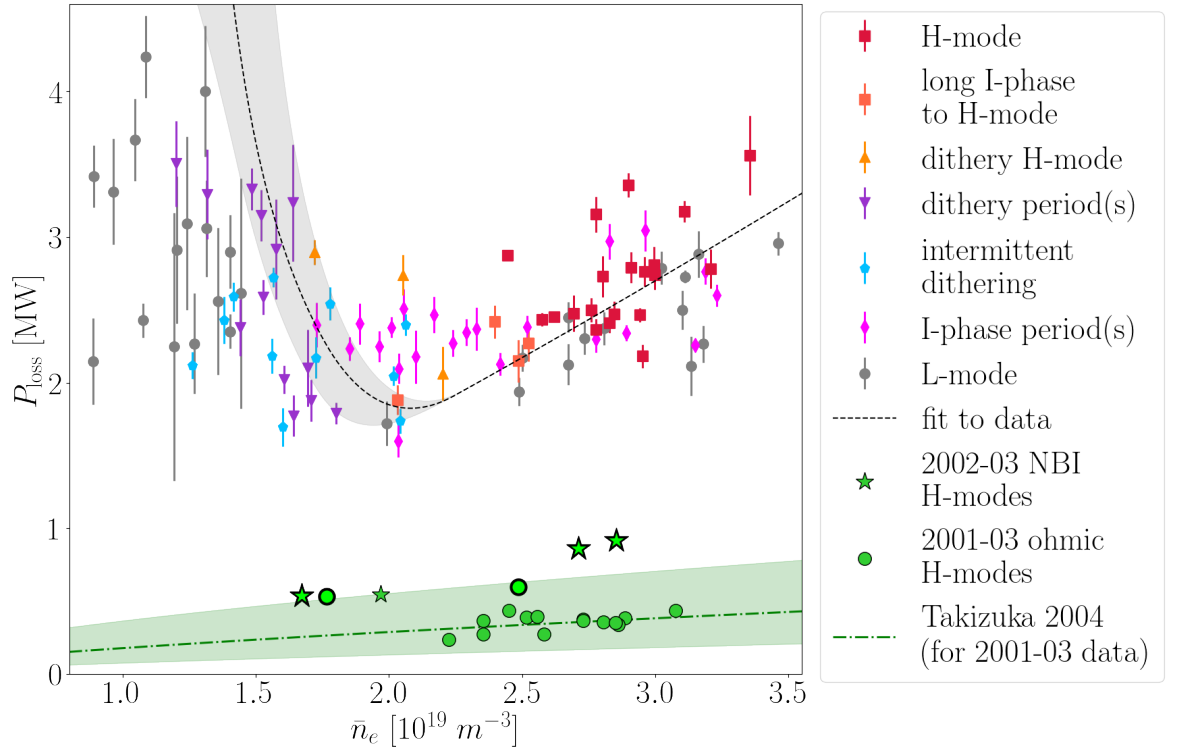


Figure 3.9:  $P_{\text{loss}}^{\text{TR}}$  vs  $\bar{n}_e$  results of this study, compared with the ohmic and NBI-heated H-modes used in the Takizuka scaling [80] (in green). The Takizuka scaling (Equation 3.8) is plotted for the MAST data from 2001-2003 (green dot-dashed line). Ohmic transitions are plotted as circles, NBI-heated transitions as stars, and the five Single-null transitions (three NBI-heated and two ohmic) are shown with larger marker size and thicker borders.

modifications and upgrades between then and the time of the new data set (2011-2013). The vessel for the ITPA data set was stainless steel, as opposed to the carbon wall found in the main data set used in this thesis. The divertor design was different, with the ribbed divertor replaced by the updated MAST improved divertor (MID) with fan-shaped tiles in late 2003 [49]. The MID led to an increase in  $P_{LH}$ , seen as well in the reduction in frequency of ohmic H-modes after its installation. Sixteen of the L-H transitions in the ITPA database were ohmic H-modes, while four were NBI-heated. The magnetic field, major and minor radius and plasma current were all smaller for the ITPA dataset (0.42T, 0.77m, 0.53m, 630kA vs 0.55T, 0.85m, 0.65m, 740kA), and the elongation (1.9 vs 1.78) and triangularity (0.38 vs 0.48) were slightly different as well. Five of the shots in the ITPA database were in a Single-null configuration, while the rest were in Double-null. Figure 3.9 shows the MAST H-modes used in the Takizuka scaling plotted in green alongside the  $P_{\text{loss}}^{\text{TR}}$  data from the MAST study analysed in this project, while the green line shows the Takizuka scaling using

parameters from the ITPA dataset (as seen in Table 3.2). The ITPA data lies very close to the scaling, with the transitions furthest away from it being either NBI-heated (stars) or Single-null (larger markers with thicker border). While at first glance this appears to suggest that SN transitions have a higher  $P_{LH}$  than DN transitions, this data set is too small to draw any conclusions about  $P_{LH}$  for DN vs SN, especially since there is such an overlap between NBI-heated and SN transitions.

### 3.5.3 Alternative $P_{\text{net}}$ definitions

While all other plots show the results for  $P_{\text{loss}}^{\text{TR}} = P_{\text{ohm}}^{\text{TR}} + P_{\text{cap}}^{\text{NBI}} - dW/dt$ , the impact of using the EFIT estimate of  $P_{\text{ohm}}$ , as well as the results for  $P_{\text{sep}}$  (i.e. subtracting the radiated power as well) were investigated and are compared with the main results for  $P_{\text{loss}}^{\text{TR}}$  in this section.

#### 3.5.3.1 Use of EFIT for $P_{\text{ohm}}$

As obtaining TRANSP runs was unsuccessful for some shots in the database, the results for a second method for the calculation of  $P_{\text{loss}}$ , which uses the ohmic power estimated by EFIT, were checked and compared against the TRANSP results, with one comparison shown in Figure 3.10. To enable the inclusion of all shots in the database, even those without TRANSP runs, this EFIT method  $P_{\text{loss}}^{\text{EF}}$  uses the injected power as the NBI power, i.e.  $P_{\text{NBI}} = P_{\text{inj}}^{\text{NBI}}$  instead of the TRANSP-calculated captured power  $P_{\text{cap}}^{\text{NBI}}$ . Especially at low densities  $P_{\text{inj}}^{\text{NBI}}$  is expected to be an overestimate, as can be seen in the larger spread in  $P_{\text{loss}}^{\text{EF}}$  values for low densities in Figure 3.10 compared with e.g. Figure 3.8 or 3.9. While generally the TRANSP method is  $P_{\text{loss}}^{\text{TR}} = P_{\text{ohm}}^{\text{TR}} + P_{\text{cap}}^{\text{NBI}} - \frac{dW}{dt}$ , both panels in Figure 3.10 show the results of a  $P_{\text{loss}}$  calculation using  $P_{\text{NBI}} = P_{\text{inj}}^{\text{NBI}}$  so that the only difference between them is that Figure 3.10a uses  $P_{\text{ohm}}^{\text{TR}}$  and Figure 3.10b uses  $P_{\text{ohm}}^{\text{EF}}$ , highlighting the effect of the different  $P_{\text{ohm}}$  values explicitly. No significant qualitative difference in the  $P_{LH}$  curve is seen between the TRANSP and EFIT methods, but the fit to the high density branch is modified slightly,

$$\text{TRANSP method} \left( P_{\text{ohm}}^{\text{TR}} + P_{\text{cap}}^{\text{NBI}} - \frac{dW}{dt} \right): P_{LH}^{\text{TR}} = (11.35 \pm 2.30) \times \bar{n}_{e20}^{(1.19 \pm 0.16)} \quad (3.10)$$

$$\text{EFIT method} \left( P_{\text{ohm}}^{\text{EF}} + P_{\text{inj}}^{\text{NBI}} - \frac{dW}{dt} \right): P_{LH}^{\text{EF}} = (10.41 \pm 2.20) \times \bar{n}_{e20}^{(1.09 \pm 0.17)} \quad (3.11)$$

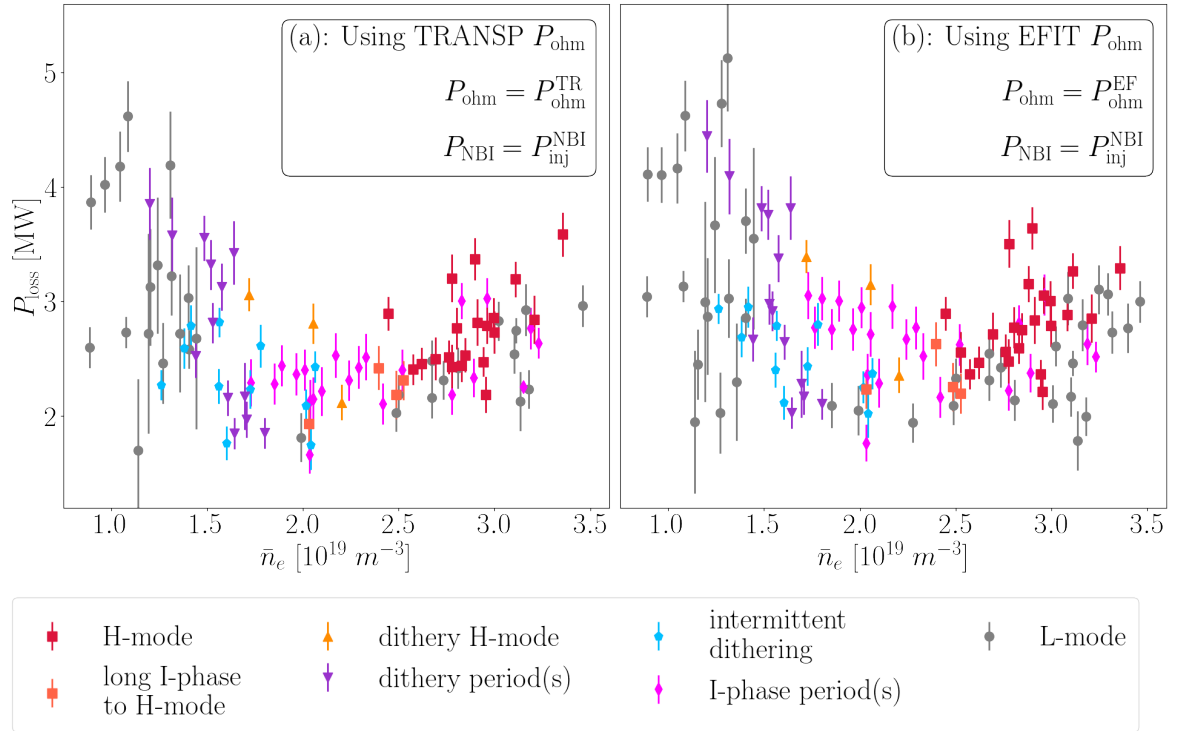


Figure 3.10:  $P_{\text{loss}}$  vs  $\bar{n}_e$  using (a) TRANSP and (b) EFIT to calculate  $P_{\text{ohm}}$ . Using EFIT to estimate  $P_{\text{ohm}}$  enables the inclusion of shots for which TRANSP runs were not successfully completed, so  $P_{\text{NBI}}$  in the  $P_{\text{loss}}^{\text{EF}}$  (EFIT method) calculation simply corresponds to the injected beam power  $P_{\text{inj}}^{\text{NBI}}$ . To show the effect of the two  $P_{\text{ohm}}$  options explicitly,  $P_{\text{inj}}^{\text{NBI}}$  is also used for the TRANSP plot in (a), although the TRANSP method generally ( $P_{\text{loss}}^{\text{TR}}$ ) uses  $P_{\text{cap}}^{\text{NBI}}$ .

although both fit parameters are still within one standard deviation of one another between the two methods.

### 3.5.3.2 Correcting for $P_{\text{rad}}$ (comparison of $P_{\text{sep}}$ and $P_{\text{loss}}$ )

The net power  $P_{\text{net}}$  can be defined as the loss power  $P_{\text{loss}}$ , which is most commonly used in power threshold studies and throughout this thesis, or as the power crossing the separatrix  $P_{\text{sep}}$ , which is additionally corrected for radiated power losses  $P_{\text{rad}}$ . The results for  $P_{\text{sep}}$  are shown for one example plot only in Figure 3.11a compared with the results for  $P_{\text{loss}}^{\text{TR}}$ . As  $P_{\text{sep}}$  is calculated by subtracting  $P_{\text{rad}}$  from  $P_{\text{loss}}$ , the values are all reduced.  $P_{\text{rad}}$  has a slight density dependence, ranging from  $\sim 0.2\text{MW}$  at  $\bar{n}_e \sim 1.0 \times 10^{19}\text{m}^{-3}$  to  $\sim 0.43\text{MW}$  at  $\bar{n}_e \sim 3.5 \times 10^{19}\text{m}^{-3}$ , as shown in Figure 3.11b, but the qualitative picture of the  $P_{\text{LH}}$  curve

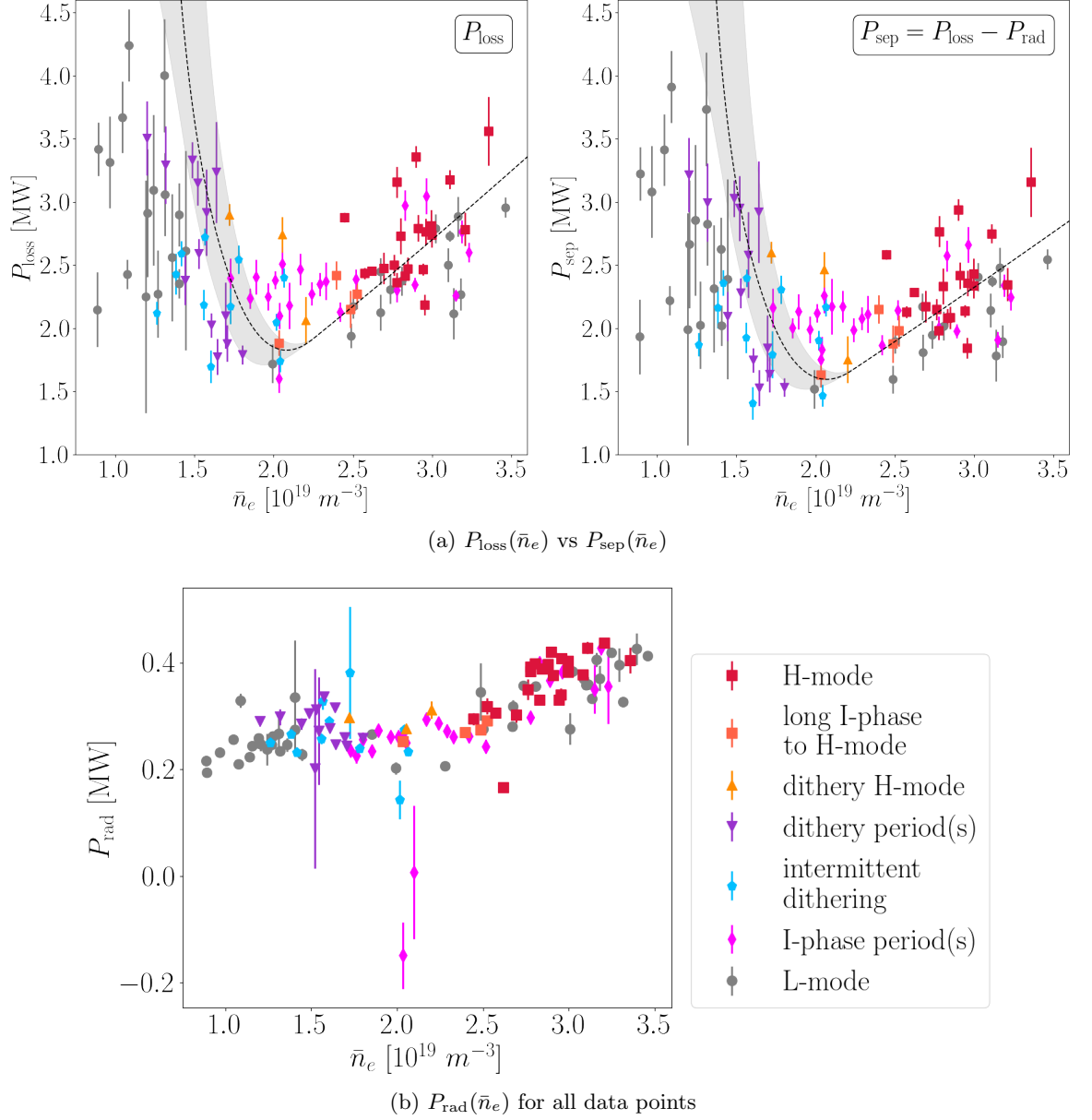


Figure 3.11: (a)  $P_{\text{loss}}(\bar{n}_e)$  compared with  $P_{\text{sep}}(\bar{n}_e)$ , showing the effect of subtracting  $P_{\text{rad}}$  as  $P_{\text{sep}} = P_{\text{loss}} - P_{\text{rad}}$ . (b) Radiated power loss  $P_{\text{rad}}$  from bolometer data (with error bars representing oscillations in time) of all studied transitions or other chosen time points plotted against density  $\bar{n}_e$ . Aside from occasional outliers from times of strong oscillations in  $P_{\text{rad}}$ , there appears to be a weak positive density dependence of  $P_{\text{rad}}$  independent of transition or regime type.

does not change. The fit to the high-density branch is changed to

$$\text{For } P_{\text{loss}}: P_{LH} = (11.35 \pm 2.30) \times \bar{n}_{e20}^{(1.19 \pm 0.16)} \quad (3.12)$$

$$\text{For } P_{\text{sep}}: P_{LH} = (8.94 \pm 2.17) \times \bar{n}_{e20}^{(1.12 \pm 0.19)} \quad (3.13)$$

but as the  $P_{LH}$  scaling laws are for  $P_{\text{loss}}$ , it does not make sense to compare them to this fit.

### 3.5.4 Impact of H-mode control through $\delta r_{\text{sep}}$

Since the H-mode control technique described in Chapter 2.4.1, along with the limited ability to scan the heating power during a discharge, results in  $P_{\text{loss}}|_{t=t_{LH}} \geq P_{LH}$  rather than  $= P_{LH}$ , the  $P_{LH}$  curve must be drawn to approximately separate the regions of the plot that contain H-modes (i.e. are H-mode accessible) from those that do not. The H-mode points show much scatter. Colour-coding to represent how soon after the drop in  $\delta r_{\text{sep}}$  the transition occurred makes the picture clearer. In Figure 3.12, the scale goes from yellow (L-H  $\sim$  0ms after drop) to red (L-H  $\geq$  30ms after drop). The points with  $P_{\text{loss}}$  much larger than the minimum  $P_{\text{loss}}$  found for H-modes in that density range generally show a shorter delay, and those with the longest delay appear to lie on or close to a potential  $P_{LH}$  curve.

### 3.5.5 Impact of transition time selection

As mentioned in Section 3.4.2, the results in this thesis are presented for the choice of L-mode  $\rightarrow$  I-phase transition as the transition time for H-modes with a preceding I-phase, or more generally the points for non-L-mode behaviour categories are chosen as the time of transition out of the L-mode phase. As an aside, Figure 3.13 shows the effect on  $P_{\text{loss}}(\bar{n}_e)$  of taking the second transition (I-phase  $\rightarrow$  H-mode) instead for H-modes with an I-phase. Due to the increase in density during the I-phase as well as the increase in stored energy which leads to a decrease in  $P_{\text{loss}}$ , the points are shifted to a different parameter space, and in the density range for most H-modes the new points overlap with the L-mode parameter space. For all other results and figures, the L-mode  $\rightarrow$  I-phase transition is chosen.

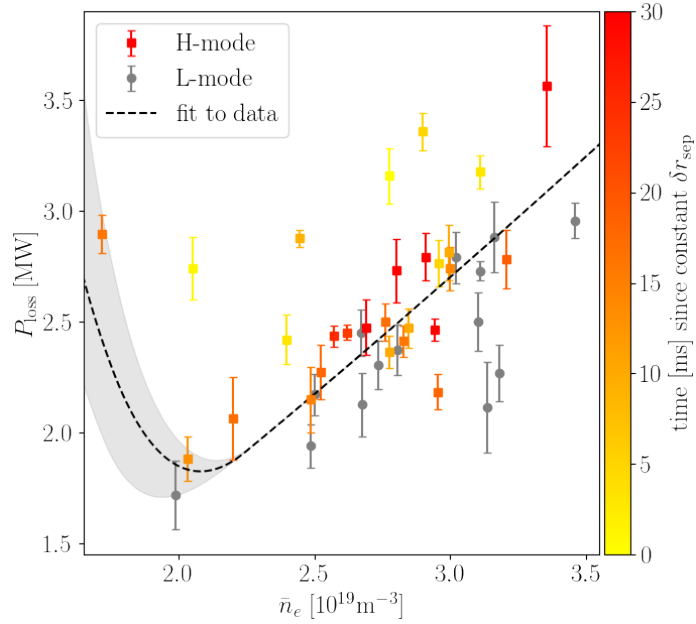


Figure 3.12:  $P_{\text{loss}}$  vs  $\bar{n}_e$  results for H-mode points (L-modes in grey), showing the time in ms between the beginning of the constant  $\delta r_{\text{sep}}$  region and the start of the H-mode period or the pre-H I-phase (if present). The colour bar has been restricted to 30 ms, though a number of points had values of 70 – 110ms. Points towards the yellow end of the spectrum have very little delay between reaching the desired configuration and entering H-mode, so their  $P_{\text{loss}}(\bar{n}_e)$  combination must be interpreted as being  $\geq P_{LH}$ , not simply  $= P_{LH}$ .

### 3.6 Comparison with $n_{e,\text{min}}$ scaling

In the density range between the high-density and low-density branches,  $P_{LH}$  occupies a minimum value. The density at which  $P_{LH}$  is minimal,  $n_{e,\text{min}}$ , is a useful measure for the description of the  $P_{LH}$  curve and the choice of experimental density ranges. For this dataset, the experimental value found for  $n_{e,\text{min}}$  appears to be around  $2 - 2.2 \times 10^{19} \text{ m}^{-3}$ . From experimental observations on ASDEX Upgrade of the ratio of energy confinement time  $\tau_E$  to electron-ion energy exchange time  $\tau_{ei}$ , where at minimum  $P_{LH}$  the energy confinement time  $\tau_E$  was nine times greater than the electron-ion energy exchange time  $\tau_{ei}$ , i.e.  $\tau_E/\tau_{ei} = 9$ , a scaling for  $n_{e,\text{min}}$ , was derived by Rytter et al. [1]

$$n_{e,\text{min}}^{\text{scal}} \simeq 0.7 I_p^{0.34} B_T^{0.62} a^{-0.95} (R_0/a)^{0.4} \quad (3.14)$$

in  $10^{19} \text{ m}^{-3}$ , using units of MA for the current  $I_p$ , T for the toroidal magnetic field  $B_T$  and m for the major and minor radii  $R_0$  and  $a$  respectively. This was derived by combining the

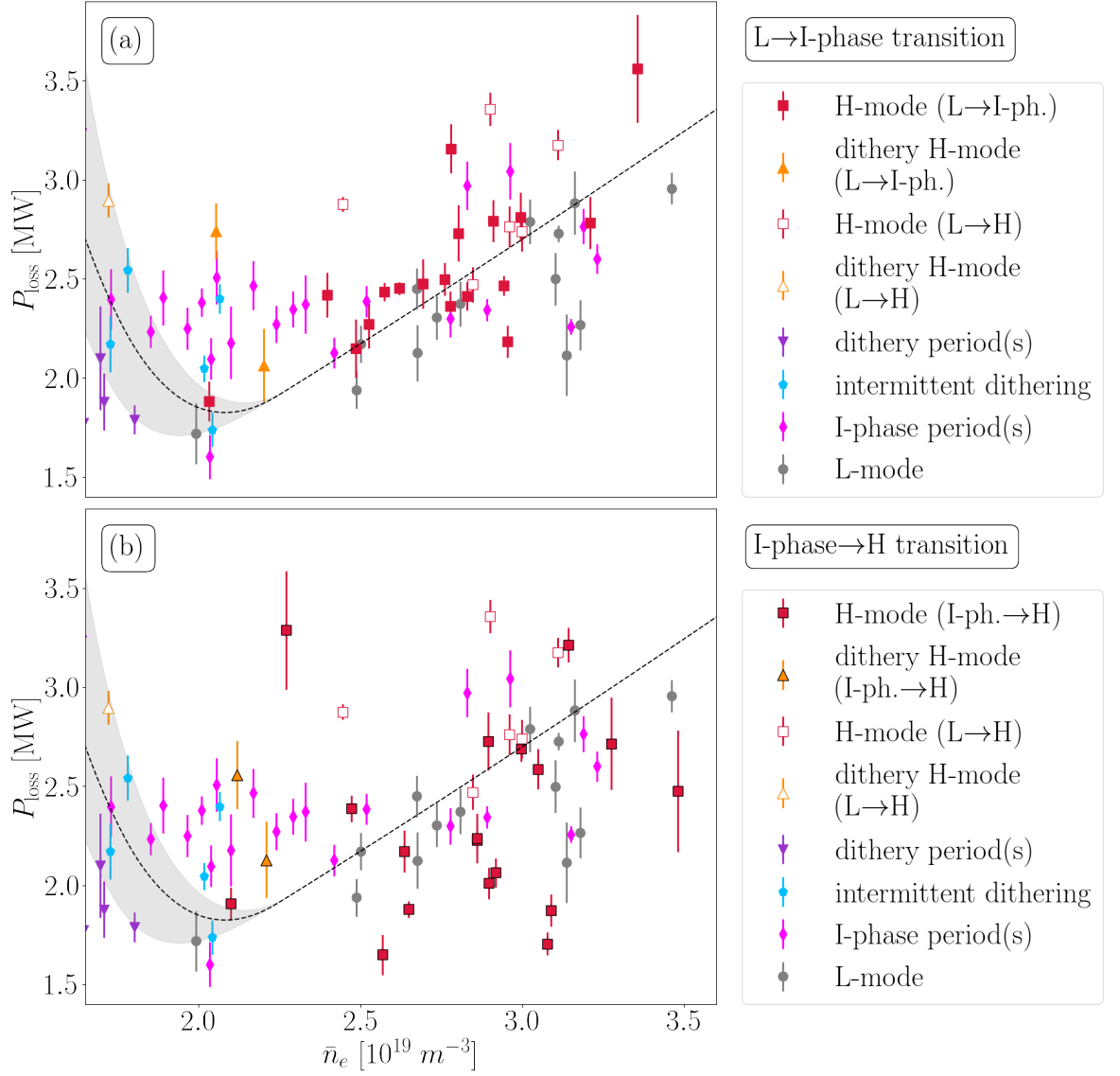


Figure 3.13:  $P_{\text{loss}}$  vs  $\bar{n}_e$  results showing the impact of the pre-H I-phase in the transition time selection for H-modes. L-mode, dithery and I-phase points are unchanged for both panels, and transitions directly from L- to H-mode without intermediate I-phases are marked with open symbols in both plots. Those H-mode transitions which do pass through an intermediate I-phase are plotted for  $t_{LH} = \text{L-mode} \rightarrow \text{I-phase}$  in (a) and  $t_{LH} = \text{I-phase} \rightarrow \text{H-mode}$  in (b). The fit plotted in both panels is for the method used in (a) (which is used as the transition time definition for all other figures, see e.g. Figure 3.8). Due to the increase in density and stored energy during the I-phase, I-phase→H-mode transitions (b) are located further into the L-mode parameter space.

Martin scaling (1.15) for  $P_{LH}$  with the L-mode confinement scaling from the 1997 ITER database [84],

$$\tau_{\text{th}} = 0.023 I_p^{0.96} B_T^{0.03} \kappa^{0.64} R_0^{1.83} (R/a)^{0.06} \bar{n}_e^{0.40} M_{\text{eff}}^{0.20} P^{-0.73}, \quad (3.15)$$

where  $M_{\text{eff}}$  is the effective mass in atomic mass units and  $P$  is the power in MW.

To test the validity of this expression for MAST, the value of  $n_{e,\text{min}}$  was calculated with the parameters of this experiment, returning  $n_{e,\text{min}}^{\text{scal}} = 0.73 \times 10^{19} \text{ m}^{-3}$ . This value is plotted as a magenta vertical line in Figure 3.8, and can clearly be seen to be a strong underestimate of the experimental  $n_{e,\text{min}}$  found for this dataset, and it is actually lower than the lowest density L-mode points. This could indicate that the density minimum of  $P_{LH}$  observed in this dataset involves a different physical mechanism than that observed on ASDEX Upgrade or other conventional tokamaks.

In order to see if modifying the Martin scaling to reflect the leading factor and density dependence of the MAST data improves the  $n_{e,\text{min}}$  prediction, I first re-evaluated the Ryter scaling in Equation 3.14 and then modified it with the inclusion of the adjusted  $P_{LH}$  scaling for the MAST dataset used in this thesis. Unless otherwise specified, the units of  $n_e$  are  $10^{19} \text{ m}^{-3}$ , and  $P$  is in MW.

### 3.6.1 Re-evaluating $n_{e,\text{min}}$ scaling

Inserting an estimate for the surface area of the plasma

$$S \approx 2\pi R_0 \times 2\pi \sqrt{\frac{a^2 + \kappa^2 a^2}{2}} = 4\pi^2 R_0 a \sqrt{\frac{1 + \kappa^2}{2}}$$

into the Martin scaling (Equation 1.15) gives

$$P = 0.2134 n_e^{0.72} B_T^{0.8} R_0^{0.94} a^{0.94} (1 + \kappa^2)^{0.47} \quad (3.16)$$

Ryter et al. used the fact that for their dataset, the electron-ion energy exchange time was  $\tau_{ei}^{\text{energy}} = \tau_E/9$  at minimum  $P_{LH}$ . We can estimate the electron-ion collision time as,

$$\tau_{ei} = 3.44 \times 10^{-8} \frac{1}{n_e \ln \Lambda} (T_e [\text{eV}])^{3/2} \quad (3.17)$$

and the electron-ion energy exchange time is related to the collision time through the mass ratio as [85]

$$\tau_{ei}^{\text{energy}} = \frac{m_i}{2m_e} \tau_{ei} = 3.44 \times 10^{-8} \left( \frac{m_i}{2m_e} \right) \frac{1}{n_e \ln \Lambda} (T_e[\text{eV}])^{3/2} \quad (3.18)$$

The energy confinement time is  $\tau_E = W/P$  (with  $P = P_{\text{loss}}$  being the loss power), and the stored energy in eV is  $W = \int 3n_e T_e dV$ , where  $T_e$  is in eV and  $n_e$  is in  $\text{m}^{-3}$ . Estimating the plasma volume as

$$V = 2\pi R_0 \times \pi a \times \kappa a = 2\pi^2 \kappa a^2 R_0 \quad (3.19)$$

and converting the units of  $P$  to MW and  $n_e$  to  $10^{19} \text{ m}^{-3}$ , we can find an approximate expression for  $T_e$  in eV,

$$T_e[\text{eV}] = 1.0541 \times 10^4 \frac{\tau_E P}{\kappa a^2 R_0 n_e} \quad (3.20)$$

which we can then insert into the expression for  $\tau_{ei}^{\text{energy}}$  (Equation 3.18),

$$\tau_{ei}^{\text{energy}} = 0.03723 \left( \frac{m_i}{2m_e} \right) \tau_E^{3/2} P^{3/2} \kappa^{-3/2} a^{-3} R_0^{-3/2} n_e^{-5/2} (\ln \Lambda)^{-1} = \tau_E/9 \quad (3.21)$$

Rearranging for  $\tau_E$ , we get

$$\tau_E = 8.9069 \left( \frac{m_i}{2m_e} \right)^{-2} P^{-3} \kappa^3 a^6 R_0^3 n_e^5 (\ln \Lambda)^2 \quad (3.22)$$

Now we set that equal to Equation 3.15 and rearrange to get:

$$n_e^{4.6} = 2.582 \times 10^{-3} \left( \frac{m_i}{2m_e} \right)^2 (\ln \Lambda)^{-2} I_p^{0.96} B_T^{0.03} \kappa^{-2.36} R_0^{-1.17} a^{-6} (R_0/a)^{0.06} M_{\text{eff}}^{0.2} P^{2.27} \quad (3.23)$$

then insert Equation 3.16 for  $P$  and rearrange for  $n_e$ :

$$n_e^{2.97} = 7.753 \times 10^{-5} \left( \frac{m_i}{2m_e} \right)^2 I_p^{0.96} B_T^{1.85} R_0^{0.96} a^{-3.87} (R_0/a)^{0.06} M_{\text{eff}}^{0.2} \kappa^{-2.36} (1 + \kappa^2)^{1.07} (\ln \Lambda)^{-2} \quad (3.24)$$

and finally

$$n_e = 0.04113 \left( \frac{m_i}{2m_e} \right)^{0.67} I_p^{0.32} B_T^{0.62} a^{-0.97} (R_0/a)^{0.34} M_{\text{eff}}^{0.07} \kappa^{-0.79} (1 + \kappa^2)^{0.36} (\ln \Lambda)^{-0.67} \quad (3.25)$$

To arrive at Ryter et al.'s expression for  $n_{e,\text{min}}$ , we must combine the mass ratio,  $M_{\text{eff}}$ ,  $\ln \Lambda$  and  $\kappa$  with the leading factor. Ryter et al. had  $\kappa \sim 1.6$  in their experiments, so we use this value. They worked with deuterium plasmas, so we can assume  $M_{\text{eff}} = 2$  and  $\frac{m_i}{2m_e} = 1835.25$ . For tokamak plasmas,  $\ln \Lambda \sim 10 - 20$ . Trialling different values of  $\ln \Lambda$  gives

$$n_e = 7.468 I_p^{0.32} B_T^{0.62} a^{-0.97} (R_0/a)^{0.34} (\ln \Lambda)^{-0.67} \quad (3.26)$$

$$= 1.0035 I_p^{0.32} B_T^{0.62} a^{-0.97} (R_0/a)^{0.34} \text{ [for Coulomb log of 20]} \quad (3.27)$$

$$= 1.5966 I_p^{0.32} B_T^{0.62} a^{-0.97} (R_0/a)^{0.34} \text{ [for Coulomb log of 10]} \quad (3.28)$$

Equation 3.14 has a leading factor of 0.7, so we are out by 1.43-2.28. We could match the leading factor either by assuming that  $\ln \Lambda = 30$ , which is highly unlikely, or by using the hydrogen ion mass instead of the deuteron mass in  $\frac{m_i}{2m_e} = 918.076$ , such that

$$n_e = 4.68126 I_p^{0.32} B_T^{0.62} a^{-0.97} (R_0/a)^{0.34} (\ln \Lambda)^{-0.67} \quad (3.29)$$

$$= 0.629 I_p^{0.32} B_T^{0.62} a^{-0.97} (R_0/a)^{0.34} \text{ [for Coulomb log of 20]} \quad (3.30)$$

$$= 1.0008 I_p^{0.32} B_T^{0.62} a^{-0.97} (R_0/a)^{0.34} \text{ [for Coulomb log of 10]} \quad (3.31)$$

which would give a factor of 0.7 for  $\ln \Lambda = 17$ .

### 3.6.2 Modifying $n_{e,\text{min}}$ scaling with adjusted $P_{LH}$

To see if modifying the Martin scaling improves the  $n_{e,\text{min}}$  scaling, we can take the  $P_{LH}$  fit to the high-density branch

$$P_{LH} = 11.35 n_{e20}^{1.19} = 0.7328 n_{e19}^{1.19} \quad (3.32)$$

Assuming the  $B_T$  and  $S$  dependence is the same as for the Martin scaling, we can factor out the values for the MAST data set,  $B_T = 0.55\text{T}$  and  $S = 24.0\text{m}^2$ , to get

$$P_{LH} = 0.7328 n_{e19}^{1.19} \times \frac{B_T^{0.8}}{0.55^{0.8}} \times \frac{S^{0.94}}{24^{0.94}} = 0.05961 n_{e19}^{1.19} B_T^{0.8} S^{0.94} \quad (3.33)$$

If we now insert the estimate for the surface area, we get (as an alternative to Equation 3.16)

$$P = 1.363 n_e^{1.19} B_T^{0.8} R_0^{0.94} a^{0.94} (1 + \kappa^2)^{0.47} \quad (3.34)$$

We can now insert it into Equation 3.23 and rearrange for  $n_e$ :

$$n_e^{1.9} = 5.213 \times 10^{-3} \left( \frac{m_i}{2m_e} \right)^2 I_p^{0.96} B_T^{1.85} R_0^{0.96} a^{-3.87} (R_0/a)^{0.06} M_{\text{eff}}^{0.2} \kappa^{-2.36} (1 + \kappa^2)^{1.07} (\ln \Lambda)^{-2} \quad (3.35)$$

and then

$$n_e = 0.06275 \left( \frac{m_i}{2m_e} \right)^{1.05} I_p^{0.51} B_T^{0.97} a^{-1.53} (R_0/a)^{0.54} M_{\text{eff}}^{0.11} \kappa^{-1.24} (1 + \kappa^2)^{0.56} (\ln \Lambda)^{-1.05} \quad (3.36)$$

Using  $M_{\text{eff}} = 2$  and  $\kappa = 1.78$  (for MAST dataset),

$$n_e = 0.07343 \left( \frac{m_i}{2m_e} \right)^{1.05} I_p^{0.51} B_T^{0.97} a^{-1.53} (R_0/a)^{0.54} (\ln \Lambda)^{-1.05} \quad (3.37)$$

$$= 196.22 I_p^{0.51} B_T^{0.97} a^{-1.53} (R_0/a)^{0.54} (\ln \Lambda)^{-1.05} \quad (3.38)$$

$$= 8.446 I_p^{0.51} B_T^{0.97} a^{-1.53} (R_0/a)^{0.54} \text{ [for Coulomb log of 20]} \quad (3.39)$$

$$= 17.49 I_p^{0.51} B_T^{0.97} a^{-1.53} (R_0/a)^{0.54} \text{ [for Coulomb log of 10]} \quad (3.40)$$

Or if we use hydrogenic mass ratio:

$$n_e = 94.82 I_p^{0.51} B_T^{0.97} a^{-1.53} (R_0/a)^{0.54} (\ln \Lambda)^{-1.05} \quad (3.41)$$

$$= 4.08 I_p^{0.51} B_T^{0.97} a^{-1.53} (R_0/a)^{0.54} \text{ [for Coulomb log of 20]} \quad (3.42)$$

$$= 8.45 I_p^{0.51} B_T^{0.97} a^{-1.53} (R_0/a)^{0.54} \text{ [for Coulomb log of 10]} \quad (3.43)$$

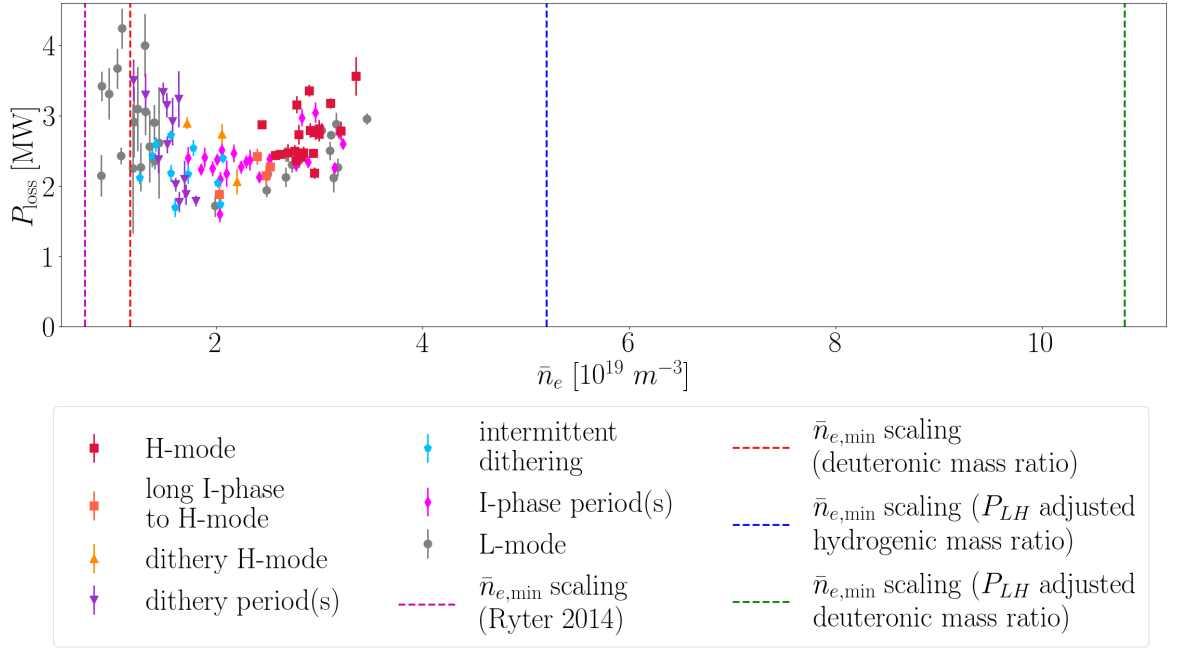


Figure 3.14: The dataset plotted with vertical dashed lines showing the original  $n_{e,\min}$  scaling result by Ryter *et al.* [1] (in magenta), the scaling result if using a deuteronic mass ratio in the derivation (in red), the scaling results after adjusting for the  $P_{LH}$  scaling of the MAST dataset (with the hydrogenic mass ratio in blue and the deuteronic mass ratio in green).

For MAST values of  $I_p = 0.74$ ,  $B_T = 0.55$ ,  $a = 0.65$  and  $R_0 = 0.85$ , we get

$$n_{e,\min} = 0.0789 \times \left( \frac{m_i}{2m_e} \right)^{1.05} \times (\ln \Lambda)^{-1.05} \quad (3.44)$$

Using  $\ln \Lambda = 17$ :

$$n_{e,\min} = 10.8 \times 10^{19} \text{ m}^{-3} \quad (3.45)$$

$$n_{e,\min} = 5.2 \times 10^{19} \text{ m}^{-3} \quad (3.46)$$

for deuteronic and hydrogenic mass ratio respectively. These values are now much too large, and are again outside of the experimental range studied in the dataset, this time much higher. This would actually make them less plausible than the original values for the  $n_{e,\min}$  scaling by Ryter *et al.*, since if either of these values were  $n_{e,\min}$ , then the densities studied in the dataset should not have been capable of transitioning to H-mode.

Returning to the  $n_{e,\min}$  scaling as described by Ryter *et al.* [1], the original scaling as applied to the MAST dataset gave a value of  $n_{e,\min} = 0.73 \times 10^{19} \text{ m}^{-3}$ . When examining this

derivation for the previous section, this value could only realistically be obtained by using the hydrogen mass ratio  $\frac{m_i}{2m_e} = 918.076$ . As the MAST plasma is made up of deuterium ions, we can derive another estimate for  $n_{e,\min}$  from the scaling by substituting the deuteronic mass ratio  $\frac{m_i}{2m_e} = 1835.25$  instead. This would result in a value of  $n_{e,\min} = 1.17 \times 10^{19} \text{ m}^{-3}$ , which is still significantly lower than the observed value, but nonetheless an improvement. Figure 3.14 shows the four options for the  $n_{e,\min}$  scaling results. In conclusion, none of the derived options for the  $n_{e,\min}$  scaling match the observed behaviour of the MAST dataset.

The fact that the Ryter scaling for  $n_{e,\min}$  is so far off from the experimentally determined  $n_{e,\min}$  for this MAST dataset, even with attempts to adjust it, indicates that the density minimum for  $P_{LH}$  observed in this dataset could involve a different physical mechanism than that of ASDEX Upgrade studied by Ryter *et al.* [1]. The original  $n_{e,\min}$  scaling values of  $n_{e,\min} = 0.73 \times 10^{19} \text{ m}^{-3}$  or  $n_{e,\min} = 1.17 \times 10^{19} \text{ m}^{-3}$  could describe a density minimum which is not observed in this dataset because  $P_{LH}$  starts increasing at a higher density value due to another, different effect, which is perhaps not present or present at a different relative value in the ASDEX Upgrade dataset. On the other hand, the mismatch of the scaling and the experimental dataset could also be due to differences between the devices, whether that is due to the spherical/conventional divide, differences in configuration or divertors, or different responses of the plasmas to their respective heating methods. The low-density branch and possible physical mechanisms causing it are explored through the heat flux and (beam) heating efficiencies in the following chapter.

### 3.7 Summary

For this Chapter, the dataset of an L-H transition experiment on MAST was analysed to form the basis of a power threshold study. The study was motivated by the necessary reliance on empirical scaling laws to predict the power threshold  $P_{LH}$  for new devices or scenarios, laws which were created based mostly on conventional tokamak data and which are accurate only in limited situations, usually not at all for spherical tokamaks. This project involved the first comprehensive power threshold study of MAST data, with the density dependence of  $P_{LH}$  investigated to reveal the first picture of the low density branch of  $P_{LH}$  on MAST.

The power threshold  $P_{LH}$  is defined as the net power  $P_{\text{net}}$  required for a tokamak plasma to transition from L-mode to H-mode. Several options for the definition of  $P_{\text{net}}$  are possible,

including  $P_{\text{loss}} = P_{\text{ohm}} + P_{\text{aux}} - dW/dt$  and  $P_{\text{sep}} = P_{\text{loss}} - P_{\text{rad}}$ , and each term in  $P_{\text{net}}$  could potentially be sourced from multiple locations and requires careful consideration. The different versions of  $P_{\text{net}}$  and its components have all been explored and presented in this Chapter, and the most common version used in scaling laws and most other studies uses  $P_{\text{loss}}$ , which for the case of this MAST study uses a  $P_{\text{ohm}}$  estimate from TRANSP, the captured NBI power for  $P_{\text{aux}}$  (also estimated by TRANSP), and  $dW/dt$  estimated from a high time resolution ( $\Delta t = 0.2\text{ms}$ ) EFIT calculation.

To determine  $P_{LH}$ , it is necessary to identify each H-mode and its transition time  $t_{LH}$  as well as L-modes which do not transition (to give a lower boundary). Aside from the obvious L-H transitions seen in the combination of a sharp drop in  $D_\alpha$  emission and a simultaneous steep rise in the line averaged density  $\bar{n}_e$ , shots in this dataset contained a number of intermediate plasma confinement states. Distinct ‘‘behaviour categories’’ from L-modes to dithery periods, I-phases and H-modes were identified and time periods in each shot were classified based on their signatures in the  $D_\alpha$  and  $\bar{n}_e$  traces. The categories were described in qualitative and quantitative ways, including with an analysis of the  $D_\alpha$  fluctuation frequencies. Both (pre-H) I-phases and dithery periods are potential candidates for limit-cycle-oscillations (LCOs), although the two categories are quite distinct in the  $D_\alpha$  signals, with I-phases being very regular oscillations of  $f \sim 3\text{-}4\text{kHz}$  and dithery periods being very irregular fluctuations of  $f \sim 1\text{-}2\text{kHz}$ . The transitions from L-mode to any of the higher confinement states as well as corresponding steady-state L-mode points were plotted in a number of results plots, and a line to separate L-mode and H-mode points (or H-mode-accessible and H-mode-inaccessible regions) can be drawn by fitting to the low-density and high-density branches separately.

The  $P_{LH}$  boundary reveals a similar non-monotonic density dependence as seen on other devices (e.g. JET [32], C-Mod [33], ASDEX Upgrade [42], HL-2A [43]), with a minimum  $P_{LH} \sim 2\text{MW}$  at  $n_{e,\text{min}} \sim 2\text{-}2.5 \times 10^{19}\text{m}^{-3}$ . H-modes above  $2.5 \times 10^{19}\text{m}^{-3}$  are ELMy, with no or short pre-H I-phases, while H-modes below this density have longer pre-H I-phases or are dithery. I-phases with no subsequent H-mode are found at the  $P_{LH}$  boundary in a wide range for  $\bar{n}_e > 1.6 \times 10^{19}\text{m}^{-3}$ . Dithery periods are located on the low-density branch, in a narrower density range of  $1.2 \times 10^{19}\text{m}^{-3} < \bar{n}_e < 2 \times 10^{19}\text{m}^{-3}$  but a wider  $P_{\text{loss}}$  range, reflecting the steep increase in the low-density branch. L-modes are ubiquitous both at very low densities and at higher densities and lower powers, but it is harder to achieve lasting

L-modes around  $n_{e,\min}$ , especially without considering purely ohmically heated shots.

The fit to the high density branch of the data is  $P_{LH} = (11.35 \pm 2.30) \times \bar{n}_{e20}^{(1.19 \pm 0.16)}$ . The widely used ITER scaling by Martin *et al.* [40] and the aspect-ratio adjusted Takizuka scaling [80] were both compared with the data, and while the Takizuka scaling was marginally better, both under-predicted  $P_{LH}$  by at least an order of magnitude. Although the Takizuka scaling was developed with a database that included MAST shots, and the MAST data at the time (2001-03) appeared to fit the modified scaling well,  $P_{LH}$  for the more recent MAST shots (2011-13) is much higher at similar densities. Most parameters ( $I_p$ ,  $B_T$ ,  $\kappa$ ,  $\delta$  etc) are actually somewhat different between the two datasets, but by far the biggest factor is likely due to the change in divertor, with the original ribbed divertor replaced by the updated MAST improved divertor (MID) with fan-shaped tiles in late 2003 [49]. The increase in  $P_{LH}$  due to the new divertor was immediately visible in a significant reduction in the frequency of the previously ubiquitous ohmic H-modes.

The limited understanding of how divertors and configurations affect  $P_{LH}$  especially for STs clearly demonstrates the need for more studies in this field. Additionally, with different heating methods potentially preferentially heating either ions or electrons, and the ion heat flux possibly being a critical L-H transition parameter, the heating method will likely result in further differences in the L-H transition behaviour. Some of the effects of different heating methods on L-H transitions are discussed in Chapter 4.

As a final comparison between the MAST dataset and a scaling derived from other devices, the scaling for  $n_{e,\min}$  developed by Ryter *et al.* [1] was compared with our results. The scaling predicted  $n_{e,\min}^{\text{scal}} \sim 0.73 \times 10^{19} \text{m}^{-3}$  which is much lower than the value found  $n_{e,\min} \sim 2\text{-}2.5 \times 10^{19} \text{m}^{-3}$  and actually lower than the lowest density points measured. I re-evaluated the  $n_{e,\min}$  scaling by incorporating a modified  $P_{LH}$  scaling for MAST based on a fit to the data but that resulted in a value of  $n_{e,\min}$  which was in turn much too high. If we return to the original version of the scaling  $n_{e,\min}^{\text{scal}} \ll n_{e,\min}$ , there are two possible reasons why the observed  $n_{e,\min}$  is higher than the scaling. (1) The scaling could be describing a density minimum which exists in the MAST data but is not observed because  $P_{LH}$  is affected by another, different effect causing an increase in  $P_{LH}$  starting at a higher  $n_{e,\min}$ , and this effect is perhaps not present or present at a different relative value in the ASDEX Upgrade dataset. (2) The mismatch of the scaling and the experimental dataset could also be due to differences between the devices, whether that is due to the spherical/conventional

divide, differences in configuration or divertors, or different responses of the plasmas to their respective heating methods. The low-density branch and possible physical mechanisms causing it are explored further through the heat flux and (beam) heating efficiencies in the following chapter.

### 3.7.1 Absorbed beam power calculations by TRANSP

The  $P_{\text{loss}}^{\text{TR}}$  calculations in this chapter were performed with the captured beam power returned by TRANSP as the auxiliary heating term,  $P_{\text{NBI}} = P_{\text{cap}}^{\text{NBI}}$ , for which shine-through losses are subtracted from the injected beam power  $P_{\text{inj}}^{\text{NBI}}$ . This variable is generally sufficient for power threshold studies on many other tokamaks, as further NBI (fast ion) losses make up a smaller fraction of the total  $P_{\text{loss}}$  and can thus be neglected without too much issue. When the terms in the energy balance equations for the heat flux (Chapter 4) were investigated, it became apparent that  $P_{\text{cap}}^{\text{NBI}}$  was much larger than the sum of the beam heating powers absorbed by the electrons and ions, with a significant discrepancy especially for low-density plasmas. Further investigation revealed that while  $P_{\text{cap}}^{\text{NBI}}$  does subtract shine-through losses from the injected power, the additional fast ion losses such as orbit or charge-exchange losses (which are not considered by  $P_{\text{cap}}^{\text{NBI}}$ ) are significant for MAST plasmas, especially at low densities. The following chapter (Chapter 4) includes an investigation into the sources of the beam losses and describes the effect of using the beam power absorbed by the plasma  $P_{\text{heat}}^{\text{NBI}}$  (corrected for all losses) instead of the captured beam power  $P_{\text{cap}}^{\text{NBI}}$  in the net power calculations, i.e.  $P_{\text{loss,th}}$  instead of  $P_{\text{loss}}$ , with results shown in Figure 4.12. The more comprehensive TRANSP analysis required for these calculations was performed on a smaller set of H-mode and dithery transitions, so the full power threshold results of Figure 3.8 including e.g. L-modes and I-phases are not yet available for  $P_{\text{loss,th}}$ .

## Chapter 4

# Heat flux studies

### 4.1 Motivation

The L-H power threshold  $P_{LH}$  is a useful measure to quantitatively compare how different scenarios can make H-mode access more or less difficult, i.e. by requiring a larger or smaller amount of power input. To try and understand the reasons behind this behaviour we should explore the microscopic physics underlying the transition. The U-shaped density dependence of  $P_{LH}$  commonly found on a range of tokamak devices, with a low-density and high-density branch described by an increase in  $P_{LH}$  as the density moves away from  $n_{e,min}$  on either side, suggests that the two branches are caused by different mechanisms, and something appears to trigger the transition between regimes at densities approaching  $n_{e,min}$ .

L-H transition theory as described by Malkov et al. [30] connecting the microscopic transition dynamics and the macroscopic physics of the power threshold suggests that the increase in  $P_{LH}$  for decreasing  $\bar{n}_e$  in the low-density branch is due to a decrease in both the collisional electron-to-ion energy transfer and the heating fraction which is coupled to the ions. These processes strengthen the edge electric field shear, which is one of the triggers likely needed for the L-H transition. The increase in  $P_{LH}$  along the high-density branch in turn is suggested to be caused by an increase of the damping of turbulence-driven shear flows due to increasing ion collisionality.

Experimental studies on ASDEX-Upgrade [1] and C-Mod [29] have postulated that the  $E_r$  well is driven mainly by the ion heat flux at the plasma edge  $q_{i,edge}$  through its role in the increase of the ion pressure gradient  $|\nabla p_i|$ . For heating methods of electron cyclotron resonant heating (ECRH) on AUG and ion cyclotron heating (ICH) on C-Mod, the surface

integrated edge ion heat flux  $Q_{i,edge}$  at transition was found to increase linearly with  $\bar{n}_e$ , even in the low-density branch where  $P_{LH}$  has a non-monotonic density dependence. These results suggested a possibly critical  $Q_{i,edge}$  per particle for H-mode access. Meanwhile, the electron heat flux  $Q_{e,edge}$  on AUG followed a similar  $\bar{n}_e$  dependence to  $P_{LH}$ . It was suggested that a reduced electron-ion coupling at low density could therefore contribute to a higher  $P_{LH}$  requirement [1]. Studies on AUG using NBI heating showed no density dependence for either  $Q_{i,edge}$  or  $Q_{e,edge}$ , and in cases of no additional ECRH heating (NBI only)  $Q_{e,edge} \sim Q_{i,edge}$ . These results are examined in more detail and compared with results generated from MAST data during this study at the end of this chapter.

## 4.2 Method: Interpretative simulations with TRANSP

The heat flux study of this chapter follows on from the power threshold analysis described in the previous chapter as part of an investigation into L-H transitions on MAST. As in the previous chapter, the analysis involved NBI-heated plasma discharges from the same dataset of L-H transitions produced as part of a dedicated experiment, introduced in Chapter 2. Most of the quantities explored in this chapter, such as the ion and electron heat fluxes as well as components of the energy balance equations and beam heating and loss terms, were generated using the transport code TRANSP [73] for interpretative simulations. In contrast with the use of TRANSP in the power threshold study to generate global (one-dimensional, time-varying) quantities, this chapter involves two-dimensional (time- and space-varying) variables, i.e. profiles of quantities for each time point, with the edge region just inside the LCFS of particular interest for L-H transition physics. As they are flux quantities and thus constant on a flux surface, the experimental data input and the 2D TRANSP output variables can be mapped onto flux surfaces generated by the equilibrium solver EFIT and consequently more generally be plotted as a function of the normalised effective radius  $\rho_{eff,N}$  (defined in Chapter 1). The profiles of various different quantities as well as their edge or separatrix values are therefore easy to compare both with each other and with results from other devices.

The toroidal rotation velocity estimated by the CXRS diagnostic on the South NBI beam was checked for a dependence on density, loss power and NBI power (both injected and captured), and no significant correlation was found. A single value for the core  $v_{tor}$

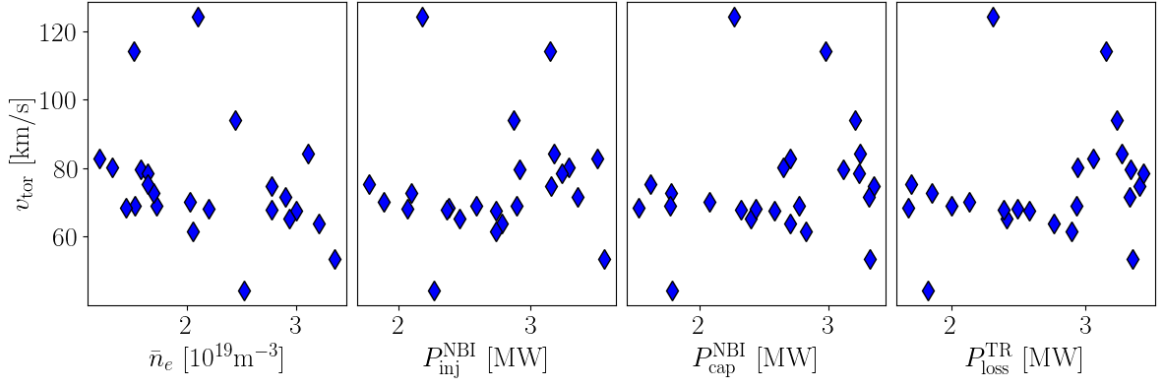


Figure 4.1: The CXRS diagnostic on each heating beam (here South NBI) returns radial profiles of ion temperature and toroidal rotation velocity. The values of the core toroidal velocity  $v_{\text{tor}}$  at transition time for all shots included in the heat flux study are plotted against the corresponding values of line-averaged density  $\bar{n}_e$ , loss power  $P_{\text{loss}}^{\text{TR}}$ , as well as injected and captured NBI powers  $P_{\text{inj}}^{\text{NBI}}$  and  $P_{\text{cap}}^{\text{NBI}}$ . None of the quantities investigated show a significant correlation with the toroidal velocity.

was found for each transition by interpolating in time to  $t_{LH}$  and the profile in space to the radial location of the magnetic axis. The results are shown in Figure 4.1 plotted against line-averaged density  $\bar{n}_e$ , loss power  $P_{\text{loss}}^{\text{TR}}$ , as well as injected and captured NBI powers  $P_{\text{inj}}^{\text{NBI}}$  and  $P_{\text{cap}}^{\text{NBI}}$ . No relationships between the quantities were identified, although a dependence of toroidal velocity on NBI power would be expected.

#### 4.2.1 Energy balance in a tokamak

Integrated modelling codes attempt to model the complex conditions in a tokamak plasma by solving the fluid differential equations of particle, momentum and energy balances, which are consistently coupled with an equilibrium solver, heating and radiation physics models, and transport models [72]. These codes can be run as predictive simulations where the evolution of profiles is predicted by models, or as interpretative simulations, where temperature and density profiles are provided from experimental measurements and the transport coefficients, which are not otherwise measurable, are inferred. For the work in this chapter, interpretative simulations with TRANSP [73] were performed together with NUBEAM [74] for the NBI heating source. NUBEAM models fast ion orbits using a guiding centre approximation with a finite Larmor radius correction. The output of an interpretative simulation provides a comprehensive description of the plasma with consistent time resolution and spatial coordinates, and contains synthetic diagnostic data which can be directly compared with experimental

data, such as the neutron rate in TRANSP which can be compared with data from the fission chamber diagnostic on MAST [64].

The collective behaviour of particles can be described with the distribution function  $f(t, \vec{r}, \vec{v})$  for time  $t$ , radial position  $\vec{r}$  and velocity  $\vec{v}$ . For a tokamak plasma, the total derivative of  $f(t, \vec{r}, \vec{v})$  with respect to  $t$  is described by the Fokker-Planck equation,

$$\frac{\partial f}{\partial t} + \vec{v} \cdot \nabla f + \vec{a} \cdot \nabla_v f = \underbrace{\left( \frac{\partial f}{\partial t} \right)_c}_{\text{collision term}}. \quad (4.1)$$

Equations of particle, momentum and energy balance, which are numerically solved in integrated modelling codes, can be derived by taking moments of the velocity distribution function  $f(t, \vec{r}, \vec{v})$ , i.e. multiplying the Fokker-Planck equation by  $g = v^n$  (for the  $n$ th moment) and integrating over  $d^3v$ . The electron and ion energy balance equations are derived from the second moment, i.e.  $g = v^2 = \vec{v} \cdot \vec{v}$ ,

$$\frac{\partial(n \langle \vec{v} \cdot \vec{v} \rangle)}{\partial t} + \nabla \cdot (n \langle (\vec{v} \cdot \vec{v}) \vec{v} \rangle) - n \left\langle \frac{d(\vec{v} \cdot \vec{v})}{dt} \right\rangle = \int v^2 \underbrace{\left( \frac{\partial f}{\partial t} \right)_c}_{\text{collision term}} d^3v \quad (4.2)$$

where  $n(t, \vec{r}) = \int_{-\infty}^{\infty} f d^3v$  is the particle number density. The full derivation of all the balance equations are detailed in Appendix A, while just the results of the derivation of the energy balance equations are given here for reference. Using the following definitions

$$\begin{aligned} \text{velocity: } \vec{v} &= \underbrace{\vec{u}}_{\text{fluid velocity}} + \underbrace{\vec{w}}_{\text{thermal velocity}} \\ \text{pressure: } p &= \frac{nm}{3} \langle w^2 \rangle \\ \text{heat flux: } \vec{q} &= \frac{nm}{2} \langle w^2 \vec{w} \rangle \end{aligned} \quad (4.3)$$

we can write the electron and ion energy balance equations for an NBI-heated plasma as

$$\begin{aligned} \frac{\partial}{\partial t} \left( \frac{3}{2} p_e \right) + \nabla \cdot \left( \frac{5}{2} p_e \vec{u}_e \right) + \vec{u}_i \cdot \nabla p_i + \nabla \cdot \vec{q}_e \\ = P_{\text{ohm}} - P_{\text{equi}} - P_{\text{rad}} - P_{\text{iz}} - P_{\text{rec}} + P_{\text{NBI}}^e + P_{\text{FUS}}^e \end{aligned} \quad (4.4)$$

$$\begin{aligned}
\frac{\partial}{\partial t} \left( \frac{3}{2} p_i \right) + \nabla \cdot \left( \frac{5}{2} p_i \vec{u}_i \right) - \vec{u}_i \cdot \nabla p_i + \nabla \cdot \vec{q}_i \\
= P_{\text{equi}} - P_{\text{cx}} - P_{\text{rec}} + P_{\text{NBI}}^i + P_{\text{FUS}}^i
\end{aligned} \tag{4.5}$$

where the source and sink terms are defined as

$$\begin{aligned}
\frac{\partial}{\partial t} \left( \frac{3}{2} p_e \right) &: \text{Rate of electron energy change} \\
\frac{\partial}{\partial t} \left( \frac{3}{2} p_i \right) &: \text{Rate of ion energy change} \\
\nabla \cdot \left( \frac{5}{2} p_e \vec{u}_e \right) + \vec{u}_e \cdot \nabla p_e &: \text{Energy loss rate due to convective electron heat transport} \\
\nabla \cdot \left( \frac{5}{2} p_i \vec{u}_i \right) - \vec{u}_i \cdot \nabla p_i &: \text{Energy loss rate due to convective ion heat transport} \\
\nabla \cdot \vec{q}_e &: \text{Energy loss rate due to conductive electron heat transport} \\
\nabla \cdot \vec{q}_i &: \text{Energy loss rate due to conductive ion heat transport} \\
P_{\text{ohm}} &: \text{Ohmic heating} \\
P_{\text{equi}} &: \text{Equilibration power} \\
P_{\text{rad}} &: \text{Radiated energy loss rate} \\
P_{\text{iz}} &: \text{Energy loss rate due to impact ionisation} \\
P_{\text{rec}} &: \text{Energy loss rate due to recombination} \\
P_{\text{cx}} &: \text{Energy loss rate due to charge exchange} \\
P_{\text{NBI}}^e, P_{\text{NBI}}^i &: \text{NBI heating to electrons and ions, respectively} \\
P_{\text{FUS}}^e, P_{\text{FUS}}^i &: \text{Alpha heating to electrons and ions, respectively}
\end{aligned}$$

#### 4.2.2 Setting up TRANSP runs with OMFIT profiles

While TRANSP runs were performed for the initial power threshold study to estimate ohmic powers and captured beam powers, these involved a relatively simple setup since only global quantities were studied. For the heat flux study in this chapter, the components of the energy balance equations are investigated in more detail including in the spatial dimension as profiles, so a more extensive TRANSP setup with equilibrium calculations and profile fitting of diagnostic data for each time step is required. This can be quite an involved process and requires good quality data from Thomson scattering (TS) and Charge exchange (CXRS) diagnostics, so not all shots from the power threshold study were included.

The TRANSP setup process involves

1. **Choosing start and end times as well as the size of the time step.** The simulation results, especially when using the PID controller for anomalous diffusivity  $D_{\text{an}}$ , to match neutron rates (more detail on this is found in the following section), were optimised when the start time was chosen to be as close to the beam start time as possible. This then required profile fittings for a large number of time points between the beam start and the time periods of interest, making the whole process rather time intensive. The end time was generally set as several time steps after the transition time (or other time point of interest). Different step sizes were explored, and a step size of 5ms was ultimately chosen as a compromise between available diagnostic data resolution and desired time resolution of physical processes.
2. **Calculating the equilibrium with EFIT.** The setup process allowed for a few choices in the EFIT settings, including which diagnostic data would be used to constrain the equilibrium. The less-constrained version uses data from the  $D_\alpha$  and magnetics diagnostics, whereas the next step up includes Thomson scattering (TS) data as well for a pressure-constrained calculation. This latter option was attempted initially, but it quickly became clear that this would not be possible without extensive assistance from an EFIT expert for each shot individually, and as there was anyway no guarantee it would have given more reliable results (the effects of the EFIT reconstruction choice were tested and no significant changes were found in the results), the equilibrium for each time step was calculated with a  $D_\alpha$  and magnetics-constrained EFIT, manually checked for inconsistencies, and the timeslice narrowed if necessary. The choice to leave the core pressure profile unconstrained is not just logistically justified but also accounts for the fact that on MAST, the fast ion pressure is a significant contribution to the pressure profile while the TS diagnostic is only sensitive to the thermal electron pressure and can't capture this contribution [86].
3. **Setup for profile fitting.** The data for all available diagnostics is fetched and mapped to flux coordinates provided by the EFIT calculation from the previous step. Essential diagnostics for these TRANSP simulations are TS (providing electron density and temperature profiles) and CXRS (providing ion temperature and plasma rotation profiles).  $q$ -profile data from the MSE diagnostic is not essential but is fetched and fitted when

available. An ELM filter working with  $D_\alpha$  diagnostic data is part of the routines provided by OMFIT [87], a comprehensive integrated modelling framework which enables users to interact with multiple physics codes, and its settings are manually optimised to find and filter out or mask ELMs where present. The data is then time averaged and interpolated (especially necessary for shots where the TS diagnostic was set to “burst” mode and the time resolution is not consistent) and sliced to provide profiles for each TRANSP simulation time step. For each available diagnostic, the data is then first manually inspected to remove any channels (usually in the edge) or time steps (occasionally at the start) with spurious or “bad” data, as well as the HFS core channels for TS.

4. **Profile fitting.** This is the most time-intensive step in the process. For each time step, profiles of  $n_e$ ,  $T_e$  and  $T_i$  data are fitted with a core polynomial and edge exponential (modified mtanh) blend [88]. The process is done through the OMFIT GUI and involves adjusting several fit settings such as polynomial order, limits for pedestal width and mtanh symmetry location. The data can also optionally be transformed (with logarithm or square root) before fitting to ensure positive values, the SOL data points can optionally be excluded from the fit, or the values at the separatrix or the core can be constrained manually if necessary. The fit settings frequently had to be newly adjusted for each time step, but after noticing general trends for profiles in L- or H-mode as well as at low or high densities I was able to create a few templates to use and modify slightly. Some profile fits were bad due to poor data quality so couldn't be improved, but in cases where there were just a few channels with low-quality data these could be excluded for individual timesteps too. Both TS and CXRS have variable data quality, and the choices made during profile fitting can introduce further uncertainties to the calculated values of the heat flux components. Since CXRS data is not always available in the SOL and edge regions, the  $T_i$  profiles had to be extrapolated, increasing the uncertainty in their accuracy further, though this has not been quantified at this time.
5. **Setting up TRANSP.** When all the profiles have been fit, the TRANSP run can be set up. The diffusion of beam-sourced fast ions out of the plasma is not well captured by the TRANSP model equations (while NUBEAM has some capabilities in modelling

fast ion orbits, the amount of outward diffusion is still uncertain), so an anomalous diffusivity  $D_{\text{an.}}$  can be set to adjust the fast ion population.  $D_{\text{an.}}$  is time-varying and is usually calculated or set to achieve as close a match as possible of TRANSP-calculated neutron rates to experimental neutron rates measured by the fission chamber diagnostic. More on anomalous diffusivity and the process of matching neutron rates is described in the next section.

### 4.2.3 Matching neutron rates with anomalous diffusivity

While plans for future tokamak reactors aim to generate power primarily from thermonuclear reactions, i.e. fusion between thermalised ions, these made an almost negligible contribution to total fusion reactions on MAST throughout its lifetime. The relatively low ion temperatures of typically  $T_i \lesssim 2$  keV in the core resulted in the majority of D-D fusion reactions involving at least one beam ion, with  $\sim 80\%$  occurring between a beam ion and a thermal ion (beam-thermal) and  $\sim 20\%$  between two beam ions (beam-beam) [89, 90]. For the data set used in this project,  $\sim 90\%$  of fusion reactions were beam-thermal,  $\sim 10\%$  were beam-beam, and less than  $\sim 1.5\%$  were thermonuclear.

Fusion reactions are the most significant source of neutrons in the plasma, so a measure of the neutron emission rate will present a good approximation of the fusion reaction rate. The neutron rate is measured in experiments as a global quantity of high time resolution with the fission chamber (FC) diagnostic which was introduced in Chapter 2, as well as spatially resolved data from the neutron camera which has not been considered in this work. TRANSP contains routines to give an estimate of the neutron rate a particular simulation would produce as collected by a synthetic diagnostic, which for an interpretative simulation can then be directly compared with the experimental FC data to validate the simulation results.

Fusion reactions on MAST almost always involve energetic (fast) ions sourced by the neutral heating beams, with fast ion physics essentially synonymous with beam physics. The neutron rate is therefore also highly linked with fast ion behaviour in MAST plasmas, and any comprehensive transport model code like TRANSP must find some way to calculate or describe fast ion transport. Since, as previously mentioned, the outward diffusion of beam-sourced fast ions out of the plasma is not well captured by the TRANSP model equations, fast ion losses beyond those from classical collisions are estimated by setting an ad hoc beam-ion

diffusion coefficient,  $D_{\text{an.}}$ . The anomalous fast ion diffusivity  $D_{\text{an.}}$  is added to the classical diffusion model to approximate the effect of fast ion redistribution and losses observed in experiments [91], and it is set to adjust the fast ion population so that the neutron rate estimated by TRANSP matches the experimental values. The existence of the MHD modes presumed responsible for fast ion losses must then be verified separately.

In the TRANSP setup, anomalous diffusion is unrelated to the other diagnostic data input and is addressed after the profile fitting is complete, so that simulations can be run with different anomalous diffusivities but otherwise identical settings, allowing the effects to be compared directly and  $D_{\text{an.}}$  to be optimised for the closest possible neutron match. For a simulation, anomalous diffusion can be switched on or off, and  $D_{\text{an.}}$  can either be set manually or varied during the simulation in response to the match between predicted and experimental neutron rates with the use of a Proportional-integral-derivative (PID) controller.  $D_{\text{an.}}$  can optionally be zero-, one- or two-dimensional (constant or varying in time and space), and for this project was assumed (in non-zero cases) to be constant in space (i.e. constant inside the separatrix - this is the commonly used and accepted form of setting  $D_{\text{an.}}$  values manually) but varying in time.

To investigate the effects of  $D_{\text{an.}}$  on predicted neutron rates as well as other TRANSP outputs such as components of the beam heating or energy balance equations, a reference TRANSP run with no anomalous diffusion, i.e.  $D_{\text{an.}} = 0$ , was performed for each shot. For a few shots at the lowest density the TRANSP run with no anomalous diffusion consistently failed as the confined fast ion density would grow too large, so for these shots the reference runs are not available. How well the neutron rates are predicted can be estimated with  $(\nu_n^{\text{calc.}} - \nu_n^{\text{meas.}})/((\nu_n^{\text{calc.}} + \nu_n^{\text{meas.}})/2)$ , where  $\nu_n^{\text{calc.}}$  is the predicted rate and  $\nu_n^{\text{meas.}}$  is the measured rate. The neutron rate matches and their corresponding  $D_{\text{an.}}$  values at  $t_{\text{LH}} \pm 10\text{ms}$  for the selected TRANSP runs are shown in Figure 4.2c-d, while panels a-b show example time traces of  $D_{\text{an.}}$  and the measured and calculated neutron rates for one shot, along with the calculated neutron rate for  $D_{\text{an.}} = 0$ . These results show that the reference runs without anomalous diffusion consistently over-estimate the neutron rate by a significant amount, from 30 – 40% at low injected beam powers  $P_{\text{inj}}^{\text{NBI}}$  and/or high density  $\bar{n}_e$  to 170% at high  $P_{\text{inj}}^{\text{NBI}}$  and/or low  $\bar{n}_e$ .

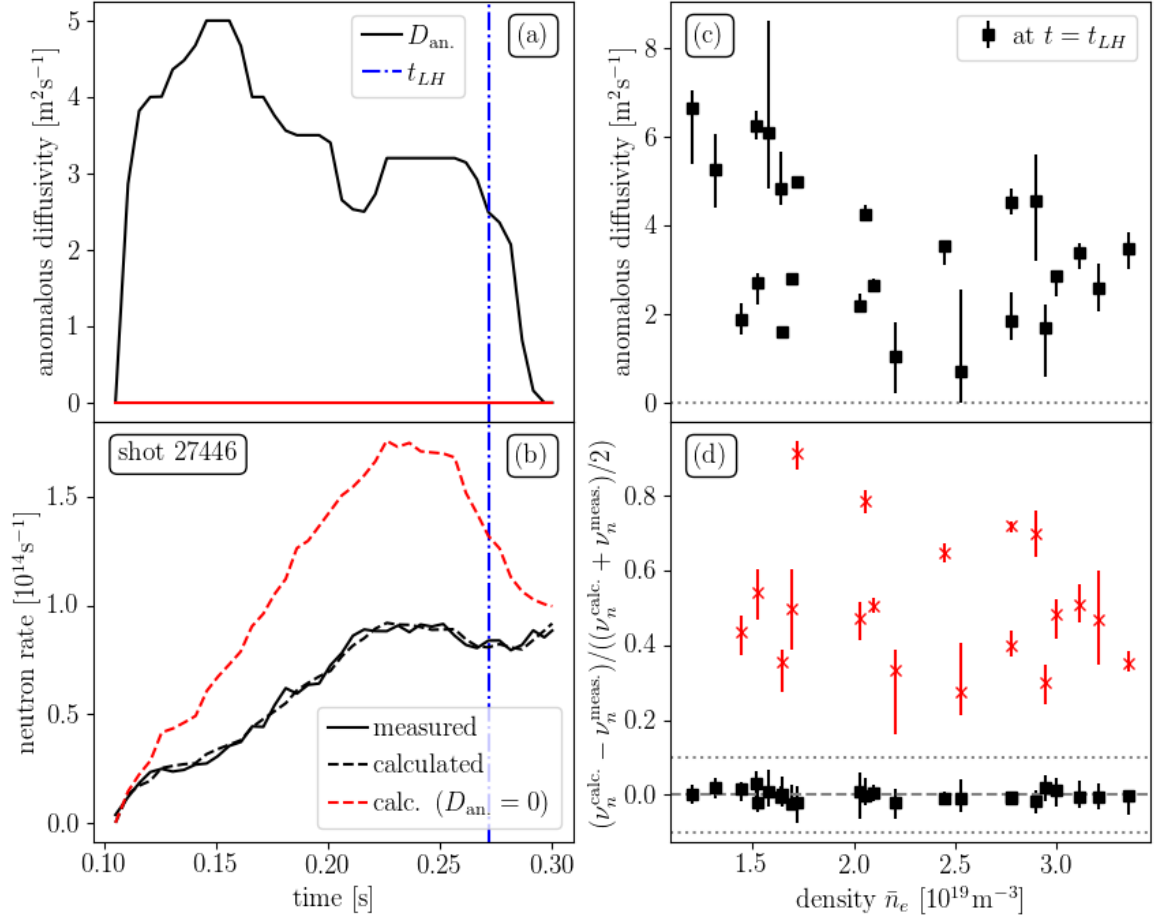


Figure 4.2: Time traces of (a) the anomalous diffusivity and (b) neutron rates for an example shot. The solid line in (b) shows the measured neutron rate, while the dashed lines show the predicted neutron rates for a TRANSP run with no anomalous diffusion (red) and one with  $D_{an.}$  adjusted to match the measured neutron rate. The results for all considered shots are shown on the right, with  $D_{an.}$  in (c) and neutron rate match in (d), with black again showing the calculated values when adjusting  $D_{an.}$  to match the neutron rates and red the values at  $D_{an.} = 0$ . The values are taken at the transition time and the error bars represent the range in values for  $t_{LH} \pm 10ms$ . The neutron rate match is calculated as  $(\nu_n^{calc.} - \nu_n^{meas.}) / ((\nu_n^{calc.} + \nu_n^{meas.}) / 2)$  with  $\nu_n^{calc.}$  as the predicted rate and  $\nu_n^{meas.}$  as the measured rate. A perfect match is 0.0, and  $\pm 10\%$  are marked as grey dotted lines.

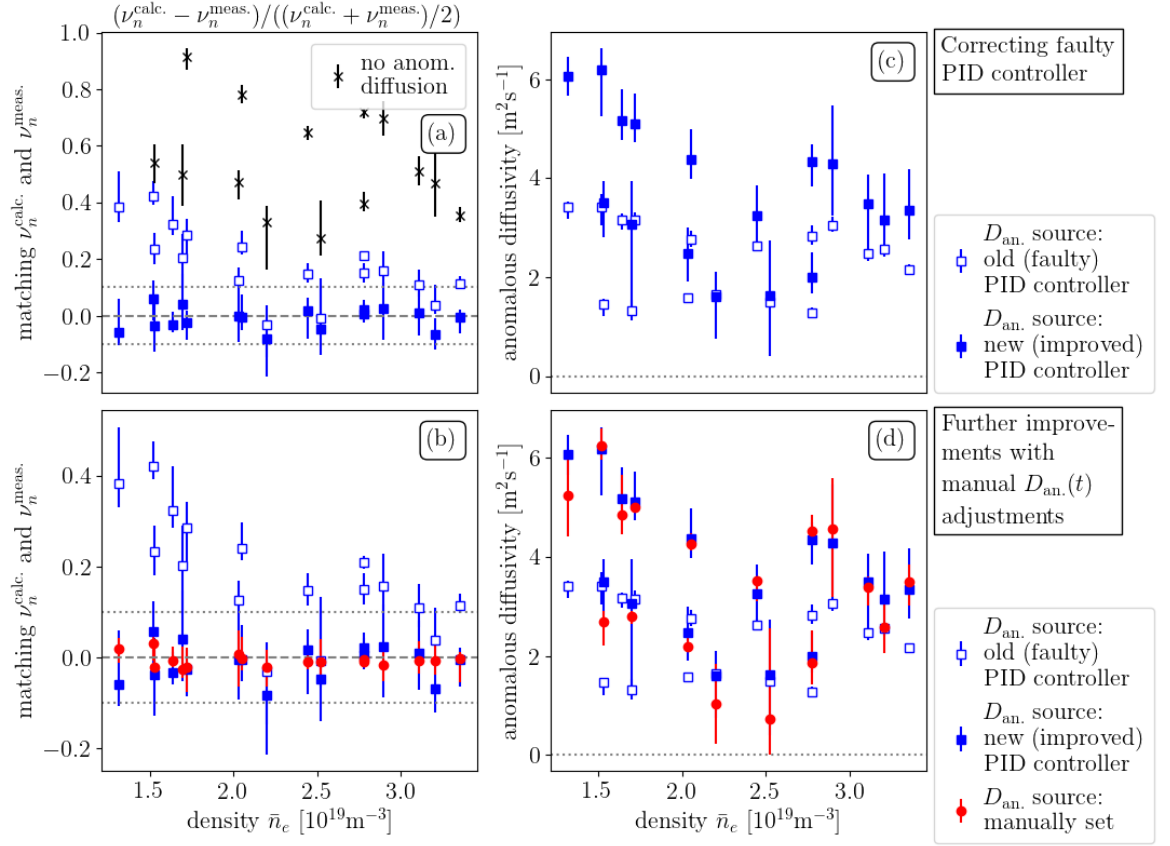


Figure 4.3: Neutron rate match and anomalous diffusivity comparisons for the initial faulty PID controller, the corrected PID controller version and the results of further manual improvements to the anomalous diffusivity. The values are taken at the transition time and the error bars represent the range in values for  $t_{LH} \pm 10\text{ms}$ .

#### 4.2.3.1 Finding and setting $D_{\text{an.}}$

The initial attempts used the TRANSP PID controller with pre-arranged (MAST default) settings. The neutron rate match was often very poor, but even after multiple enquiries it wasn't clear if these results were to be expected or how to improve them. Further enquiries eventually revealed the possibility of manually creating a data file of the expected time history of  $D_{\text{an.}}$  and incorporating it into the TRANSP simulation. This option was chosen for all further simulations, with an often laborious cycle of testing an expected  $D_{\text{an.}}$  time history and adjusting it based on the neutron rate match.

With support from the resident TRANSP expert Bhavin Patel, PhD, the PID controller settings were found to be faulty and eventually fixed, resulting in a much more reasonable neutron rate match. The manual process employed in the meantime had in fact resulted in matches which were even closer, so the simulation results using these manual  $D_{\text{an.}}$  input

files were chosen to present the results of this study. The improved neutron rate match of the manual  $D_{\text{an}}$  input files can be explained intuitively, as the PID controller was adjusting the  $D_{\text{an}}$  values during the simulation and could only respond to and correct for effects from the  $D_{\text{an}}$  values after they were visible in the neutron rate match, often leading to an over-correction of smaller changes. The PID controller nevertheless allowed for a better starting point for shots which were simulated after its repair.

Figure 4.3 shows the neutron rate matches (a-b) and  $D_{\text{an}}$  values (c-d) for the transition times of each shot included in this study. The top two panels (a and c) show the results for the old faulty PID controller (empty squares) and the new improved PID controller (filled squares) along with the neutron rate matches for the reference runs with  $D_{\text{an}} = 0$  (black ‘x’s in panel a). Before the PID controller settings were improved, its results showed a similar trend to the  $D_{\text{an}} = 0$  reference runs, i.e. over-estimating the neutron rate, though not as severe in magnitude. The improved PID controller resulted in predicted neutron rates which were within 10% of the measured values (horizontal dotted lines in panels a-b), but the manual adjustment of  $D_{\text{an}}$  produced matches which were even closer (within 5%, see red diamonds in panels b and d). As seen in Figure 4.2a, close neutron rate matches were achieved with  $D_{\text{an}}$  evolving significantly throughout the modelled time slice, while Figure 4.2c shows that the values of  $D_{\text{an}}$  at transition time have a wide spread with  $\sim 0.8 - 6.8\text{m}^2\text{s}^{-1}$ , and the large error bars on some points show the fluctuating nature of the  $D_{\text{an}}$  time history.

During the process of manually adjusting the  $D_{\text{an}}$  time traces to achieve closer neutron rate matches between TRANSP and experimental measurements, some previous work by Ceconello *et al.* [86] investigating systematic discrepancies between the two on MAST was explored and conclusions were applied to the MAST dataset used in this Chapter. However, I realised afterwards that I had mistakenly assumed that neutron rates  $\nu_n$  measured by the two available neutron diagnostics, the fission chamber and the neutron camera (which is to be introduced in Appendix B), should be in reasonable agreement, and that therefore the systematic discrepancy between measured and predicted neutron rate would be similar for both, while the paper [86] actually showed that they were significantly different and the neutron deficit actually occurred in the opposite direction for the two diagnostics. At this point there was no more time to re-do the TRANSP runs required to show the effects of the fission chamber discrepancy, so the work on this with the mistaken assumptions is instead presented in Appendix B.

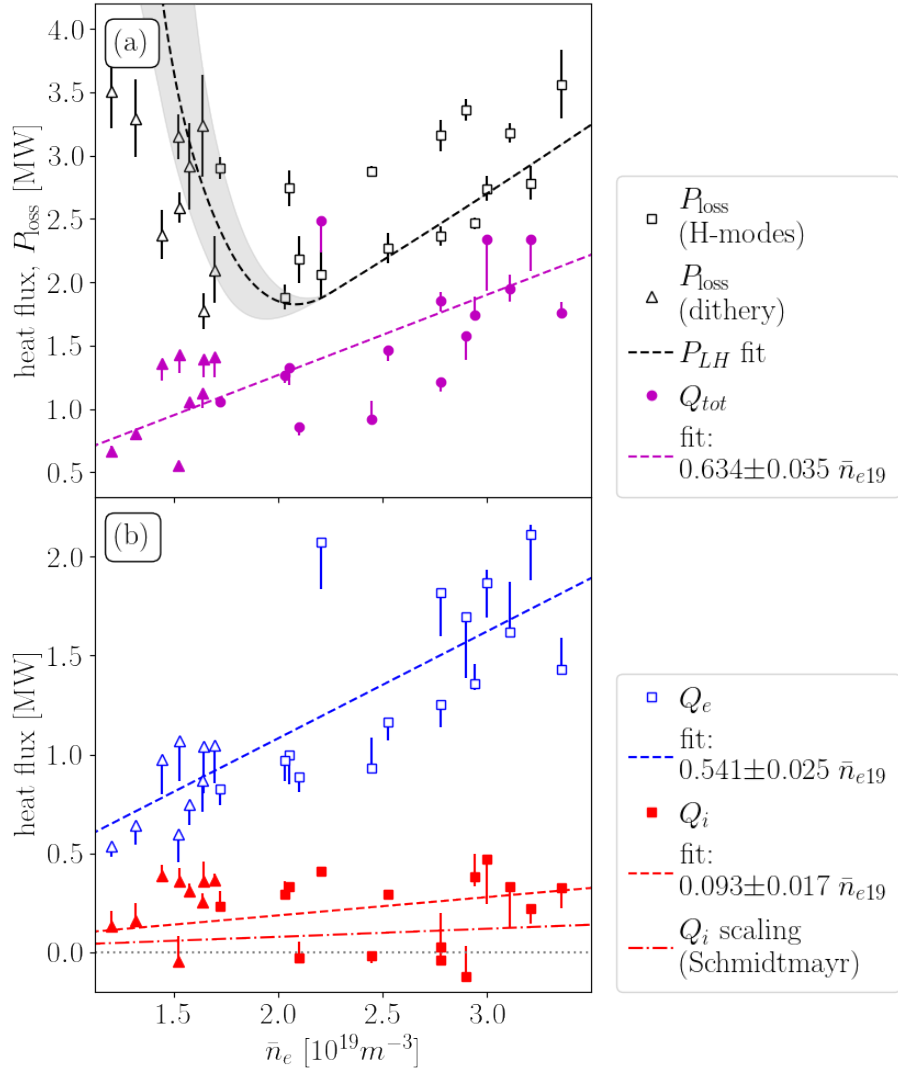


Figure 4.4: (a)  $P_{\text{loss}}$  and total heat flux  $Q_{\text{tot}}$  values shown for selected L-H transitions (squares) and some low-density dithery periods (triangles). Also shown are the  $P_{LH}$  density fit from Section 5 and a linear density fit for  $Q_{\text{tot}}$ . (b) The  $Q_e$  and  $Q_i$  values at the separatrix for these points, with corresponding linear density fits and the  $Q_i$  density scaling from [29]. The error bars represent the range of values between  $0.85 < \rho_N < 1.0$ .

### 4.3 Results

Figure 4.4 shows the results of the heat flux analysis at the separatrix against line-averaged electron density for selected L-H transitions (squares) and dithery periods in the low density region (triangles). The associated  $P_{\text{loss}}$  values are shown alongside the total heat flux  $Q_{\text{tot}} = Q_e + Q_i$  in panel (a). The non-monotonic density dependence of  $P_{LH}$  is contrasted with the fairly linear density dependence of  $Q_{\text{tot}}$ , such that a low-density shot has a lower  $Q_{\text{tot}}$

than a high-density shot with the same  $P_{\text{loss}}$ . Panel (b) shows the electron and ion heat fluxes,  $Q_e$  and  $Q_i$  respectively. Since occasional mismatches between diagnostic data and EFIT equilibrium introduce a small uncertainty in the separatrix location, error bars are plotted on  $Q_e$  and  $Q_i$  showing the range of values for  $0.85 < \rho_N < 1.0$  with  $\rho_N$  as defined by TRANSP, using the equilibrium provided by the EFIT calculations performed during the TRANSP setup (and  $\rho_N$  is equivalent to  $\rho_{\text{eff},N}$  as defined in Section 2.1). Previous studies found a linear  $\bar{n}_e$  dependence for  $Q_i$ , so the data was fit with linear fits for both  $Q_i$  and  $Q_e$ , with  $Q_{i,\text{fit}} = 0.09\bar{n}_{e19}$  and  $Q_{e,\text{fit}} = 0.54\bar{n}_{e19}$  for units of MW and  $10^{19}m^{-3}$ . The scaling for  $Q_i$  from AUG and C-Mod (named here after the lead author Schmidtmayr) [29],

$$Q_{i,\text{scal}}^{LH} = 0.0029\bar{n}_{e19}^{1.05\pm 0.1} B_T^{0.68\pm 0.3} S^{0.93\pm 0.2} \quad (4.6)$$

predicts  $Q_{i,\text{scal}} \simeq 0.037\bar{n}_{e19}$  for MAST (shown as a dot-dashed line), which is lower than that found for the data here. However, while a linear density dependence for  $Q_e$  fits the data reasonably well, the  $Q_i$  data shows significant scatter and the linear fit is poor, with  $R^2 = -0.18$ , suggesting that for this data  $Q_i$  shows no density dependence. By contrast, the linear density fits for  $Q_e$  and  $Q_{\text{tot}}$  have  $R^2$  values of 0.61 and 0.44 respectively. The  $Q_i$  values mostly lie above the scaling from [29], though in some cases  $Q_i$  is negative. The linear density dependence of  $Q_e$  which is clearly seen in Figure 4.4b was not seen on other devices. The fraction of  $Q_{\text{tot}}$  contributed by  $Q_e$  is consistently high throughout the density range, with  $Q_i$  contributing less than 30%.

The terms in the energy balance are investigated to identify the sources of the density dependence. The largest contributions to  $Q_e$  and  $Q_i$  are the heating terms, specifically the heating by beams. The total beam heating of the plasma  $P_{\text{heat}}^{\text{NBI}}$  is the sum of the beam heating of the electrons, the beam heating of the ions, and the power from thermalised beam ions. It shows a clear density dependence with  $P_{\text{heat}}^{\text{NBI}} \approx 0.6\bar{n}_{e19}$ . Since  $P_{\text{heat}}^{\text{NBI}}$  was found to be much lower than the captured beam power  $P_{\text{cap}}^{\text{NBI}}$ , the beam heating and loss terms were studied in more detail to identify the cause of the discrepancy. As Figure 4.5 shows, there is a general trend of lower beam heating of the plasma  $P_{\text{heat}}^{\text{NBI}}$  for lower densities, independent of injected beam power  $P_{\text{inj}}^{\text{NBI}}$ . If  $P_{\text{heat}}^{\text{NBI}}$  is normalised to  $P_{\text{inj}}^{\text{NBI}}$ , we can see that in addition to the decreasing fraction of injected beam power heating the plasma (from  $\sim 75\%$  at high  $\bar{n}_e$  to  $\sim 15\%$  at low  $\bar{n}_e$ ), there is a second set of transitions which have higher heating fractions than

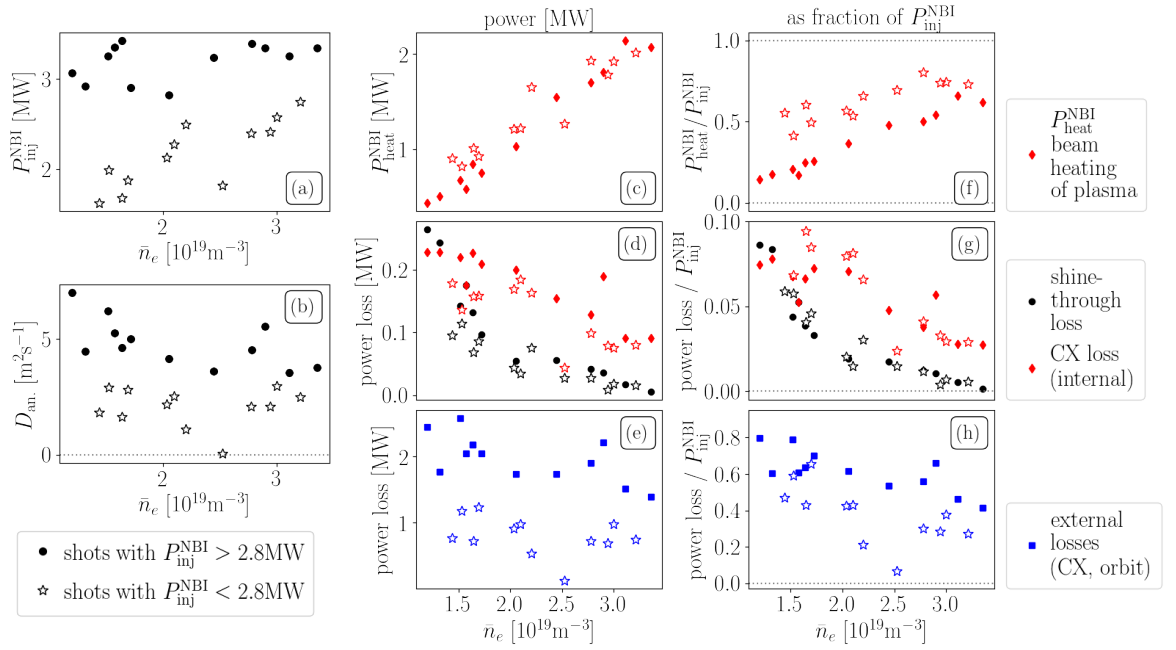


Figure 4.5: For all considered H-mode and dithery shots, the values at the transition are plotted for (a) the injected beam power  $P_{\text{inj}}^{\text{NBI}}$ , (b) the anomalous diffusivity  $D_{\text{an.}}$ , (c) the total beam heating of the plasma  $P_{\text{heat}}^{\text{NBI}}$  with all losses subtracted, (d) the shine-through and charge-exchange (re-neutralisation) losses inside the LCFS, and (e) the losses outside of the LCFS (charge-exchange and orbit losses). The right hand side panels (f)-(h) show the quantities (c)-(e) normalised to  $P_{\text{inj}}^{\text{NBI}}$ . In all plots, the open star symbols mark a set of transitions which occurred at lower  $P_{\text{inj}}^{\text{NBI}}$  ( $< 2.8 \text{MW}$ ).

transitions at equivalent density. These are marked with open star symbols in Figure 4.5. In the top left panel (a) of Figure 4.5, it can be seen that these points all had lower values of  $P_{\text{inj}}^{\text{NBI}}$ . These results suggest that the fraction of injected beam power which contributes to heating the plasma decreases for lower densities as well as for higher injected powers.

### 4.3.1 Beam heating efficiency

The clear density dependence of the beam heating of the plasma  $P_{\text{heat}}^{\text{NBI}}$ , with low-density plasmas of the same injected NBI power  $P_{\text{inj}}^{\text{NBI}}$  showing much lower heating than equivalent high-density plasmas, suggests a reduced efficiency of NBI and associated higher fast ion losses for lower densities. Figure 4.5 shows the losses which have been identified as possessing a density dependence with higher losses at low density. These are shine-through losses, orbit losses (beam ion is lost from confinement on its first poloidal orbit), and charge-exchange (re-neutralisation of beam ions) losses both inside and outside of the separatrix. Shine-through losses are taken into account in the  $P_{\text{loss}}$  study with the usage of  $P_{\text{cap}}^{\text{NBI}}$ , but while they show a

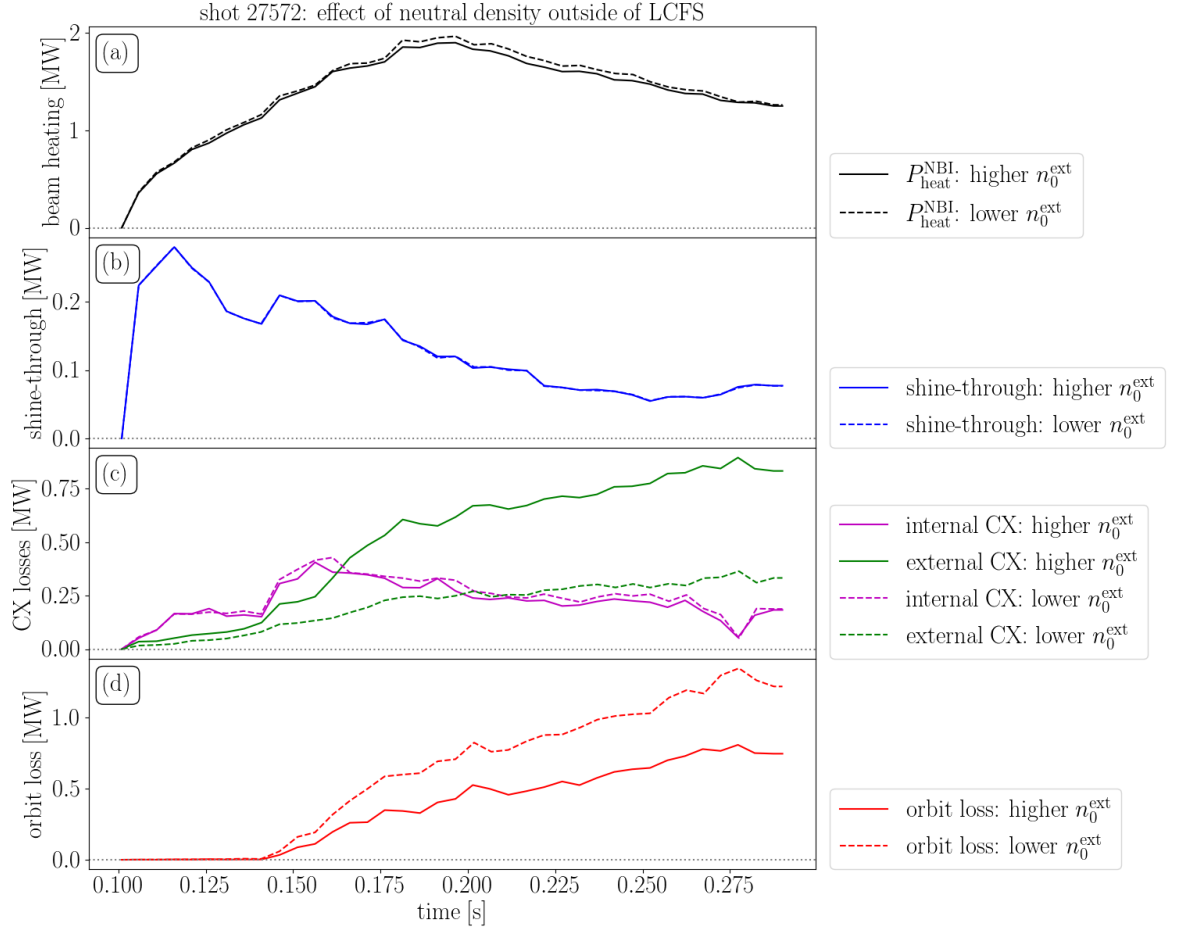


Figure 4.6: Two TRANSP runs with different values set for the neutral density outside the LCFS (solid lines:  $n_0^{\text{ext}} = 5.0 \times 10^{11} \text{cm}^{-3}$ , dashed lines:  $n_0^{\text{ext}} = 1.0 \times 10^{11} \text{cm}^{-3}$ ) are compared, showing (a) the beam heating of the plasma  $P_{\text{heat}}^{\text{NBI}}$ , (b) shine-through losses, (c) internal and external charge-exchange losses and (d) orbit losses. Shine-through losses are unaffected by the change in neutral density, as are the beam power absorbed by the plasma  $P_{\text{heat}}^{\text{NBI}}$  and internal charge-exchange losses (the slight difference in values is due to a discrepancy in anomalous diffusivity  $D_{\text{an}}$  as both were run with PID controller). The neutral density affects the type of external losses only, as the increase in external charge-exchange losses at higher neutral density is compensated by a decrease in orbit losses, such that the sum of the two external losses remains constant.

clear density dependence, their magnitude is much too low to account for the trend in  $P_{\text{heat}}^{\text{NBI}}$ . The largest loss terms are orbit losses and charge-exchange losses outside of the LCFS. As previously, the open star symbols denote a set of data with lower  $P_{\text{inj}}^{\text{NBI}}$ , and both orbit losses and charge-exchange losses outside of the LCFS are significantly lower for this set.

Shine-through losses are independent of the anomalous fast ion diffusivity  $D_{\text{an}}$ . Charge-exchange losses inside the LCFS are weakly dependent on  $D_{\text{an}}$ , while the external losses (orbit losses and charge-exchange losses outside of the LCFS) are strongly affected by the

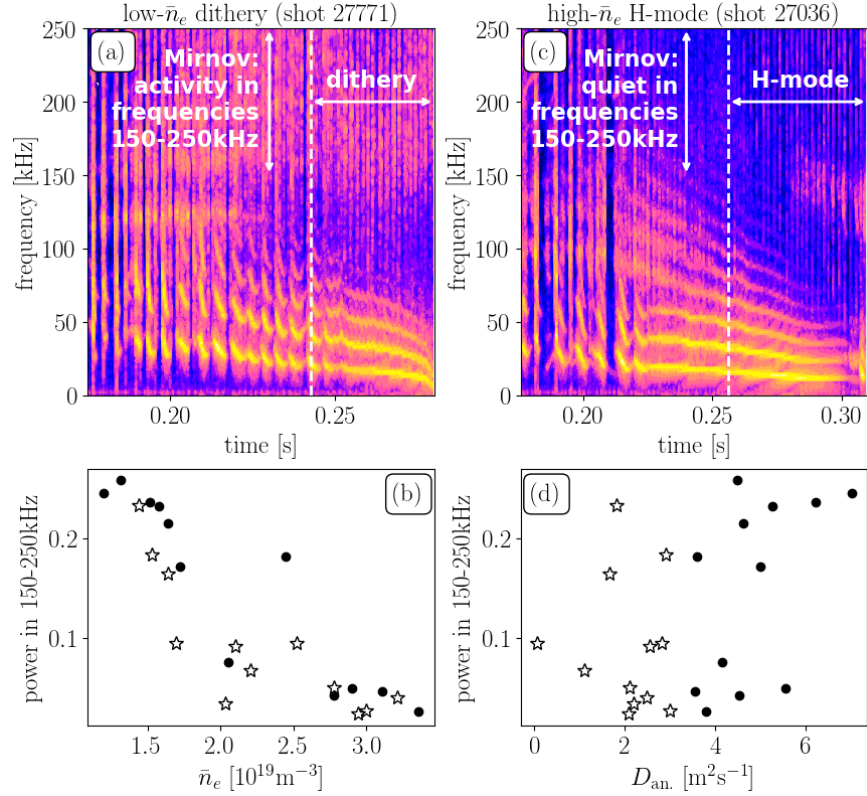


Figure 4.7: (a) shows the Mirnov coil spectrogram of a representative low-density shot (27771) with a transition to a dithery period at  $t = 0.242$  s and  $\bar{n}_e = 1.52 \times 10^{19} \text{m}^{-3}$ , while (c) shows a representative high-density shot (27036) with a transition to H-mode at  $t = 0.256$  s and  $\bar{n}_e = 3.11 \times 10^{19} \text{m}^{-3}$ . The low-density shots with higher fast ion diffusivity have stronger activity in the frequency range 150-250kHz, which is much reduced in the high-density cases. The power in this frequency range is plotted for all cases against line-averaged density in (b) and against anomalous diffusivity in (d). The open star symbols mark a set of transitions which occurred at lower  $P_{\text{inj}}^{\text{NBI}}$  ( $< 2.8$  MW) and had lower levels of fast ion losses.

value of  $D_{\text{an}}$ . The neutral density outside the LCFS determines the proportion of external losses which are due to charge-exchange, but the combined value of external losses remains constant if only the neutral density is varied, as seen in Figure 4.6. Since the neutral density outside the LCFS is not confidently known, the two external losses are combined for the results shown in Figure 4.5.

To investigate whether the increased fast ion losses at low densities or high beam powers estimated by TRANSP can be observed experimentally, the MHD activity was studied with Mirnov coil signals. Figure 4.7a and c shows representative examples of a low-density shot with a transition to a dithery period and a high-density shot with a transition to an ELMy H-mode. The low-density shot has a smaller fraction of the injected beam power heating the

plasma (0.21 vs 0.66 at transition time) with corresponding higher levels of power losses and a higher anomalous diffusion value ( $6.2 \text{ m}^2\text{s}^{-1}$  vs  $3.5 \text{ m}^2\text{s}^{-1}$ ). The spectrogram of a Mirnov coil is plotted for the entire  $I_p$  flat top. The discharges in this study generally start out with chirping modes, possibly fishbones (FBs) or TAEs (toroidal Alfvén eigenmodes), which then develop into a long-lived mode (LLM) of 15-20kHz, an internal kink mode matching the plasma rotation frequency [92], visible in the spectrogram with harmonics. Comparing the two cases in Figure 4.7, the low-density discharge has a longer period of chirping modes, and strong broadband mode activity in the frequencies 150-250kHz, which is largely absent from the high-density case. The increased activity in the 150-250kHz frequency range is found in all low-density shots.

The bottom two plots of Figure 4.7 show the power in the Mirnov signal for the frequency range of 150-250kHz plotted against line-averaged density (b) and anomalous fast ion diffusivity values  $D_{\text{an}}$  used in the TRANSP runs (d). The anomalous diffusion rate is larger for lower densities as well as for higher injected powers, suggesting that TRANSP assumes higher fast ion redistributions or losses for those situations. Some evidence of this can be seen in the Mirnov signals, with the power contained in the broadband MHD activity of frequency range 150 – 250kHz showing a strong density dependence. The power in the mode is determined from an integral of the relevant frequency range in the frequency spectrum. Looking at the Mirnov signal as it varies in time (like the second panel from the top of Figures 4.8-4.10), the signal amplitude shows no clear density dependence but appears to be lower for low  $P_{\text{inj}}^{\text{NBI}}$ , supporting the assumed lower fast ion losses for these discharges.

A number of previous studies into fast ion physics on MAST [86,89–91,93,94] have shown that stronger activity of certain MHD modes, notably frequency-chirping fishbones, TAEs, as well as LLMs [94], leads to increased redistribution and loss of the fast ion population. As was found in this project, previous studies have shown that these modes are excited at higher rates and amplitudes in low-density plasmas and in discharges with higher injected beam powers [89,93]. Depending on the density and NBI power, earlier studies on MAST have found that  $D_{\text{an}} \sim 0 - 3 \text{ m}^2\text{s}^{-1}$  were required to match neutron rates, which is the range required for low  $P_{\text{inj}}^{\text{NBI}}$  discharges in this study, while higher  $P_{\text{inj}}^{\text{NBI}}$  or low  $\bar{n}_e$  discharges required significantly larger  $D_{\text{an}}$  values of up to  $7 \text{ m}^2\text{s}^{-1}$  to match the neutron rates.

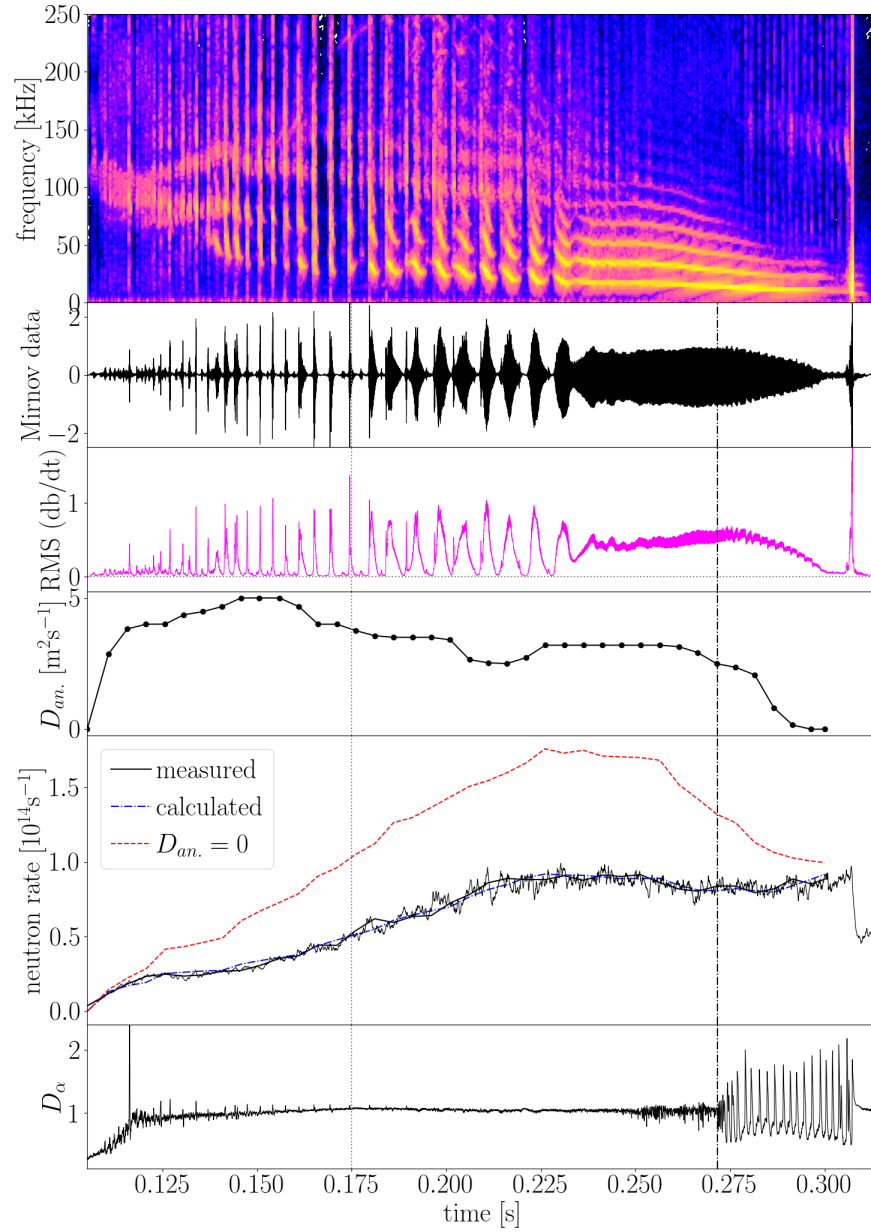


Figure 4.8: Representative evolution of MHD instabilities for an example high- $\bar{n}_e$  shot 27446 shown in Mirnov spectrogram, signal, r.m.s.,  $D_{an.}$ , neutron rates (measured and calculated) and  $D_\alpha$ . The current ramp up phase lasts until 0.175s (grey dotted line), and the transition is shown as a black dot-dashed line. The South beam starts at 0.1s with 2MW and the Southwest beam starts at 0.14s with 0.7MW, i.e. still during the  $I_p$  ramp-up phase, and last until the end of the plasma.

### 4.3.1.1 Fast ions on MAST

As previously noted, the vast majority of fusion reactions on MAST involve highly energetic (i.e. ‘fast’) beam ions, with fusion between thermal ions accounting for less than 1.5% of cases. The greatest source of fast ions are the two neutral heating beams, which result in large fast ion pressures and can excite MHD instabilities which in turn cause fast ion redistribution and losses, reducing the neutron emissivity and thus neutron rates. MHD instabilities can be driven by the background plasma equilibrium, such as sawtooth instabilities and edge localised modes (ELMs), or by the free-energy made available by the pressure from large NBI-driven super-Alfvénic fast ion populations with a steep spatial gradient, such as TAEs, FBs and LLMs, which are driven via the fundamental resonance  $v_{\parallel} = v_A$  (where  $v_A$  is the Alfvén velocity) [90, 94]. Compared with conventional tokamaks, the confining magnetic field in a spherical tokamak is quite small, resulting in the generation of fast ions with large Larmor radii  $\rho_L$  (see Equation 1.12). The small size of MAST plasmas compared with the fast ion  $\rho_L$  combined with the steep gradients in density and temperature can affect the neutron emissivity, and the fact that NUBEAM uses approximations rather than modelling full Larmor orbits could explain why such high  $D_{\text{an}}$  were required to match the TRANSP-predicted neutron rates with those measured by the fission chamber.

From an inspection of Mirnov coil diagnostic data (spectrograms, signal amplitude and r.m.s. time histories) for the NBI-heated phase of all discharges in this dataset, a common theme in the evolution of MHD modes emerges. Mirnov data for an example shot is shown in Figure 4.8 along with the anomalous diffusivity, neutron rates and  $D_{\alpha}$  signal. In general, the MHD history starts with toroidal Alfvén eigenmodes (TAEs) shortly after the beam start time during the current ramp up, with regular short-lived bursts at 80 – 110 kHz (until 0.13s, magnified view shown in Figure 4.9a). The fundamental frequency of these TAEs decreases while the plasma is still in the ramp up phase, evolving into frequency-chirping TAEs (until 0.175s, magnified view shown in Figure 4.9b) followed by chirping fishbones in most cases before the current flat top phase has developed (until 0.228s, magnified view shown in Figure 4.10a). The term “frequency-chirping” describes the quick downward trend in frequency occurring at each TAE or fishbone burst, which evolves from 100 → 40 kHz chirps in 1 – 2ms bursts for TAEs to 45 → 18kHz chirps of 3-5ms duration for fishbones. During these chirping phases, the individual bursts show a rapid decrease in frequency with the initial frequency mostly recovered with the start of the following burst, combined with

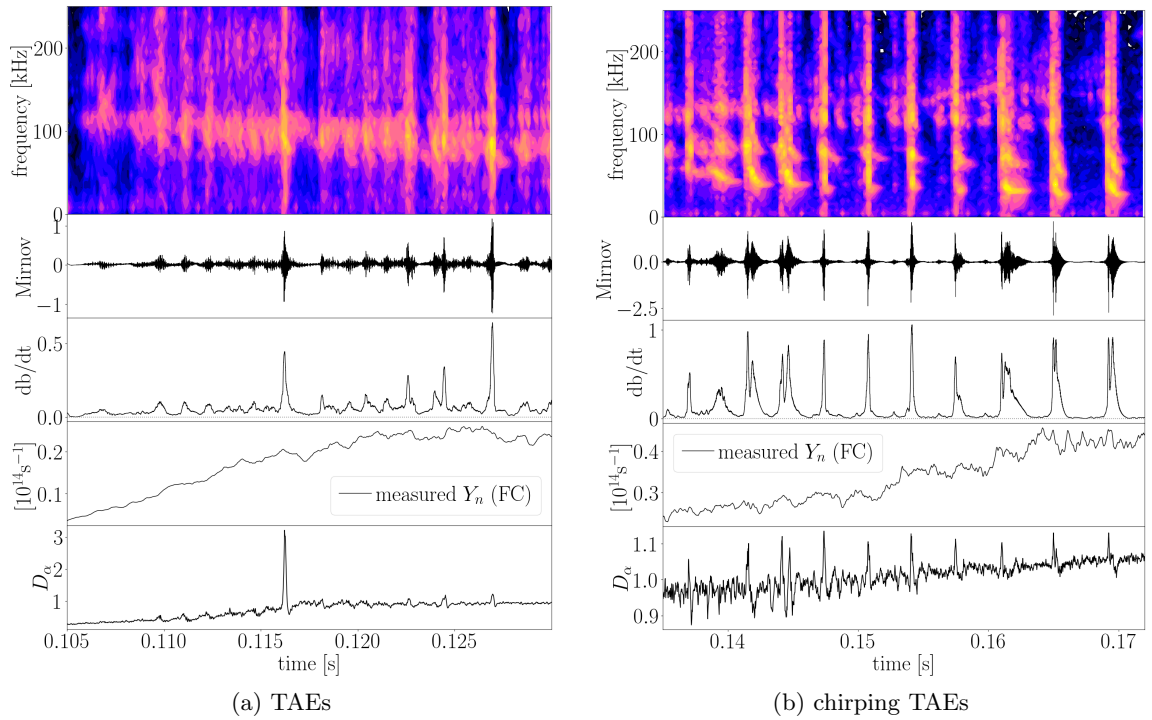


Figure 4.9: Close-ups of shot 27446: Initial (a) TAEs and (b) chirping TAEs shown in Mirnov spectrogram, signal, r.m.s., measured neutron rate and  $D_\alpha$ .

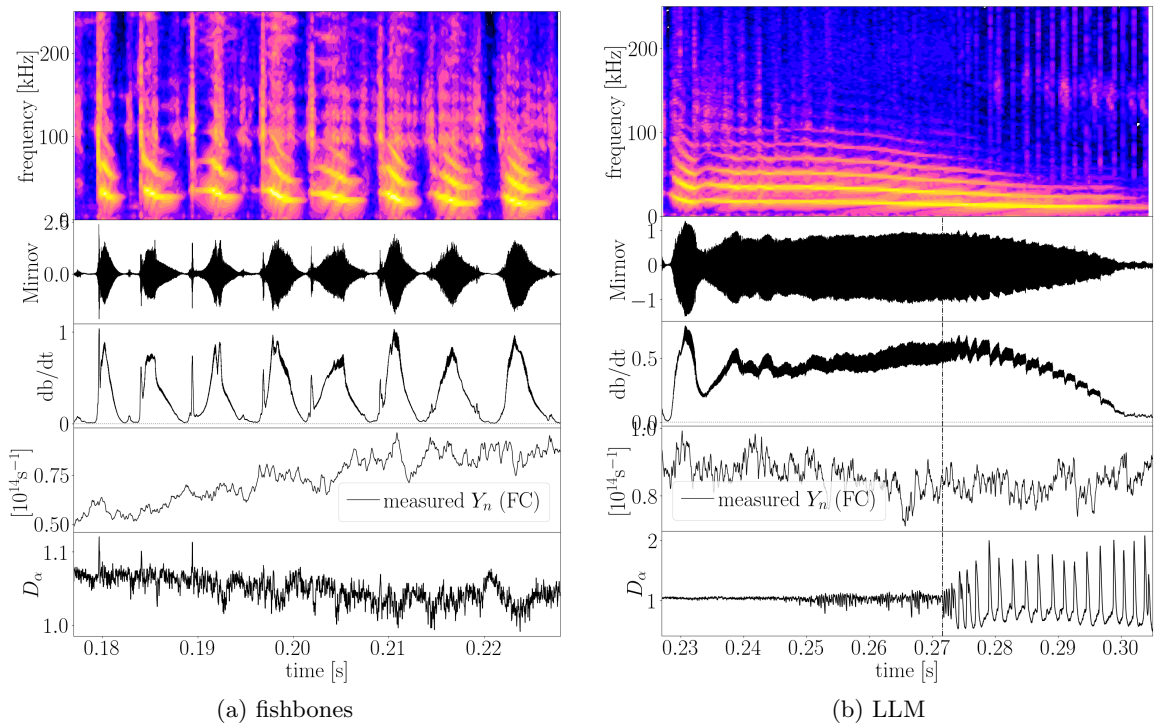


Figure 4.10: Close-ups of shot 27446: (a) fishbones and (b) LLM shown in Mirnov spectrogram, signal, r.m.s., measured neutron rate and  $D_\alpha$ .

a general trend of decreasing frequency, increasing burst-length and increasing wait time between bursts. During the flat top phase, the chirps continue to grow longer, until they evolve into a single continuous long-lived mode (LLM) which generally continues to exhibit a steady decrease in frequency from 25kHz to 8-12kHz (also known as “slowing down”) over a period of 40 – 100ms (until 0.305s, magnified view shown in Figure 4.10b). The LLM can slow down gradually or in some cases rapidly come to an abrupt halt below 5kHz with a locked mode, which results in sharp drops in density and neutron rate, a back-transition (if in H-mode or diathermy phase) and a subsequent quiet period in the Mirnov signal. An example of such a locked mode is shown in Figure 4.11, with the rapid decrease in LLM frequency and cessation of MHD activity seen in the Mirnov signal and spectrogram, and the apparent halt in plasma rotation seen in the CXRS measurement in the middle panel. The back-transition and density drop are also visible.

TAEs occur at frequencies corresponding to the toroidicity-induced gap in the Alfvén continuum (around 100kHz) [90] and are normal modes of the background plasma especially early in the discharges. As the discharge progresses, the TAEs can additionally be driven by beam ions through coupling to an energetic particle mode (EPM), resulting in the frequency-chirping and deviation from the TAE frequency as well as less regular duration and spacing between bursts. The fishbones which follow on are meanwhile EPMS with frequency chirps of longer duration, more regular and longer spacing between bursts, and frequencies approaching the core toroidal rotation frequency. When this frequency is reached, the fishbones evolve into a continuous long-lived mode with a fundamental frequency coinciding with the toroidal rotation [92], hence why a decrease in this frequency is also described as a “slowing down” of the plasma. All of these modes are closely related to the ideal-MHD internal kink mode with a rigid deformation of the region inside the  $q = 1$  magnetic flux surface [90]. These chirping and long-lived modes are also prominently visible in the BES fluctuation data, which lead to the BES data for this dataset not being usable for turbulence studies.

The general trend of the evolution of MHD instabilities seen in this dataset is characteristic of MAST and was observed throughout its runtime, such as during numerous fast ion studies [86, 89–91, 93, 94]. The extensive body of work on fast ion studies on MAST allow us to assume with reasonable confidence that the MHD modes and features seen in this dataset which closely match those studied in previous papers also indicate the presence of significant amounts of fast ion redistribution and losses. At this time it was not possible

to do the comprehensive work to independently measure the level of fast ion losses for the selected discharges themselves, as of the suite of fusion product diagnostics only the fission chamber had provided data to analyse, and the FC data was not sensitive enough to discern the effects from individual TAE bursts or fishbones [90].

### 4.3.2 Consequences for the $P_{LH}$ curve

These results appear to suggest that neutral beam heating becomes much less efficient with lower plasma densities, and also separately with higher injected beam power. While the lower heating efficiencies for low densities was also found on ASDEX Upgrade and other devices (devices of similar size to MAST), the suggested explanation of reduced electron-ion coupling does not appear to be a major concern here, instead the diminished heating efficiency affects both ion and electron heating and is likely to be caused by fast ion losses degrading beam performance. An alternative version of the power threshold plot that takes fast ion losses into account can be created by using  $P_{\text{loss,th}}(\bar{n}_e)$  instead of  $P_{\text{loss}}(\bar{n}_e)$ . For this, the captured beam power  $P_{\text{cap}}^{\text{NBI}}$  is replaced by the beam heating of the plasma  $P_{\text{heat}}^{\text{NBI}}$ . The results are shown in Figure 4.12b, along with the Takizuka scaling [80]. The scatter in the H-mode points has been significantly reduced. A fit to the H-mode points returns  $P_{LH} = (12.24 \pm 2.14) \times \bar{n}_{e20}^{(1.53 \pm 0.14)}$  (with an  $R^2$  value of 0.92), which has a higher density exponent than the previous fit and widely used scalings. The values are reduced compared with  $P_{\text{loss}}$ , but still significantly higher than those predicted by the scaling. While the low-density branch is not as clearly visible in the new H-mode points, several of the dithery points still lie above the fit, which together with the lack of low-density H-modes suggests that a low-density branch or low-density limit still exists and is not entirely explained by the reduced beam heating efficiency. It is important to note as well that even with the available injected beam power (though it resulted in much lower  $P_{\text{heat}}^{\text{NBI}}$  values, as seen in Figure 4.12c) the “dithery” points at low  $\bar{n}_e$  never achieved a transition to a full H-mode period. The reduced scatter in H-mode points can be traced back to the strong density dependence of  $P_{\text{heat}}^{\text{NBI}}$ , shown in the top right of Figure 4.12, while the higher  $P_{\text{loss,th}}$  values for the dithery transitions are due to lower values of  $dW/dt$ , as seen in the bottom right plot.  $dW/dt$  appears to follow an inverse U-curve, although the maximum occurs at a higher density than  $n_{e,\text{min}}$ . In a practical use of  $P_{LH}$  scalings, the higher injected NBI power required for H-mode access at low densities is also still relevant, as it can introduce limitations on operation.

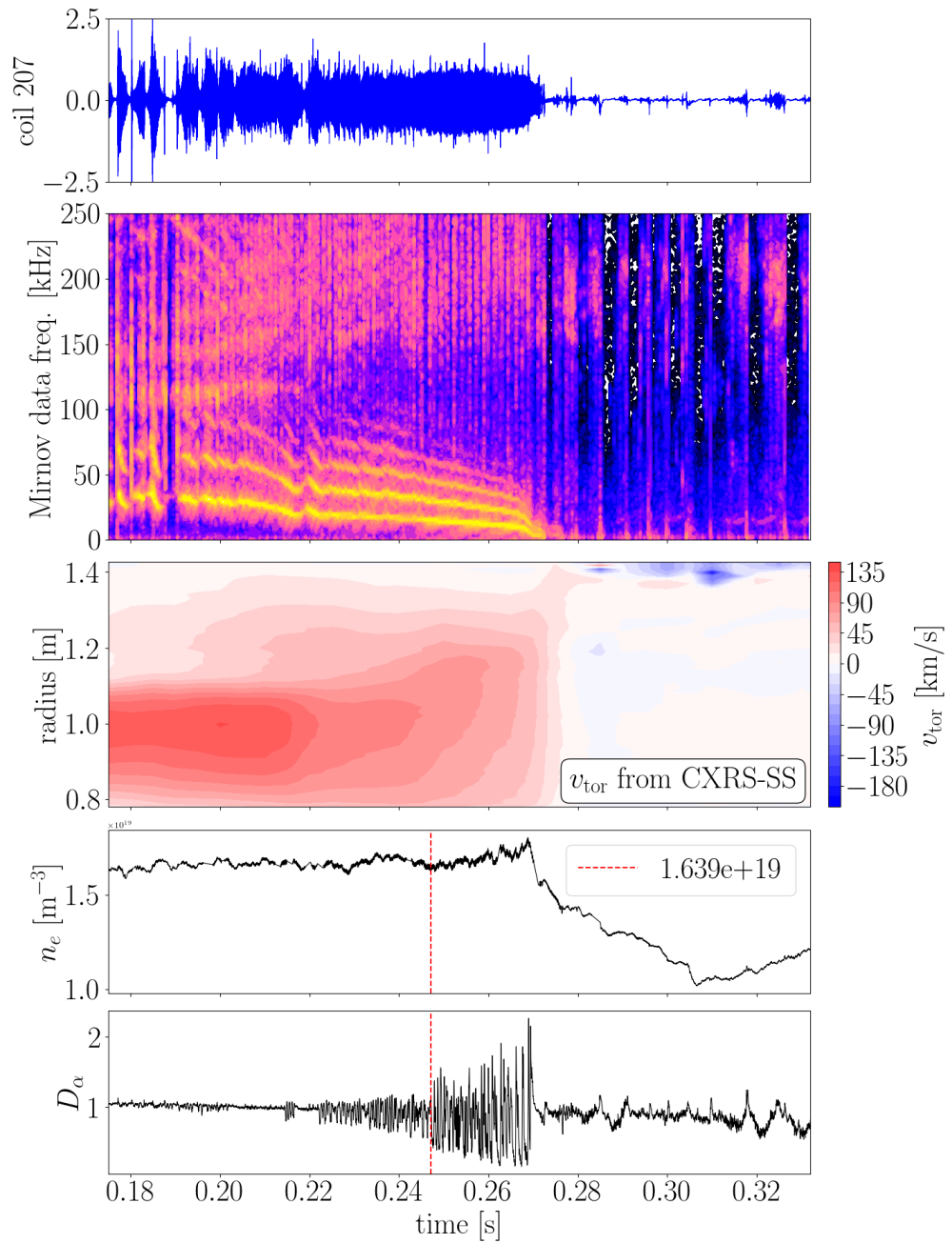


Figure 4.11: Example of a locked mode as seen in (from top to bottom): Mirnov coil signal and spectrogram, plasma rotation velocity measured with CXRS on the South beam, line-averaged density, and  $D_\alpha$ . The long-lived mode rapidly decreases in frequency, MHD mode activity and plasma rotation stop, which causes a back-transition and a large-scale loss in density. The red dashed lines in the bottom two plots show the transition time to a dihyery period.

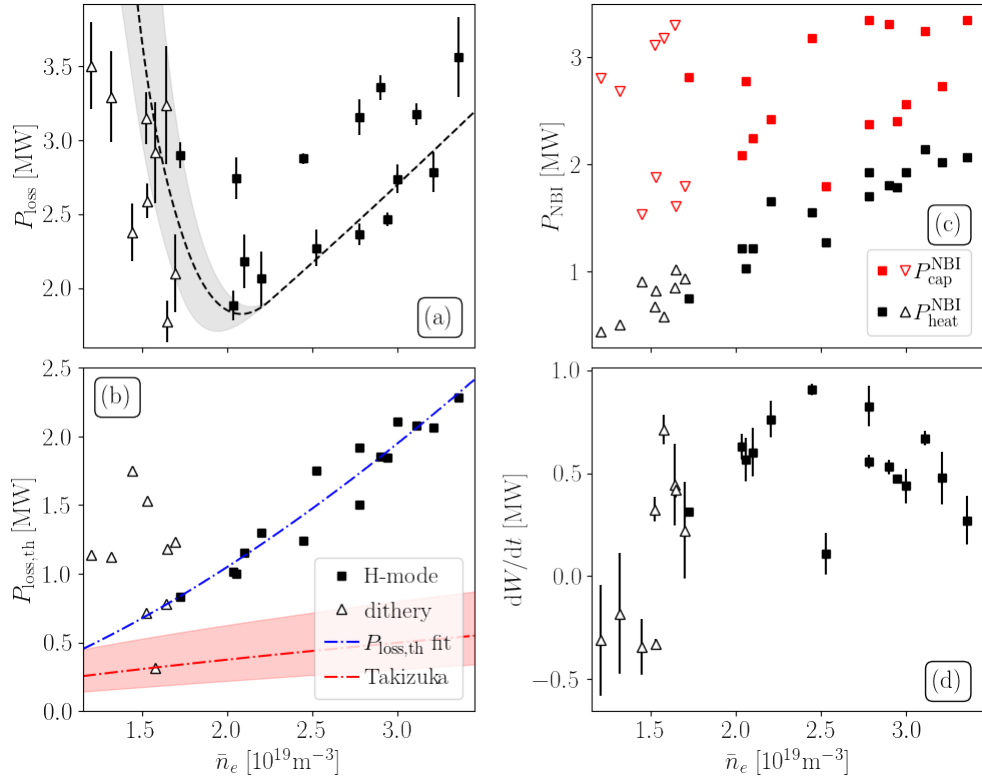
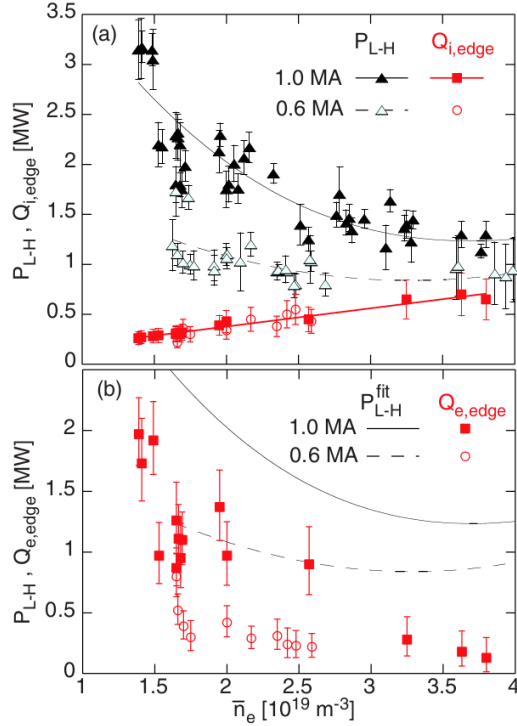


Figure 4.12: (a)  $P_{\text{loss}}$  vs  $\bar{n}_e$  for the previous method, which uses  $P_{\text{NBI}} = P_{\text{cap}}^{\text{NBI}}$ , and  $P_{\text{loss,th}}$  (b), which uses the calculated beam heating of electrons and ions,  $P_{\text{NBI}} = P_{\text{heat}}^{\text{NBI}}$ , instead. A fit to the H-mode points is shown in blue, and the Takizuka scaling [80] in red.  $P_{\text{cap}}^{\text{NBI}}$  and  $P_{\text{heat}}^{\text{NBI}}$  are compared in (c), while the  $dW/dt$  values are shown in (d).

### 4.3.3 Comparison with results from other devices

The most comprehensive results to compare with were obtained by Ryter *et al.* [1] for the ASDEX Upgrade paper this work is based on. Most of the discharges in that paper were heated with ECRH, with a few additional ones heated with a mixture of ECRH and NBI or NBI alone. The dataset of ECRH-heated L-H transitions is the basis for the authors' conclusions, finding a linear density dependence of  $Q_{i,\text{edge}}$  for the density range of the low-density branch of  $P_{LH}$ . This is seen in Figure 4.13a in the top panel. This density dependence also appears to be independent of the plasma current. The linear  $\bar{n}_e$  dependence of  $Q_{i,\text{edge}}$  was 'compensated' by  $Q_{e,\text{edge}}$  following a similar  $\bar{n}_e$  dependence as  $P_{LH}$ , i.e. increasing for decreasing  $\bar{n}_e$  as seen in the bottom panel of Figure 4.13a.  $Q_{e,\text{edge}}$  decreased to almost zero towards  $n_{e,\text{min}}$ , but with the high-density branch not shown it is not clear whether  $Q_{e,\text{edge}}$  would remain near zero or increase again with increasing density. Contrasting these results with ours, on MAST it was  $Q_{e,\text{edge}}$  which followed a linear  $\bar{n}_e$  dependence, and  $Q_{i,\text{edge}}$  showed



**Figure 1. L-H transitions with ECRH:** (a):  $P_{L-H}$ , normalized with  $B_T^{0.8}$  to  $B_T = 2.35$  T, and  $Q_{i,edge}^{L-H}$  versus line-averaged density at the L-H transition for 1 and 0.6 MA discharges. The lines are fits to the data. (b):  $Q_{e,edge}$  corresponding to the  $Q_{i,edge}$  data from (a). The lines are the  $P_{L-H}$  fits of (a), plotted for reference.

(a) Fig. 1 in reference

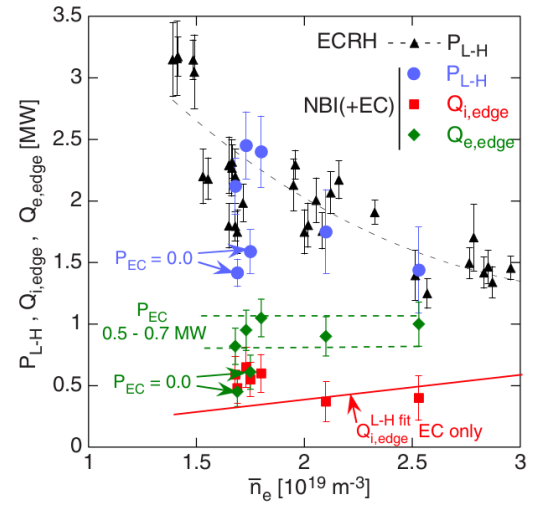


**Figure 7. L-H transitions at 1 MA:**  $P_{L-H}$  for ECRH transitions normalized with  $B_T^{0.8}$  to  $B_T = 2.35$  T and corresponding fit from figure 1.  $P_{L-H}$ ,  $Q_{i,edge}^{L-H}$  and  $Q_{e,edge}^{L-H}$  for the NBI(+EC) cases versus line-averaged density. For reference  $Q_{i,edge}^{L-H,fit}$  of figure 1 is also reported.

(b) Fig. 7 in reference

Figure 4.13: [ASDEX Upgrade results, reproduced from [1]] (a) Fig. 1: showing the ECRH-heated results for the density dependence of the low-density branch for  $P_{LH}$  and  $Q_{i,edge}$  in the top panel and  $Q_{e,edge}$  in the bottom panel. (b) Fig. 7: showing the NBI-heated results for low-density  $P_{LH}$ ,  $Q_{i,edge}$  and  $Q_{e,edge}$  along with (for reference) ECRH-heated  $P_{LH}$  and  $Q_{i,edge}$  density fit.

no clear density dependence.

The choice of heating method clearly affects the behaviour of the edge heat flux quite significantly, and we should probably not expect NBI-heated MAST plasmas to behave similarly to ECRH-heated ASDEX Upgrade plasmas. We can instead look at the results for NBI-heated ASDEX Upgrade plasmas, shown in Figure 4.13b. First we look at those plasmas which were heated with a mix of NBI and ECRH. Both  $Q_{i,\text{edge}}$  and  $Q_{e,\text{edge}}$  showed no clear density dependence, resulting in  $Q_{\text{tot}} = Q_e + Q_i$  appearing approximately constant for the measured density range, while  $P_{LH}$  for the same shots shows the characteristic low-density branch. This mismatch in the  $\bar{n}_e$  dependence of  $Q_{\text{tot}}$  and  $P_{LH}$  could be equivalent to the MAST case where shots with the same  $P_{\text{loss}}$  have different  $Q_{\text{tot}}$ , and could be an NBI feature. There are only two datapoints with pure NBI heating, and comparing them to equivalent-density shots with NBI + ECRH heating shows they have reduced values of  $P_{LH}$  and  $Q_{e,\text{edge}}$  while  $Q_{i,\text{edge}}$  appears to remain unchanged.

It is unfortunately difficult to draw any conclusions with the low number of discharges available, but the apparently constant  $Q_{i,\text{edge}}$  across the low-density branch for NBI-heated shots on ASDEX Upgrade is consistent with similar findings on MAST (see Figure 4.4). The strong density dependence of  $Q_{e,\text{edge}}$  found on MAST however was not seen for any heating method on ASDEX Upgrade.

## Chapter 5

# Turbulence studies

### 5.1 Motivation, background and previous work

Understanding and modelling the transition from L- to H-mode requires making a connection between the microscopic physics that leads to the transition and the macroscopic phenomenology of transport behaviour [95, 96]. Research into the microscopic physics of the L-H transition trigger has demonstrated the significance of the depletion of turbulence power through nonlinear kinetic energy transfer to zonal flows experimentally using Langmuir probes on EAST [97, 98], beam emission spectroscopy on DIII-D [99, 100], and gas puff imaging on C-Mod [95, 101]. Results from several studies [27, 96, 100, 101] show that the nonlinear kinetic energy transfer from drift wave turbulence to shear flow (zonal flow) is consistent with the observed turbulence power loss during a confinement transition. On the other hand, studies on ASDEX Upgrade [102] have shown the turbulent driven flows in the lead up to the L-H transition to be small, with the  $\mathbf{E} \times \mathbf{B}$  velocity dominated by mean flows. These conflicting reports show that there is not yet a consensus on the physics of the transition and more studies on this topic are required.

With both parts of the transition behaviour clearly relevant, it makes sense to study the L-H transition through the simultaneous evolution of turbulent scales and sheared  $\mathbf{E} \times \mathbf{B}$  flows [95, 96]. Using Reynolds decomposition,  $v = \langle v \rangle + \tilde{v}$ , where  $\tilde{v}$  is the fluctuation velocity, which averages out to zero as  $\langle \tilde{v} \rangle = 0$ , the momentum equation can be written as

$$\partial_t \langle v_\theta \rangle + \partial_r \langle \tilde{v}_r \tilde{v}_\theta \rangle = \mu \partial_r^2 \langle v_\theta \rangle. \quad (5.1)$$

This decomposition separates the slowly evolving flow and the fast broadband fluctuations, so that expressions for the kinetic energy of each can be obtained. Summarising the drive terms in  $\gamma_{\text{eff}}$  and the dissipative terms in  $\nu_{\text{LF}}$ , a set of model equations (described in [27, 95, 101, 103, 104]) for transition transfer dynamics can be written in the form of a standard  $K - \epsilon$  turbulence model framework [105] as

$$\begin{aligned}\partial_t \tilde{K} &= \gamma_{\text{eff}} \tilde{K} - P - \partial_r \tilde{T} \\ \partial_t \bar{K} &= P - \partial_r \bar{T} - \nu_{\text{LF}} \bar{K}\end{aligned}\quad (5.2)$$

with

$$P = \langle \tilde{v}_r \tilde{v}_\theta \rangle \partial_r \langle v_\theta \rangle, \quad \tilde{K} = \frac{1}{2} \langle \tilde{v}_\perp^2 \rangle, \quad \tilde{T} = \frac{1}{2} \langle \tilde{v}_r \tilde{v}_\theta^2 \rangle, \quad \bar{K} = \frac{1}{2} \langle v_\theta \rangle^2, \quad \bar{T} = \langle \tilde{v}_r \tilde{v}_\theta \rangle \langle v_\theta \rangle \quad (5.3)$$

where  $P$  represents a zonal flow production term,  $K$  are kinetic energies and  $T$  Reynolds stresses. The Reynolds work is represented by  $P - \partial_r \bar{T}$ , while the loss of turbulence kinetic energy is  $P + \partial_r \tilde{T}$ . Balancing the terms on the r.h.s. of equation 5.2 gives a condition for the onset of rapid turbulence suppression as

$$R_T \equiv \frac{P + \partial_r \tilde{T}}{\gamma_{\text{eff}} \tilde{K}} > 1 \quad (5.4)$$

which denotes the point at which there is enough energy transfer into ZFs to overcome the turbulence drive [95]. The parameter  $R_T$  represents a dimensionless production parameter [101], and the fulfillment of the condition  $R_T > 1$  during the transition is illustrated in figure 5.1a. As can be seen in figure 5.1b, the turbulent kinetic energy is suppressed along the entire radial correlation length during the transition, the kinetic energy transfer (and zonal flow production) however is localised to a narrow radial region in the edge.

Previous studies by Cziegler *et al.* [95] of the turbulence power and transfer during transitions from L- to H-mode have revealed a time sequence for the phenomena occurring during a transition. First the normalised Reynolds power peaks, then the turbulence power collapses, followed by a rise of the diamagnetic electric field shear, which marks the L-H transition. The observed growth in low frequency GPI velocity begins about 0.3 – 0.5ms before the  $D_\alpha$  signal drop. The steep edge gradients develop on a slower (1ms) timescale only after the turbulence phenomena have caused a transition, locking in the new H-mode

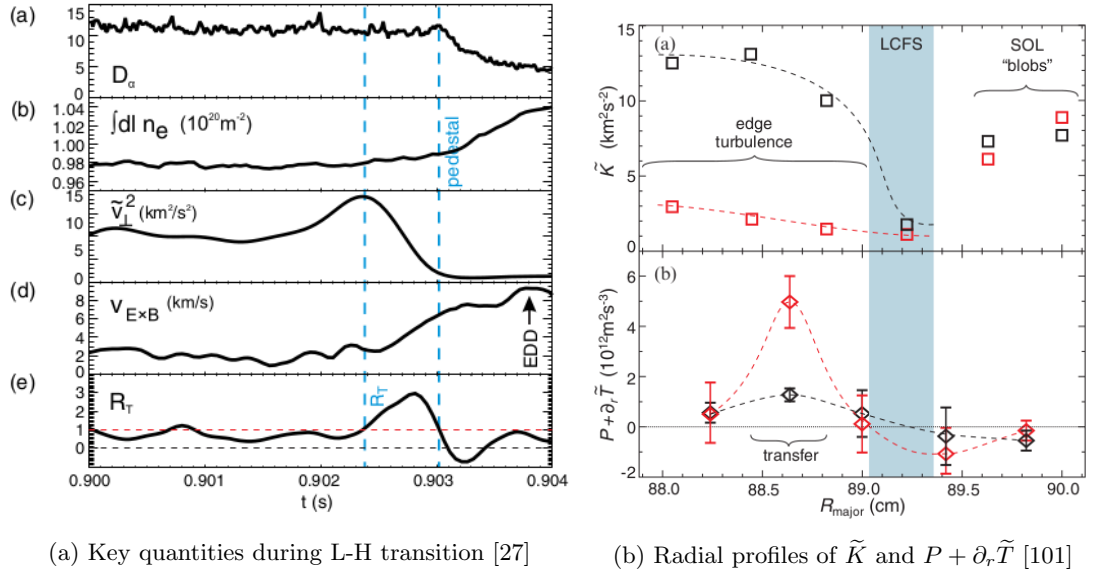


Figure 5.1: (a) [Reproduced from [27]] Time traces of  $D_\alpha$  signal, line-averaged density, turbulent kinetic energy, zonal flow, and normalised nonlinear turbulence damping during a transition. The first dashed line marks the condition  $R_T > 1$ , and the second line marks the drop in  $D_\alpha$  and pedestal formation. (b) [Reproduced from [101]] Radial profiles for total turbulent kinetic energy (top) and total kinetic energy transfer (bottom) for L-mode (black) and L-H transition (red).

state. Figure 5.1a illustrates the time sequence, with the growth in turbulence energy shortly followed by turbulence collapse ( $R_T > 1$ ), and only afterwards the growth of the pedestal and the drop in  $D_\alpha$ .

For a full predictive model and necessary understanding of the transition, not just the identification of the immediate trigger but also the changes leading up to it and the evolution of turbulence in L-mode are important to study. As with many plasma physics topics, the theoretical models often appear after the experimental evidence, and since there is currently no tested model explaining the nonlinear transfer processes leading up to the transition, experimental studies are vital for this topic [101].

The nonlinear kinetic energy transfer from source  $f_1$  to target  $f$  frequencies especially as applied to the spectral transfer from turbulence to zonal flows is calculated from

$$T_v(f, f_1) = -\text{Re}(\langle \tilde{v}_\theta^*(f) \tilde{v}_r(f - f_1) \partial_r \tilde{v}_\theta(f_1) \rangle) \quad (5.5)$$

where  $\tilde{v}_\theta^*(f)$  is a complex conjugate. Some results from previous studies on spectral transfer and coupling of Alcator C-Mod GPI data performed by Cziegler *et al.* [27, 101] are shown

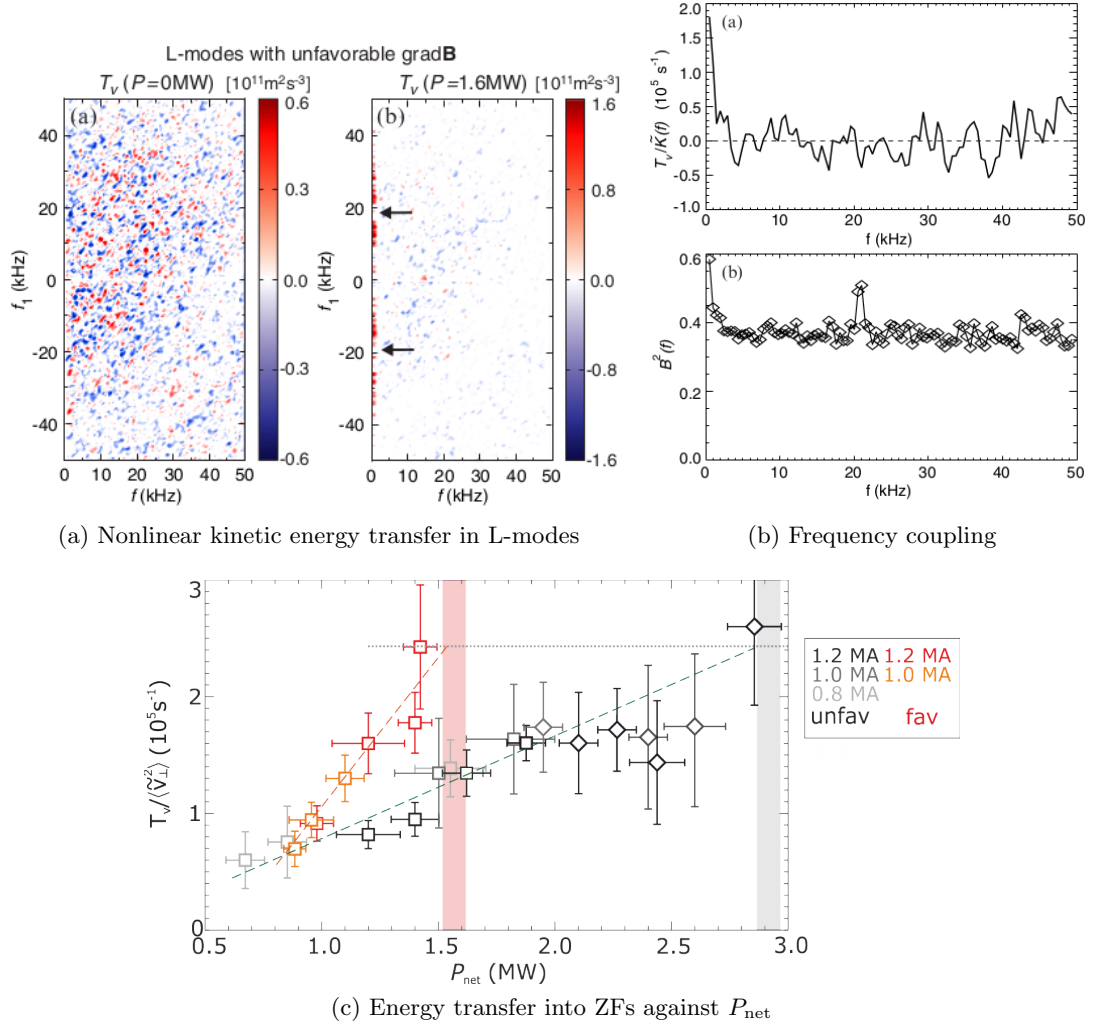


Figure 5.2: (a) [Reproduced from [101]] Nonlinear kinetic energy transfer as measured by GPI velocimetry for ohmic (left) and heated (right) L-modes in unfavourable  $\nabla \mathbf{B}$  configuration.  $P$  here refers to the auxiliary input power. (b) [Reproduced from [101]] Net kinetic energy transfer (top), showing only the ZF coupling, compared with summed bicoherence (bottom), showing both ZF and geodesic acoustic mode (GAM) coupling. (c) [Adapted from [27]] Nonlinear energy transfer into zonal flows against net power  $P_{\text{net}}$  in L-mode (squares) and I-mode (diamonds) for favourable (red and orange) and unfavourable (black and grey) configurations, showing that for the different threshold powers of favourable and unfavourable configurations, the transition into H-mode occurs at the same level of energy transfer.

in Figure 5.2. The energy transfer  $T_v$  can be represented visually with a bispectrum, such as for ohmic and heated L-modes in Figure 5.2a [101] where the latter case shows strong transfer from broadband source frequencies  $f_1$  to target frequencies  $f \sim f_{ZF}$  corresponding to zonal flows. The transfer rate into ZFs  $T_v(f = f_{ZF})$  for plasmas approaching H-mode in favourable (red and orange) and unfavourable (black and grey) configurations are shown in Figure 5.2c [27], highlighting that even with  $P_{LH}$  doubled in the unfavourable case, the value of  $T_v(f = f_{ZF})$  at H-mode entry appears to be the same for both cases.

Provided the plasma is in a long enough steady state, such as during quiescent L-mode periods, the strength of phase coupling between spectral components can be measured with the directionless bicoherence

$$b^2(f, f_1) = \frac{|\langle \tilde{v}_\theta^*(f) \tilde{v}_r(f - f_1) \partial_r \tilde{v}_\theta(f_1) \rangle|^2}{\langle |\tilde{v}_\theta(f)|^2 \rangle \langle |\tilde{v}_r(f - f_1) \partial_r \tilde{v}_\theta(f_1)|^2 \rangle}. \quad (5.6)$$

Since the L-H transition is by definition a dynamic process, it is not suitable for bicoherence measurements. Both the bicoherence and energy transfer can be collapsed into 1D signals by summing over all source functions  $f_1$ , with examples for the heated L-mode shot shown in Figure 5.2b [101]. The summed bicoherence  $B^2(f) = \sum_{f_1} b^2(f, f_1)$  in the bottom panel indicates the total amount of coupling to a given frequency component and contains a peak at the geodesic acoustic mode (GAM) frequency  $f_{GAM} \sim 20.5\text{kHz}$  which is not present in the net frequency resolved transfer function  $T_v(f) = \sum_{f_1} T_v(f, f_1)$  in the top panel (representing the rate of change of kinetic energy). A peak at the ZF frequency  $f_{ZF} \sim 0.5\text{kHz}$  is however present in both. This suggests that at GAM frequencies both GAMs and ZFs are competing for transfer of turbulence power, resulting in reduced transfer to ZFs (compared to the transfer at non-GAM frequencies) and thus reduced quenching of turbulence [101]. The impact of GAMs on the L-H transition can thus go either way, as GAMs can trigger a transition to H-mode but the competition between GAMs and ZFs can also lead to an increase in  $P_{LH}$ . While there have been numerous studies on GAMs at different devices, they have proven to be difficult to study on STs such as MAST.

## 5.2 BES data analysis

To investigate the generality of these findings, we attempted a similar turbulence analysis on MAST using the beam emission spectroscopy diagnostic (BES) which was introduced in

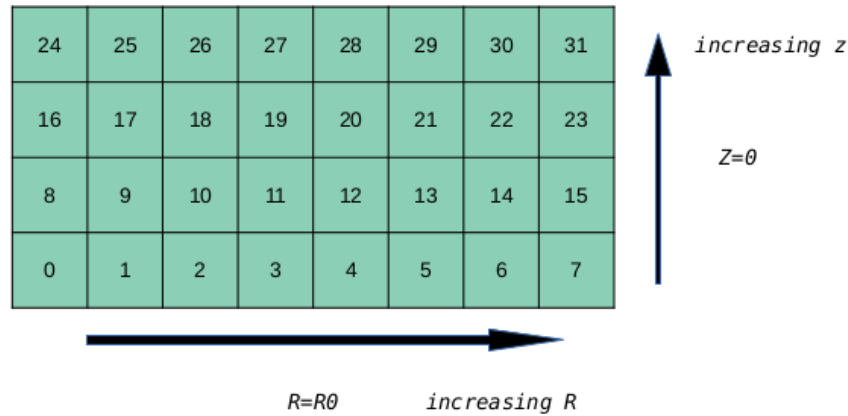


Figure 5.3: The arrangement of the BES array channel labels on MAST, with rows counting from bottom to top and columns from left to right, in the direction of increasing  $z$  (height, with midplane  $z = 0$ ) and increasing  $R$  (radius) respectively.

Chapter 2. BES enables a 2D imaging of density fluctuations at chosen radial locations along the midplane ( $z = 0$ ) with 32 channels arranged in a  $4 \times 8$  array as shown in Figure 5.3.

### 5.2.1 Requirements to obtain useful data

Since the L-H transition is primarily an edge phenomenon, the turbulence studies performed for this project focus on diagnostic data from the edge region of the plasma, i.e. just inside the LCFS. The ideal location of the BES view is thus one where the separatrix crosses the array.

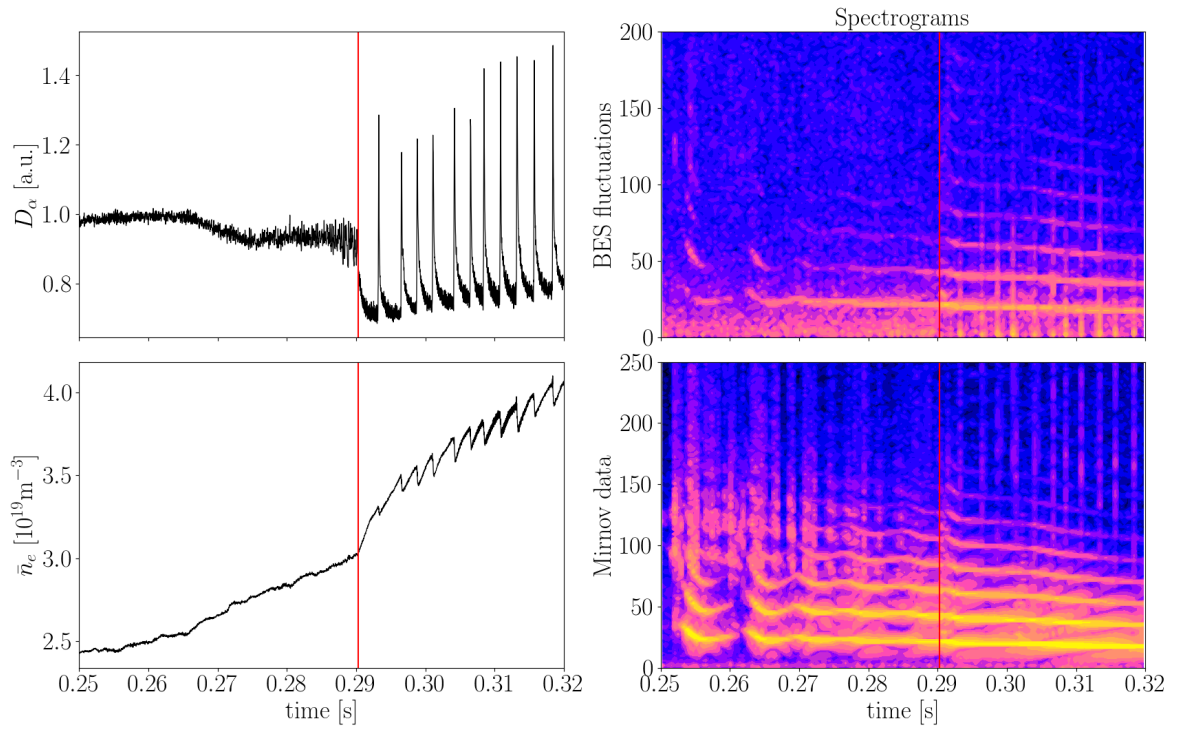
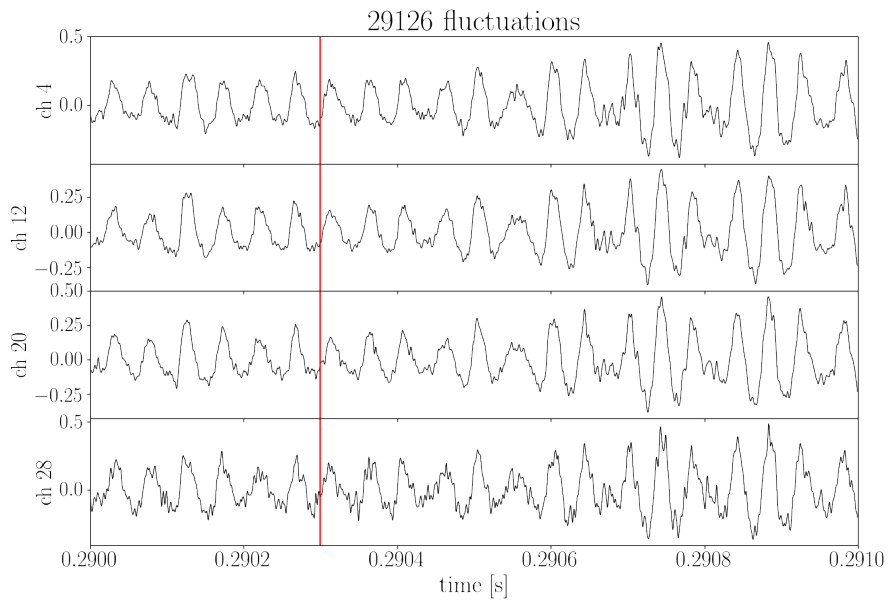
The set of shots in the L-H transition experiment on MAST which were used in the power threshold and heat flux studies of Chapters 3 and 4 would have been an excellent dataset for the turbulence studies as well, but unfortunately the BES data was not very useful as the BES view radius was too close to the core (the separatrix was not covered by the array) and the data was additionally overwhelmed by strong MHD modes, in this case mainly long-lived saturated ideal modes [92]. Attempts to recover fluctuation data to reveal information on the turbulence by filtering out the MHD modes (e.g. through subtracting the mean time series of several channels from each channel of interest) resulted in overwhelmingly noisy data without many features. Filtering the modes out by frequency was hindered by the fact that these modes have multiple strong harmonics present.

As unfortunately a cohesive set of L-H transition shots was therefore not available for the turbulence study, the MAST shot logs were searched for suitable but unconnected shots

to study instead. The requirements were: shots with NBI heating provided by the South beam and available BES data, with an L-H transition during the current flat top phase and during the South beam heating phase (with enough of a delay between beam start time and transition to capture the evolution of L-mode turbulence), where the BES view array contained the separatrix during the time period of interest. The BES data of the candidate shots was then inspected to check if it was usable. For this, spectrograms of the BES fluctuation data were inspected to check for broken channels, strong MHD modes often with harmonics, mainly long-lived modes (LLMs), fishbones or toroidal Alfvén eigenmodes (TAEs), or fluctuation data not showing features above the noise level (these latter shots were sometimes only identified after attempts to extract velocities out of the data resulted in only noise with low levels of coherence). Double null shots on MAST appeared to be especially likely to suffer from strong MHD modes which cause movement of the flux surfaces, e.g. internal kink modes such as fishbones or LLMs which produce a density perturbation on all channels. An example shot with a strong LLM seen in the BES fluctuation spectrogram as well as the spectrogram for a Mirnov coil is shown in Figure 5.4a, while the density perturbation present simultaneously in multiple channels is shown in Figure 5.4b.

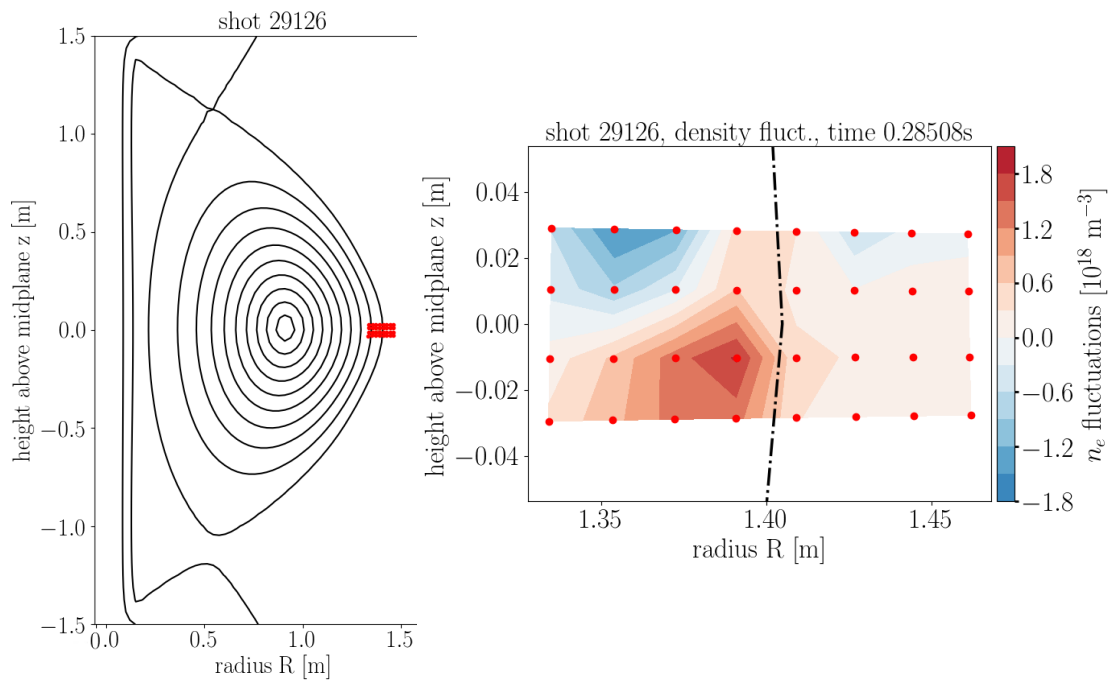
### 5.2.2 Extracting fluctuation data

There are a few steps involved in extracting fluctuation data from the raw BES signal, the initial ones have been adapted from codes by other researchers working on the diagnostic [107]. Like for other MAST data, the data files are stored on the Freia cluster and accessed through UDA. While the BES array is almost always at the midplane vertical position (i.e.  $z = 0$ ), the view radius corresponding to the centre of the array can be changed in between shots. In the diagnostic collection optics, the separation between the centres of neighbouring APD detector pixels is 2.3mm, while projected into the plasma this scales to a channel separation of 2cm. The channel separation for the array view in the plasma can be seen in Figure 5.5b. This scaling, along with the view radius fetched from the MAST shot logs, allows us to project the known array distribution of the detector pixels onto  $(R, z)$  locations for each BES channel centre in the plasma region. The positions are further scaled with the APD magnification based on the distance to the beam axis, with a function inherited from the BES RO Anthony Field which incorporates view geometry parameters such as the South beam tangency radius and beam port, the collection mirror radius and elevation as well as

(a)  $D_\alpha$ , density and spectrograms of BES fluctuation data and Mirnov data

(b) BES fluctuation data in presence of MHD mode

Figure 5.4: Strong MHD modes (fishbones developing into a long-lived mode) which overwhelm the BES data are visible in (a) BES fluctuation and Mirnov data spectrograms as well as (b) in the BES fluctuation data itself, with the data showing simultaneous and regular intensity fluctuations across multiple channels. The L-H transition is marked in red.



(a) Location of BES array with flux surfaces

(b) Density fluctuations measured by BES

Figure 5.5: (a) Flux surfaces of double null shot 29126 with the viewing location of the  $4 \times 8$  array of BES channels in red, capturing confined, edge and SOL plasma. (b) A magnified version of the same (L-mode) snapshot as (a), showing the 32 BES channels in red along with the density fluctuations as calculated from BES data. Note the steep density gradient across the separatrix as well as the filaments or ‘blobs’ which move poloidally inside the edge. As described in the text, the fluctuation data from BES is calculated by subtracting the mean and filtering out the beam signal, and the  $n_e$  profile from Thomson scattering data is used to convert this to density fluctuation data.

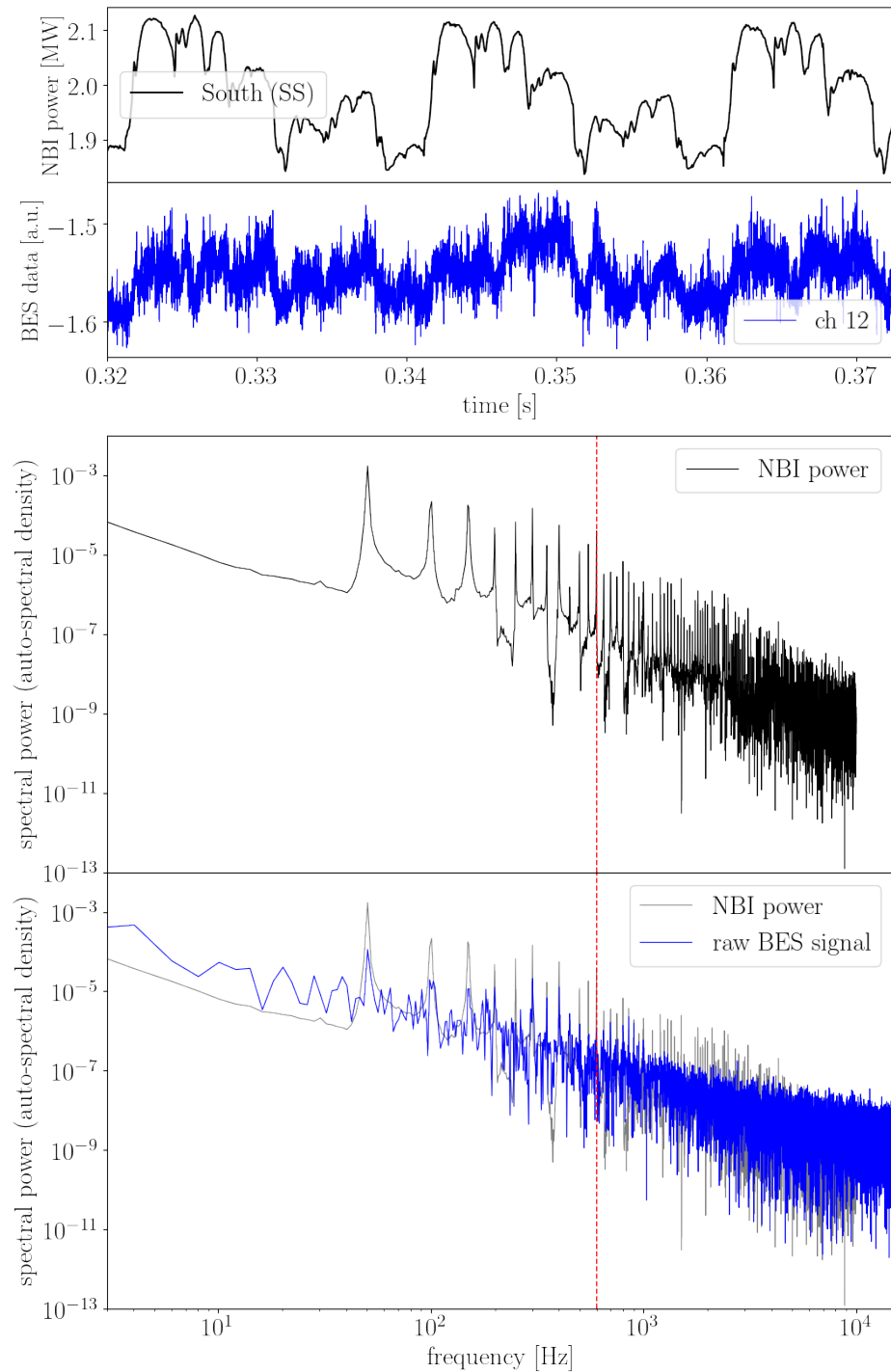


Figure 5.6: A snapshot of the variation in the NBI power trace compared with the raw BES data for sample shot 29378 along with their frequency spectra (computed as the auto-spectral density using Welch’s method [106]), to show that a low-pass filter on the BES data at 600Hz can be used as an estimate for the beam signal.

the angle between the mirror and beam port. The resulting array of  $(R, z)$  locations corresponding to each BES channel allows us to calculate the distance between channels and align the channels with flux surfaces calculated with the EFIT code. For an L-mode timepoint of a double null shot with the separatrix crossing the BES array, Figure 5.5 shows the locations of the BES channels in red along with a selection of flux surfaces calculated by EFIT. A magnified view of the same snapshot is shown in Figure 5.5b. The BES detectors collect data throughout a plasma shot, but only the data during the period where the South beam is on is actually useful, while the data before the start of the beam corresponds to background noise. As a first step, the data is therefore cut to the beam start and end times and is zero-centred by removing the mean of the pre-beam background BES data. Even during South beam operation, the BES data as fetched from Freia contains not just the fluctuation data of interest but also lower frequency variation in all channels. A large part of this is due to the structure of the NBI power signal, as can be seen in the top panels of Figure 5.6 comparing snapshots of the NBI power signal variation and the raw BES signal, and can be filtered out by dividing the BES signal by an estimate of the variation due to the beam signal. This estimate is created by applying a low-pass filter to the mean-subtracted BES signal, with the filter cutoff of 600Hz (marked in red) chosen based on the structure of the spectra of the NBI power and the BES signal, seen in the bottom panels of Figure 5.6, to ensure no significant fluctuation information is lost. The fluctuation data used in all following section of the turbulence study is thus the zero-centred BES signal divided by the low-pass filter estimated beam signal. The intensity fluctuation data from BES can be transformed into density fluctuations by multiplying the data by a density profile interpolated from Thomson scattering data. Figure 5.5b shows a contour plot of the resulting density fluctuations in all channels, where the steep density gradient crossing the separatrix is visible along with a snapshot of the poloidal movement of density filaments or ‘blobs’ inside the plasma edge.

### 5.2.3 Mode powers, phase velocities, etc

Before attempting to extract velocities out of the fluctuation data with the ultimate aim of calculating the nonlinear kinetic energy transfer, a few simpler techniques were tried on selected time periods of a sample shot. This shot, #29378, was a long LSN shot which transitioned from an L-mode with prominent TAEs and fishbones into an ELMy H-mode. Figure 5.7 shows (from top to bottom, for the entire  $I_p$  flat-top phase with South beam

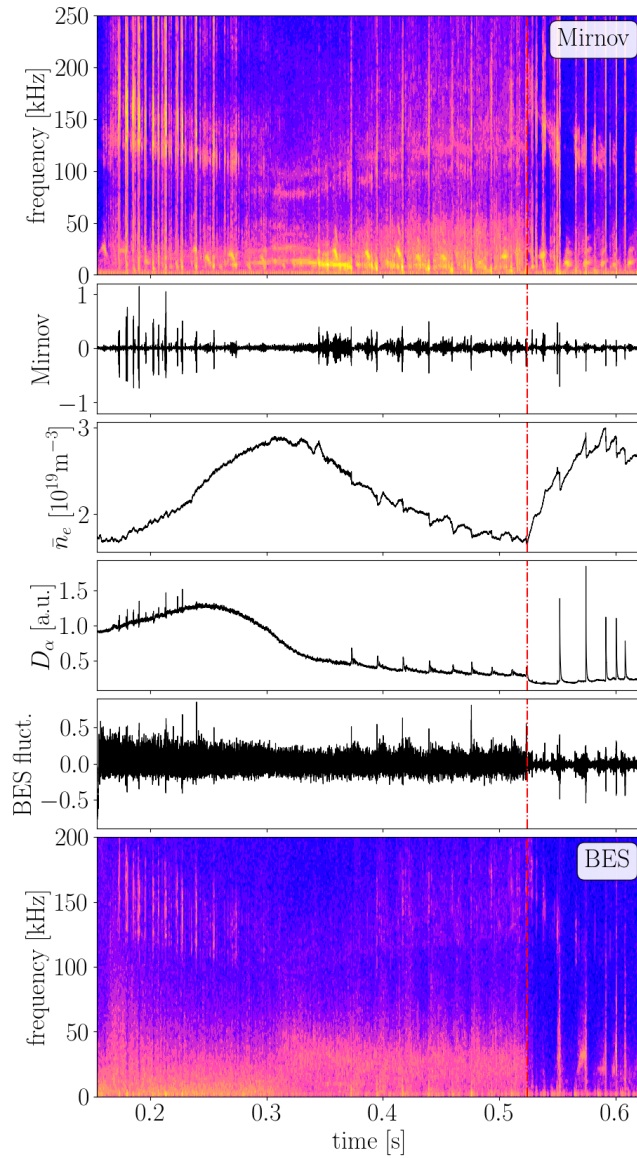


Figure 5.7: Sample shot 29378, lower single null. For the current flat-top phase with South beam heating, from top to bottom: Spectrogram and signal of Mirnov coil #207, line-averaged density,  $D_\alpha$ , fluctuation data and spectrogram of BES channel #12 (edge channel). The L-H transition is marked in red.

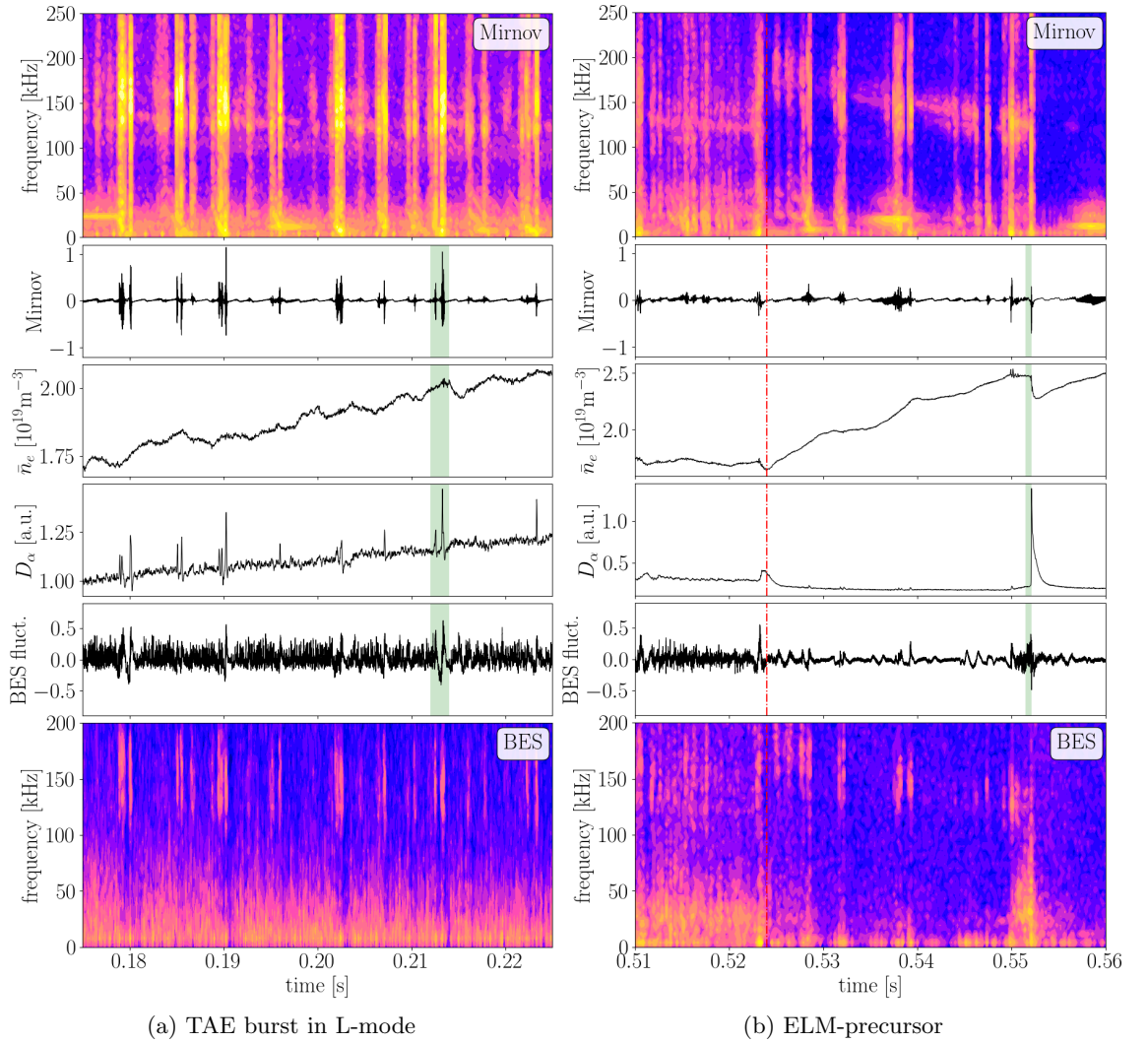


Figure 5.8: From top to bottom: Spectrogram and signal of Mirnov coil 207, line-averaged density,  $D_\alpha$ , fluctuation data and spectrogram of BES channel 12 plotted for (a) a TAE burst in L-mode 0.212 – 0.214s and (b) an ELM-precursor during H-mode 0.5515 – 0.5521s. The specific time slices analysed are shaded in green.

heating): a spectrogram and time signal of Mirnov coil #207, the line-averaged density, the  $D_\alpha$  signal, the fluctuation data and spectrogram of BES channel #12 just inside the LCFS. The L-H transition (at  $t_{LH} \approx 0.524$ s, marked in red) is clearly visible in the reduction of broadband fluctuations in both the BES fluctuation time history and spectrogram, while ELMs are visible as bright flashes during the H-mode phase. TAEs are visible during the L-mode phase as bright intermittent flashes around 150kHz, and fishbones are present especially after  $t \sim 0.3$ s.

Several time periods of interest covering events such as TAE bursts, fishbones, ELMs and

quiescent periods were investigated, with the analysis methods and results for a time period for a TAE burst during early L-mode and one for an ELM-precursor described in more detail in the rest of this section. ELM-precursors as MHD oscillations immediately preceding an ELM have been studied on multiple devices, with their features depending on the device, ELM-type, heating method and other factors [108–110]. The two time periods investigated here, 0.212 – 0.214s for the TAE burst and 0.5515 – 0.5521s for the ELM-precursor, are shown in Figure 5.8 as magnified sections of Figure 5.7. For this section, the time periods of interest were investigated for the presence and properties of particular modes through spectral and coherence/phase analysis. For most of the calculations involved in this analysis a reference channel from the BES array is chosen, which in this case was channel 5 for the TAE burst and channel 4 for the ELM-precursor, both located by the LCFS as determined by EFIT for the midpoint of each time slice.

The first task in the mode analysis was to find an estimate for the mode frequency by fitting the spectrum of the fluctuation data from a BES channel, calculated from the Fourier transform of the data. Figure 5.9 shows the spectrum of the BES data from reference channel 5 for the TAE time slice in Figure 5.9a and reference channel 4 for the ELM-precursor in Figure 5.9b, along with fits to the background noise level and to the mode. For the background, data points around the mode and the low frequency component were excluded and the remaining data was fit with an exponential. The fit can be seen as blue x's in Figure 5.9. For the mode, the background fit was subtracted from the data, and where it was apparent the initial low frequency component was again excluded, before the rest of the background-subtracted spectral data was fitted with a Gaussian,

$$f(x) = A e^{-\frac{(x-x_0)^2}{2\sigma^2}}, \quad (5.7)$$

where in this case  $x$  corresponds to frequency,  $x_0$  is the estimated mode frequency,  $\sigma$  the uncertainty and  $A$  the amplitude. This fit can be seen in Figure 5.9 plotted in green. From the fit parameters, we can find an estimate for the mode frequency with an uncertainty, resulting in  $f_{\text{TAE}} = 140.8 \pm 17.5$  kHz for the TAE and  $f_{\text{ELM-pre.}} = 32.0 \pm 11.5$  kHz for the ELM-precursor. These estimates are shown in the Figure as vertical green lines. With the Gaussian fitted to the background-subtracted power spectral density data, the Gaussian

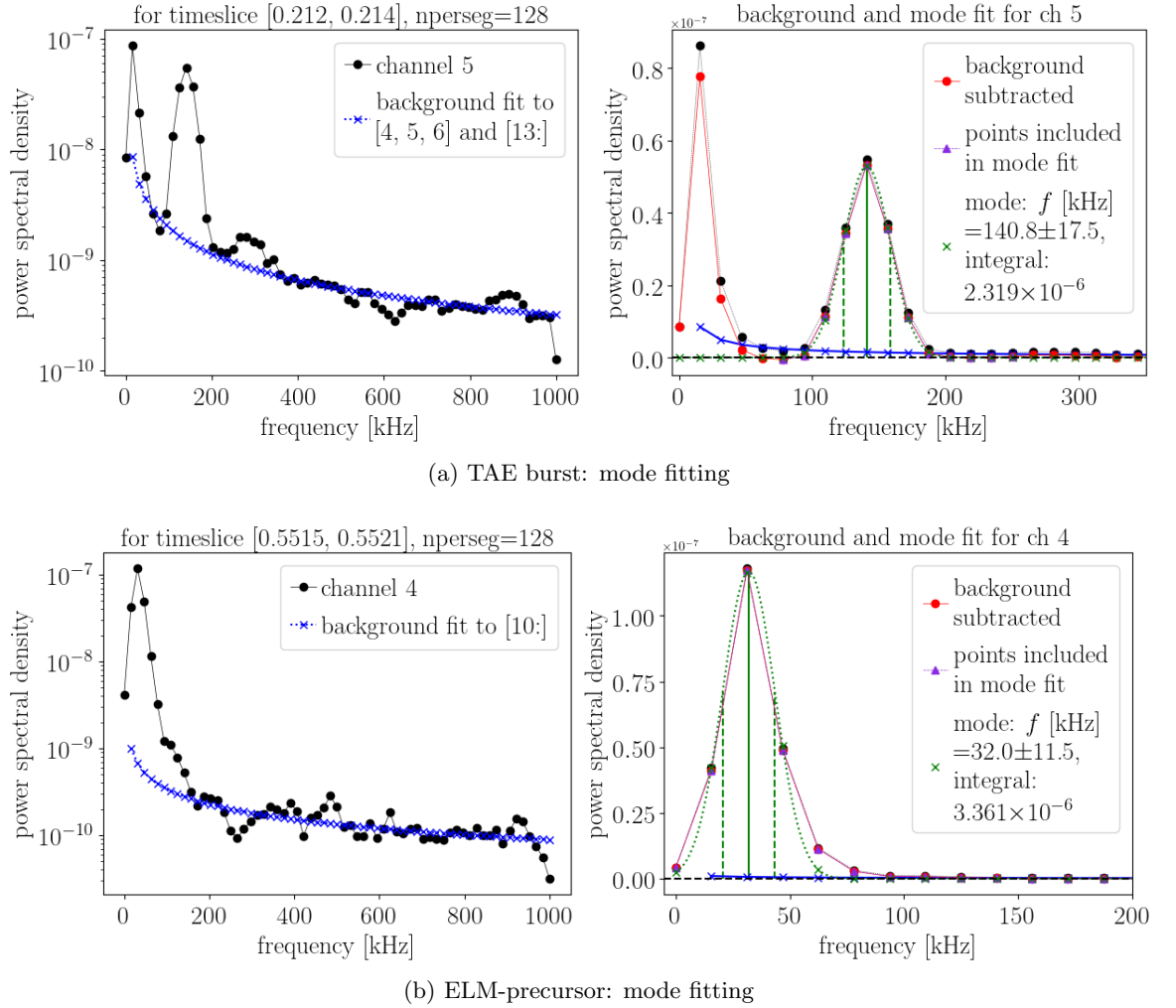


Figure 5.9: The frequency spectra of BES fluctuation data for chosen reference channels by the LCFS for the TAE burst (a) and the ELM-precursor (b) are shown along with fits to the background noise level (exponential fit, in blue) and the mode (Gaussian fit, in green). The estimated values for the mode frequency (with uncertainty) and the Gaussian integral from fit parameters are shown in the legends.

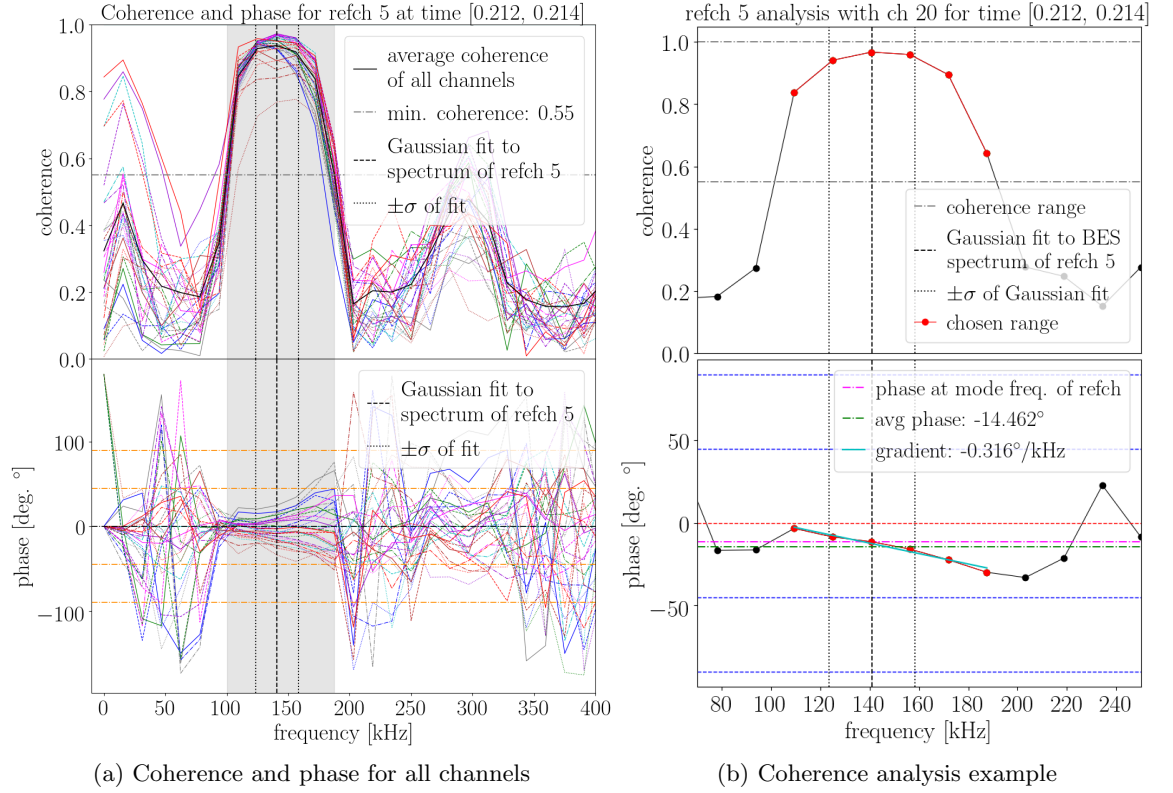


Figure 5.10: The coherence (top panels) and phase (bottom panels) between the reference channel 5 and all other channels of the array during a TAE burst at 0.212 – 0.214s (as shown in Figure 5.8a) are plotted as a function of frequency in (a), while an example of the analysis done to determine the average phase and the phase gradient in frequency space is shown for channel 20 in (b). The mode frequency found from a Gaussian fit to the BES spectrum (along with the uncertainty) is plotted as vertical lines, while the chosen accepted coherence range 0.55-1 is plotted as horizontal lines. In (b), the data points which lie in the accepted coherence range and are selected for the analysis are plotted in red. The bottom panel of (b) shows the interpolated phase at the mode frequency in pink and the average phase weighted by coherence in green, while the straight line fit to find the phase gradient is shown in cyan.

integral of the fit,

$$\text{integral} = \sqrt{2} \pi A |\sigma|, \quad (5.8)$$

can give an estimate of the relative mode power, which can be compared with the values for other channels in the array to give some information on the spatial localisation of the mode (see later figures).

Figure 5.10 shows some representative plots for the coherence analysis, with the coherence

and phase between reference channel 5 and all other channels of the array plotted as a function of frequency in Figure 5.10a, and the analysis process shown in Figure 5.10b for channel 20. The TAE mode is clearly visible in both the coherence and the phases for all channels across a broad frequency peak at around 140kHz, with all channels containing a frequency range where the coherence approaches 1 and the phase follows a clear pattern. The frequency of the coherence peak matches the mode frequency found in Figure 5.9a well, with the mode frequency and its uncertainty range plotted as vertical lines in all panels of Figure 5.10, although the coherence peak has a broader width than the mode peak in the fluctuation spectrum. For the coherence analysis, in order to filter out incoherent frequencies and select a frequency range of strong coherence, a lower limit for the accepted coherence range must be chosen. In this study, values between 0.5 and 0.75 were applied and compared. The higher the minimum coherence is, the greater the chance that only one or even no points lie within the accepted coherence range, and if the minimum coherence is too low, there is a higher likelihood of including points which do not belong to the same mode and no longer follow the same phase pattern. For both time slices, Figure 5.11 shows 2D contour plots for the average phases of the points in the accepted coherence range for the lowest minimum coherence value (0.5) and the highest (0.75). For the TAE, as the coherence peaks are so strong and well defined, changing the coherence range has basically no effect, while for the ELM-precursor the phase pattern across the array remains similar but a higher minimum coherence value leads to more channels without accepted data points (shown as blank in Figure 5.11). Aside from fringe cases at both extremes, the results were fairly similar for different coherence limit choices, and the figures in this section all show examples with a minimum coherence level of 0.55. This level is shown in the top panels of Figure 5.10 as a horizontal line, and in Figure 5.10a the frequency range where the average coherence (over the entire array) lies within the accepted coherence range is shaded grey for both coherence and phase. In the example analysis with channel 20 in Figure 5.10b, the frequency points that lie within the accepted coherence range form a straight line in the frequency-phase space in the bottom panel, allowing us to find a gradient of the phase in frequency space (plotted in cyan in Figure 5.10b). The phase gradient can reveal information on the mode movement and possible changes in its speed. A non-zero gradient in phase indicates mode movement, while a changing phase gradient is caused by a moving mode which is changing speed. Consequently a constant phase gradient would indicate a constant speed, and a constant phase (i.e. a

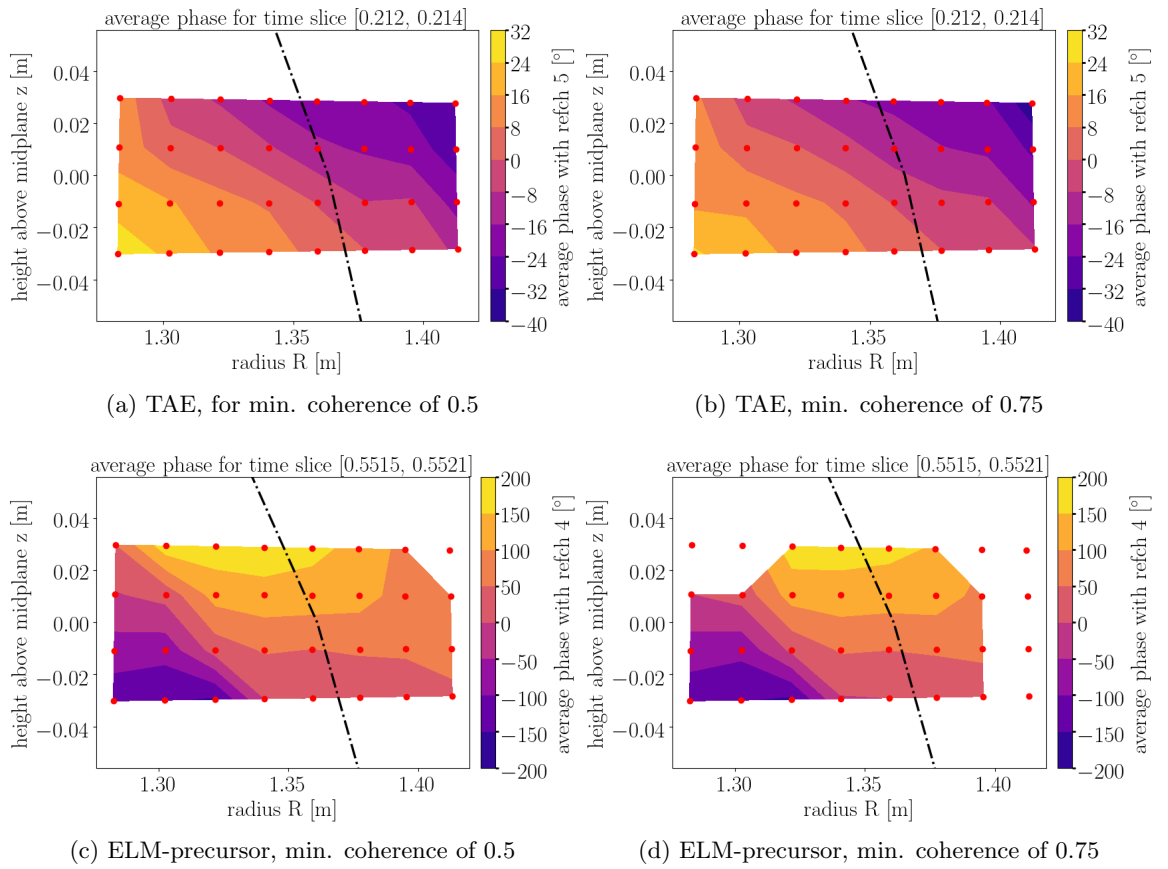


Figure 5.11: To show the consequences of picking a low (0.5) or high (0.75) minimum coherence value, the average phases of the points in the accepted coherence range are plotted as 2D contour plots with the BES channel locations and the LCFS in  $(R, z)$  space for the TAE and the ELM-precursor.

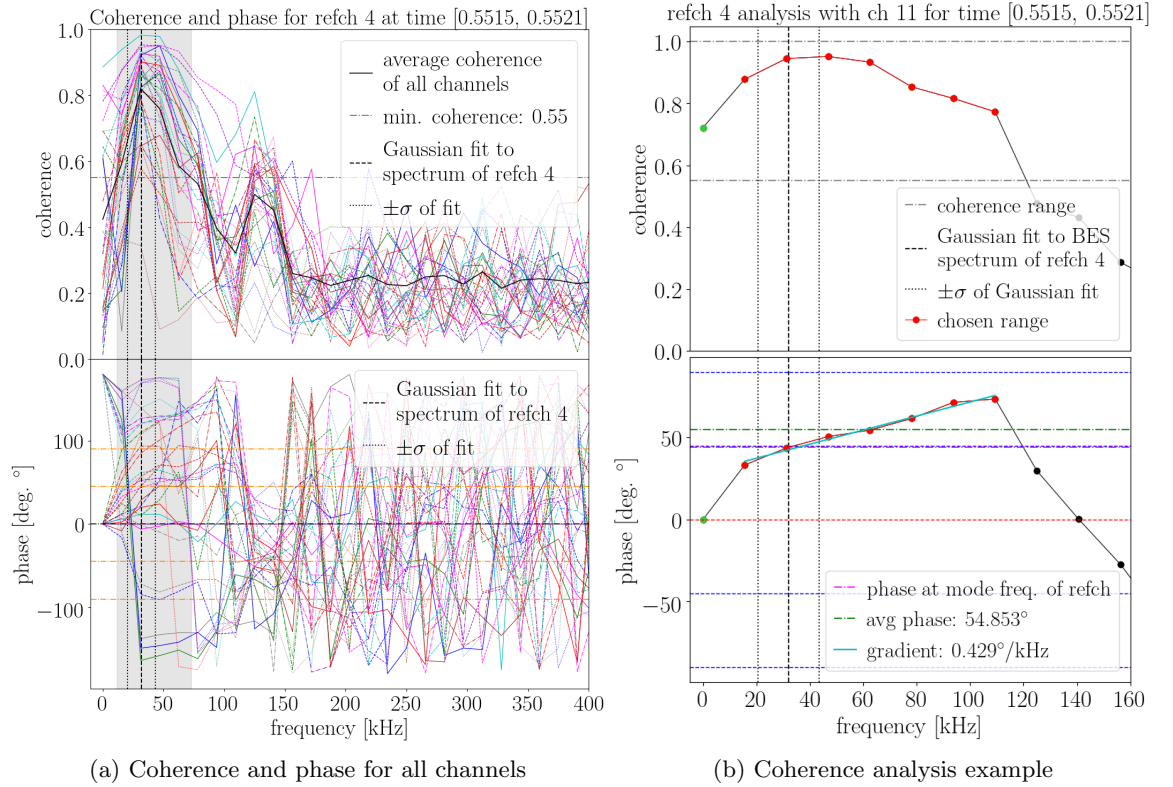


Figure 5.12: The coherence and phase (analysis) plots as shown in Figure 5.10 for the ELM-precursor time slice [0.5515, 0.5521] and reference channel 4. In contrast with the TAE burst in Figure 5.10, the much lower frequency of the mode and the coherence peak, along with the less consistent coherence across the array are clearly visible. The behaviour of the phases in frequency range of accepted coherence is also different between the two time slices. In (b), the first data point lies within the accepted coherence range, but as it is at  $f = 0$  kHz and  $\phi = 0^\circ$ , it is excluded from the analysis.

gradient of zero) would indicate no movement. For the phase of the mode, we can either take an average of the accepted points in the frequency-phase space, weighted by coherence, or an interpolated value of the phase at a chosen frequency, for example the mode frequency found in the fluctuation data spectrum. These two values are indicated in the bottom panel of Figure 5.10b as green and pink horizontal lines, respectively.

The same analysis was performed for the ELM-precursor time slice, and a similar representative plot as Figure 5.10 but for reference channel 4 is shown in Figure 5.12, with again the coherence and phase for all channels shown in Figure 5.12a and an example of the analysis shown in Figure 5.12b for channel 11. The mode is visible in the coherence in Figure 5.12a for a frequency range of around 15-70kHz, which again is much broader than the width of the peak in the fluctuation spectrum (and also with a positive skew, covering a

higher frequency range), but compared with the TAE burst in Figure 5.10 the coherence peak is less prominent and much less consistent across the array. The behaviour of the phases in the accepted frequency/coherence range is also noticeably different. To determine the data selection for the coherence analysis function, all points below the minimum coherence level were excluded, and the remaining points were split into connecting pieces. Any pieces which lay completely outside the mode frequency range as determined from the BES spectrum of the reference channel (see Figure 5.9) were neglected, so that for each channel either no pieces or one piece remained. For the ELM-precursor, due to the low mode frequency, some channels (such as the example channel 11 plotted in Figure 5.12b) returned a piece containing the first data point at frequency 0kHz and a phase of  $0^\circ$ , so in those cases that point was also excluded from the analysis.

From the spectral and coherence/phase analysis, we can end up with four parameters to use to describe the mode present in each of the two time slices, which are plotted in the four subplots in Figures 5.13 and 5.14 as a function of normalised effective radius  $\rho_{\text{eff},N}$  for all channels split into the four rows: the mode frequency (a), and mode power (c), and the phase (b) and phase gradient (d) for the mode with reference channel 4 for the ELM-precursor and reference channel 5 for the TAE burst. For the mode frequency, there are three estimates which can be provided for each channel, the frequency of the point at maximum coherence with the reference channel (plotted as solid lines with circle markers), the frequency and uncertainty from the Gaussian fit to the fluctuation data spectrum (dashed line and squares), and the frequency and uncertainty from a Gaussian fit to the coherence peak (dotted lines and diamonds). For the frequency estimates from Gaussian fits, an average of the uncertainty from fit parameters is listed in the legend, highlighting the broader width in frequency space of the coherence peak vs the spectral peak. The first estimate, i.e. the frequency at the point of maximum coherence, is limited to frequency values covered by the frequency resolution of the coherence analysis, so the lines show large step changes. If these step changes are ignored, the frequencies of the TAE mode in Figure 5.14 are in good agreement for the different methods and across the channels of the array, fluctuating slightly around 140kHz. For the ELM-precursor in Figure 5.13 the mode frequency estimates show a larger variation, and the fits to the coherence peaks result in systematically higher frequencies than the fits to the spectral peaks ( $\sim 45\text{kHz}$  vs  $\sim 30\text{kHz}$ ) - this is due to the fact that at these lower frequencies the coherence peak for the ELM-precursor has a positive skew and is therefore

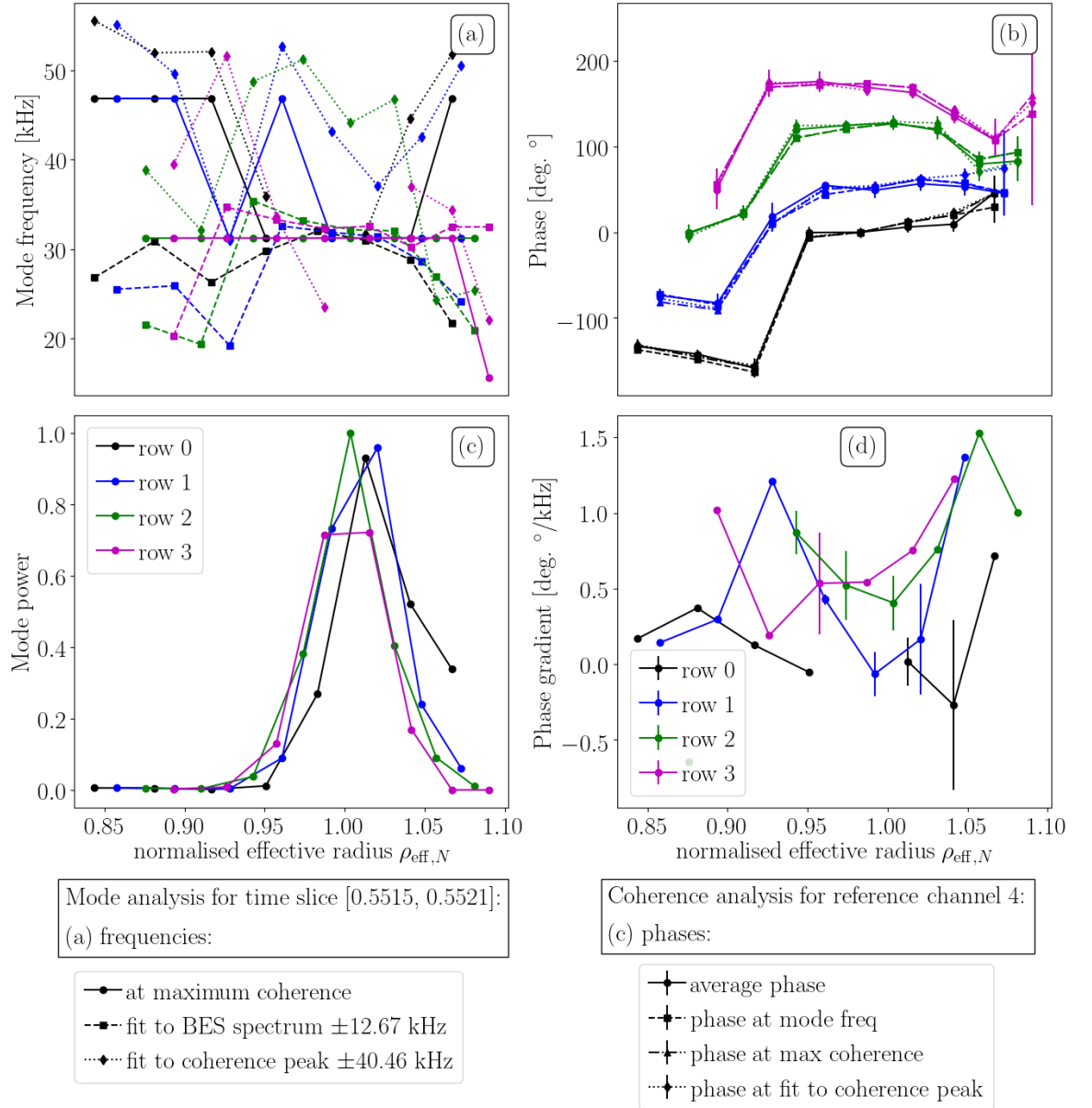


Figure 5.13: For the ELM-precursor time slice of sample shot 29378, results of the mode and coherence analyses for the channels in each of the four rows are plotted against the flux surface position (normalised effective radius  $\rho_{\text{eff},N}$ , where  $\rho_{\text{eff},N} = 1$  is the LCFS) calculated from the  $(R, z)$  position of the BES channel. Three estimates for the mode frequency are shown in (a), four estimates of the mode phase (with reference channel 4) are shown in (b), the mode power estimated from the Gaussian fit to the BES spectrum is shown in (c) and the gradient of the phase in frequency space for the points within the accepted coherence range is shown in (d). The frequency estimates are in reasonable agreement with each other and across the BES array, the different estimates for the phase agree very well with each other, and the mode power appears to be strongly localised around the LCFS.

not particularly well approximated by a Gaussian fit. The mode power estimates in (c) are calculated from the Gaussian integrals of the fits to the BES spectra, with one estimate presented for each channel (and each time slice). From Figure 5.13c, we can see that for the ELM-precursor the mode power is strongly localised at the LCFS ( $\rho_{\text{eff},N} = 1$ ), dropping off to near zero in both the confined and the SOL plasma. For the TAE burst, Figure 5.14c shows that the mode power peak is located further into the SOL (close to  $\rho_{\text{eff},N} = 1.05$ ), and the mode in general appears less spatially localised, with the mode power dropping off much more gradually in the confined plasma and still being quite strong in the outer (SOL) edge of the BES array. For the phases in (b), there are four methods to estimate the phase between each channel and the reference channel: first the average of the phases from the chosen data points within the accepted coherence range (solid lines and circles), and then the interpolated phases at the three different mode frequency options from (a), with the phase at the frequency from the BES spectrum (dashed lines and squares), at the point of maximum coherence (dot-dashed lines and triangles) and at the fit to the coherence peak (dotted line and diamonds). The errors on the phases were calculated using

$$\sigma = \sqrt{\frac{1}{2 n_d} \left( \frac{1}{|\gamma_c|^2} - 1 \right)} \quad (5.9)$$

where  $\gamma_c$  is the coherence of the selected point(s) and  $n_d$  is the number of independent records used to calculate  $\gamma_c$  [111, 112]. The gradients of the phases in frequency space for the chosen data points within the accepted coherence range are plotted in (d), with the errors representing the error on the fit. For the ELM-precursor in Figure 5.13b, the four estimates for the phase agree very well with each other, forming a region around the LCFS where the phase remains constant for four consecutive channels in each row, with the regular spacing in phase between the rows suggesting something like wavefronts perpendicular to the LCFS. There is a bit more variation in the estimates for the phase for the TAE mode, but Figure 5.14b shows that the general trend is the same for all estimates and across the entire array, with the phase displaying a consistent downward trend as  $\rho_{\text{eff},N}$  increases and from row to row, i.e. the phase decreases as you move across the array both in the positive  $R$  and the negative  $z$  direction. The phase gradients for the TAE time slice also appear to decrease with increasing  $\rho_{\text{eff},N}$ .

As an alternative method of visualising the calculated parameters, the values for all

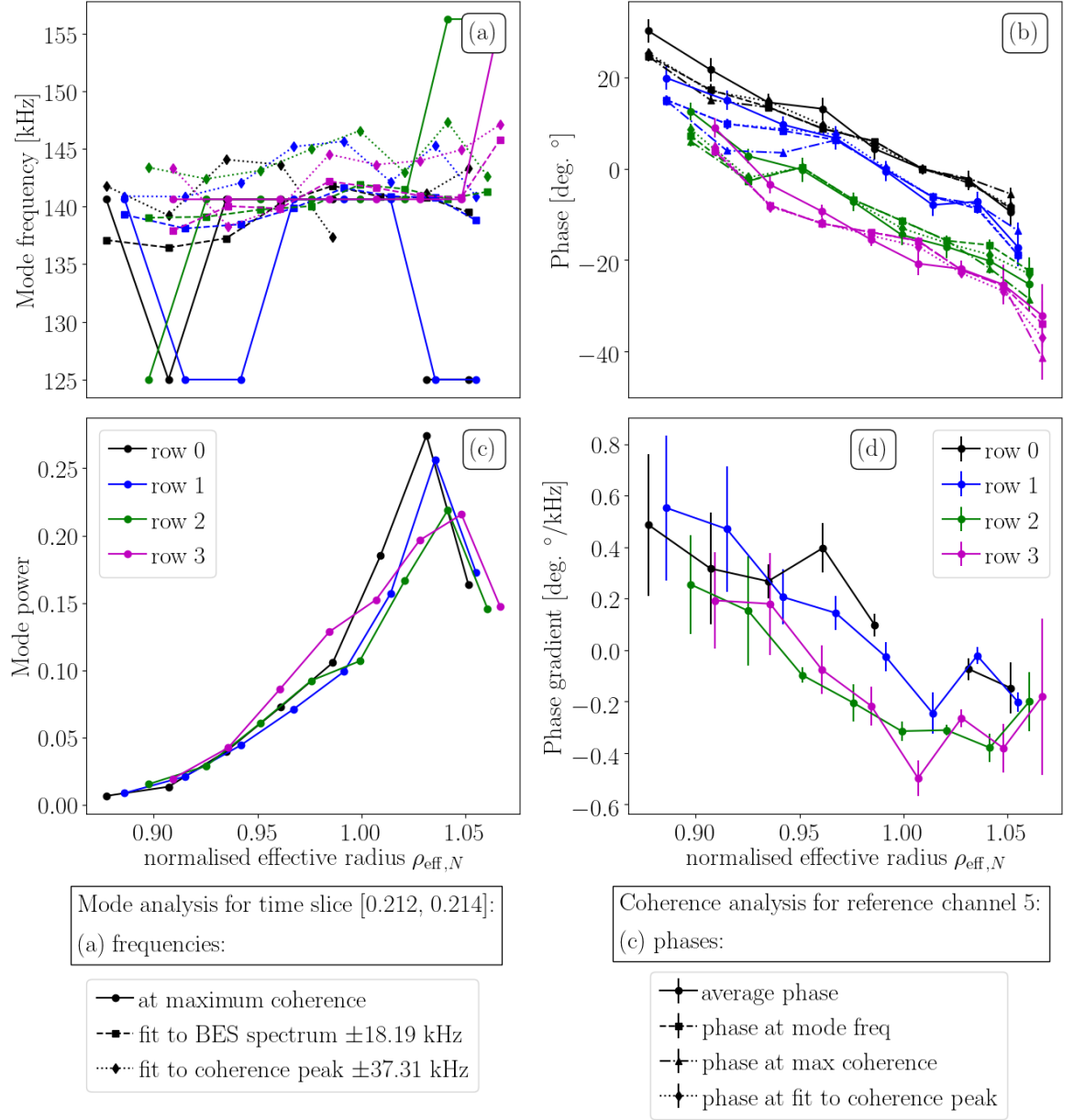


Figure 5.14: The same quantities as in Figure 5.13 are here shown for the TAE burst time slice. The mode power values in (c) are normalised to the maximum across the array of both time slices, showing that the peak is much lower than for the ELM-precursor, while the mode appears to grow strongest in the SOL and is less localised. The phases in (b) all follow a consistent downward trend as  $\rho_{\text{eff},N}$  increases, and the phase gradients in (d) also appear to decrease with increasing  $\rho_{\text{eff},N}$ .

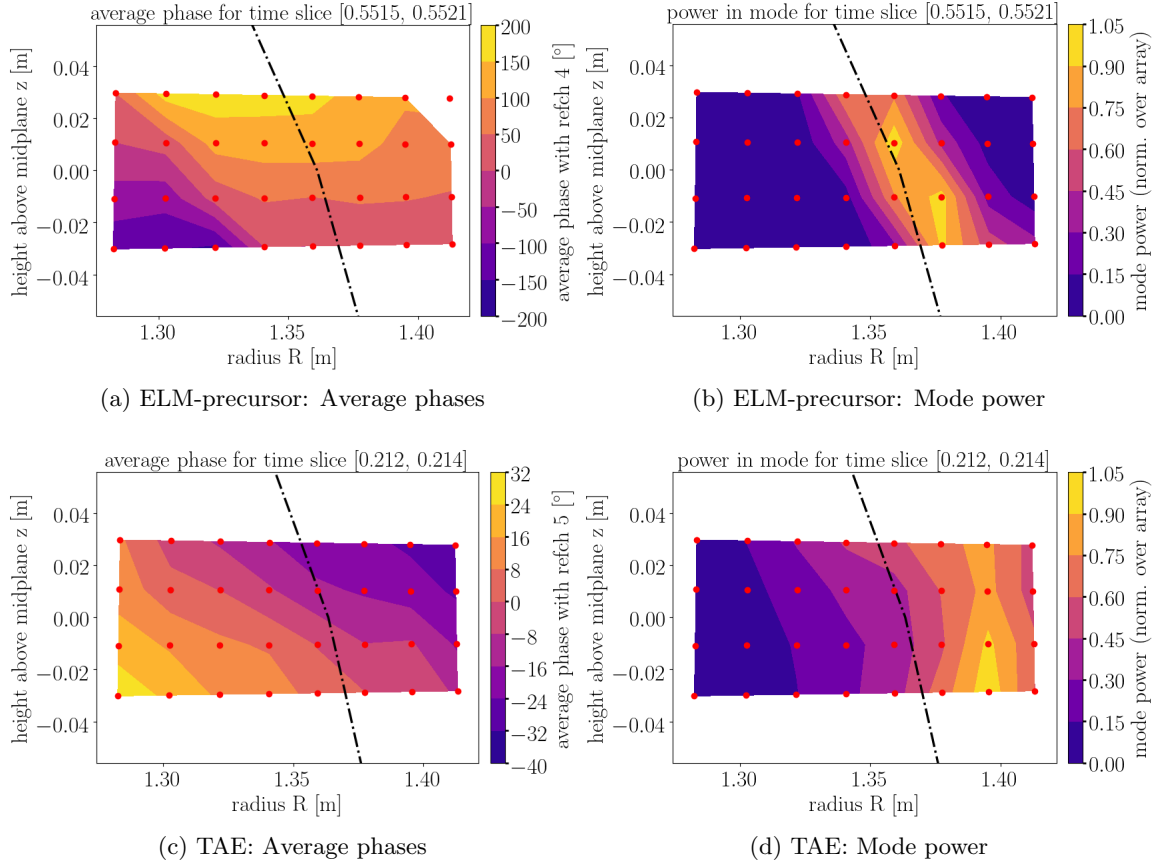


Figure 5.15: For the ELM-precursor time slice [0.5515, 0.5521] and the TAE burst time slice [0.212, 0.214] of sample shot 29378, quantities calculated in the mode and coherence analyses are plotted for the entire BES array in  $(R, z)$  space along with the LCFS (as the black dot-dashed line): (a) & (c) the average phase for the coherence peak of each channel with reference channel 4 (ELM-precursor) or 5 (TAE) by the LCFS for a minimum coherence of 0.55, and (b) & (d) the power in the mode from a Gaussian integral of the mode in the frequency spectrum, normalised over the entire array, to show the localisation of the mode in space.

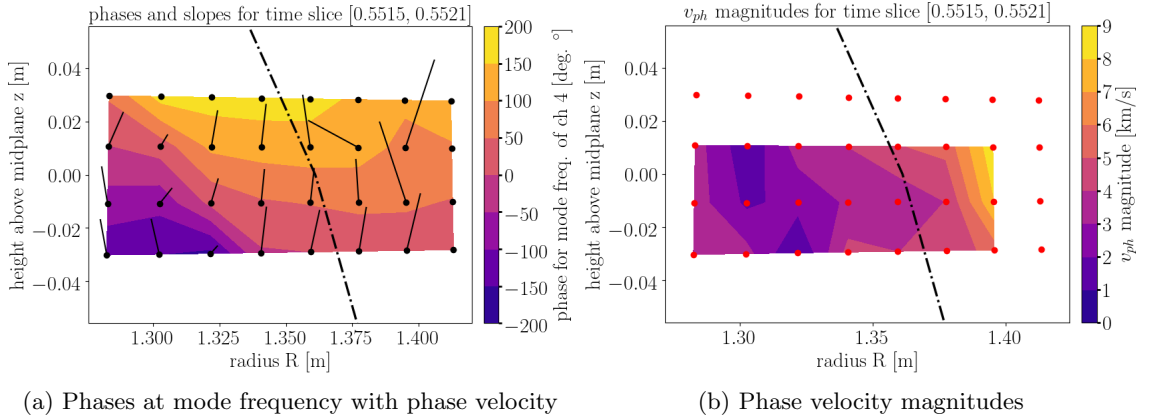


Figure 5.16: Sample shot 29378, for reference channel 4 by the LCFS (plotted as the dot-dashed line) during an ELM-precursor, with quantities shown for the channels in the BES array: (a) The phases at the mode frequency found from the Gaussian fit to the spectrum of reference channel 4, 32kHz, with the calculated phase velocity plotted in black, slopes of lines showing the direction while the line length represents the magnitude. (b) The magnitudes of the phase velocity as shown in (a). Due to the method used there is no calculated phase velocity for the top row and the column furthest into the SOL.

channels in the array can be plotted in 2D as filled contours in the  $(R, z)$  space for the locations of the midpoints of the channels in the  $4 \times 8$  BES array, along with a contour of the LCFS ( $\rho_{\text{eff},N} = 1$ ) calculated by EFIT for the midpoint of the time slice. Figure 5.15 shows such visualisations for the average phase and the mode power for the TAE time slice and the ELM-precursor. The features which were already visible in the previous plots in Figures 5.13 and 5.14 are clearly highlighted in Figure 5.15 as well. The strong spatial localisation of the ELM-precursor to the channels by the LCFS is visible in Figure 5.15b, while for the TAE, the mode power in Figure 5.15d shows that the mode is strongest in the SOL with a much more gradual fall-off in both directions. The wavefronts for the ELM-precursor visible in Figure 5.15a are present across multiple channels from confined to SOL plasma and close to perpendicular to the LCFS, while those of the TAE in Figure 5.15c are regular across the entire array but angled to be neither parallel nor perpendicular to the LCFS, and the change in phase takes place over a much larger distance.

Wavefronts like those in the ELM-precursor in Figure 5.15a make good candidates to attempt to find a phase velocity. We can estimate the magnitude of the phase velocities

from the phase differences between channels and the spatial separation between channels,

$$v_{ph} = \frac{\omega}{k} \quad \text{where} \quad \omega = 2\pi f \quad \text{and} \quad k = \frac{d\phi}{dx} \approx \frac{\Delta\phi}{\Delta x}. \quad (5.10)$$

The direction can be found through geometrical considerations of vertically and horizontally adjacent channels. The results of a preliminary study of the phase velocities for the ELM-precursor mode are shown in Figure 5.16a, with Figure 5.16b showing the values of the magnitude. Due to the method used in determining  $v_{ph}$ , the top row and right-most column have no estimates for  $v_{ph}$ , but the results nevertheless appear to match the wavefronts well.

#### 5.2.4 Velocimetry

The terms in the kinetic energy transfer calculations all contain velocities, which due to the Reynolds decomposition are mostly velocity fluctuations. Investigating the transfer of energy from turbulence to zonal flows and its role in the L-H transition therefore requires experimental measurements of poloidal  $v_\theta$  and radial velocities  $v_r$ . The two-dimensional measurements of intensity (i.e. density) fluctuations provided by the BES system allow for extraction of fluctuation velocities. While the time resolution is fairly high, the spatial resolution is quite low and there are only four channels in each column, limiting the quality of the velocity extractions somewhat. If the BES data is of good enough quality, time histories of poloidal and radial velocities at different flux surface locations can be generated.

The velocities in this project were calculated using a cross-correlation time delay estimation (CCTDE) method [113]. In this method, the time trace of the fluctuation data of one channel is shifted to introduce a time delay with respect to the data of a reference channel and then cross-correlated. This is repeated with different values of the time shift to return a plot of the cross-correlation coefficient vs time delay, and a Gaussian fit to the peak of the data then returns the time delay  $\delta t$ . The channel separation of the BES array can be mapped to the viewing location to give  $\delta x$ . This process is repeated for multiple channels (for the poloidal velocity this is done for the channels along a flux surface), and the data points can be plotted on a  $\delta x - \delta t$  graph, where a linear fit to the data should return the velocity as the inverse of the gradient. The points included in the gradient fit estimate are weighted by each channel's coherence with the reference channel, so that only features which are actually present in both channels are included.

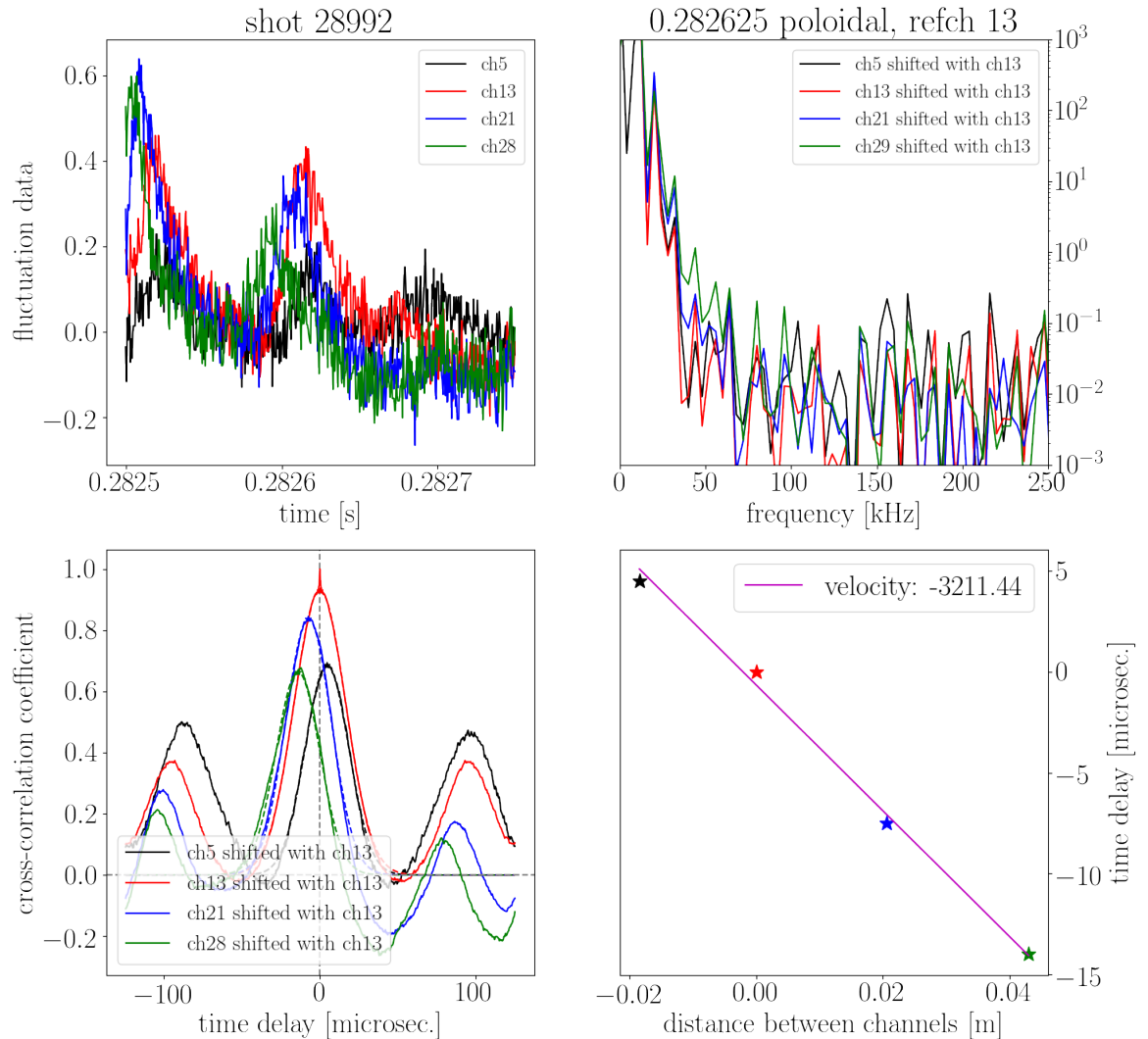


Figure 5.17: An example of a good fit achieved by the CCTDE velocimetry method for the poloidal velocity in reference channel 13 (SOL) of a lower single null shot during L-mode. The top left panel shows the fluctuation data (the  $250\mu\text{s}$  corresponding to the correlation window size for this timepoint) of the four channels which are closest to the flux surface of reference channel, while the bottom left panel shows the cross-correlation coefficient of each channel with the reference channel as a function of the time delay imposed on the data before correlating, along with a Gaussian fit (dashed line) and the peak of the fitted Gaussian (star symbol). The time delay values at the Gaussian peaks are plotted with the distance between the corresponding BES channels in the bottom right panel, and a straight line fit weighted by the values of the cross-correlation coefficient at the peaks returns the gradient, from which the velocity (shown in the label in units of m/s) can be determined. The top right panel shows the frequency spectra of the cross-correlation coefficient plots in the bottom left panel.

The CCTDE method which was written for this analysis has been summarised into a flexible routine which can be used by anyone provided they have (access to) fluctuation data,  $(R, z)$  locations for each channel of the fluctuation data and an equilibrium (i.e. flux surfaces) for the shot in question. The method can even be applied to fluctuation data from diagnostics other than BES, as shown in velocimetry results from Mirnov coil data in Section 5.2.4.4. The user can choose whether to calculate poloidal, radial or both velocities; which channels to include; whether to remove the poloidal average before calculating velocities; whether to fit the cross-correlation coefficient with a Gaussian or just choose the maximum peak, and if fitting with a Gaussian, what fraction of the cross-correlation coefficient data to include in the fit; the time slice over which to calculate velocities; the size of the correlation window over which to perform the cross-correlation; and whether to pass the fluctuation data through an initial bandpass filter.

The default option for the bandpass filter is a lower limit of

$$f_0 = \frac{f_s}{2N} \quad (5.11)$$

where  $f_s = 2\text{MHz}$  is the sampling frequency and  $N$  is the size of the correlation window (i.e. the number of time points in the sample), and an upper limit of  $250\text{MHz}$  which approximately corresponds to the noise level in the BES frequency spectrum. Different sizes of the correlation window  $N$  were explored in the analysis, with lower values resulting in more noise in the velocity data while higher values can lose some of the finer structures from the fluctuation data. For useful velocimetry data, the minimum window size is  $N = 200$ , corresponding to a time length of  $100\mu\text{s}$ , the maximum window size is  $N = 1000$ , corresponding to a time length of  $500\mu\text{s}$ , and the default window size  $N = 500$  corresponds to a time length of  $250\mu\text{s}$ .

#### 5.2.4.1 Poloidal velocities

In double null plasmas, the magnetic axis is close to the midplane height, i.e.  $z \approx 0$ , making the midplane and therefore the middle of the BES array a line of symmetry for the flux surfaces in a poloidal view of the plasma. For DN plasmas the flux surfaces are therefore well aligned with the columns in the BES array, as seen in Figure 5.5b, and the poloidal velocity (i.e. the velocity of filaments along the flux surfaces) is well approximated

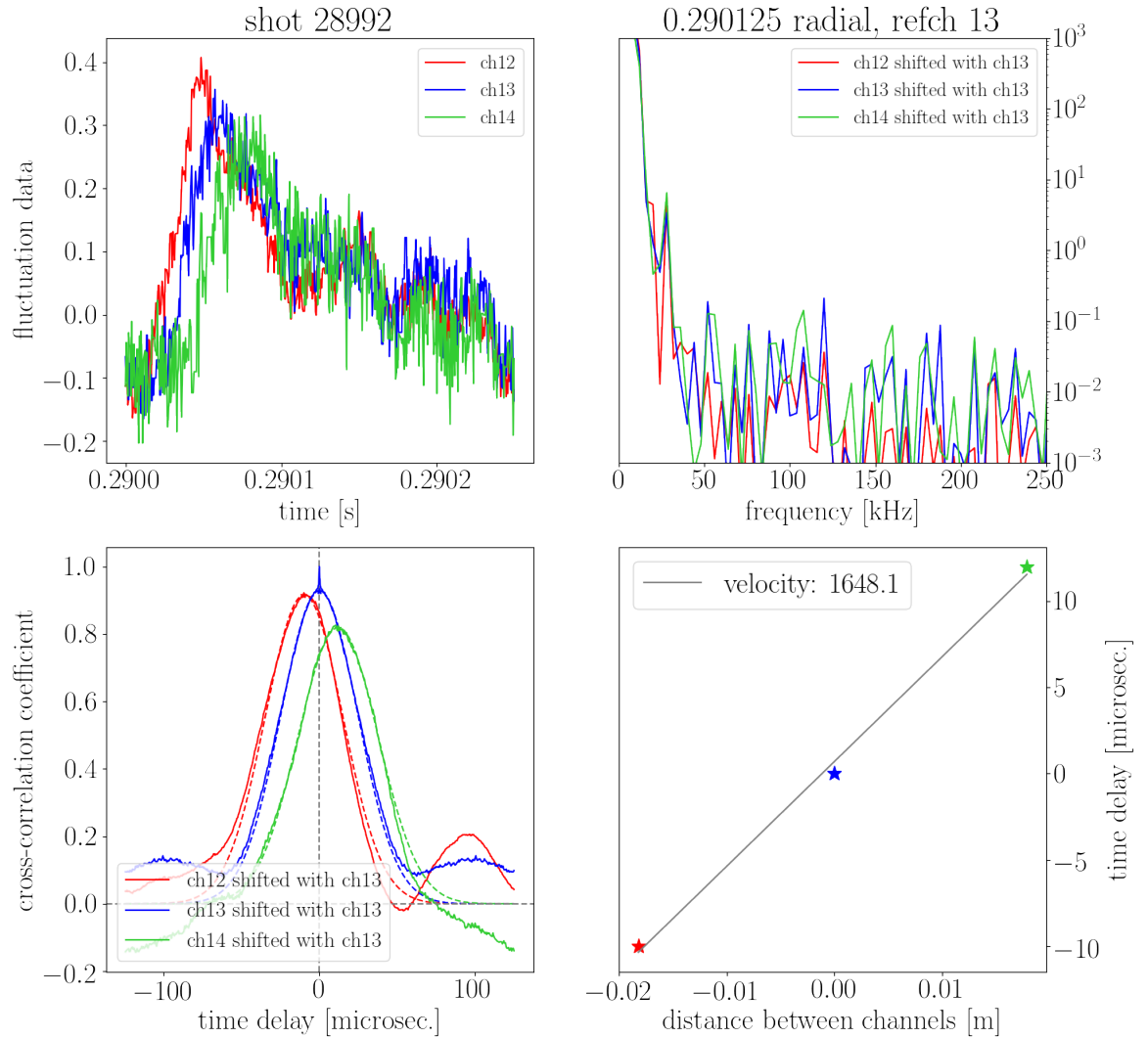


Figure 5.18: An example of a good fit achieved by the CCTDE velocimetry method for the radial velocity in reference channel 13 (SOL) of a lower single null shot during L-mode. The top left panel shows the fluctuation data (the  $250\mu\text{s}$  correlation window for this timepoint) of the reference channel and its nearest neighbours along the radial direction (perpendicular to the flux surface), while the bottom left panel shows the cross-correlation coefficient of each channel with the reference channel as a function of the time delay imposed on the data before correlating, along with a Gaussian fit (dashed line) and the peak of the fitted Gaussian (star symbol). The time delay values at the Gaussian peaks are plotted with the distance between the corresponding BES channels in the bottom right panel, and a straight line fit weighted by the values of the cross-correlation coefficient at the peaks returns the gradient, from which the velocity (shown in the label in units of m/s) can be determined. The top right panel shows the frequency spectra of the cross-correlation coefficient plots in the bottom left panel.

by calculating velocities with the channels in each column, i.e. a ‘vertical’ velocity. For lower single null shots however, such as shot 29378 in Figure 5.13, the magnetic axis of the plasma is located below the midplane in  $z$ -space, so the flux surfaces captured by the BES array will be angled with respect to the BES columns, and the channels aligned on the same flux surface as the reference channel may not lie in the same column. In this case, to calculate the poloidal velocity, the equilibrium reconstruction from EFIT has to be incorporated in the CCTDE routine. For each reference channel, the flux surface value corresponding to the  $(R, z)$  location of the centre of the channel view is determined from an interpolation of the EFIT equilibrium, and then for each of the four rows the channel whose  $(R, z)$  location aligns closest with the flux surface of the reference channel is selected. The poloidal velocity is then calculated from the four selected channels according to the CCTDE method described previously. As the plasma equilibrium shape evolves during a discharge, the above calculations are performed for each new equilibrium within the chosen time slice, ensuring that any shape changes are taken into account for the velocimetry.

#### 5.2.4.2 Radial velocities

Poloidal velocities are the velocities of structures moving poloidally along the flux surfaces, while radial velocities are those arising from movement radially outwards i.e. perpendicular to the flux surfaces. To calculate radial velocities with the CCTDE velocimetry method, the EFIT equilibrium is included in a similar manner, with a line perpendicular to the LCFS and intersecting the coordinates of the reference channel used to find the channel selection for the velocimetry calculations. In this process, for each of the eight columns the channel whose coordinates are closest to the perpendicular line is selected, unless the nearest channel is located more than 1.2cm away from the line in which case the column is skipped. This is to ensure that once the perpendicular line has moved outside of the array area no more channels are included in the velocimetry calculation. This method would allow up to eight channels to be included in the radial velocity calculations, but in practice the list of channels was reduced to the nearest neighbours for the CCTDE, as seen in Figure 5.18.

As charged particle motion is strongly enhanced along flux surfaces and generally suppressed between flux surfaces, poloidal velocities are expected to be stronger and more regular than radial velocities, so any poloidal velocity component which might be included in the radial velocity measurement can easily overwhelm the actual radial velocities. Initial cal-

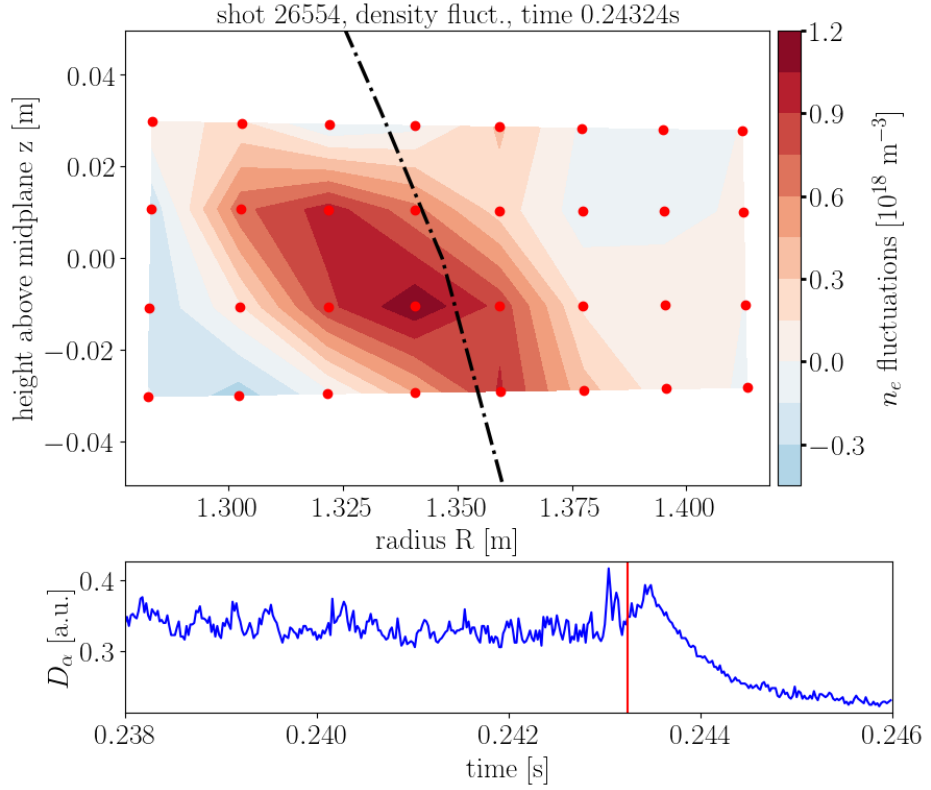


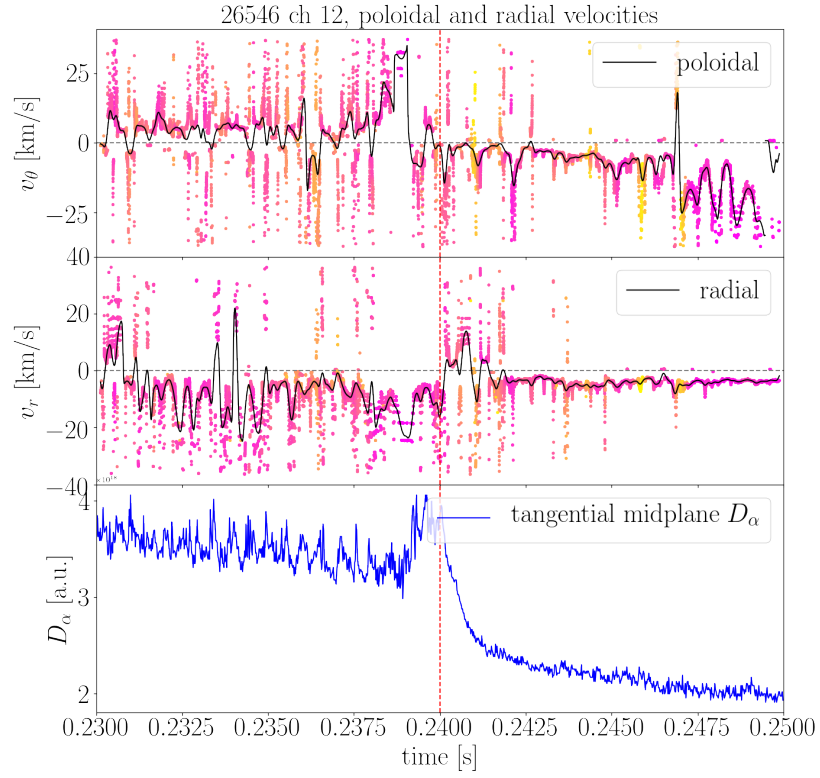
Figure 5.19: Tilted filament structures moving poloidally, like this one during the L-H transition of a lower single null shot, can introduce an apparent but false radial velocity. This is known as the barber pole effect and can cause significant issues in the estimation of radial velocities from BES data.

Calculations of radial velocities with the method described above results in values which are unusually high at times, and some attempts have been made to investigate them, though more efforts are needed to reveal the velocities occurring from true radial motion. Radial velocity calculations are impeded by a number of effects which can inflate the calculated velocity magnitudes, introduce features which are not present in the plasma itself or blend poloidal and radial velocity ‘measurements’ together. One such effect is known as the “barber pole illusion”, the common optical illusion effect as seen on spinning barber poles. It describes the effect of an apparent radial velocity introduced through the poloidal movement of a tilted structure, such as in Figure 5.19 where the poloidally upwards movement of this tilted structure would be captured as an outward movement to increasing radius in the radial velocity. The barber pole illusion is known to affect CCTDE-type velocimetry techniques and can be very laborious to circumvent [114, 115]. This and other effects can cause the measured radial velocity to contain poloidal velocity components, and it can be difficult to

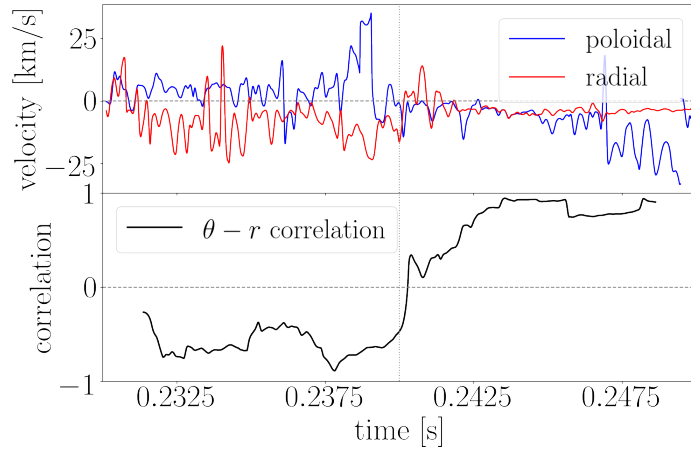
disentangle these to arrive at a true radial velocity. Some attempts were made to identify the poloidal velocity components present in the radial velocity, but their conclusions have not yet been implemented in the CCTDE method.

To identify poloidal velocity components in the radial velocity, the two velocities can be cross-correlated (without time delay). An example for such a calculation is shown in Figure 5.20, with the poloidal and radial velocities for the L-H transition of a LSN shot separatrix channel shown in the top figure and the correlation between them shown in the bottom. In Figure 5.20a, the results for the velocity calculations for each timepoint are plotted as points, colour-coded by the maximum value of the cross-correlation coefficient (yellow for low correlation and magenta for high correlation), and the black lines show the interpolated velocity traces. These interpolated velocity traces are used for the  $\theta - r$  correlation and plotted in the top panel of Figure 5.20b,  $v_\theta$  in blue and  $v_r$  in red, and the  $\theta - r$  correlation value as a function of time is plotted in the bottom panel. The velocities show a consistent moderate anti-correlation during the L-mode phase which switches to a strong (positive) correlation of the two in the H-mode phase. For channels in the SOL for the same shot,  $v_\theta$  and  $v_r$  were quite strongly anti-correlated throughout the whole timeslice (not shown). Strong and consistent correlation or anti-correlation can indicate that the radial velocity may contain poloidal velocity components.

The velocimetry method can also introduce a false poloidal velocity component in the radial velocity through the channel selection based on the equilibrium data. As described in the beginning of this section, the channels selected to be included in the radial velocity calculation are determined by drawing a line perpendicular to the LCFS which intersects with the reference channel. For each BES array column, the channel which lies closest to this line is then chosen. As can be seen in Figure 5.21a, most channels will be poloidally displaced from the perpendicular line by a non-zero distance. This poloidal displacement can introduce poloidal velocity components into the radial velocity calculation. To estimate how great this effect is, an alternative estimate for the radial velocity can be calculated by using the channels which are closest to the line but poloidally displaced in the opposite direction (i.e. the second closest channels). The radial velocity estimates for the original method (the ‘best fit’, in black) and the alternative second closest channel method (‘poloidal displacement’, in red) are plotted in Figure 5.21b. If the two velocities cancel out, the calculated radial velocity is likely to be due to the channel separation rather than a true velocity, though the

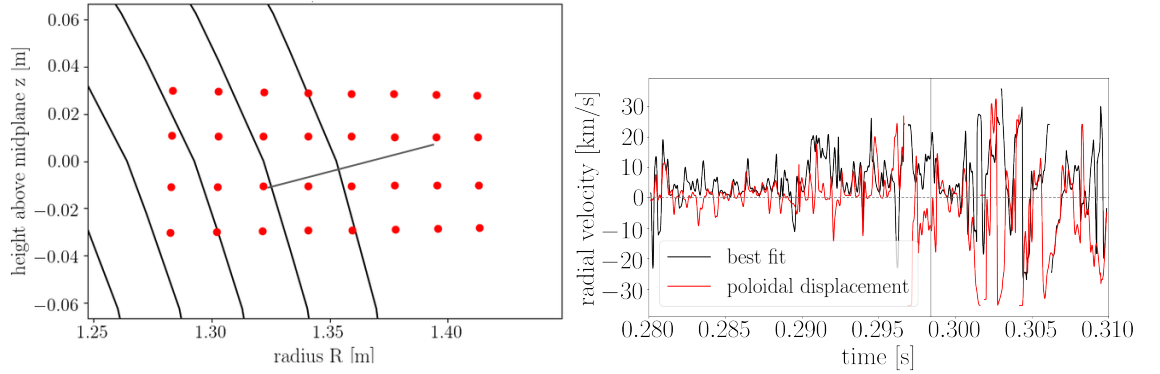


(a) Poloidal and radial velocities



(b) Poloidal-radial velocity correlation

Figure 5.20: (a) The poloidal  $v_\theta$  and radial velocity  $v_r$  as determined from the BES data of an edge channel from a LSN shot using the CCTDE velocimetry method. The results for each timestep are plotted as points, colour coded by maximum correlation value (yellow for low correlation and magenta for high correlation), while the black lines show the interpolated velocity traces. The tangential midplane  $D_\alpha$  signal is plotted in the third panel, and the L-H transition is shown as the red dashed vertical line. (b) The poloidal (blue) and radial (red) velocity traces from (a) are shown in the top panel, and the correlation between poloidal and radial velocities is shown in the bottom panel. The L-H transition at 0.24s is indicated by a vertical red (a) or grey (b) dotted line.



(a) Perpendicular (radial) line and BES channels (b) Effect of poloidal displacement on radial velocities

Figure 5.21: (a) The  $(R, z)$  locations of all channels in the BES array are plotted along with contours of some flux surfaces (including the LCFS as the outermost contour). The radial direction for  $v_r$  calculations is found by plotting a line from the reference channel perpendicular to the LCFS. The channels that lie closest to the perpendicular line and are therefore included in the radial velocity calculation are poloidally displaced from the line by varying amounts. (b) To check if the radial velocities are true radial velocities or a measure of the poloidal displacement, an alternative radial velocity (in red) is calculated using the nearest channels poloidally displaced from the perpendicular line in the opposite direction.

relative poloidal distances of the two channels to the line must be taken into account as well.

### 5.2.4.3 Results

For those shots for which the CCTDE method managed to produce good results, i.e. (for a large proportion of timepoints) the cross-correlation coefficient for channels along the same poloidal (or radial) line contained a peak with high correlation value that was well fitted with a Gaussian, and the straight line fit through the time delay values of the Gaussian peaks has a low uncertainty (examples are shown in Figures 5.17 and 5.18), there were several features in common for velocities across the L-H transition. Figure 5.22 shows the poloidal velocities across the L-H transition for an edge ( $\psi = 0.99$ ) and a SOL ( $\psi = 1.04$ ) channel of a LSN shot along with the midplane  $D_\alpha$  signal, with the L-H transition marked by a red vertical line. In the L-mode phase, the edge channel contains a steady poloidal velocity of 5 – 10km/s, with almost all timepoints returning a good fit with a high correlation value (magenta points). The SOL channel contains a velocity in the opposite direction to the edge, slightly lower at a few km/s and with more noise and fluctuations though still strongly correlated. The opposite directions of the velocities of the edge and SOL channels during L-mode is consistent with the existence of a velocity shear at the separatrix. The poloidal velocity in the edge channels is also found to reverse in direction as the shot transitions into H-mode, though the

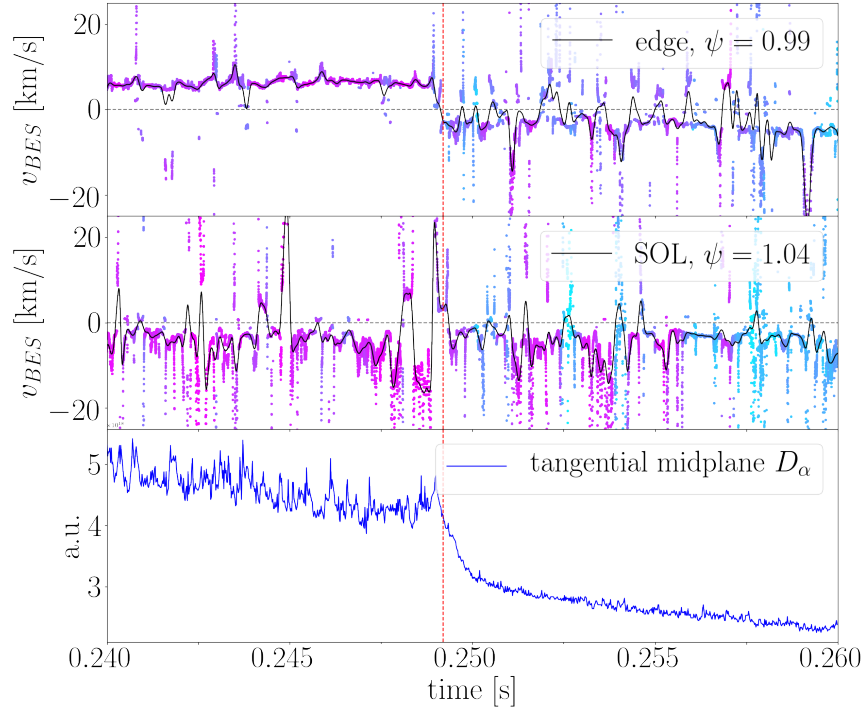


Figure 5.22: Results for the poloidal velocimetry technique for a lower single null shot during an L-H transition, showing the poloidal BES velocity  $v_{BES}$  in the edge (at  $\psi_N = 0.99$ ) and in the SOL (at  $\psi_N = 1.04$ ) along with the tangential midplane  $D_\alpha$  signal. The results for each timestep are plotted as points, colour coded by maximum correlation value (cyan for low correlation and magenta for high correlation), while the black lines show the interpolated velocity traces. The velocity shear across the separatrix can be seen in the L-mode phase.

velocity in H-mode is much less steady and consistent than that of the L-mode phase. For channels across the BES array, H-mode velocities show strong fluctuations and the peaks in the cross-correlation are much more likely to have low values (low correlation values are shown as cyan points in Figure 5.22 and yellow points in Figures 5.20a and 5.23). While the radial velocity method hasn't been refined to filter out effects mentioned in the previous section, some common features have been noted. In confined channels and edge channels further into the confined region, the radial velocity appears to fluctuate strongly during L-mode, even in cases where the poloidal velocity remains steady (shown in Figure 5.23). In channels which are right by the separatrix or further out in the SOL, the radial velocity during L-mode appears to be in the outward (inward) direction when the poloidal velocity direction is pointing to the lower (upper) divertor, as seen in the “opposite” direction of the velocities shown in Figure 5.20a.

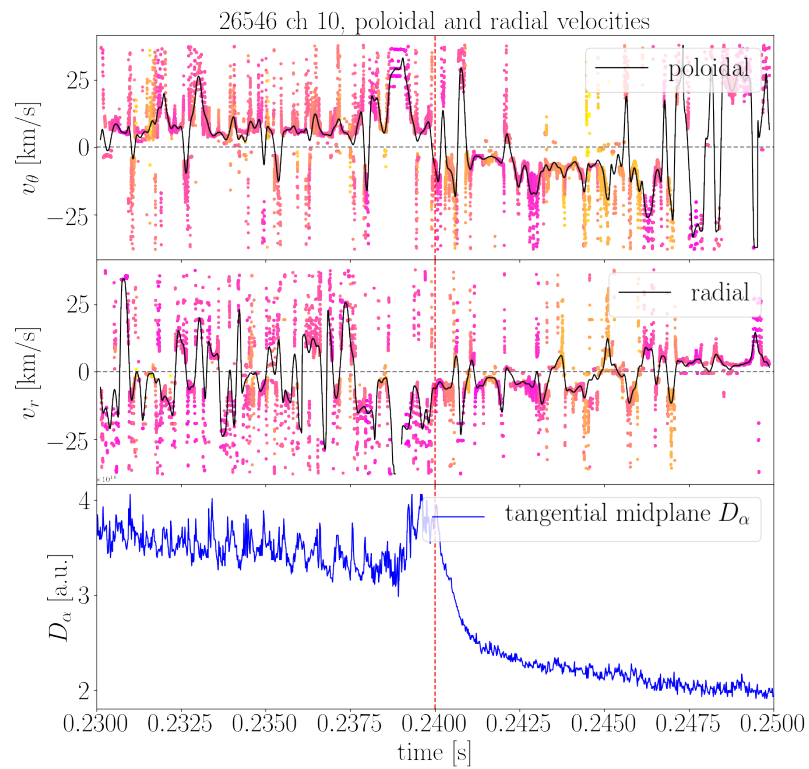


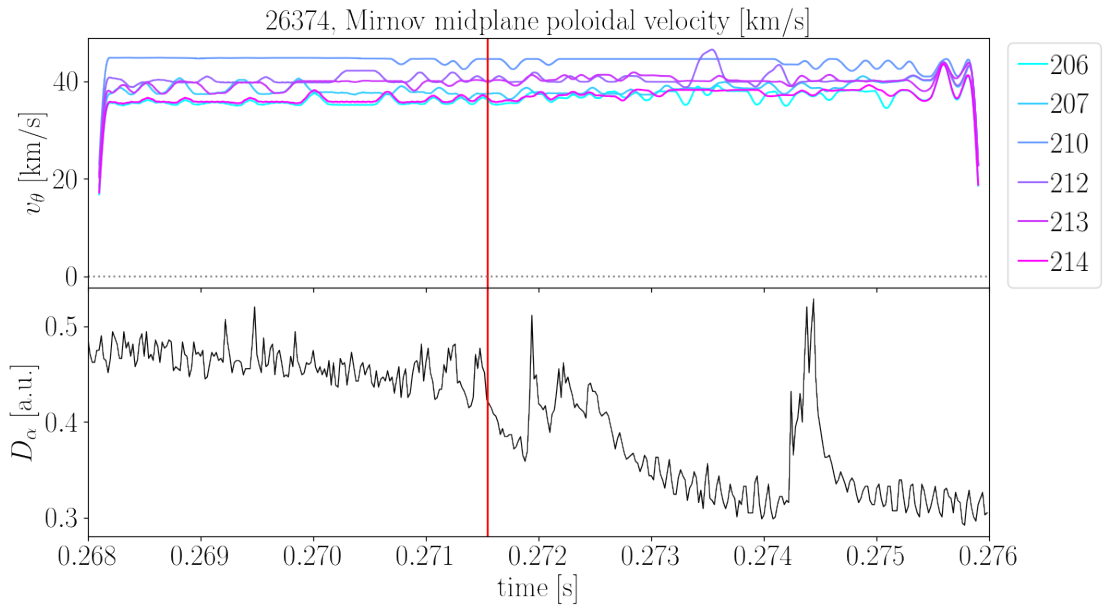
Figure 5.23: The poloidal  $v_\theta$  and radial velocity  $v_r$  as determined from the BES data of an edge channel from a LSN shot using the CCTDE velocimetry method. The results for each timestep are plotted as points, colour coded by maximum correlation value (yellow for low correlation and magenta for high correlation), while the black lines show the interpolated velocity traces. The tangential midplane  $D_\alpha$  signal is plotted in the third panel, and the L-H transition is shown as the red dashed vertical line. Shown as an example of strongly fluctuating  $v_r$  in L-mode even with steady  $v_\theta$ .

#### 5.2.4.4 Mirnov velocimetry

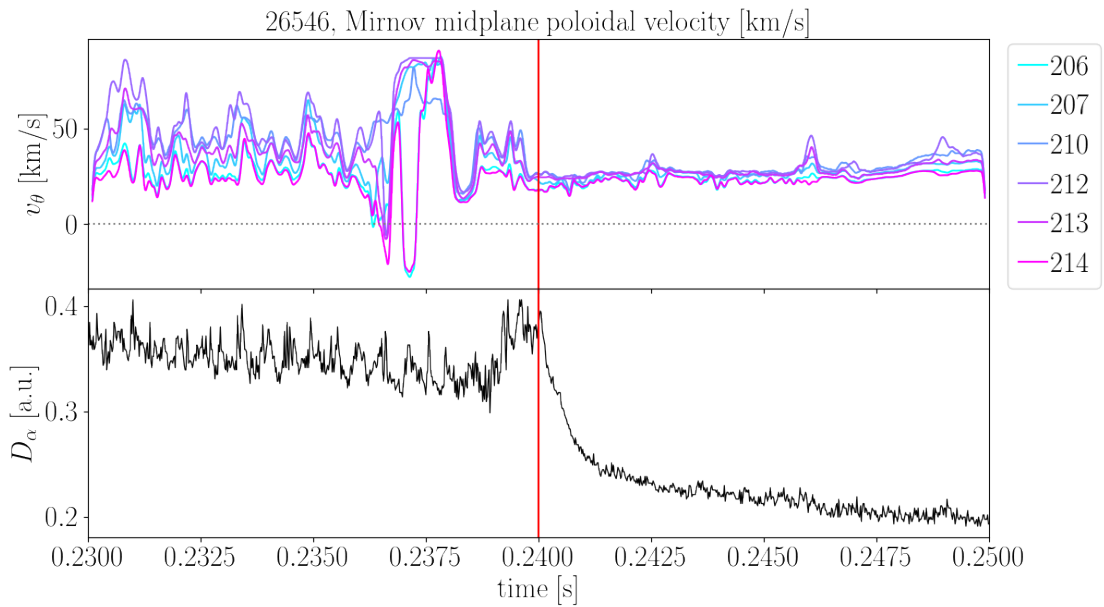
A modified version of the CCTDE velocimetry method can be applied to Mirnov coil data as well. To achieve this, the Mirnov coils must first be mapped onto the LCFS, so that the poloidal distance between them can be determined. Once that has been done, the velocities are again found by cross-correlating different coil data with that of a reference coil, adding an incremental time delay. The cross-correlation coefficient is again fitted with Gaussians, and the velocity is determined from the straight line fit to the Gaussian peak time delay values and their corresponding poloidal distance from the reference coil. Most cases achieved good fits with strong correlation values, irrespective of whether or not the CCTDE achieved results with the BES data. Where the BES method failed due to strong LLM presence though, the Mirnov velocimetry results are characterised by a constant velocity of around 40 – 50km/s (with an example shown in Figure 5.24a). The shots which achieved decent BES velocimetry results showed more fluctuations in the Mirnov velocity data (with an example shown in Figure 5.24b). There were no clear trends visible, but the Mirnov velocity values were usually between 20 and 80 km/s. If these Mirnov velocities are measuring anything, they are likely to be measuring the velocity of the MHD instabilities and have no relation to velocimetry measurements from BES which attempt to measure turbulence velocity through density fluctuations.

#### 5.2.5 Wavenumber-frequency spectra

Along with the 1D frequency spectrum (e.g. Figure 5.6) and spectrograms (e.g. Figure 5.7b), higher order spectra can also be generated from BES fluctuation data. Incorporating the spatial dimension (in the poloidal direction) along with the temporal dimension in the Fourier transform leads to the generation of 2D wavenumber-frequency spectra  $S(k_\theta, f)$  for each radial location of a BES array row. Similar to the poloidal velocity calculations in the previous section, the channels to include for each radial location are chosen by mapping the BES array channels onto the equilibrium data and choosing channels lying on the same poloidal flux surface. Wavenumber-frequency spectra have previously been used to show the propagation direction and speed of turbulence at different radial locations [2, 116] (example plots shown in Figure 5.25), and similar calculations were attempted for the MAST BES data available in this study. As can be seen in Figure 5.25, the  $k - f$  spectra generated from GPI data on C-mod showed characteristic flows in the electron diamagnetic direction



(a) In presence of strong MHD modes



(b) Example shot with less MHD

Figure 5.24: Results from applying the velocimetry method to Mirnov coil data with coils at  $R = 1.85\text{m}$  for (a) a double null shot with a strong LLM and (b) a LSN shot which was able to image turbulence with the BES system. The interpolated poloidal velocity lines for six reference coils the same radial location plotted on the same axis with  $D_\alpha$  data. L-H transitions marked in red.

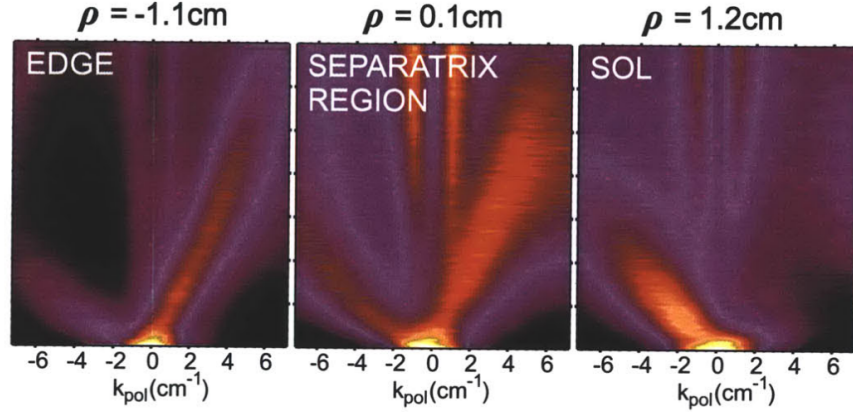


Figure 5.25: Reproduced from I. Cziegler’s thesis [2]: Ohmic L-mode turbulence features visible in conditional poloidal wavenumber-frequency spectra at three radial locations, measured using GPI on Alcator C-Mod.  $k_\theta > 0$  corresponds to propagation vertically upwards (in the electron diamagnetic drift direction), characteristic in the edge, and  $k_\theta < 0$  corresponds to downward propagation (in the ion diamagnetic drift direction), characteristic of the SOL. Both features are seen in the separatrix region (middle panel), along with two narrow vertical spikes in the centre caused by noise.

(EDD) in the edge and in the ion diamagnetic direction (IDD) in the SOL, while the  $k - f$  spectra of the separatrix region contained features of both. The example  $k - f$  spectra can be well fitted with linear dispersion relations ( $v_{ph} = v_g = 2\pi f/k_\theta$ ) and phase velocities of  $v_{ph} \sim 2\text{km/s}$  in the IDD for the SOL and  $v_{ph} \sim 4\text{km/s}$  in the EDD for the edge. Unlike the GPI diagnostic used for the  $k - f$  spectra of C-Mod data [2] like Figure 5.25, the BES diagnostic on MAST has only four pixels in the poloidal direction and the  $k - f$  spectra are therefore limited both by the size and the spatial resolution of the BES array.

Figure 5.26a-c show the initial  $k_\theta - f$  spectra produced for a LSN shot during a quiescent L-mode period, for a confined, edge and SOL channel respectively. The region at low frequency is very bright, and the signal strength drops off for higher frequencies. To reveal information on the higher frequencies as well, the normalisation in form of a conditional spectrum [2]

$$S(k_\theta|f) = \frac{S(k_\theta, f)}{\sum_k S(k_\theta, f)} \quad (5.12)$$

is used instead, as was done with GPI data from C-Mod [2]. The conditional spectra for the three radial locations of the LSN shot are shown in Figure 5.26d-f, with the features being much clearer to discern. Unlike the spectra from C-Mod, the  $k - f$  spectra from MAST BES

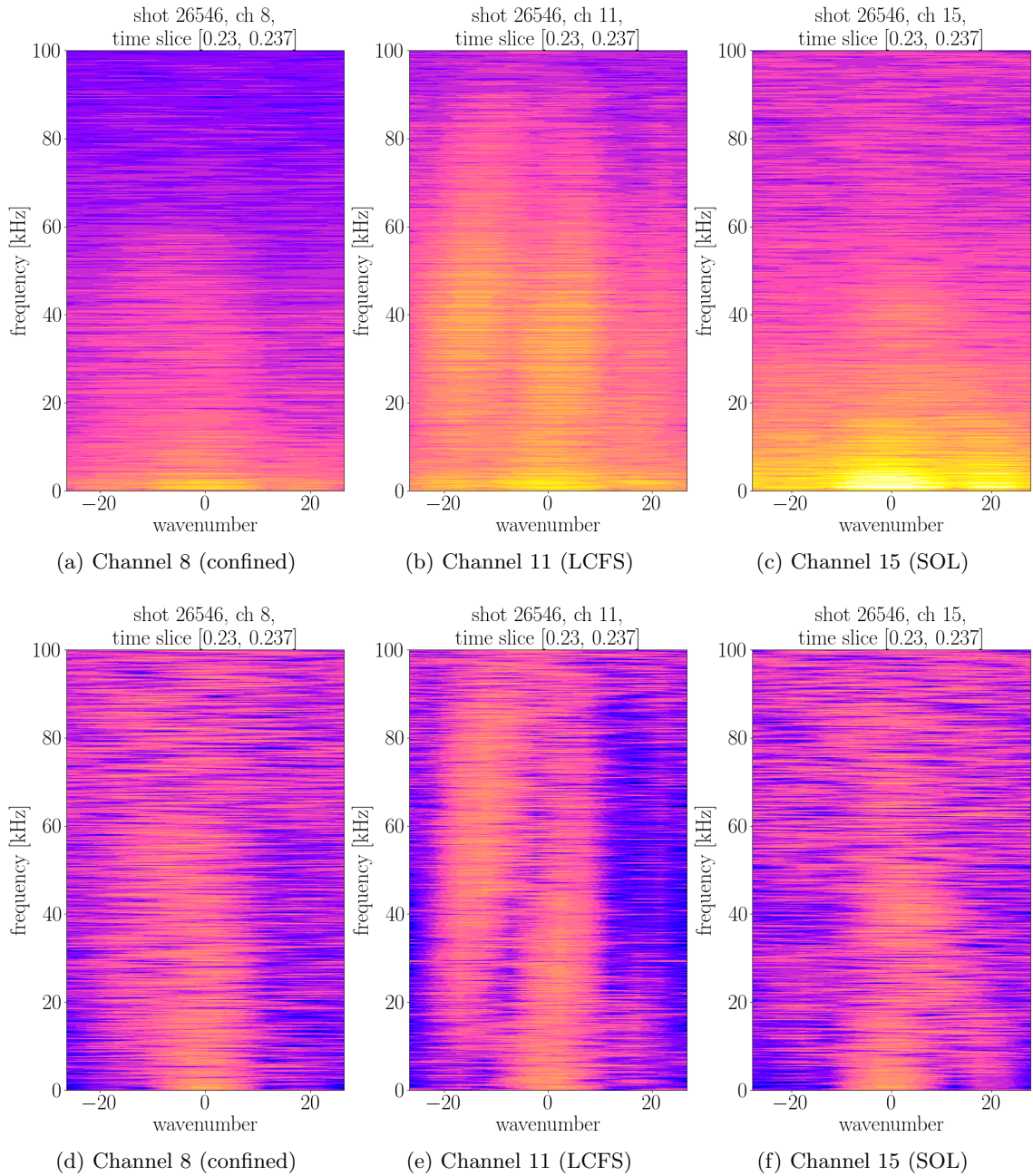


Figure 5.26: Wavenumber-frequency spectra of L-mode BES data for three radial locations of a LSN shot: (a) in the confined plasma, (b) at the LCFS and (c) in the SOL. Normalised (conditional) spectra for the same three locations are shown in (d)-(f).

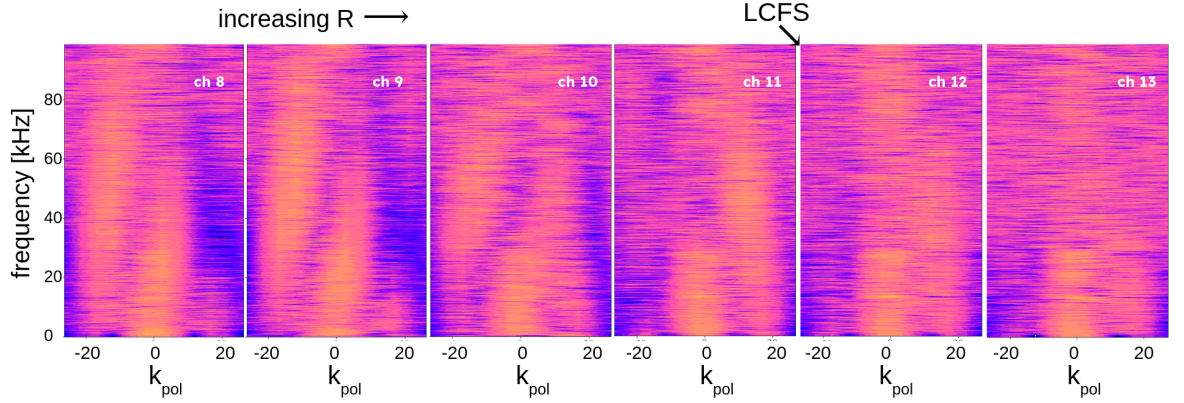


Figure 5.27: For another LSN, the structure of the  $k - f$  spectrum changes for locations of increasing radius, with the ‘blob’ moving from negative  $k_\theta$  to positive  $k_\theta$  while the ‘lobes’ appear to flip around the  $k = 0$  axis.

data don’t appear to have a clear phase velocity or dispersion relation visible. Instead the channels in the edge near the separatrix appear to contain a ‘blob’ made up of two lobes, and the lobes are oriented in a different direction to the overall ‘blob’ structure. This behaviour can be seen again in Figure 5.27 for six consecutive channels of a different LSN shot. In this case, going from confined to SOL plasma, the ‘blob’ structure appears to move from negative to positive  $k_\theta$ , and the ‘lobe’ structure appears to get flipped around the  $k = 0$  axis as the LCFS is approached. It is possible that the irregular structure of the  $k - f$  spectra is due to a poor approximation of “poloidality” for single null shots, and that a midplane-symmetrical double null shot has a higher chance of generating clear features.

Unfortunately, the same problems we encountered in the velocimetry, i.e. the strong long-lived MHD modes, also make reading the  $k - f$  spectra difficult for the double null shots. An example edge channel of a DN shot with a strong LLM is shown in Figure 5.28, with the original  $k - f$  spectrum shown on the left and the normalised/conditional spectrum shown in the middle. The LLM of frequency around 20kHz can clearly be seen across the  $k_\theta$ -space and in its multiple harmonics. The conditional spectrum shows the strength of the mode especially at  $k = 0$ , so another version of the  $k - f$  spectrum with the central wavenumber filtered out is plotted on the right. While some faint features can be recovered, the MHD mode is too overwhelming and ultimately the spatial resolution of the BES array too low to make a quantitative or qualitative analysis of the  $k - f$  spectra.

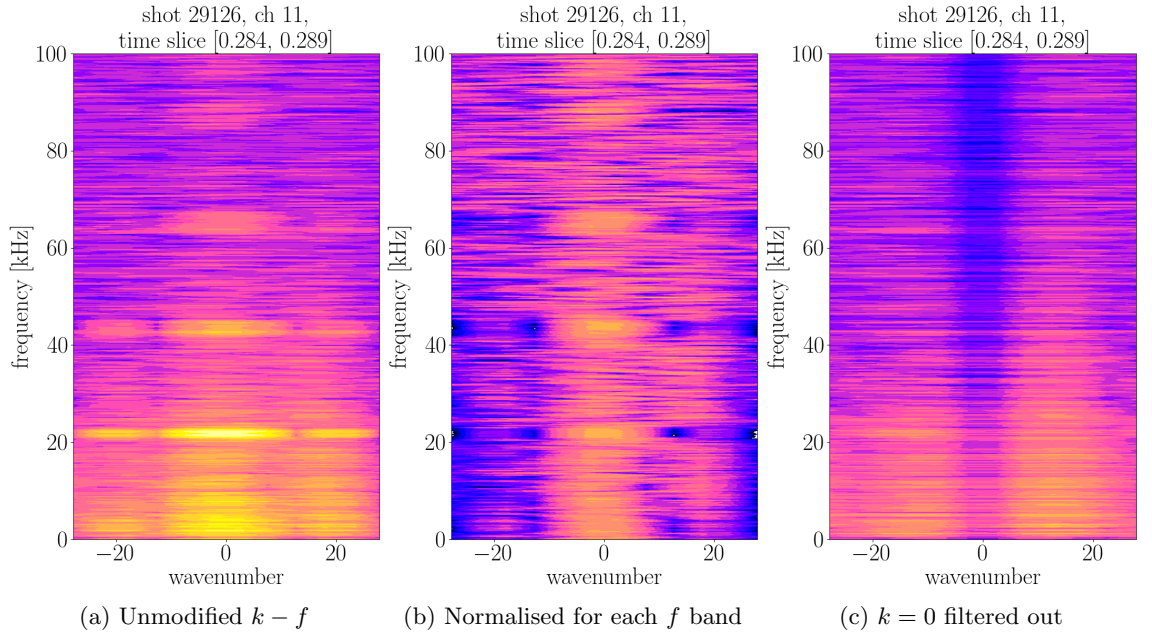


Figure 5.28: Wavenumber-frequency spectra for an edge channel of a DN shot with strong long-lived MHD mode of frequency  $\approx 20\text{kHz}$ . The original  $k - f$  spectrum is shown in (a), the normalised (conditional) spectrum is shown in (b), and for (c)  $k = 0$  has been filtered out.

### 5.2.6 Further steps to energy transfer

The initial aim of this chapter was to investigate the edge turbulence in L-modes approaching and transitioning to H-mode, and to attempt to reproduce experimental findings from other devices such as C-Mod about the importance of the nonlinear kinetic energy transfer from turbulence to zonal flows within the dynamics of the L-H transition. The model equations describing these dynamics found in the beginning of this Chapter feature many velocity terms, which due to the Reynolds decomposition applied to separate turbulence fluctuations and slowly varying mean flows are mostly in the form of small-scale velocity fluctuations. This was in part what motivated the design and refinement of the velocimetry methods described in the Chapter. These techniques have been applied to 2D density fluctuations measured by the BES turbulence diagnostic on MAST. While progress has been made in extracting velocities from the fluctuating BES signal, there are still systematic effects present which introduce significant errors and uncertainties into fluctuation velocity measurements, some of which have been identified but not yet addressed, while others might not yet have been recognised so far. The small scales involved as well as low spatial resolution of the BES array

can easily lead to results which are overwhelmed by noise or systematic errors.

As the dataset used for the turbulence analysis of BES data was by necessity made up of unconnected shots from different experiments, with very different experimental aims and setups, and no statistical or comprehensive analysis could be performed to draw any conclusions on the combined shots, I instead hoped to use BES data collected during our L-H transition experiments on MAST-U to make a quantitative analysis of the energy transfer between turbulence and zonal flows and verify previous assumptions of its importance in the L-H transition. The four additional rows (leading to an  $8 \times 8$  array) will also improve the data collection significantly. To prepare for these experiments, techniques from intermediate steps towards transfer calculations were tested on selected MAST shots.

Due to a number of difficulties with the BES system on MAST-U, including the loss of components during storage due in part to the delay in launching MAST-U as well as device-wide signal interference issues, there was no BES data available for first experimental campaign and the data in the second campaign was not of good enough quality to apply any of the analysis methods developed for MAST BES data. Since then, strides have been made in improving the data quality, and it is likely that these methods will be successfully applied to BES data of future campaigns, and some of the aims discussed in the beginning of this chapter will hopefully be answered by researchers continuing this work.

## Chapter 6

# Conclusion and further work

As the different Chapters have highlighted, the project of this Thesis was not easy to fit neatly into one topic area. Confinement transitions, especially the more well-known transition from L- to H-mode, are processes with complex dynamics and many demonstrated aspects and potential triggers. L-H transitions have been the topic of multiple studies across different devices, and while the studies have revealed some consensus on the evolution of certain physical mechanisms leading up to and during the transition, the relative importance of the different triggers are still a topic of debate. Some theoretical frameworks exist for describing parts of the transition, and a few of them have limited recognition across different research groups, but neither a fully recognised comprehensive model nor a theoretical simulation framework is so far able to describe the transition with all its aspects. Both experimental and theoretical work on the transition are still ongoing with new findings revealed regularly, so L-H transition studies continue to remain an important and active area of study to this day.

As the vast majority of existing tokamak devices are based on the conventional aspect ratio design, our knowledge base for low aspect ratio or spherical tokamaks is still rather sparsely populated, although we do know that there are some scenarios in which the two design concepts can exhibit rather different behaviours. One of these scenarios is the L-H transition, demonstrated in the significant differences in the threshold power  $P_{LH}$ . As we do not yet have a model to reliably predict  $P_{LH}$ , we instead have to rely on empirical scaling laws to estimate the dependence of  $P_{LH}$  on selected parameters, including density, toroidal magnetic field and plasma surface area. These scaling laws are based on large databases of transitions on mostly conventional aspect ratio tokamaks, and usually predict the high

density branch of  $P_{LH}$  quite well for other conventional tokamaks. Attempting to apply these scaling laws to spherical tokamaks like MAST however can under certain conditions lead to a rather poor performance, with the experimental  $P_{LH}$  significantly higher than that predicted by the scaling laws. A few potential causes for this discrepancy have been suggested, including a change in divertor conditions, but as a number of features could explain it and a consensus does not yet exist, further studies of spherical tokamaks and their transition dynamics are required.

The mix of topic areas found in these chapters and the analysis of different datasets analysed which are not always clearly related is due to the dynamic evolution of the thesis project, based on what data (and of what quality) was available at different times, how the experiment (planning and execution) on MAST-U was progressing, and what avenues were explored but proved less fruitful. There were a few topics where analysis work had been carried out but no useful results were obtained, and the concluding analysis work for other topics has not yet been performed. Most significantly, the work on MAST-U (including the experiment design, planning, execution and the data analysis) was originally supposed to comprise a separate chapter, but time constraints in the write-up of this thesis (outside of my control) led to a condensing of this work down into a section of this Chapter. In spite of some set-backs mostly out of my control, detailed investigations into the power threshold and ion and electron heat flux were produced for a set of MAST data, with comparisons to earlier MAST data as well as MAST-U data, and the significant impact of the apparent density dependence of the heating efficiency of neutral beams on MAST was explored. The turbulence work in Chapter 5 has provided valuable foundations for further work in this area, which will hopefully be usable for future projects.

## 6.1 Conclusion of MAST work

The analysis with MAST data can be categorised into three main topics, the power threshold analysis described in Chapter 3, the heat flux analysis described in Chapter 4, and the turbulence analysis described in Chapter 5. The power threshold and heat flux studies were performed on the same dataset, while the turbulence analysis was done with a collection of unconnected shots as the BES data of the main dataset was overwhelmed by MHD modes. In Chapter 3 the first comprehensive  $P_{LH}(n_e)$  curve, including the low-density branch, was

produced for MAST. In this process, a detailed study of the types of transition behaviours and intermediate confinement states, possibly equivalent to phenomena such as limit-cycle oscillations (LCOs), was performed using mainly  $D_\alpha$  data to characterise the types of fluctuations seen. The different boundary states can be quite clearly separated in multiple aspects both qualitatively and quantitatively, and are found in different regions of the  $P_{LH}(n_e)$  curve. A fit to the high density branch of the  $P_{LH}(n_e)$  curve was performed, and the results were compared with different scaling laws, which all underestimated  $P_{LH}$  significantly. In Chapter 4, comprehensive interpretative TRANSP simulations were performed for the same dataset in order to investigate the ion and electron heat flux in the edge. To achieve this, manual time histories of the anomalous diffusivity  $D_{an.}$  were created to optimise the match between measured neutron rates and those predicted by TRANSP. The large fast ion losses inferred from high  $D_{an.}$  values were verified by inspecting Mirnov coil data for MHD modes. The ion and electron heat flux values were compared with  $P_{LH}$  values, and while  $Q_e$  showed a strong linear density dependence,  $Q_i$  did not appear to have any density dependence. The results from a previous study on ASDEX Upgrade could therefore not be verified with the NBI-heated MAST data. Instead, the study revealed the strong density dependence of the NBI heating efficiency, with the lowest density plasmas absorbing only  $\sim 15\%$  of the injected beam power. The largest source of beam power losses is due to orbit losses and external charge-exchange losses, i.e. fast ions lost from the plasma. Plasmas of similar densities but different injected beam powers appeared to receive the same absorbed beam heating, suggesting that increasing the beam power beyond a certain value appears to be practically pointless in terms of heating the plasma. With these new conclusions of the NBI heating efficiency, the  $P_{LH}(n_e)$  curve was recreated with the absorbed NBI power instead. While all values were lower, the low-density branch is still clearly visible and the values are still significantly above the Takizuka scaling. The U-shaped density dependence of the MAST  $P_{LH}$  data appears to be caused primarily by the  $dW/dt$  term. In Chapter 5, the density fluctuations measured by beam emission spectroscopy (BES) of selected L-H transition shots were analysed. The first procedure involved a coherence and phase analysis of a TAE and an ELM-precursor, finding mode frequencies, locations and powers as well as phase velocities for channels across the BES array. As a first step towards calculating the energy transfer between spectral components, a velocimetry technique based on CCTDE was developed, which was applied on BES data to find poloidal and radial velocities. The poloidal velocity

shear across the separatrix and a reversal in velocity across the L-H transition has been demonstrated. The poloidal velocity technique is quite reliable, but for the radial velocity effects such as the barber pole illusion can introduce false velocity components. A few of these effects are explored in the Chapter, but a full treatment of them to reveal true radial velocities has not yet been performed. Higher order spectra such as wavenumber-frequency spectra were also explored, but the low spatial resolution in the poloidal direction makes the results quite difficult to interpret. While the initial motivation was to perform energy transfer calculations and present bispectra of the results, this has not yet been achieved at this time.

## 6.2 MAST-U experiments

The original project aims focused in part on the study of turbulence in L-H transitions comparing novel divertor configurations, and a large part of the project would have included experiments on MAST-U measuring edge turbulence with the BES system for conventional and Super-X divertor configurations. The first proposals for MAST-U experiments were written and submitted within a few months of starting the PhD. At the time I started the PhD, the first campaign of MAST-U had already been delayed by several years, and further delays took place during the course of my PhD, so that the first experiments which I was able to take part in occurred in October 2021, three years after starting. The experiment proposal we initially submitted, “Characterisation of  $P_{LH}$  and H-mode quality in conventional and Super-X divertors” was very ambitious, as we were aiming to conduct a power threshold study and measure edge turbulence with BES and Doppler backscattering (DBS) for both conventional and Super-X divertor plasmas. Power threshold studies, especially for brand new devices such as MAST-U, require a large number of shots to cover the density and power space with a high enough resolution to be able to draw a  $P_{LH}(n_e)$  curve with confidence. As MAST-U during its first campaigns is heated entirely with neutral beams, power scans have to be performed on a shot-by-shot basis as the power cannot be varied during the shot itself beyond “no beams”, “one beam” and “two beams”. As the characterisation of  $P_{LH}$  for the new device was desirable for most other researchers too, and our proposal’s themes of attempting to understand the effects of divertor configuration on edge and SOL transport as well as plasma performance were well aligned with the motivations behind MAST-U’s

design concept, our proposal was accepted and merged with other L-H transition proposals before being allocated 30 shots, and I was able to play an active role in the experiments as a co-scientific coordinator (SC).

The process of performing experiments on MAST-U was very challenging. As it was essentially a completely new device, there was a steep learning curve even for more experienced researchers, and several plasma control features as well as diagnostics only became available part-way through the campaign. The turbulence study aspect of the experiment was no longer possible as data from the BES diagnostic was not available during this campaign. Our first experiment days took place before scenario development had been completed, and as the particular plasma scenario we required for our experiments was unique, we had to essentially perform our own scenario development while we were trying to perform our experiments. Very early on in the experimental campaign, it became clear that  $P_{LH}$  for the conventional configuration on MAST-U was very low, as plasmas would frequently transition to H-mode ohmically and maintaining L-mode plasmas with NBI heating appeared almost impossible. We therefore decided to focus our experiments on the Super-X configuration, which while the configuration had been demonstrated by others before us, no one had so far achieved an L-H transition in the Super-X phase. As we wanted to keep the plasma in L-mode while the configuration transitions from conventional to Super-X, we decided we would have to keep the plasma in a disconnected double null initially (see Chapter 2 for an explanation), and start the heating beams only once the Super-X phase has been reached (typically 0.4s after the start of the current ramp). To maximise the number of data points, we also staggered the beam start times, giving us three power points per Super-X phase. The late beam start times created some issues, as the beams introduced a density ramp and the radial outward expansion of the plasma, leading to increased wall interactions. Frequent locked modes on MAST-U also appeared to require an early application of beams to control. Most of the shots in our experiments were terminated early (before the current ramp down) through vertical instabilities, which often meant that the shots terminated before the plasma would have been able to transition to H-mode even if the  $P_{\text{net}}(n_e)$  combination had been enough. Throughout our experiments, we frequently found the plasma shape (such as the outer radius) and density difficult to control, and the neutral beams (especially South) were frequently unreliable.

In the end, we achieved a limited power and density scan for 600kA Super-X shots,

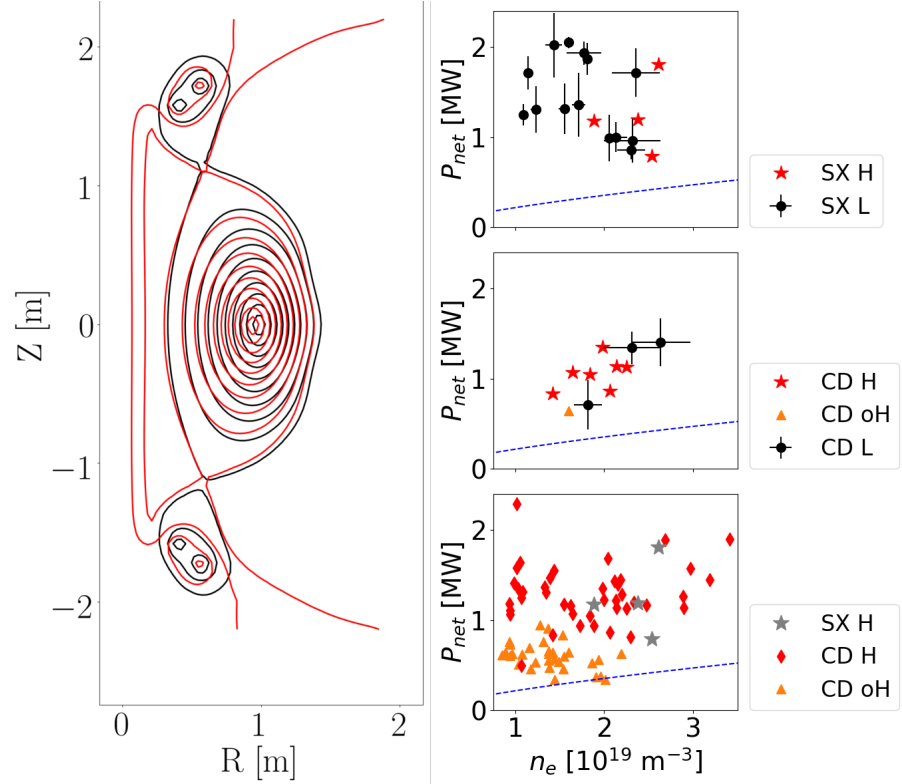


Figure 6.1: Initial results from a power threshold study of MAST-U data comparing a conventional and Super-X divertor configuration. Representative flux surfaces for a conventional configuration (black) and a Super-X configuration (red) are plotted on the left, while the plots on the right show  $P_{\text{net}}(n_e)$  values for (from top to bottom): (1) the H-mode and L-mode points of the Super-X shots in our experiments, (2) H-mode and L-mode points of a different experiment performed in a conventional configuration, and (3) all conventional H-mode points at the same plasma current ( $I_p \sim 600\text{kA}$ ). Heated H-mode points are plotted in red, ohmic H-modes are plotted as orange triangles and L-mode points are plotted in black (with the range of values found in the steady-state periods represented with error bars). The Takizuka scaling for  $P_{LH}$  is also plotted as a blue dashed lines in all panels.

including four H-modes which were at that point the only L-H transitions during the Super-X phase. The results for our Super-X shots are shown in the top panel on the right hand side of Figure 6.1. As we did not perform our own conventional divertor shots, I included results from another experiment of 600kA conventional divertor L- and H-modes in the middle panel. To highlight the relative ease of achieving H-modes in the conventional divertor configuration on MAST-U, I added all conventional 600kA heated and ohmic H-modes in the bottom panel. All panels also include the Takizuka scaling for  $P_{LH}$  as applied to MAST-U. With the difficulties in creating repeatable plasma shots and the lack of reliable information on the fraction of absorbed heating power, the  $P_{net}$  values can not really be compared with other devices such as MAST or scaling laws (although a comparison between MAST-U results and those from Chapter 3 is shown in Figure 6.3, suggesting MAST-U might behave closer to early MAST than later MAST after the installation of the new divertor), and while the first campaign appeared to suggest H-mode entry was much easier for conventional divertor configurations, results from the second campaign have created some doubts in these assumptions. Overall, we cannot yet say anything reliable about  $P_{LH}$  on MAST-U. Strong arguments can be made for the case that a power threshold study should be performed when a device is more mature, as the high repeatability requirements and large number of comparable shots needed for such a study are unlikely to be possible for a device this young. If the BES diagnostic had been available during these campaigns, a better experiment topic would have been to study the edge and SOL turbulence for a few comparable conventional and Super-X shots. As MAST-U matures and people become more and more familiar with the device, these studies are more likely to achieve good and usable results. Once additional heating methods have been installed on MAST-U, it will become a great device to study the effects of different heating methods on ion and electron heat fluxes and consequently the L-H transition.

### 6.3 MAST, MAST-U and potential extrapolation to STEP

In Chapters 3 and 4, overall essentially three sets of data points for the density dependence of  $P_{LH}$  on MAST were generated: The initial  $P_{loss}$  calculation for the L-H transition study from 2011 – 13 with  $P_{cap}^{NBI}$ , the adjusted  $P_{loss,th}$  for this dataset using  $P_{heat}^{NBI}$ , and a dataset from an earlier version of MAST used in the ITPA database and for the Takizuka scaling.

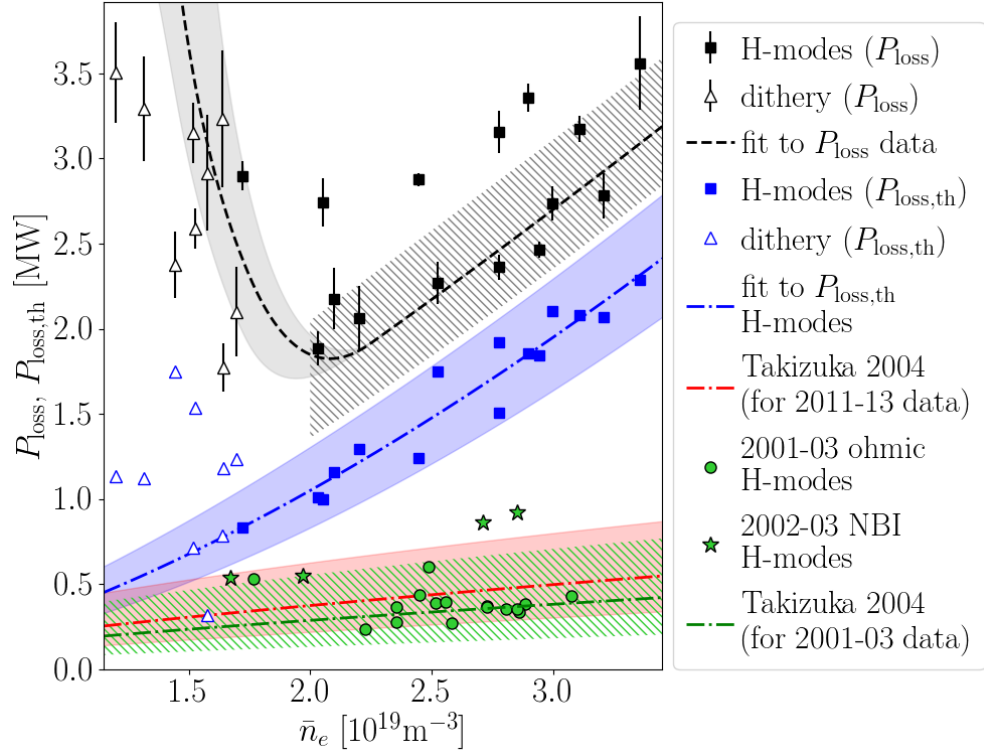


Figure 6.2: The initial  $P_{\text{loss}}$  values (with  $P_{\text{NBI}}$  corrected for shine-through losses only) for selected H-mode and dithery transitions in black are plotted along with their  $P_{\text{loss,th}}$  values (with  $P_{\text{NBI}}$  corrected for fast ion losses as well) in blue. The early MAST data used in the ITPA database are plotted in green, and the Takizuka scalings for both sets of MAST data are shown in red and green respectively.

The three versions of MAST  $P_{LH}$  data are shown in Figure 6.2, along with the Takizuka scalings for both MAST parameter collections and fits to the high-density branches of the two 2011 – 13 datasets with uncertainty bands. It can be seen that the  $P_{\text{loss,th}}$  adjustment reduced  $P_{LH}$ , which is also clear from the two fit equations, but that the data still doesn't align well with the Takizuka scaling. The earlier MAST data however matches its Takizuka scaling quite well, although the NBI-heated transitions lie a little above the uncertainty band.

While the differing methods between the estimates for  $P_{LH}$  on MAST and MAST-U mean a direct comparison cannot be made, Figure 6.3 nonetheless shows the two MAST datasets in (a), along with MAST-U data from (b) our Super-X experiments, (c) another conventional divertor experiment and (d) all CD H-modes (NBI-heated and ohmic) for the chosen MAST-U  $I_p \sim 600 \text{kA}$ . MAST-U appears to align closer with the early MAST data for  $P_{LH}$ , also demonstrated by the ease of ohmic H-mode in conventional divertor. Parameters for the

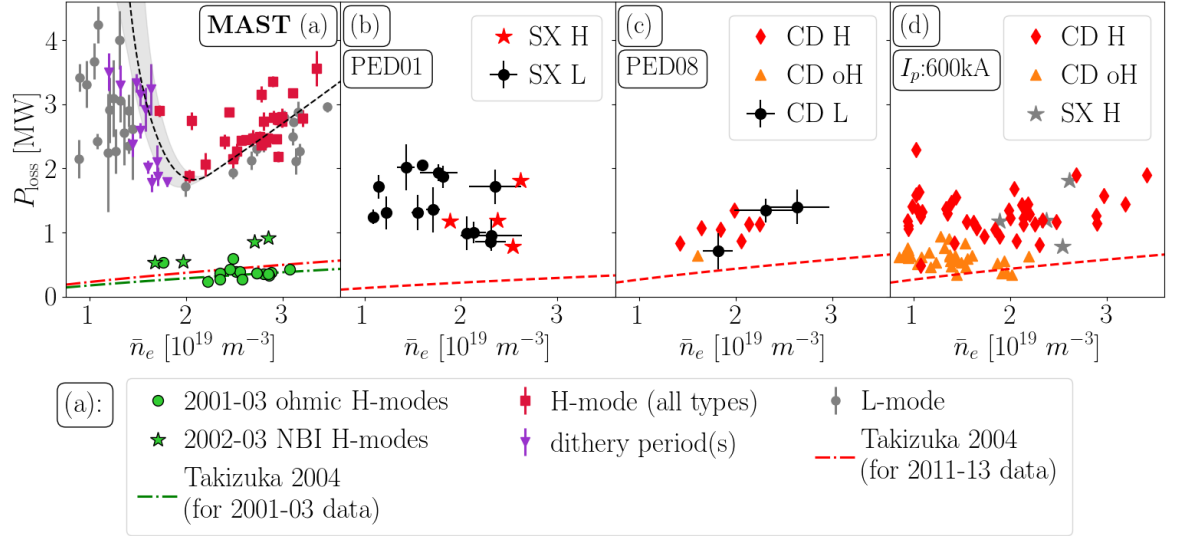


Figure 6.3: Comparison of (a) MAST  $P_{LH}$  study ( $I_p \sim 750\text{kA}$ ) and pre-divertor change ITPA MAST H-modes ( $I_p \sim 640\text{kA}$ ) (see Chapter 3) with MAST-U data (all at  $I_p \sim 600\text{kA}$ ) from (b) Super-X (SX)  $P_{LH}$  study, (c) data from one conventional divertor (CD) experiment, and (d) all CD H-modes from the first campaign. As in Figure 6.1, L: L-modes, H: NBI heated H-modes and oH: ohmic H-modes. The Takizuka scaling is plotted for each case, with (a) showing both scalings for the parameters of each experiment (and time period), (b) showing the scaling for MAST-U SX parameters, and (c) and (d) showing the scaling for MAST-U CD parameters.

ITPA MAST data, the 2011 – 13 MAST data and the MAST-U data shown in this Chapter are given in Table 6.1. Of note are the different plasma currents and divertor designs.

One important application for empirical  $P_{LH}$  scaling laws is for future tokamaks, since providing an estimate for the power required for a particular plasma scenario to transition to H-mode is essential in determining how much auxiliary heating power will be necessary or what operating conditions will be possible or desirable. With the existing experience of designing and operating several spherical tokamaks (such as START, MAST and MAST-U), the UK government is proposing its next national fusion device to be a DEMO-class spherical tokamak called STEP (Spherical Tokamak for Energy Production). As has been touched on as part of the initial motivation for the project in Chapter 1 and demonstrated with data from different time periods on MAST in Chapter 3 as well as from MAST-U in this Chapter, spherical tokamaks have been studied much less extensively than conventional tokamaks and the power threshold and general L-H transition behaviour is less well understood, with empirical scaling laws for  $P_{LH}$  often not capturing the qualitative or quantitative relationship between  $P_{LH}$  and its parameter dependencies. From MAST data, summarised in Figure 6.2,

Parameter	MAST [ITPA]	MAST [this project]	MAST-U experiments
Dates of data collection	2001 – 2003	2011 – 2013	2021
First wall material	Stainless steel	C (graphite)	C (graphite)
Divertor design	Ribbed	MID	baffled with advanced capabilities
Major radius $R_0$ [m]	0.74 – 0.89	0.85	0.85
Minor radius $a$ [m]	0.48 – 0.62	0.65	0.65
Aspect ratio $A$	1.4 – 1.6	1.3	1.3
Plasma current $I_p$ [MA]	0.5 – 0.65	0.72 – 0.76	0.59 – 0.6
Toroidal magnetic field $B_T$ [T]	0.42 – 0.63	0.5 – 0.6	0.54 – 0.6
Elongation $\kappa$	1.64 – 2.02	1.73 – 1.83	1.96 – 2.18
Triangularity $\delta$	0.27 – 0.5	0.46 – 0.49	0.33 – 0.52

Table 6.1: Some of the differences between the MAST dataset used in the Takizuka scaling (ITPA), the MAST dataset used in this project and the MAST-U data of this Chapter.

we can see that the Takizuka scaling (Equation 3.8) appears to estimate  $P_{LH}$  quite well for early transitions in 2001 to 2003 (in green), before the replacement of the initial ribbed divertor with an updated “MAST improved divertor (MID)” with fan-shaped tiles, while for a later L-H transition study dataset from 2011 to 2013, the scaling law underestimates  $P_{LH}$  significantly and doesn’t capture the correct density dependence either. This is true for both the initial method of calculating  $P_{\text{loss}}$  with only shine-through losses subtracted from  $P_{\text{NBI}}$  (plotted in black) and the updated method of calculating  $P_{\text{loss,th}}$  with all beam (fast ion) losses accounted for (plotted in blue). For MAST-U data on the other hand (seen in Figures 6.1 and 6.3b-d), the first experimental campaign suggested that  $P_{LH}$  for scenarios with a conventional divertor configuration was once again quite low and reasonably well estimated by the Takizuka scaling, highlighted by the ease of obtaining ohmic H-modes, but even Super-X H-modes appear to have a lower  $P_{LH}$  than H-modes from the 2011 to 2013 MAST study. While the divertor (both in general design and in choice of configuration) appears to have a significant impact on  $P_{LH}$ , the exact mechanisms or relationships between  $P_{LH}$  and its multiple parameter dependencies are not yet established, and the large number of these potential parameters as well as the complexity of their interactions means that many more large-scale and detailed experimental studies are required to determine a more reliable

scaling law which we could use to confidently predict  $P_{LH}$  for a new device such as STEP.

In the absence of a definitive scaling law to use, we can nevertheless estimate potential values for the required  $P_{LH}$  of different design concepts for STEP by using the existing scaling law by Takizuka et al. [80] as well as fits to the high-density branch of the  $P_{LH}$  study with MAST data. For the parameters of one such example concept [117], which are listed in Table 6.2, the Takizuka scaling estimates  $P_{LH} \sim 90\text{MW}$ , which would be well within the capabilities of the auxiliary heating power  $P_{\text{aux}} < 250\text{MW}$  [117], so H-mode operation appears feasible. As was shown with the various results from MAST and MAST-U data plotted in this thesis, the scaling could be providing a reasonable estimate or it could be predicting a value for  $P_{LH}$  which is much less than what would be seen in practice. Since it is not clear which properties or parameters of the 2011 to 2013 MAST L-H transition study led to the significant increase in  $P_{LH}$  compared to the Takizuka estimate, it is difficult to determine whether STEP would also be affected by this discrepancy. To see what impact this discrepancy, if it did apply, might have on the design of STEP, the Takizuka scaling was modified to incorporate the leading factor and the density dependence of the fit to the MAST  $P_{LH}$  data. For these calculations, following a similar method to the one used in Chapter 3.6.2, the Takizuka scaling of Equation 3.8 was modified with respect to the two fitting options,

$$\text{For } P_{\text{loss}}: P_{LH} = 11.35 \times \bar{n}_{e20}^{1.19} \quad (6.1)$$

$$\text{For } P_{\text{loss,th}}: P_{LH} = 12.24 \times \bar{n}_{e20}^{1.53}, \quad (6.2)$$

and the results of the modified Takizuka scalings with the STEP concept parameters are listed in Table 6.2 as v.1 and v.2 respectively. As can be seen in the Table, these modified scalings would result in predicted  $P_{LH}$  values greater than 900MW, even up to almost 2200MW as the highest value in the range, which in turn would be 360 – 880% of the available auxiliary heating power mentioned in the design concept, i.e. making H-mode operation effectively impossible. We should note that as a DEMO-class device, STEP would be expected to derive much of its heating power from  $\alpha$ -particles (although this would not be the case immediately after starting operations), and that these estimates are likely significant overestimates of the actual expected  $P_{LH}$  since the different heating methods (ECRH and EBW) will not be introducing the additional co-current plasma rotation that neutral beams do on MAST, and

Parameter	STEP [concept [117]]	parameter range
Major radius $R_0$ [m]	3.6	—
Minor radius $a$ [m]	2.0	—
Aspect ratio $A$	1.8	—
Plasma current $I_p$ [MA]	21.5	20.0 – 22.0
Toroidal magnetic field $B_T$ [T]	3.2	—
Elongation $\kappa$	2.93	—
Surface area $S$ [m <sup>2</sup> ] $S \approx 4\pi^2 Ra \sqrt{\frac{1+\kappa^2}{2}}$	622.26	—
Effective charge $Z_{\text{eff}}$	1.4*	1.1 – 1.8*
$P_{LH}$ (from Takizuka) at $\bar{n}_e = 2 \times 10^{20} \text{m}^3$ [MW]	90.2	67.0 – 118.6
$P_{LH}$ (MAST-adj. Takizuka v.1) at $\bar{n}_e = 2 \times 10^{20} \text{m}^3$ [MW]	1244.4	924.3 – 1635.7
$P_{LH}$ (MAST-adj. Takizuka v.2) at $\bar{n}_e = 2 \times 10^{20} \text{m}^3$ [MW]	1658.3	1231.8 – 2179.9

Table 6.2: The parameters of an example STEP design concept [117] which were used to calculate  $P_{LH}$  with the Takizuka scaling and two versions of the scaling adjusted with the leading factor and density dependence of MAST  $P_{LH}$  data (v.1 for the fit to  $P_{\text{loss}}$  and v.2 for the fit to  $P_{\text{loss,th}}$ ). \*For  $Z_{\text{eff}}$ , the values from the MAST study were used.

other experiments on early MAST and on MAST-U have demonstrated lower  $P_{LH}$  already. There are too many unknown variables, including how the divertor affects  $P_{LH}$  and what impact the different heating methods and their dominant channels (ion or electron) will have on  $P_{LH}$ , to be able to confidently predict  $P_{LH}$  for any STEP concept or scenario at this time, but the large range of possible values and the uncertainty whether the available auxiliary heating power will be able to match  $P_{LH}$  make this an exceedingly important area of study that requires more work.

## Appendix A

# Derivation of energy balance

[This derivation has been adapted from [72]]

The collective behaviour of particles can be described with the distribution function  $f(t, \vec{r}, \vec{v})$ . For collisionless plasmas, the total derivative of  $f(t, \vec{r}, \vec{v})$  with respect to  $t$  is zero, resulting in the Vlasov equation

$$\frac{df(t, \vec{r}, \vec{v})}{dt} = \frac{\partial f}{\partial t} + \vec{v} \cdot \nabla f + \vec{a} \cdot \nabla_v f = 0 \quad (\text{A.1})$$

but for a tokamak plasma collisions are important, so a collision term  $\left(\frac{\partial f}{\partial t}\right)_c$  is added and we arrive at the Fokker-Planck equation,

$$\frac{\partial f}{\partial t} + \vec{v} \cdot \nabla f + \vec{a} \cdot \nabla_v f = \left(\frac{\partial f}{\partial t}\right)_c. \quad (\text{A.2})$$

The integral of the velocity distribution function  $f(t, \vec{r}, \vec{v})$  over the whole velocity space gives the particle number density  $n(t, \vec{r})$

$$n(t, \vec{r}) = \int_{-\infty}^{\infty} f(t, \vec{r}, \vec{v}) d\vec{v} \quad (\text{A.3})$$

so for a function  $g(v)$  we can write

$$\int_{-\infty}^{\infty} g \frac{f}{n} d^3v = \langle g \rangle \quad \implies \quad \int_{-\infty}^{\infty} g f d^3v = n \langle g \rangle. \quad (\text{A.4})$$

Equations of particle, momentum and energy balance, which are numerically solved in integrated modelling codes, can be derived by taking moments of the velocity distribution

function  $f(t, \vec{r}, \vec{v})$ , i.e. multiplying Equation A.2 by  $g = v^n$  (for the  $n$ th moment) and integrating over  $d^3v$ ,

$$\underbrace{\int g \frac{\partial f}{\partial t} d^3v}_{\textcircled{1}} + \underbrace{\int g \vec{v} \cdot \nabla f d^3v}_{\textcircled{2}} + \underbrace{\int g \vec{a} \cdot \nabla_v f d^3v}_{\textcircled{3}} = \int g \left( \frac{\partial f}{\partial t} \right)_c d^3v$$

$$\underbrace{\frac{\partial(n \langle g \rangle)}{\partial t} - n \left\langle \frac{\partial g}{\partial t} \right\rangle}_{\textcircled{1}} + \underbrace{\nabla \cdot (n \langle g \vec{v} \rangle) - n \langle \vec{v} \cdot \nabla g \rangle}_{\textcircled{2}} - \underbrace{n \langle \vec{a} \cdot \nabla_v g \rangle}_{\textcircled{3}} = \int g \left( \frac{\partial f}{\partial t} \right)_c d^3v \quad (\text{A.5})$$

where we solved term  $\textcircled{3}$

$$\begin{aligned} \int g \vec{a} \cdot \nabla_v f d^3v &= \int \nabla_v \cdot (g \vec{a} f) d^3v - \int f \nabla_v \cdot (g \vec{a}) d^3v \\ &= [g \vec{a} f]_{-\infty}^{\infty} - \int (f g \nabla_v \cdot \vec{a} + f \vec{a} \cdot \nabla_v g) d^3v \\ &= 0 - \int f \vec{a} \cdot \nabla_v g d^3v, \end{aligned} \quad (\text{A.6})$$

using  $\nabla_v \cdot \vec{a} = 0$  since  $m \vec{a} = q (\vec{E} + \vec{v} \times \vec{B})$ .

Recognising that

$$n \left( \left\langle \frac{\partial g}{\partial t} \right\rangle + \langle \vec{v} \cdot \nabla g \rangle + \langle \vec{a} \cdot \nabla_v g \rangle \right) = n \left\langle \frac{dg}{dt} \right\rangle \quad (\text{A.7})$$

we can simplify Equation A.5 to get

$$\frac{\partial(n \langle g \rangle)}{\partial t} + \nabla \cdot (n \langle g \vec{v} \rangle) - n \left\langle \frac{dg}{dt} \right\rangle = \int g \left( \frac{\partial f}{\partial t} \right)_c d^3v \quad (\text{A.8})$$

which we can now use to derive the zeroth, first and second moment.

## A.1 Particle balance

The zeroth moment, i.e.  $g = v^0 = 1$ , returns the particle balance

$$\frac{\partial n}{\partial t} + \nabla \cdot (n \vec{u}) = \int \left( \frac{\partial f}{\partial t} \right)_c d^3v \quad (\text{A.9})$$

with the rate of particle density change and the particle transport on the left hand side balanced with the collisional particle source on the right hand side. Note that the velocity

$\vec{v}$  is made up of the fluid velocity  $\vec{u}$  and the thermal velocity  $\vec{w}$ ,

$$\begin{aligned}
\vec{v} &= \underbrace{\vec{u}}_{\text{fluid velocity}} + \underbrace{\vec{w}}_{\text{thermal velocity}} \\
\implies \langle \vec{v} \rangle &= \langle \vec{u} + \vec{w} \rangle = \langle \vec{u} \rangle + \underbrace{\langle \vec{w} \rangle}_{=0} = \langle \vec{u} \rangle = \vec{u} \\
\implies \langle \vec{v} \vec{v} \rangle &= \langle (\vec{u} + \vec{w})(\vec{u} + \vec{w}) \rangle = \langle \vec{u} \vec{u} + \vec{w} \vec{w} + 2\vec{u} \vec{w} \rangle \\
&= \langle \vec{u} \vec{u} \rangle + \langle \vec{w} \vec{w} \rangle + 2\vec{u} \underbrace{\langle \vec{w} \rangle}_{=0} = \vec{u} \vec{u} + \langle \vec{w} \vec{w} \rangle
\end{aligned} \tag{A.10}$$

so the particle transport term in Equation A.9 contains the fluid velocity only.

In TRANSP, the particle source terms are calculated with atomic data and the NBI module NUBEAM. The electron particle balance is solved by TRANSP, and the ion density is consistently calculated assuming quasi-neutrality.

## A.2 Momentum balance

Taking the first moment,  $g = v^1 = \vec{v}$ ,

$$\frac{\partial(n\vec{u})}{\partial t} + \nabla \cdot (n\langle \vec{v} \vec{v} \rangle) - n \left\langle \frac{d\vec{v}}{dt} \right\rangle = \int \vec{v} \left( \frac{\partial f}{\partial t} \right)_c d^3v, \tag{A.11}$$

replacing  $\langle \vec{v} \vec{v} \rangle$  with its components as defined in Equation A.10 and multiplying by the mass  $m$  gives

$$m \frac{\partial(n\vec{u})}{\partial t} + \underbrace{m \nabla \cdot (n(\vec{u} \vec{u} + \langle \vec{w} \vec{w} \rangle))}_{\textcircled{A}} - \underbrace{mn \left\langle \frac{d\vec{v}}{dt} \right\rangle}_{n\vec{F}} = \int m \vec{v} \left( \frac{\partial f}{\partial t} \right)_c d^3v. \tag{A.12}$$

The second term  $\textcircled{A}$  can be rewritten as

$$\begin{aligned}
m \nabla \cdot (n(\vec{u} \vec{u} + \langle \vec{w} \vec{w} \rangle)) &= m \nabla \cdot n(\vec{u} \vec{u}) + \nabla \cdot \underbrace{(mn \langle \vec{w} \vec{w} \rangle)}_{\vec{P}: \text{ pressure tensor}} \\
&= m(\nabla \cdot n \vec{u}) \vec{u} + m(n \vec{u} \cdot \nabla) \vec{u} + \nabla \cdot \vec{P}
\end{aligned} \tag{A.13}$$

so using definitions of the force  $\vec{F} \equiv m \left\langle \frac{d\vec{u}}{dt} \right\rangle$  and the pressure tensor  $\overleftarrow{P} \equiv mn \langle \vec{w} \vec{w} \rangle$  we have

$$\underbrace{mn \frac{\partial \vec{u}}{\partial t}}_{\textcircled{1}} + \underbrace{m \vec{u} \frac{\partial n}{\partial t}}_{\textcircled{2}} + \underbrace{m (\nabla \cdot n \vec{u}) \vec{u}}_{\textcircled{2}} + \underbrace{m (n \vec{u} \cdot \nabla) \vec{u}}_{\textcircled{1}} + \nabla \cdot \overleftarrow{P} - n \vec{F} = \int m \vec{v} \left( \frac{\partial f}{\partial t} \right)_c d^3v \quad (\text{A.14})$$

The first four terms on the left hand side can be combined as

$$\begin{aligned} \textcircled{1} : mn \left( \frac{\partial \vec{u}}{\partial t} + (\vec{u} \cdot \nabla) \vec{u} \right) &= mn \frac{d\vec{u}}{dt} \\ \textcircled{2} : m \vec{u} \left( \frac{\partial n}{\partial t} + \nabla \cdot (n \vec{u}) \right) &= m \vec{u} \int \left( \frac{\partial f}{\partial t} \right)_c d^3v. \end{aligned} \quad (\text{A.15})$$

Inserting these into Equation A.14, we arrive at

$$\begin{aligned} mn \frac{d\vec{u}}{dt} + m \vec{u} \int \left( \frac{\partial f}{\partial t} \right)_c d^3v + \nabla \cdot \overleftarrow{P} - n \vec{F} &= \int m \vec{v} \left( \frac{\partial f}{\partial t} \right)_c d^3v \\ mn \frac{d\vec{u}}{dt} = n \vec{F} - \nabla \cdot \overleftarrow{P} + \int m (\vec{v} - \vec{u}) \left( \frac{\partial f}{\partial t} \right)_c d^3v \end{aligned} \quad (\text{A.16})$$

and finally replacing  $\vec{v} - \vec{u} = \vec{w}$  to obtain the momentum balance equation

$$mn \frac{d\vec{u}}{dt} = n \vec{F} - \nabla \cdot \overleftarrow{P} + \int m \vec{w} \left( \frac{\partial f}{\partial t} \right)_c d^3v \quad (\text{A.17})$$

where the rate of momentum change on the left hand side is balanced with the electromagnetic force, the pressure gradient force and the collisional friction force.

### A.3 Energy balance

For the second moment, i.e.  $g = v^2 = \vec{v} \cdot \vec{v}$ ,

$$\underbrace{\frac{\partial (n \langle \vec{v} \cdot \vec{v} \rangle)}{\partial t}}_{\textcircled{1}} + \underbrace{\nabla \cdot (n \langle (\vec{v} \cdot \vec{v}) \vec{v} \rangle)}_{\textcircled{2}} - \underbrace{n \left\langle \frac{d(\vec{v} \cdot \vec{v})}{dt} \right\rangle}_{\textcircled{3}} = \int v^2 \left( \frac{\partial f}{\partial t} \right)_c d^3v \quad (\text{A.18})$$

we can decompose the velocity into its components and recognise that

$$\begin{aligned}
\textcircled{1} : \langle \vec{v} \cdot \vec{v} \rangle &= \langle (\vec{u} + \vec{w}) \cdot (\vec{u} + \vec{w}) \rangle = \langle u^2 \rangle + \langle w^2 \rangle + \underbrace{\langle 2\vec{u} \cdot \vec{w} \rangle}_{=0} = u^2 + \langle w^2 \rangle \\
\textcircled{2} : \langle (\vec{v} \cdot \vec{v}) \vec{v} \rangle &= \langle ((\vec{u} + \vec{w}) \cdot (\vec{u} + \vec{w})) (\vec{u} + \vec{w}) \rangle \\
&= \langle (u^2 + w^2 + 2\vec{u} \cdot \vec{w}) \cdot (\vec{u} + \vec{w}) \rangle \\
&= \langle u^2 \vec{u} \rangle + \langle w^2 \vec{u} \rangle + \underbrace{\langle 2(\vec{u} \cdot \vec{w}) \vec{u} \rangle}_{=0} + \underbrace{\langle u^2 \vec{w} \rangle}_{=0} + \langle w^2 \vec{w} \rangle + \langle 2(\vec{u} \cdot \vec{w}) \vec{w} \rangle \\
&= u^2 \vec{u} + \langle w^2 \rangle \vec{u} + \langle w^2 \vec{w} \rangle + 2\vec{u} \cdot \langle \vec{w} \vec{w} \rangle \\
\textcircled{3} : \left\langle \frac{d(\vec{v} \cdot \vec{v})}{dt} \right\rangle &= \left\langle 2\vec{v} \cdot \frac{d\vec{v}}{dt} \right\rangle
\end{aligned} \tag{A.19}$$

Inserting these into Equation A.22 and multiplying by  $\frac{m}{2}$  we get

$$\begin{aligned}
&\frac{\partial}{\partial t} \left( \frac{nm}{2} u^2 + \frac{nm}{2} \langle w^2 \rangle \right) \\
&+ \nabla \cdot \left( \frac{nm}{2} u^2 \vec{u} + \frac{nm}{2} \langle w^2 \rangle \vec{u} + \frac{nm}{2} \langle w^2 \vec{w} \rangle + \frac{nm}{2} 2\vec{u} \cdot \langle \vec{w} \vec{w} \rangle \right) \\
&- \frac{nm}{2} \left\langle 2\vec{v} \cdot \frac{d\vec{v}}{dt} \right\rangle = \int \frac{1}{2} m v^2 \left( \frac{\partial f}{\partial t} \right)_c d^3v
\end{aligned} \tag{A.20}$$

Recognising

$$\begin{aligned}
\text{pressure: } \frac{nm}{2} \langle w^2 \rangle &= \frac{3}{2} p \\
\text{heat flux: } \frac{nm}{2} \langle w^2 \vec{w} \rangle &= \vec{q} \\
\text{pressure tensor: } nm \langle \vec{w} \vec{w} \rangle &= \overleftrightarrow{P} = p \overleftrightarrow{I} + \overleftrightarrow{\pi} \\
\text{force: } \frac{d\vec{v}}{dt} &= \frac{\vec{F}}{m} = \frac{1}{m} \langle q \vec{E} + q \vec{v} \times \vec{B} \rangle \\
\implies m \left\langle \vec{v} \cdot \frac{d\vec{v}}{dt} \right\rangle &= \langle \vec{v} \cdot \vec{F} \rangle = \langle \vec{v} \cdot q \vec{E} \rangle + \langle \vec{v} \cdot (q \vec{v} \times \vec{B}) \rangle = \vec{u} \cdot (q \vec{E})
\end{aligned} \tag{A.21}$$

we can insert these quantities into the equation to get

$$\begin{aligned}
&\frac{\partial}{\partial t} \left( \frac{nm}{2} u^2 + \frac{3}{2} p \right) + \nabla \cdot \left( \frac{nm}{2} u^2 \vec{u} + \frac{3}{2} p \vec{u} + \vec{q} + \vec{u} \cdot \overleftrightarrow{P} \right) - nq \vec{u} \cdot \vec{E} \\
&= \int \frac{1}{2} m v^2 \left( \frac{\partial f}{\partial t} \right)_c d^3v
\end{aligned} \tag{A.22}$$

The first term in the time derivative and the divergence can be rewritten as

$$\begin{aligned}
& \frac{\partial}{\partial t} \left( \frac{nm}{2} u^2 \right) + \nabla \cdot \left( \frac{nm}{2} u^2 \vec{u} \right) \\
&= \frac{m}{2} \left( n \frac{\partial u^2}{\partial t} + u^2 \frac{\partial n}{\partial t} + n \nabla \cdot (u^2 \vec{u}) + u^2 \vec{u} \cdot \nabla n \right) \\
&= \frac{nm}{2} \left( \frac{\partial u^2}{\partial t} + \nabla \cdot (u^2 \vec{u}) \right) + \frac{mu^2}{2} \underbrace{\left( \frac{\partial n}{\partial t} + \vec{u} \cdot \nabla n \right)}_{\text{use particle balance (Eq A.9)}} \\
&= \frac{nm}{2} \left( \frac{\partial u^2}{\partial t} + \vec{u} \cdot \nabla u^2 + u^2 \nabla \cdot \vec{u} \right) + \frac{mu^2}{2} \left( \int \left( \frac{\partial f}{\partial t} \right)_c d^3v - n \nabla \cdot \vec{u} \right) \\
&= \frac{nm}{2} \left( \frac{\partial u^2}{\partial t} + \vec{u} \cdot \nabla u^2 \right) + \frac{mu^2}{2} \int \left( \frac{\partial f}{\partial t} \right)_c d^3v + \underbrace{\frac{nm u^2}{2} \nabla \cdot \vec{u} - \frac{nm u^2}{2} \nabla \cdot \vec{u}}_{\text{cancel}} \\
&= \frac{nm}{2} \frac{du^2}{dt} + \frac{mu^2}{2} \int \left( \frac{\partial f}{\partial t} \right)_c d^3v
\end{aligned} \tag{A.23}$$

We can take an inner product of  $\vec{u}$  to the momentum balance equation (Eq A.17)

$$\begin{aligned}
mn \vec{u} \cdot \frac{d\vec{u}}{dt} &= n \vec{u} \cdot \vec{F} - \vec{u} \cdot (\nabla \cdot \overleftarrow{P}) + \vec{u} \cdot \int m \vec{w} \left( \frac{\partial f}{\partial t} \right)_c d^3v \\
\frac{nm}{2} \frac{du^2}{dt} &= nq \vec{u} \cdot \vec{E} - \vec{u} \cdot (\nabla \cdot \overleftarrow{P}) + \int m \vec{u} \cdot \vec{w} \left( \frac{\partial f}{\partial t} \right)_c d^3v
\end{aligned} \tag{A.24}$$

Rewriting Equation A.22

$$\begin{aligned}
& \frac{\partial}{\partial t} \left( \frac{3}{2} p \right) + \nabla \cdot \left( \frac{3}{2} p \vec{u} + \vec{q} + \vec{u} \cdot \overleftarrow{P} \right) \underbrace{- nq \vec{u} \cdot \vec{E} + nq \vec{u} \cdot \vec{E}}_{\text{cancel}} - \vec{u} \cdot (\nabla \cdot \overleftarrow{P}) \\
& \quad + \int m \vec{u} \cdot \vec{w} \left( \frac{\partial f}{\partial t} \right)_c d^3v + \frac{mu^2}{2} \int \left( \frac{\partial f}{\partial t} \right)_c d^3v = \int \frac{1}{2} m v^2 \left( \frac{\partial f}{\partial t} \right)_c d^3v \\
& \frac{\partial}{\partial t} \left( \frac{3}{2} p \right) + \nabla \cdot \left( \frac{3}{2} p \vec{u} + \vec{q} \right) + \overleftarrow{P} \cdot (\nabla \cdot \vec{u}) + \underbrace{\vec{u} \cdot (\nabla \cdot \overleftarrow{P}) - \vec{u} \cdot (\nabla \cdot \overleftarrow{P})}_{\text{cancel}} \\
&= \frac{m}{2} \int \underbrace{(v^2 - 2 \vec{u} \cdot \vec{w} - u^2)}_{w^2} \left( \frac{\partial f}{\partial t} \right)_c d^3v
\end{aligned} \tag{A.25}$$

So we finally have the energy balance equation:

$$\frac{\partial}{\partial t} \left( \frac{3}{2} p \right) + \nabla \cdot \left( \frac{3}{2} p \vec{u} + \vec{q} \right) + \overleftarrow{P} \cdot (\nabla \cdot \vec{u}) = \int \frac{1}{2} m n w^2 \left( \frac{\partial f}{\partial t} \right)_c d^3v \tag{A.26}$$

With the assumption of isotropic pressure, i.e.  $\overleftrightarrow{P} = p \overleftrightarrow{I}$ , the energy balance can be written as

$$\begin{aligned} \frac{\partial}{\partial t} \left( \frac{3}{2} p \right) + \nabla \cdot \left( \frac{3}{2} p \vec{u} + \vec{q} \right) + \nabla \cdot (p \vec{u}) - \vec{u} \cdot \nabla p &= \int \frac{1}{2} m n w^2 \left( \frac{\partial f}{\partial t} \right)_c d^3 v \\ \frac{\partial}{\partial t} \left( \frac{3}{2} p \right) + \nabla \cdot \left( \frac{5}{2} p \vec{u} \right) - \vec{u} \cdot \nabla p + \nabla \cdot \vec{q} &= \int \frac{1}{2} m n w^2 \left( \frac{\partial f}{\partial t} \right)_c d^3 v \end{aligned} \quad (\text{A.27})$$

The collisional heating or energy loss term is modelled as

for electrons:

$$\begin{aligned} &\int \frac{1}{2} m_e w_e^2 \left( \frac{\partial f_e}{\partial t} \right)_c d^3 v \\ &= -P_{equi} - \underbrace{\int m_e \vec{w}_e \left( \frac{\partial f}{\partial t} \right)_c d^3 v (\vec{u}_e - \vec{u}_i)}_{\text{collisional friction force}} - P_{rad} - P_{iz} - P_{rec} + P_{NBI}^e + P_{FUS}^e \end{aligned} \quad (\text{A.28})$$

for ions:

$$\int \frac{1}{2} m_i w_i^2 \left( \frac{\partial f_i}{\partial t} \right)_c d^3 v = P_{equi} - P_{cx} - P_{rec} + P_{NBI}^i + P_{FUS}^i$$

[next bit I'm confused].

In stationary state (i.e.  $\frac{d\vec{u}}{dt} \sim 0$ ), taking the inner product  $\cdot \vec{u}$  to the momentum balance equation (Eq A.17) for electrons and ions,

$$\begin{aligned} \text{electrons: } 0 &= -\vec{u}_e \cdot \nabla p_e - n_e e \vec{E} \cdot \vec{u}_e + \vec{u}_e \cdot \int \frac{1}{2} m_e \vec{w}_e \left( \frac{\partial f_e}{\partial t} \right)_c d^3 v \\ \text{ions: } 0 &= -\vec{u}_i \cdot \nabla p_i + n_i e \vec{E} \cdot \vec{u}_i + \vec{u}_i \cdot \int \frac{1}{2} m_i \vec{w}_i \left( \frac{\partial f_i}{\partial t} \right)_c d^3 v \\ &= -\vec{u}_i \cdot \nabla p_i + n_i e \vec{E} \cdot \vec{u}_i - \vec{u}_i \cdot \int \frac{1}{2} m_e \vec{w}_e \left( \frac{\partial f_e}{\partial t} \right)_c d^3 v \end{aligned} \quad (\text{A.29})$$

which we can add together to get the collisional friction force term in the electron heating:

$$\begin{aligned} 0 &= -\vec{u}_e \cdot \nabla p_e - \vec{u}_i \cdot \nabla p_i + \underbrace{\vec{E} \cdot (n_i e \vec{u}_i - n_e e \vec{u}_e)}_{=P_{oh}} + \int \frac{1}{2} m_e \vec{w}_e \left( \frac{\partial f_e}{\partial t} \right)_c d^3 v \cdot (\vec{u}_e - \vec{u}_i) \\ \implies \int \frac{1}{2} m_e \vec{w}_e \left( \frac{\partial f_e}{\partial t} \right)_c d^3 v \cdot (\vec{u}_e - \vec{u}_i) &= -P_{oh} + \vec{u}_e \cdot \nabla p_e + \vec{u}_i \cdot \nabla p_i \end{aligned} \quad (\text{A.30})$$

Replacing the collisional heating term in the energy balance equation gives us the final version

of the electron energy balance

$$\begin{aligned} \frac{\partial}{\partial t} \left( \frac{3}{2} p_e \right) + \nabla \cdot \left( \frac{5}{2} p_e \vec{u}_e \right) + \vec{u}_e \cdot \nabla p_i + \nabla \cdot \vec{q}_e \\ = P_{oh} - P_{equi} - P_{rad} - P_{iz} - P_{rec} + P_{NBI}^e + P_{FUS}^e \end{aligned} \quad (\text{A.31})$$

and ion energy balance

$$\begin{aligned} \frac{\partial}{\partial t} \left( \frac{3}{2} p_i \right) + \nabla \cdot \left( \frac{5}{2} p_i \vec{u}_i \right) - \vec{u}_i \cdot \nabla p_i + \nabla \cdot \vec{q}_i \\ = P_{equi} - P_{cx} - P_{rec} + P_{NBI}^i + P_{FUS}^i \end{aligned} \quad (\text{A.32})$$

where the source and sink terms are defined as

- $\frac{\partial}{\partial t} \left( \frac{3}{2} p_e \right)$  : Rate of electron energy change
- $\frac{\partial}{\partial t} \left( \frac{3}{2} p_i \right)$  : Rate of ion energy change
- $\nabla \cdot \left( \frac{5}{2} p_e \vec{u}_e \right) + \vec{u}_e \cdot \nabla p_i$  : Energy loss rate due to convective electron heat transport
- $\nabla \cdot \left( \frac{5}{2} p_i \vec{u}_i \right) - \vec{u}_i \cdot \nabla p_i$  : Energy loss rate due to convective ion heat transport
- $\nabla \cdot \vec{q}_e$  : Energy loss rate due to conductive electron heat transport
- $\nabla \cdot \vec{q}_i$  : Energy loss rate due to conductive ion heat transport
- $P_{oh}$  : Ohmic heating
- $P_{equi}$  : Equilibration power
- $P_{rad}$  : Radiated energy loss rate
- $P_{iz}$  : Energy loss rate due to impact ionisation
- $P_{cx}$  : Energy loss rate due to charge exchange
- $P_{NBI}^e, P_{NBI}^i$  : NBI heating to electrons and ions, respectively
- $P_{FUS}^e, P_{FUS}^i$  : Alpha heating to electrons and ions, respectively

## Appendix B

# TRANSP neutron deficit - Cecconello 2019

During discussions on the neutron rate match between experimental measurements from the fission chamber and predictions from TRANSP/NUBEAM, previous work by Cecconello *et al.* [86] showing a systematic discrepancy between measured and TRANSP-predicted neutron rates on MAST was highlighted. This work was performed after a similar discrepancy had been found on JET [118], though while the JET study focused on fission chamber neutron rate measurements and found TRANSP to over-predict the neutron rate by 0 – 50% depending on plasma scenario, Cecconello’s MAST study found that TRANSP over-predicted both neutron and proton rates by  $\sim 40\%$  independent of plasma scenario. This value refers to the match between synthetic diagnostics in TRANSP/NUBEAM and the neutron camera (NC) [119] and charged fusion product detector array (CFPD) [120] diagnostics on MAST for neutron and proton rates respectively (see the D-D fusion reaction rates in Equation 1.2 for the origins of protons and neutrons respectively). The absolutely calibrated fission chamber (FC) diagnostic introduced in Chapter 2 measures the total neutron source yield  $Y_n$  with a time resolution of  $10\mu\text{s}$  but no spatial resolution while the NC consists of four collimated lines of sight (steerable between the inboard and outboard sides) which measure the field of view volume integrated neutron emissivity  $\nu_n$  with a time resolution of  $\sim 1\text{ms}$ . The spatial resolution of the neutron count rate profile which can be produced with the NC relies on repeatable discharges, with the lines of sight moved in between discharges and the results combined to produce a multi-shot profile. Before the upgrade, MAST was able to reliably

produce repeatable discharges for most plasma scenarios so this was easily achieved. The requirements of setting the tangency radii of the lines of sight and the multiple repeated and otherwise identical discharges to produce neutron count rate profiles with the NC meant that this diagnostic was not suitable for the studies performed in this project, and instead the FC was used for neutron rate measurements, along with its corresponding synthetic diagnostic in TRANSP. The study by Cecconello *et al.* on the ‘neutron deficit’ or discrepancy between measured and predicted neutron rates concentrated mainly on the NC (and CFPD for protons). The discrepancies between measured and predicted values can be accounted for with the introduction of a scaling factor  $k$ ,

$$\text{measurements} = k \times \text{predictions.} \quad (\text{B.1})$$

For the neutron and proton count rates (CRs) measured with the NC and the CFPD respectively, Cecconello *et al.* found  $k \approx 0.7$ , with the profile shape in good agreement. When investigating the findings by Cecconello *et al.* for the dataset of MAST shots used for this chapter, I had initially assumed that the neutron rates measured by the fission chamber and the neutron camera should be in reasonable agreement, with the main difference being that one measured the total neutron yield and the other measured the neutron emission at particular locations, but that otherwise any trend in ‘neutron deficit’ should be common among both. With this assumption, I generated new sets of TRANSP runs to match the predicted neutron rates to the FC neutron yield including a factor of  $k = 0.7$ . The neutron rate matches and  $D_{\text{an.}}$  values for these runs are shown in Figure B.1(b and d) along with those from the main study (i.e.  $k = 1$ ). After completing this work however, I noticed that the authors did also separately look at a comparison between the FC neutron yield  $Y_n$  measurements and predictions for these discharges and finding that a match between these required  $k \approx 1.1$  instead of 0.7 [86]. The authors further mentioned that this correction factor should account for drifts since the fission chamber’s absolute calibration and that introducing a non-zero anomalous diffusion  $D_{\text{an.}}$  recovered agreement between the measured and synthetic neutron yield data in non-quiescent scenarios, which would suggest no ‘neutron deficit’ existing after all. The apparently very different behaviour by the FC and the NC was not discussed further, so it is unclear whether the authors found any reasons for or consequences of this difference. In conclusion, this process has left me rather confused, with regards to whether or not there

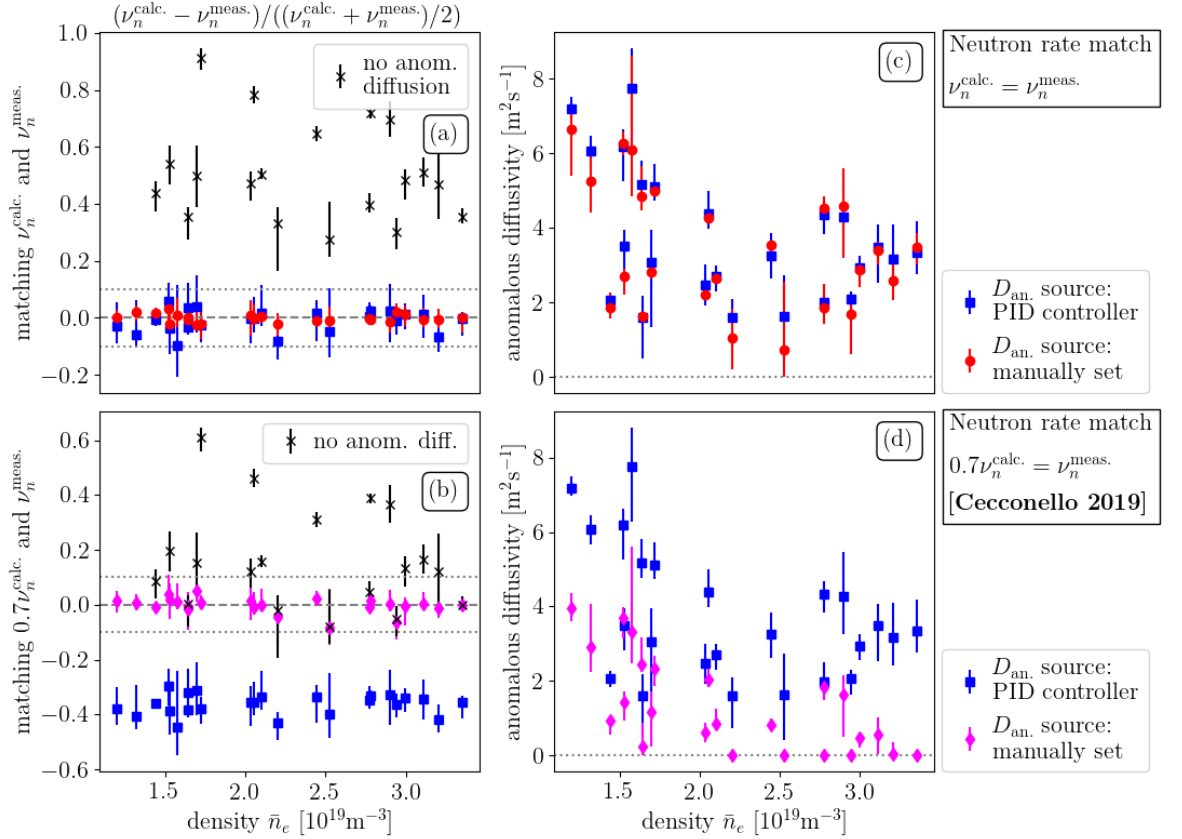


Figure B.1: Neutron rate match and anomalous diffusivity comparisons for PID controller and manual adjustments of the anomalous diffusivity, for neutron rate matches with and without the inclusion of the ‘‘Cecconello factor’’. Note that the factor used was based on a false assumption, so the figure simply shows the dependence on  $D_{\text{an.}}$ .

should be a neutron deficit which cannot be explained by (and corrected with) anomalous diffusion of fast ions, as well as why the neutron rates measured by the fission chamber and the neutron camera are so different, and why they should not be affected in similar ways by fast ion physics or TRANSP calculations. Unfortunately, the mistaken assumption was noticed too late to investigate this further.

# List of References

- [1] F. Ryter, L. Barrera Orte, B. Kurzan, R. M. McDermott, G. Tardini, E. Viezzer, M. Bernert, and R. Fischer. Experimental evidence for the key role of the ion heat channel in the physics of the L-H transition. *Nuclear Fusion*, 54(8), 2014.
- [2] I. Cziegler. *Turbulence and Transport Phenomena in Edge and Scrape-Off-Layer Plasmas*. Ph.D. thesis, Massachusetts Institute of Technology, 2011.
- [3] L. Howlett, I. Cziegler, S. Freethy, H. Meyer, et al. L-H transition studies on MAST: power threshold and heat flux analysis. *Nuclear Fusion*, 63(5):052001, 2023.
- [4] S. J. Ling, J. Sanny, and W. Moebs. *University Physics Volume 3*. OpenStax, 2016.
- [5] Y. Asaoka, K. Okano, T. Yoshida, and K. Tomabechi. Requirements of Tritium Breeding Ratio for Early Fusion Power Reactors. *Fusion Technology*, 30(3P2A):853, 1996.
- [6] J. Wesson. *Tokamaks*. Oxford University Press, 2011.
- [7] A. E. Costley. Towards a compact spherical tokamak fusion pilot plant. *Philosophical Transactions of the Royal Society A: Mathematical, Physical and Engineering Sciences*, 377, 2019.
- [8] L. Spitzer and R. Härm. Transport Phenomena in a Completely Ionized Gas. *Phys. Rev.*, 89:977, 1953.
- [9] Y.-K. Peng. The physics of spherical torus plasmas. *Physics of Plasmas*, 7(5):1681, 2000.
- [10] Y.-K. Peng and D. Strickler. Features of spherical torus plasmas. *Nuclear Fusion*, 26(6):769, 1986.

- [11] F. Troyon, R. Gruber, H. Saurenmann, S. Semenzato, and S. Succi. MHD-limits to plasma confinement. *Plasma Physics and Controlled Fusion*, 26(1A):209, 1984.
- [12] A. Sykes, et al. High-performance of the START spherical tokamak. *Plasma Physics and Controlled Fusion*, 39(12B):B247, 1997.
- [13] W. M. Tang. Microinstability theory in tokamaks. *Nuclear Fusion*, 18(8):72, 1978.
- [14] P. Niskala, T. P. Kiviniemi, S. Leerink, and T. Korpilo. Gyrokinetic simulations of interplay between geodesic acoustic modes and trapped electron mode turbulence. *Nuclear Fusion*, 55(7):8, 2015.
- [15] C. S. Chang, S. Ku, G. R. Tynan, R. Hager, R. M. Churchill, I. Cziegler, M. Greenwald, A. E. Hubbard, and J. W. Hughes. Fast Low-to-High Confinement Mode Bifurcation Dynamics in a Tokamak Edge Plasma Gyrokinetic Simulation. *Physical Review Letters*, 118(17):6, 2017.
- [16] P. H. Diamond, S. I. Itoh, K. Itoh, and T. S. Hahm. Zonal flows in plasma - A review. *Plasma Physics and Controlled Fusion*, 47(5):127, 2005.
- [17] Z. Lin, T. S. Hahm, W. W. Lee, W. M. Tang, and R. B. White. Turbulent transport reduction by zonal flows: Massively parallel simulations. *Science*, 281(5384):4, 1998.
- [18] K. Miki, P. H. Diamond, Ö. D. Gürçan, G. R. Tynan, T. Estrada, L. Schmitz, and G. S. Xu. Spatio-temporal evolution of the L  $\rightarrow$  I  $\rightarrow$  H transition. *Physics of Plasmas*, 19(9):17, 2012.
- [19] N. Winsor, J. L. Johnson, and J. M. Dawson. Geodesic Acoustic Waves in Hydromagnetic Systems. *The Physics of Fluids*, 11(11):3, 1968.
- [20] ASDEX Team. The H-Mode of ASDEX. *Nuclear Fusion*, 29(11):82, 1989.
- [21] ITER Organisation. In *ITER research plan within staged approach*, ITR-Report 18-003. 2018.
- [22] F. Wagner, et al. Regime of Improved Confinement and High Beta in Neutral-Beam-Heated Divertor Discharges of the ASDEX Tokamak. *Physical Review Letters*, 49(19):5, 1982.

- [23] E. Viezzer, T. Pütterich, R. M. McDermott, G. D. Conway, M. Cavedon, M. G. Dunne, R. Dux, and E. Wolfrum. Parameter dependence of the radial electric field in the edge pedestal of hydrogen, deuterium and helium plasmas. *Plasma Physics and Controlled Fusion*, 56(7), 2014.
- [24] K. H. Burrell, et al. Physics of the L-mode to H-mode transition in tokamaks. *Plasma Physics and Controlled Fusion*, 34(13):1859, 1992.
- [25] R. M. McDermott, et al. Edge radial electric field structure and its connections to H-mode confinement in Alcator C-Mod plasmas. *Physics of Plasmas*, 16(5):12, 2009.
- [26] H. Zohm. Edge localized modes (ELMs). *Plasma Physics and Controlled Fusion*, 38(2):105, 1996.
- [27] I. Cziegler, A. E. Hubbard, J. W. Hughes, J. L. Terry, and G. R. Tynan. Turbulence Nonlinearities Shed Light on Geometric Asymmetry in Tokamak Confinement Transitions. *Physical Review Letters*, 118(10):5, 2017.
- [28] K. Ida, S. Hidekuma, Y. Miura, T. Fujita, M. Mori, K. Hoshino, N. Suzuki, and T. Yamauchi. Edge Electric-Field Profiles of H-Mode Plasmas in the JFT-2M Tokamak. *Physical Review Letters*, 65(11):4, 1990.
- [29] M. Schmidtmayr, et al. Investigation of the critical edge ion heat flux for L-H transitions in Alcator C-Mod and its dependence on B T. *Nuclear Fusion*, 58(5):9, 2018.
- [30] M. A. Malkov, P. H. Diamond, K. Miki, J. E. Rice, and G. R. Tynan. Linking the micro and macro: L-H transition dynamics and threshold physics. *Physics of Plasmas*, 22(032506):12, 2015.
- [31] C. F. Maggi, et al. L-H power threshold studies in JET with Be/W and C wall. *Nuclear Fusion*, 54(2):023007, 2014.
- [32] Y. Andrew, et al. H-mode access in the low density regime on JET. *Plasma Physics and Controlled Fusion*, 48(4):479, 2006.
- [33] Y. Ma, J. W. Hughes, A. E. Hubbard, B. LaBombard, R. M. Churchill, T. Golfino, N. Tsujii, and E. S. Marmor. Scaling of H-mode threshold power and L-H edge conditions with favourable ion grad-B drift in Alcator C-Mod tokamak. *Nuclear Fusion*, 52(2):17, 2012.

- [34] Y. Ma, J. W. Hughes, A. E. Hubbard, B. LaBombard, and J. L. Terry. H-mode power threshold reduction in a slot-divertor configuration on the Alcator C-Mod tokamak. *Plasma Physics and Controlled Fusion*, 54(8):6, 2012.
- [35] Y. Andrew, et al. JET divertor geometry and plasma shape effects on the L-H transition threshold. *Plasma Physics and Controlled Fusion*, 46(A87):7, 2004.
- [36] T. Fukuda, et al. H mode transition threshold power scaling and its relation to the edge neutrals in JT-60U. *Nuclear Fusion*, 37(9):15, 1997.
- [37] E. Righi, et al. Isotope scaling of the H-mode power threshold on JET. *Nuclear Fusion*, 39(3):309, 1999.
- [38] P. Gohil, G. McKee, D. Schlossberg, L. Schmitz, and G. Wang. Dependence of the H-mode power threshold on toroidal plasma rotation in the DIII-D tokamak. In *Journal of Physics: Conference Series*, volume 123, page 012017. IOP Publishing, 2008.
- [39] G. McKee, et al. Dependence of the L-to H-mode power threshold on toroidal rotation and the link to edge turbulence dynamics. *Nuclear Fusion*, 49(11):115016, 2009.
- [40] Y. R. Martin and T. Takizuka. Power requirement for accessing the H-mode in ITER. *Journal of Physics: Conference Series*, 123(1):11, 2008.
- [41] P. Sauter, T. Pütterich, F. Ryter, E. Viezzer, E. Wolfrum, G. D. Conway, R. Fischer, B. Kurzan, R. M. McDermott, and S. K. Rathgeber. L- to H-mode transitions at low density in ASDEX Upgrade. *Nuclear Fusion*, 52(1):5, 2012.
- [42] F. Ryter, et al. Survey of the H-mode power threshold and transition physics studies in ASDEX Upgrade. *Nuclear Fusion*, 53(11):113003, 2013.
- [43] W. L. Zhong, et al. Stimulated effect of SMBI on low-to-high confinement transition of tokamak plasmas. *Nuclear Fusion*, 60(8):7, 2020.
- [44] T. N. Carlstrom, P. Gohil, J. G. Watkins, K. H. Burrell, S. Coda, E. J. Doyle, R. J. Groebner, J. Kim, R. A. Moyer, and C. L. Rettig. Experimental survey of the L-H transition conditions in the DIII-D tokamak. *Plasma Physics and Controlled Fusion*, 36(7 A):6, 1994.

- [45] C. Braams and P. Stott. *Nuclear Fusion: Half a Century of Magnetic Confinement Fusion Research*. CRC Press, 2002.
- [46] UK Atomic Energy Authority: STEP site location. <https://step.ukaea.uk/step-siting/>. Accessed: 2024-05-30.
- [47] M. Cox. The Mega Amp Spherical Tokamak. *Fusion Engineering and Design*, 46(2):397, 1999.
- [48] A. Sykes, et al. First results from MAST. *Nuclear Fusion*, 41(10):1423, 2001.
- [49] A. Darke, R. Hayward, G. Counsell, and K. Hawkins. The MAST improved divertor. *Fusion Engineering and Design*, 75-79:285, 2005. Proceedings of the 23rd Symposium of Fusion Technology.
- [50] J. Luxon. A design retrospective of the DIII-D tokamak. *Nuclear Fusion*, 42(5):614, 2002.
- [51] U. Stroth, et al. Overview of ASDEX Upgrade results. *Nuclear Fusion*, 53(10):104003, 2013.
- [52] D. A. Homfray, et al. Overview of MAST Neutral Beam System performance. In *23rd IEEE/NPSS Symposium on Fusion Engineering*, pages 1–4. 2009.
- [53] I. T. Chapman, et al. Overview of MAST results. *Nuclear Fusion*, 55(10):19, 2015.
- [54] J. R. Harrison, et al. Overview of new MAST physics in anticipation of first results from MAST Upgrade. *Nuclear Fusion*, 59, 2019.
- [55] W. Morris, et al. MAST accomplishments and upgrade for fusion next-steps. *IEEE Transactions on Plasma Science*, 42(3):13, 2014.
- [56] E. Havlíčková, W. Fundamenski, M. Wischmeier, G. Fishpool, and A. W. Morris. Investigation of conventional and Super-X divertor configurations of MAST Upgrade using scrape-off layer plasma simulation. *Plasma Physics and Controlled Fusion*, 56(7):075008, 2014.
- [57] K. J. Brunner, T. O’Gorman, G. Naylor, R. Scannell, G. Cunningham, R. Sharples, and N. A. Dipper. FPGA-Based High Bandwidth Integral Electron Density Interferometer For MAST-U. 2016.

- [58] R. Scannell, et al. Design of a new Nd: YAG Thomson scattering system for MAST. *Review of Scientific Instruments*, 79(10), 2008.
- [59] R. Scannell, M. Walsh, M. Dunstan, J. Figueiredo, G. Naylor, T. O’Gorman, S. Shibaev, K. Gibson, and H. Wilson. A 130 point Nd: YAG Thomson scattering diagnostic on MAST. *Review of Scientific Instruments*, 81(10), 2010.
- [60] R. Scannell, M. Walsh, P. Carolan, N. Conway, A. Darke, M. Dunstan, D. Hare, and S. Prunty. Enhanced edge Thomson scattering on MAST. *Review of scientific instruments*, 77(10), 2006.
- [61] M. Wisse. *Charge-Exchange Spectroscopy in the MAST Tokamak*. Ph.D. thesis, University College Cork, 2007.
- [62] C. Vincent. *FPGA Based Diagnostics for the Mega-Amp Spherical Tokamak Upgrade*. Ph.D. thesis, Centre for Advanced Instrumentation, Durham University, 2021.
- [63] C. Vincent, S. Allan, G. Naylor, R. Stephen, S. Bray, A. Thornton, and A. Kirk. Fission chamber data acquisition system for neutron flux measurements on the Mega-Amp Spherical Tokamak Upgrade. *Review of Scientific Instruments*, 93(9):093509, 2022.
- [64] K. Stammers and M. Loughlin. The calibration of the MAST neutron yield monitors. *Nuclear Instruments and Methods in Physics Research Section A: Accelerators, Spectrometers, Detectors and Associated Equipment*, 562(1):521, 2006.
- [65] M. Fox. *Statistical structure of plasma turbulence from BES measurements in MAST and the effect of flow shear*. Ph.D. thesis, University of Oxford, 2016.
- [66] I. G. Kiss, B. Mészáros, D. Dunai, S. Zoletnik, T. Krizsanóczy, A. R. Field, and R. Gaffka. Mechanical design of the two dimensional beam emission spectroscopy diagnostics on MAST. *Fusion Engineering and Design*, 86(6-8):4, 2011.
- [67] S. Gibson. *Measurement of the current profile in fusion tokamaks using the motional Stark effect diagnostic*. Ph.D. thesis, Durham University, 2021.
- [68] A. R. Field, D. Dunai, R. Gaffka, Y. C. Ghim, I. Kiss, B. Mészáros, T. Krizsanóczy, S. Shibaev, and S. Zoletnik. Beam emission spectroscopy turbulence imaging system for the MAST spherical tokamak. *Review of Scientific Instruments*, 83(1):10, 2012.

- [69] A. R. Field, D. Dunai, N. J. Conway, S. Zoletnik, and J. Sárközi. Beam emission spectroscopy for density turbulence measurements on the MAST spherical tokamak. *Review of Scientific Instruments*, 80(7):12, 2009.
- [70] L. L. Lao, H. S. John, R. D. Stambaugh, A. G. Kellman, and W. Pfeiffer. Reconstruction of current profile parameters and plasma shapes in tokamaks. *Nuclear Fusion*, 25(16):12, 1985.
- [71] N. Conway, M. De Bock, C. Michael, M. Walsh, P. Carolan, N. Hawkes, E. Rachlew, J. McCone, S. Shibaev, and G. Wearing. The MAST motional Stark effect diagnostic. *Review of Scientific Instruments*, 81(10), 2010.
- [72] H.-T. Kim. Seoul National University, Lecture notes: Integrated modelling theory for fusion plasmas, 2021.
- [73] R. Hawryluk. In *Physics of Plasma Close to Thermonuclear Conditions (Proc. Course Varenna, 1979)*, CEC, Brussels, volume 1. 1980.
- [74] R. J. Goldston, D. McCune, H. Towner, S. Davis, R. Hawryluk, and G. Schmidt. New techniques for calculating heat and particle source rates due to neutral beam injection in axisymmetric tokamaks. *Journal of computational physics*, 43(1):61, 1981.
- [75] R. J. Akers, et al. L-H Transition in the Mega-Amp Spherical Tokamak. *Physical Review Letters*, 88(3):4, 2002.
- [76] M. Greenwald. Density limits in toroidal plasmas. *Plasma Physics and Controlled Fusion*, 44(8):R27, 2002.
- [77] B. Dudson. *Edge turbulence in the Mega-Amp Spherical Tokamak*. Ph.D. thesis, University of Oxford, 2007.
- [78] F. Ryter, et al. H mode power threshold database for ITER. *Nuclear Fusion*, 36(1217):48, 1996.
- [79] H. Meyer, Y. Andrew, P. G. Carolan, G. Cunningham, E. Delchambre, A. R. Field, A. Kirk, P. Molchanov, V. Rozhansky, and S. Voskoboynikov. Active control of the H-mode transition on MAST. *Plasma Physics and Controlled Fusion*, 50(1):9, 2008.

- [80] T. Takizuka. Roles of aspect ratio, absolute  $B$  and effective  $Z$  of the H-mode power threshold in tokamaks of the ITPA database. *Plasma Physics and Controlled Fusion*, 46(5A):A227, 2004.
- [81] P. B. Snyder, H. R. Wilson, J. R. Ferron, L. L. Lao, A. W. Leonard, T. H. Osborne, A. D. Turnbull, D. Mossessian, M. Murakami, and X. Q. Xu. Edge localized modes and the pedestal: A model based on coupled peeling-ballooning modes. *Physics of Plasmas*, 9(5):7, 2002.
- [82] A. Kirk, et al. ELM characteristics in MAST. *Plasma Physics and Controlled Fusion*, 46(3):551, 2004.
- [83] G. Birkenmeier, et al. Magnetic structure and frequency scaling of limit-cycle oscillations close to L- to H-mode transitions. *Nuclear Fusion*, 56(8), 2016.
- [84] S. Kaye, et al. ITER L-mode confinement database. *Nuclear Fusion*, 37(9):1303, 1997.
- [85] I. Cziegler. York Plasma Institute, Lecture notes: Magnetic confinement fusion, 2018.
- [86] M. Cecconello, W. Boeglin, D. Keeling, S. Conroy, I. Klimek, R. Perez, et al. Discrepancy between estimated and measured fusion product rates on MAST using TRANSP/NUBEAM. *Nuclear Fusion*, 59(1):016006, 2018.
- [87] O. Meneghini, et al. Integrated modeling applications for tokamak experiments with OMFIT. *Nuclear Fusion*, 55(8):083008, 2015.
- [88] E. Stefanikova, M. Peterka, P. Bohm, P. Bilkova, M. Aftanas, M. Sos, J. Urban, M. Hron, and R. Panek. Fitting of the Thomson scattering density and temperature profiles on the COMPASS tokamak. *Review of Scientific Instruments*, 87(11):9, 2016.
- [89] D. Keeling, et al. Mitigation of MHD induced fast-ion redistribution in MAST and implications for MAST-Upgrade design. *Nuclear Fusion*, 55(1):013021, 2014.
- [90] O. Jones, et al. Measurements and modelling of fast-ion redistribution due to resonant MHD instabilities in MAST. *Plasma Physics and Controlled Fusion*, 57(12):125009, 2015.

- [91] M. Turnyanskiy, C. Challis, R. Akers, M. Cecconello, D. Keeling, A. Kirk, R. Lake, S. Pinches, S. Sangaroon, and I. Wodniak. Measurement and control of the fast ion redistribution on MAST. *Nuclear Fusion*, 53(5):053016, 2013.
- [92] I. T. Chapman, M. D. Hua, S. D. Pinches, R. J. Akers, A. R. Field, J. P. Graves, R. J. Hastie, and C. A. Michael. Saturated ideal modes in advanced tokamak regimes in MAST. *Nuclear Fusion*, 50(4):16, 2010.
- [93] I. Klimek, et al. TRANSP modelling of total and local neutron emission on MAST. *Nuclear Fusion*, 55(2):023003, 2015.
- [94] M. Cecconello, et al. Energetic ion behaviour in MAST. *Plasma Physics and Controlled Fusion*, 57(1):014006, 2014.
- [95] I. Cziegler, G. R. Tynan, P. H. Diamond, A. E. Hubbard, J. W. Hughes, J. H. Irby, and J. L. Terry. Zonal flow production in the L-H transition in Alcator C-Mod. *Plasma Physics and Controlled Fusion*, 56(7):9, 2014.
- [96] L. Schmitz. The role of turbulence-flow interactions in L-to H-mode transition dynamics: recent progress. *Nuclear Fusion*, 57(2):025003, 2017.
- [97] P. Manz, et al. Zonal flow triggers the L-H transition in the Experimental Advanced Superconducting Tokamak. *Physics of Plasmas*, 19(7):6, 2012.
- [98] G. R. Tynan, et al. Turbulent-driven low-frequency sheared  $E \times B$  flows as the trigger for the H-mode transition. *Nuclear Fusion*, 53(7):7, 2013.
- [99] C. Holland, G. R. Tynan, R. J. Fonck, G. R. McKee, J. Candy, and R. E. Waltz. Zonal-flow-driven nonlinear energy transfer in experiment and simulation. *Physics of Plasmas*, 14(5):12, 2007.
- [100] Z. Yan, G. McKee, R. Fonck, P. Gohil, R. Groebner, and T. Osborne. Observation of the L-H confinement bifurcation triggered by a turbulence-driven shear flow in a tokamak plasma. *Physical review letters*, 112(12):125002, 2014.
- [101] I. Cziegler, G. R. Tynan, P. H. Diamond, A. E. Hubbard, J. W. Hughes, J. H. Irby, and J. L. Terry. Nonlinear transfer in heated L-modes approaching the L-H transition threshold in Alcator C-Mod. *Nuclear Fusion*, 55(8):9, 2015.

- [102] M. Cavedon, T. Pütterich, E. Viezzer, G. Birkenmeier, T. Happel, F. M. Laggner, P. Manz, F. Ryter, and U. Stroth. Interplay between turbulence, neoclassical and zonal flows during the transition from low to high confinement mode at ASDEX Upgrade. *Nuclear Fusion*, 57(1), 2017.
- [103] P. Manz, M. Xu, N. Fedorczak, S. Thakur, and G. Tynan. Spatial redistribution of turbulent and mean kinetic energy. *Physics of Plasmas*, 19(1), 2012.
- [104] G. R. Tynan, I. Cziegler, P. H. Diamond, M. Malkov, A. E. Hubbard, J. W. Hughes, J. L. Terry, and J. H. Irby. Recent progress towards a physics-based understanding of the H-mode transition. *Plasma Physics and Controlled Fusion*, 58(4):11, 2016.
- [105] S. B. Pope. *Turbulent flows*. Cambridge University, 2000.
- [106] P. Welch. The use of fast Fourier transform for the estimation of power spectra: A method based on time averaging over short, modified periodograms. *IEEE Transactions on audio and electroacoustics*, 15(2):70, 1967.
- [107] Personal communication or repositories.
- [108] T. Kass, S. Günter, M. Maraschek, W. Suttrop, H. Zohm, and A. U. Team. Characteristics of type I and type III ELM precursors in ASDEX upgrade. *Nuclear Fusion*, 38(1):111, 1998.
- [109] Y. Sechrest, T. Munsat, D. Battaglia, and S. Zweben. Two-dimensional characterization of ELM precursors in NSTX. *Nuclear Fusion*, 52(12):123009, 2012.
- [110] N. Oyama. Progress and issues in understanding the physics of ELM dynamics, ELM mitigation, and ELM control. *Journal of Physics: Conference Series*, 123(1):012002, 2008.
- [111] S. J. Freethy, T. Görler, A. J. Creely, G. D. Conway, T. Happel, C. Koenen, P. Hennequin, and A. E. White. Validation of gyrokinetic simulations with measurements of electron temperature fluctuations and density-temperature phase angles on ASDEX Upgrade. *Physics of Plasmas*, 25(5):11, 2018.
- [112] D. E. Smith, E. J. Powers, and G. S. Caldwell. Fast-Fourier-Transform Spectral-Analysis Techniques as a Plasma Fluctuation Diagnostic Tool. *IEEE Transactions on Plasma Science*, 2(4):261, 1974.

- [113] C. Holland, G. R. Tynan, G. R. McKee, and R. J. Fonck. Investigation of the time-delay estimation method for turbulent velocity inference. *Review of Scientific Instruments*, 75(10):4278, 2004.
- [114] Y.-C. Ghim, A. R. Field, D. Dunai, S. Zoletnik, L. Bardóczy, and A. A. Schekochihin. Measurement and physical interpretation of the mean motion of turbulent density patterns detected by the beam emission spectroscopy system on the mega amp spherical tokamak. *Plasma Physics and Controlled Fusion*, 54(9):15, 2012.
- [115] Y. Enters, S. Thomas, M. Hill, and I. Cziegler. Testing image-velocimetry methods for turbulence diagnostics. *Review of Scientific Instruments*, 94(7), 2023.
- [116] I. Cziegler, J. L. Terry, J. W. Hughes, and B. LaBombard. Experimental studies of edge turbulence and confinement in Alcator C-Mod. *Physics of Plasmas*, 17(5):8, 2010.
- [117] H. Meyer. The physics of the preferred plasma scenario for STEP. In *48th EPS Conference of Plasma Physics*, page 4. 2022.
- [118] H. Weisen, et al. The ‘neutron deficit’ in the JET tokamak. *Nuclear Fusion*, 57(7):076029, 2017.
- [119] M. Cecconello, et al. The 2.5MeV neutron flux monitor for MAST. *Nuclear Instruments and Methods in Physics Research Section A: Accelerators, Spectrometers, Detectors and Associated Equipment*, 753:72, 2014.
- [120] R. V. Perez, et al. Investigating fusion plasma instabilities in the Mega Amp Spherical Tokamak using mega electron volt proton emissions (invited)a). *Review of Scientific Instruments*, 85(11):11D701, 2014.